DGK Deutsche Geodätische Kommission
bei der Bayerischen Akademie der Wissenschaften

Reihe C | Dissertationen | Heft Nr. 697

Andrea Heiker

Mutual validation of Earth orientation parameters, geophysical excitation functions and second degree gravity field coefficients

München 2013

Verlag der Bayerischen Akademie der Wissenschaften
in Kommission beim Verlag C. H. Beck

ISSN 0065-5325 ISBN 978-3-7696-5109-6

Diese Arbeit ist gleichzeitig veröffentlicht in:
Wissenschaftliche Arbeiten der Fachrichtung Geodäsie und Geoinformatik der Leibniz Universität Hannover
ISSN 0174-1454, Nr. 304, Hannover 2012

DGK Deutsche Geodätische Kommission
bei der Bayerischen Akademie der Wissenschaften

Reihe C | Dissertationen | Heft Nr. 697

Mutual validation of Earth orientation parameters, geophysical excitation functions and second degree gravity field coefficients

Von der Fakultät für Bauingenieurwesen und Geodäsie
der Gottfried Wilhelm Leibniz Universität Hannover
zur Erlangung des Grades
Doktor-Ingenieur (Dr.-Ing.)
genehmigte Dissertation

von

Dipl.-Ing. Andrea Heiker

geboren
am 04.08.1976 in Damme (Niedersachsen)

München 2013

Verlag der Bayerischen Akademie der Wissenschaften
in Kommission bei der C. H. Beck'schen Verlagsbuchhandlung München

ISSN 0065-5325 ISBN 978-3-7696-5109-6

Diese Arbeit ist gleichzeitig veröffentlicht in:
Wissenschaftliche Arbeiten der Fachrichtung Geodäsie und Geoinformatik der Leibniz Universität Hannover
ISSN 0174-1454, Nr. 304, Hannover 2012

Adresse der Deutschen Geodätischen Kommission:

Deutsche Geodätische Kommission

Alfons-Goppel-Straße 11 ● D – 80 539 München

Telefon +49 – 89 – 23 031 1113 ● Telefax +49 – 89 – 23 031 - 1283 / - 1100

e-mail hornik@dgfi.badw.de ● http://www.dgk.badw.de

Prüfungskommission

Vorsitzender:	Prof. Dr.-Ing. habil. Christian Heipke
Referent:	Prof. Dr.-Ing. habil. Hansjörg Kutterer
Korreferenten:	Prof. Dr.-Ing. habil. Jürgen Müller
	apl. Prof. Dr.-Ing. habil. Michael Schmidt

Tag der Einreichung der Arbeit: 26.10.2012

Tag der mündlichen Prüfung: 21.12.2012

© 2013 Deutsche Geodätische Kommission, München

Alle Rechte vorbehalten. Ohne Genehmigung der Herausgeber ist es auch nicht gestattet,
die Veröffentlichung oder Teile daraus auf photomechanischem Wege (Photokopie, Mikrokopie) zu vervielfältigen

ISSN 0065-5325 ISBN 978-3-7696-5109-6

Abstract

Geophysical processes continuously change the mass distribution of the Earth, including oceans and atmosphere. Continuous mass redistributions change the Earth's gravity field, the tensor of inertia and the relative angular momentum. The variations of the tensor of inertia and the relative angular momentum cause Earth rotation variations. The instantaneous rotation axis and velocity are measured continuously. The time variable gravity field is determined by satellites. The excitation functions model the variations of the tensor of inertia and the relative angular momentum caused by the Earth largest subsystems (atmosphere, oceans and continental hydrology). The Earth Orientation Parameters (EOP), the Gravity Field Coefficients of second degree (GFC2) and the excitation functions depend linearly on the tensor of inertia. This dissertation aims at the validation of the time series by the identification and quantification of the inconsistencies.

The time series are linked by the tensor of inertia, which allows the mutual validation. Three of six tensor elements can be determined redundantly from the time series. Therefore, they are validated by a constrained, linear, least-squares Gauss-Helmert Model (GHM). As the time series originate from different sources, Variance and Covariance Components (VCC) have to be estimated within the adjustment algorithm. This dissertation derives the necessary formulas, which require the multiple calculation of traces of large matrix products. In order to avoid costly numerical calculations of the traces, the Stochastic Monte-Carlo Trace Estimator (SMCTE) which estimates variance components in an unconstrained Gauss-Markov Model (GMM) is proposed in literature. In this work, the SMCTE is extended such that covariance components in a constrained GHM can be estimated.

The sensitivity analysis investigates the extent to which different geophysical models effect the results. The chosen core-mantle coupling model and the approximation of the unobserved time derivatives of the polar motion by analytic functions show the largest effects. In total, nine time series (1×EOP, 2×excitation functions, 5×GRACE GFC2, 1×SLR GFC2), covering nearly six years, are validated by the proposed least-squares adjustment solver. The results consist in adjusted residuals for all time series, the adjusted tensor of inertia and a posteriori Variance Covariance Matrices (VCM), which reflect the relative accuracy of the time series.

The adjusted tensor of inertia results from the weighted average of the individual solutions. The weights are determined by the estimation of the VCC. The equatorial mass terms and the differences between the polar motion and the equatorial motion terms roughly contribute the same weight to the equatorial tensor elements. The axial tensor element is mainly determined by the axial mass terms. The GFC2 have the smallest weight. The residuals of a time series contain those parts of the signal, which are not present in the other time series. Therefore, they contain the inconsistencies. The residuals of most time series are dominated by annual periods. The GFC2 and the gravity field coefficients of higher degrees are correlated due to the joint adjustment of all gravity field coefficients. To analyze the effects of the correlations, the constrained GHM is extended to account for gravity field coefficients up to degree/order 10. The larger the correlations, the larger are the residuals of the gravity field coefficients of higher degrees. The resulting residual potential maps are mainly effected by C_{20}, C_{21} and S_{21} residuals. However, the effect of the residuals of higher degrees is visible in the residual potential maps. Correlations have a significant effect on the calculation of potential maps. Therefore, a release of more covariance information is recommended.

Key words: constrained Gauss-Helmert-Model, estimation of Variance and Covariance Components, validation, Earth Orientation Parameters, Gravity Field Coefficients of second degree, excitation functions

Kurzfassung

Geophysikalische Prozesse verändern kontinuierlich die Massenverteilungen innerhalb des Erdkörpers, zu dem auch Atmosphäre und Ozeane gehören. Durch die Massenumverteilungen ändern sich das Schwerefeld, der Trägheitstensor und der relative Drehimpuls der Erde. Die Variationen des Trägheitstensors und des relativen Drehimpulses verursachen Veränderungen der Rotation der Erde. Die aktuelle Rotationsachse und Rotationsgeschwindigkeit werden durch kontinuierliche Messungen erfasst. Das variable Schwerefeld wird mit Hilfe von Satelliten bestimmt. Die Anregungsfunktionen modellieren für einzelne Subsysteme (Atmosphäre, Ozeane, kontinentale Hydrologie) die Variationen des Trägheitstensors (Massenterme) und der relativen Drehimpulse (Bewegungsterme). Die Erdorientierungsparameter (EOP), die Schwerefeldkoeffizienten zweiten Grades (GFC2) und die Anregungsfunktionen sind linear vom Trägheitstensor abhängig. Das Ziel der Arbeit ist es, die Zeitreihen zu validieren, indem vorhandene Inkonsistenzen identifiziert und quantifiziert werden.

Die gegenseitige Validierung der Zeitreihen erfolgt mit Hilfe des Trägheitstensors. Drei der sechs Elemente des Trägheitstensors können redundant aus den Zeitreihen bestimmt werden, so dass die Zeitreihen mit Hilfe eines bedingten, linearen Gauß-Helmert Ausgleichungsmodells nach der Methode der kleinsten Quadrate validiert werden. Da die Zeitreihen aus unterschiedlichen Quellen stammen, müssen zusätzlich Varianz- und Kovarianzkomponenten geschätzt werden. Die vorliegende Arbeit leitet die benötigten Formeln her, die die mehrfache Berechnung von Spuren großer Matrizenprodukte erfordern. Um die nummerisch sehr aufwendigen Berechnungen der Spuren zu umgehen, wird in der Literatur ein Stochastischer Monte-Carlo Spurschätzer (SMCTE) vorgeschlagen, der Varianzkomponenten in einem Gauß-Markov Modell ohne zusätzliche Bedingungsgleichungen schätzt. Der bestehende SMCTE wird im Rahmen der Arbeit so erweitert, dass auch Kovarianzkomponenten in einem bedingten Gauß-Helmert Modell geschätzt werden können.

Im Rahmen der Sensitivitätsanalyse wird ferner untersucht, inwieweit unterschiedliche geophysikalische Modelle die Ergebnisse beeinflussen. Das gewählte Modell für die Kern-Mantel-Kopplung und die Approximation der unbeobachteten Zeitableitung der Polbewegung durch analytische Funktionen besitzen den größten Einfluss. Insgesamt neun Zeitreihen (1×EOP, 2×Anregungsfunktionen, 5×GRACE GFC2, 1×SLR GFC2), die einen Zeitraum von fast sechs Jahren abdecken, werden mit Hilfe des vorgeschlagen Ausgleichungsalgorithmus validiert. Aus der Ausgleichung resultieren ausgeglichene Residuen für alle Zeitreihen, der ausgeglichene Trägheitstensor und a posteriori Varianzkovarianzmatrizen, die die relative Genauigkeiten der Zeitreihen reflektieren.

Der ausgeglichene Trägheitstensor ist ein gewichtetes Mittel der Einzellösungen. Die Gewichte werden über die Varianzkomponentenschätzung bestimmt. Die äquatorialen Massenterme und die Differenz aus der Polbewegung und den äquatorialen Bewegungstermen tragen mit ungefähr demselben Gewicht zu den äquatorialen Trägheitstensorelementen bei. Das axiale Tensorelement wird zum größten Teil durch die axialen Massenterme bestimmt. Die Schwerefeldkoeffizienten besitzen jeweils die geringsten Gewichte. Die Residuen einer Zeitreihen enthalten diejenigen Signalanteile, die nicht in den anderen Zeitreihen enthalten sind. Sie enthalten somit die Inkonsistenzen. Die Residuen der meisten Zeitreihen sind von jährliche Perioden dominiert. Zwischen den GFC2 und den Schwerefeldkoeffizienten höheren Grades existieren Korrelationen, die durch die gemeinsame Bestimmung aller Schwerefeldkoeffizienten entstanden sind. Um den Einfluss der Korrelationen zu untersuchen, wurde das bedingte Gauß-Helmert Modell um Schwerefeldkoeffizienten bis zum Grad/Ordnung 10 erweitert. Je höher die Korrelationen sind, desto größer sind die Residuen der Schwerefeldkoeffizienten höheren Grades. Die resultierenden Residuenpotentialkarten sind durch C_{20}, C_{21} und S_{22} Residuen dominiert. Ein Einfluss der Residuen höheren Grades ist in den Residuenpotentialkarten erkennbar. Korrelationen spielen somit eine wesentliche Rolle bei der Berechnung von Potentialkarten. Daher sollten Korrelationen vermehrt veröffentlicht werden.

Stichwörter: bedingtes Gauß-Helmert-Modell, Varianz-Kovarianzkomponentenschätzung, Validierung, Erdorientierungsparameter, Schwerefeldkoeffizienten zweiten Grades, Anregungsfunktionen

Contents

Abbreviations **9**

Nomenclature: Geophysical parameters **10**

1. Introduction and motivation **12**
1.1. Historical development and current situation of the Earth rotation research 12
1.2. Objective and outline of the dissertation 13

2. Model of the rotating Earth **17**
2.1. Reference systems and reference frames 17
2.1.1. Celestial and terrestrial reference systems and frames 17
2.1.2. Transformation between the ITRS and GCRS 17
2.2. Theory of the Earth's rotation 18
2.2.1. Euler Liouville Equation 18
2.2.2. Euler Liouville Equation for a deformable Earth 21
2.2.3. IERS Earth Orientation Parameters and the rotation vector of the Earth 24
2.2.4. Excitation functions from geophysical models 26
2.3. Gravity field of the Earth 27

3. Estimation of Variance and Covariance Components in a constrained Gauss-Helmert Model **31**
3.1. Least-squares adjustment in a constrained Gauss-Helmert Model 31
3.2. Best Invariant Quadratic Estimation of Variance and Covariance Components 34
3.3. Stochastic Monte-Carlo Trace Estimator 37

4. Combined analysis of EOP, GFC2 and geophysical excitation functions in a constrained GHM **41**
4.1. Preprocessing of the data: Filter 41
4.2. Realisation of the Gauss-Helmert Model 42
4.2.1. Functional model 42
4.2.2. Stochastic model 46
4.3. Sensitivity analysis 47
4.3.1. Comparison of time series with different units 47
4.3.2. Splines versus numerical differentiation 49
4.3.3. Effect of different numerical values for geophysical constants 49

5. Results **52**
5.1. Data description 52
5.1.1. Earth Orientation Parameters 52
5.1.2. Gravity field coefficients 52
5.1.3. Excitation functions 55
5.1.4. Comparison of preliminary tensor elements obtained from the time series 57
5.2. Mutual validation of EOP, excitation functions and GFC2 59
5.2.1. A priori setting of the adjustment model and adjustment 59
5.2.2. Adjusted residuals 61
5.2.3. Partial redundancies and a posteriori stochastic model 66
5.2.4. Summary and open questions 70
5.3. Investigation of further open questions 71
5.3.1. Effect of the filter on the least-squares adjustment 71
5.3.2. Effect of the tensor trace constraint 72
5.3.3. Effect of covariances on the gravity field coefficients of higher degrees 74

6. Summary and outlook **77**
6.1. Summary 77
6.2. Outlook 78

Appendix A. Removing long periodic tidal variations from EOP **80**

Appendix B. Theorems from Koch (1999) **81**

Appendix C. Förstner's approach and the estimation of covariance components **82**

Appendix D. Algorithm: Pseudocode of the extended SMCTE **84**

Appendix E. Reduction of unknown parameters (spline coefficients) **85**

Lebenslauf / Curriculum Vitae **95**

Danksagung / Acknowledgement **96**

Abbreviations

AAM	Atmospheric Angular Momentum functions
BIQUE	Best Invariant Quadratic Estimation
CIP	Celestial Intermediate Pole
CSR	University of Texas Center for Space Research
DORIS	Doppler Orbit determination and Radio positioning Integrated on Satellite
EAMF	Effective Angular Momentum Functions
ECCO	Estimating the Circulation and Climate of the Ocean
ECMWF	European Center for Medium-range Weather Forecast
ELE	Euler Liouville Equation
EOP	Earth Orientation Parameters
DLR	Deutsche Forschungsanstalt für Luft und Raumfahrt
GCRS	Geocentric Celestial Reference System
GFC2	Gravity Field Coefficients of second degree
GFZ	GeoForschungsZentrum Potsdam
GHM	Gauss-Helmert Model
GMM	Gauss-Markov Model
GNSS	Global Navigation Satellite Systems
GPS	Global Positioning System
GRACE	Gravity Recovery and Climate Experiment
GRGS	Groupe de Recherche de Géodésie Spatiale
HAM	Hydrological Angular Momentum functions
ICRF	International Celestial Reference Frame
ICRS	International Celestial Reference System
IERS	International Earth Rotation and References Systems Service
ITRF	International Terrestrial Reference Frame
ITRS	International Terrestrial Reference System
J2000.0	Epoch identifier: January 1st 2000, 12:00 UTC
JPL	Jet Propulsion Laboratory
LLR	Lunar Laser Ranging
LOD	Length Of Day
LSDM	Land Surface Discharge Model
MINQUE	Minimum Norm Quadratic Unbiased Estimation
NCEP	National Centers for Environmental Prediction
OAM	Oceanic Angular Momentum functions
OMCT	Ocean Model for Circulation and Tides
SLR	Satellite Laser Ranging
SMCTE	Stochastic Monte-Carlo Trace Estimator
TU	Tensor Unit
UTC	Coordinated Universal Time
UT1	Universal Time
VCC	Variance and Covariance Components
VCM	Variance Covariance Matrices
VLBI	Very Long Baseline Interferometry

Nomenclature: Geophysical parameters

	SI-Unit	Description
A	$\mathrm{kg\,m^2}$	smallest principal moment of inertia
A'	$\mathrm{kg\,m^2}$	average of the smallest and intermediate principal moments of inertia
A_C	$\mathrm{kg\,m^2}$	smallest principal moment of inertia of the core
A_M	$\mathrm{kg\,m^2}$	smallest principal moment of inertia of the crust and mantle
B	$\mathrm{kg\,m^2}$	intermediate principal moment of inertia
C	$\mathrm{kg\,m^2}$	largest principal moment of inertia
C_C	$\mathrm{kg\,m^2}$	largest principal moment of inertia of the core
C_{nm}		normalized gravity field coefficient of degree n and order m (Cosine term)
C_M	$\mathrm{kg\,m^2}$	largest principal moment of inertia of the crust and mantle
D_a	$\mathrm{kg\,m^2}$	coefficient relating changes in the inertia tensor to changes of LOD
D_e	$\mathrm{kg\,m^2}$	coefficient relating changes in the inertia tensor to changes of the polar motion
G	$\mathrm{m^3\,kg^{-1}\,s^{-2}}$	Newtonial constant of gravitation
M	kg	mass of the Earth
S_{nm}		normalized gravity field coefficient of degree n and order m (Sine term)
a	m	radius of a sphere having the same volume as the Earth
$\boldsymbol{c}$	$\mathrm{kg\,m^2}$	vector containing the tensor elements c_{xz}, c_{yz} and c_{zz}
$\tilde{c}$	$\mathrm{kg\,m^2}$	complex combination of the equatorial tensor elements c_{xz} and c_{yz}
c_{xx}	$\mathrm{kg\,m^2}$	change in the (x,x)-element of the Earth's tensor of inertia due to mass redistribution
c_{xy}	$\mathrm{kg\,m^2}$	change in the (x,y)-element of the Earth's tensor of inertia due to mass redistribution
c_{xz}	$\mathrm{kg\,m^2}$	change in the (x,z)-element of the Earth's tensor of inertia due to mass redistribution
c_{yy}	$\mathrm{kg\,m^2}$	change in the (y,y)-element of the Earth's tensor of inertia due to mass redistribution
c_{yz}	$\mathrm{kg\,m^2}$	change in the (y,z)-element of the Earth's tensor of inertia due to mass redistribution
c_{zz}	$\mathrm{kg\,m^2}$	change in the (z,z)-element of the Earth's tensor of inertia due to mass redistribution
$\boldsymbol{h}$	$\mathrm{kg\,m^2\,s^{-1}}$	angular momentum vector due to motion relative to the terrestrial reference frame
$\tilde{h}$	$\mathrm{kg\,m^2\,s^{-1}}$	complex combination of the equatorial angular momentum h_x and h_y
h_x	$\mathrm{kg\,m^2\,s^{-1}}$	x-component of the change in the relative angular momentum due to motion
h_y	$\mathrm{kg\,m^2\,s^{-1}}$	y-component of the change in the relative angular momentum due to motion
h_z	$\mathrm{kg\,m^2\,s^{-1}}$	z-component of the change in the relative angular momentum due to motion
k_2		second degree body tide Love number of the Earth
k_2'		second degree load Love number of the Earth
$\boldsymbol{m}$		vector containing the elements m_x, m_y and m_z
$\tilde{m}$		complex-valued position of the rotation pole in the terrestrial frame
m_x		x-component of position of the rotation pole in the terrestrial frame
m_y		y-component of position of the rotation pole in the terrestrial frame
m_z		deviation of the mean rotation velocity due to the difference UT1–UTC
n_0		parameter related to the changes of the inertia tensor due radial deformation
$\tilde{p}$	$''$	complex-valued position of the CIP in the terrestrial frame
p_x	$''$	x-component of position of the CIP in the terrestrial frame
p_y	$''$	y-component of position of the CIP in the terrestrial frame
r	m	radius

u_r	$\mathrm{m\,s^{-1}}$	radial component of the velocity vector
u_λ	$\mathrm{m\,s^{-1}}$	west-east component of the velocity vector
u_ϕ	$\mathrm{m\,s^{-1}}$	north-south component of the velocity vector
$\boldsymbol{x}$		position vector
$\tilde{\chi}$		complex combination of the excitation functions χ_x and χ_y
χ_x		x-component of the excitation functions
χ_y		y-component of the excitation functions
χ_z		z-component of the excitation functions
$\Delta k'_{an}$		modification of the degree-2 load Love number due to anelasticity
$\Delta k_{ocn,s}$		oceanic Love number for the spin of the Earth
$\Delta k_{ocn,w}$		oceanic Love number for the wobble of the Earth
ϵ_C		ellipticity of the surface of the core
λ	$^\circ$	longitude
Ω	$\mathrm{rad\,s^{-1}}$	mean rotation velocity
$\boldsymbol{\omega}$	$\mathrm{rad\,s^{-1}}$	Earth rotation vector
ϕ	$^\circ$	latitude
ρ	$\mathrm{kg\,m^{-3}}$	density
ϑ	$^\circ$	polar distance: $\vartheta = 90^\circ - \phi$

1. Introduction and motivation

1.1. Historical development and current situation of the Earth rotation research

"Eppur si muove." (Italian: And yet it moves.) According to a popular legend, Galileo Galilei has muttered this phrase just after he was forced to recant the theory of heliocentrism. The Catholic Church dismissed the theory of heliocentrism in 1616 and declared it as contrary to the Holy Scripture. Galilei (1632) defended the ideas of Copernicus (1543), who proposed a heliocentric world system in which the Moon rotates about the Earth in a spherical orbit; the Earth rotates about its own axis in one day and rotates about the Sun in one year. After this publication, Galileo Galilei was ordered to Rome and was forced to abjure in 1633. He was not rehabilitated until 1992, when pope John Paul II issued a declaration acknowledging the committed error (Cowell, 1992).

The arising Age of Enlightenment fueled the progress in natural sciences. Isaac Newton and Leonard Euler (Newton, 1687; Euler, 1765) predicted that the Earth's rotation and figure axis are divergent and that the pole describes a circular motion. Based on the known flattening of the Earth, Euler (1765) predicted a period of approximately 10 months for the polar motion, which could not be detected by the astronomers. Seth Carlo Chandler (Chandler, 1891) detected a wobble with a dominant period of approximately 14 months more than 100 years after Euler's publication. Since then, this wobble has been called the Chandler wobble in his honor. According to Newcomb (1902, page 116), the Earth is more rigid than steel but not perfectly rigid. He explained the large deviation between the Euler and the Chandler frequency by the elastic reaction of the Earth.

The variations of the polar motion and the rotation velocity have been observed since approximately 1850. The Earth Orientation Parameters (EOP) were first derived from astronomic observations. Nowadays, they are obtained with high accuracy by combining five different measurement techniques: Very Long Baseline Interferometry (VLBI), Satellite Laser Ranging (SLR), Global Navigation Satellite Systems (GNSS), Doppler Orbit determination and Radio positioning Integrated on Satellite (DORIS) and Lunar Laser Ranging (LLR). These techniques are sensitive to different EOP. Therefore, only the combination of all techniques delivers the complete set of EOP with sufficient accuracy. Additionally, SLR allows to determine the time variable gravity field with a low spatial resolution. However, the gravity field coefficients and the EOP cannot be simultaneously determined by SLR. Therefore, either the EOP or the gravity field coefficients have to be considered as fixed parameters. Furthermore, the Gravity Recovery and Climate Experiment (GRACE) observes the time variable gravity field with a high spatial resolution since 2002 (Tapley et al., 2004).

The divergent figure and rotation axis of the Earth would coincide over time due to dissipation caused by the anelastic reaction of the Earth's body. Then, the amplitude of the Chandler wobble would be damped. However, the amplitude of the Chandler period is not decreasing, it is excited by geophysical processes. The amplitude and the phase of the Chandler wobble changes continuously. It is widely accepted that not only the atmosphere, oceans and hydrology but also the postglacial rebound and earthquakes excite the Chandler wobble, (e.g. Gross, 1986; Wahr, 1988; Aoyama and Naito, 2000; Gross, 2000; Aoyama et al., 2003; Liao et al., 2003; Gibert and Le Mouël, 2008; Zotov and Bizouard, 2012). Though, the exact excitation mechanisms are currently not completely understood. Seitz and Stuck (2004), Seitz (2005) and Chao and Chung (2011) excited Earth models with purely random functions. The modeled polar motion time series show a similar pattern as the observed polar motion time series. It is therefore concluded that random events might play an important role for the excitation of the Chandler wobble.

The changes of the Earth's rotation axis and velocity are caused by geophysical processes in the Earth's core, mantle, oceans and atmosphere. The distribution of the masses varies and the motions of the masses generate currents. The mass redistribution changes directly the gravity field of the Earth and the Earth's tensor of inertia. The currents lead to variations of the Earth's relative angular momentum. Variations of the tensor of inertia and the relative angular momentum change the Earth's rotation. The contributions of the largest subsystems of the Earth (atmosphere, oceans and continental hydrology) to the Earth rotation variations are approximated by models. The modeled excitation functions provide the contribution of the subsystems to the total relative angular momentum and tensor of inertia. The variations of the Earth's rotation induce further indirect effects, which have to be considered if the Earth's rotation is described by models. Figure 1.1 gives an overview over the direct and indirect effects caused by geophysical processes.

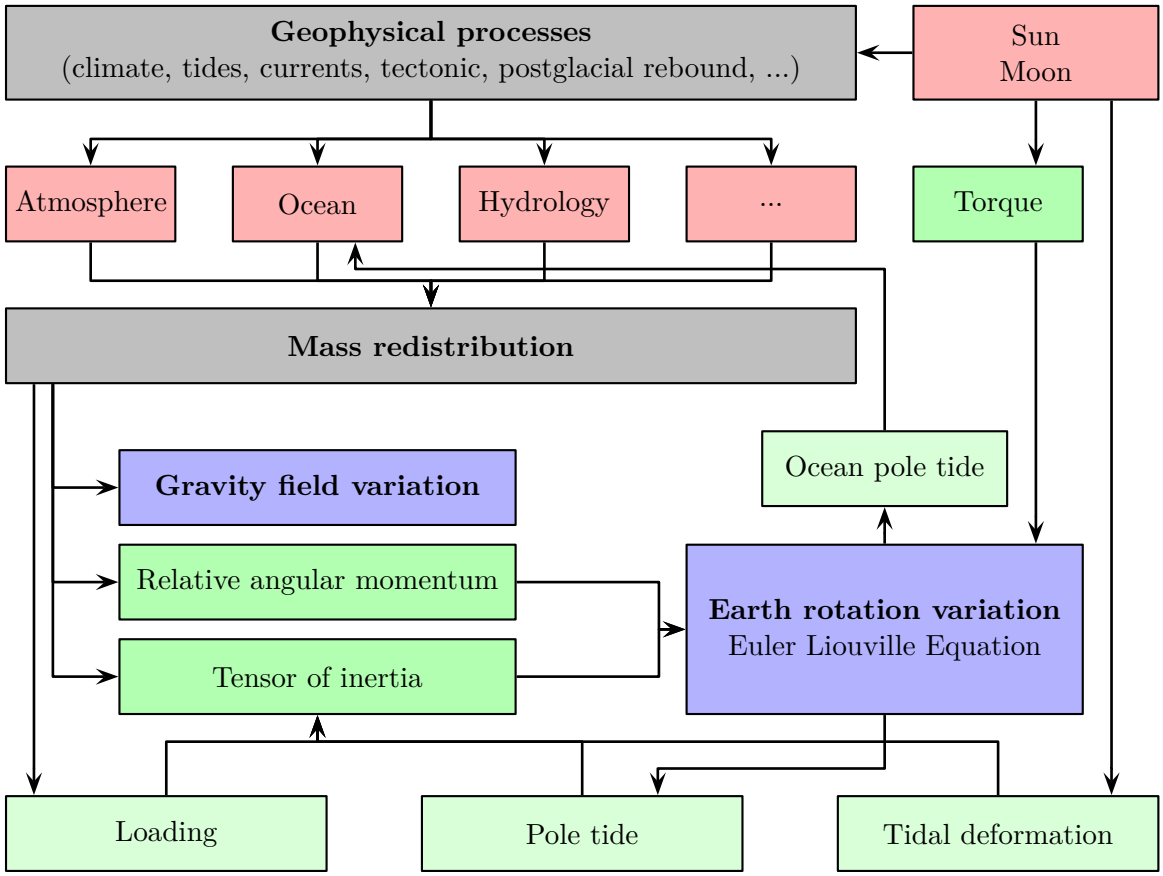

Figure 1.1: The graph describes the Earth rotation variations due to geophysical processes. Red boxes denote the effects caused by the Earth's subsystems. Direct effects are depicted with green boxes and indirect effects with light green boxes (Seitz, 2004, modified).

1.2. Objective and outline of the dissertation

This dissertation aims at the mutual validation of the EOP, Gravity Field Coefficients of second degree (GFC2) and excitation functions. As mentioned before, the mass redistribution causes variations of the Earth rotation and the gravity field coefficients. The GFC2 are functionally related to the tensor of inertia. According to Figure 1.1, Earth rotation variations are caused by the variations of the tensor of inertia and the relative angular momentum. The excitation functions model the contributions of the Earth's largest subsystems (atmosphere, oceans and continental hydrology) to the tensor of inertia (mass terms) and to the angular momentum (motion terms). Smaller subsystems (e.g. cryosphere, core) are neglected so far. The available excitation functions are assumed to model the effect of the mass redistribution on the total relative angular momentum and the total tensor of inertia with sufficient accuracy. Therefore, the common link between the EOP, the GFC2 and the excitation functions is the Earth's total tensor of inertia. All time series depend linearly on the Earth's tensor of inertia. Inconsistencies between the time series might arise due to different or inaccurate geophysical models and due to measurement errors. As the time series are derived independently, the common relation to the tensor of inertia allows the independent mutual validation by quantifying the inconsistencies of the time series. In particular, systematic periodic patterns in the inconsistencies are of interest.

The data are partly delivered with stochastic information, in terms of standard deviations and covariances. However, complete stochastic information is not available for all time series. Furthermore, the given stochastic information reflects the internal uncertainty of the specific time series. The internal uncertainty describes the variations of measurement results, obtained by repeated measurements of the same object under specified conditions (JCGM, 2008). Therefore, the given stochastic information does not describe the agreement of time series from different origins. The validation has to consider all available a priori stochastic information and has to provide an appropriate a posteriori stochastic model which reflects the agreement of time series from different origins.

Three of the six elements of the tensor of inertia can be redundantly determined by

1. the difference of the EOP and the motion terms of the excitation functions,
2. the mass terms of the excitation function and
3. the GFC2.

According to Rochester and Smylie (1974), the trace of the tensor of inertia is invariant to mass redistributions as long as the principle of mass conservation holds. Their result allows to constrain the determination of the tensor of inertia by a further linear relation. Since all functional relations between the time series and the tensor of inertia are linear and since at least three of the six tensor elements are redundantly determinable, a constrained linear least-squares adjustment is chosen as a suitable method for the mutual validation. The constrained least-squares adjustment has to include an estimation of Variance and Covariance Components (VCC), in order to obtain the demanded a posteriori stochastic model.
Koch (1999) developed the Best Invariant Quadratic Estimation (BIQUE) of VCC in an unconstrained Gauss-Markov Model (GMM). His approach is adapted in this dissertation to obtain a BIQUE of VCC in a constrained Gauss-Helmert Model (GHM). The resulting formulas are identical to the formulas in Yu (1992), who obtained the BIQUE of VCC in a constrained GHM in a different way. The estimation of VCC requires the calculation of several traces of matrix products. If the least-squares adjustment problem considers a large amount of measurements, the calculation of the traces requires therefore a large number of floating point operations. Förstner (1979) proposed an alternative to the original approach, which reduces the number of floating point operations essentially. Since the exact calculation of the traces remains computationally intensive, even with Förstner's approach, Koch and Kusche (2002), Kusche and Klees (2002) and Kusche (2003) proposed an efficient Stochastic Monte-Carlo Trace Estimator (SMCTE). Their approach is based on Förstner's approach and avoids the exact calculation of the traces. It approximates the traces of symmetric matrices by a stochastic Monte-Carlo sampler. However, doubt arises during the work on this dissertation that Förstner's approach is in any case suitable for the estimation of covariance components. Appendix C contains an example in which a covariance component can be successfully estimated with the original approach, whereas the estimation fails using Förstner's approach. Therefore, Förstner's approach is not considered further in this dissertation. Since the SMCTE of Koch and Kusche (2002), Kusche and Klees (2002) and Kusche (2003) is based on Förstner's approach, their SMCTE is extended within this dissertation to deal with the original approach and asymmetric matrices. The resulting least-squares adjustment model is a universal, linear least-squares solver, suitable for each adjustment problem, which can be handled by linearization with sufficient accuracy.
The mutual validation is performed by the proposed least-squares adjustment model. The EOP, GFC2 and excitation functions are considered as (pseudo)observations, whereas the Earth's total tensor of inertia is considered as unknown. The a priori Variance Covariance Matrices (VCM) are either delivered together with the time series or approximated by empirical auto- and crosscorrelation functions. The functional model of the least-squares adjustment is basically described by geophysical models, relating each time series to the tensor of inertia. As the time series possess different temporal resolutions (daily and monthly), the daily time series have to be downsampled to monthly epoch values. The functional model additionally requires the unobserved time derivatives of the polar motion. Two approaches for the downsampling and the approximation of the time derivatives are analyzed within a sensitivity analysis. The first approach approximates the monthly epoch values and the time derivatives by cubic splines. The second approach calculates monthly averages and approximates the time derivatives by difference quotients. The sensitivity analysis additionally investigates different geophysical constants, and the finally chosen formulation of the functional model is based on the results of the sensitivity analysis.
The mutual validation is performed by applying the proposed least-squares adjustment algorithm. The residuals contain the inconsistencies and are analyzed in the time domain and in the frequency domain. The frequency analysis reveals dominant periods. The a posteriori stochastic model is obtained from the adjusted VCC and reflects the agreement of different time series. A comparison of the a priori and the adjusted VCM points to the quality of the a priori stochastic models.
Based on the initial task of the mutual validation, Figure 1.2 illustrates the content of this dissertation. The literature provides the functional models and some basic ideas developed further within this disser-

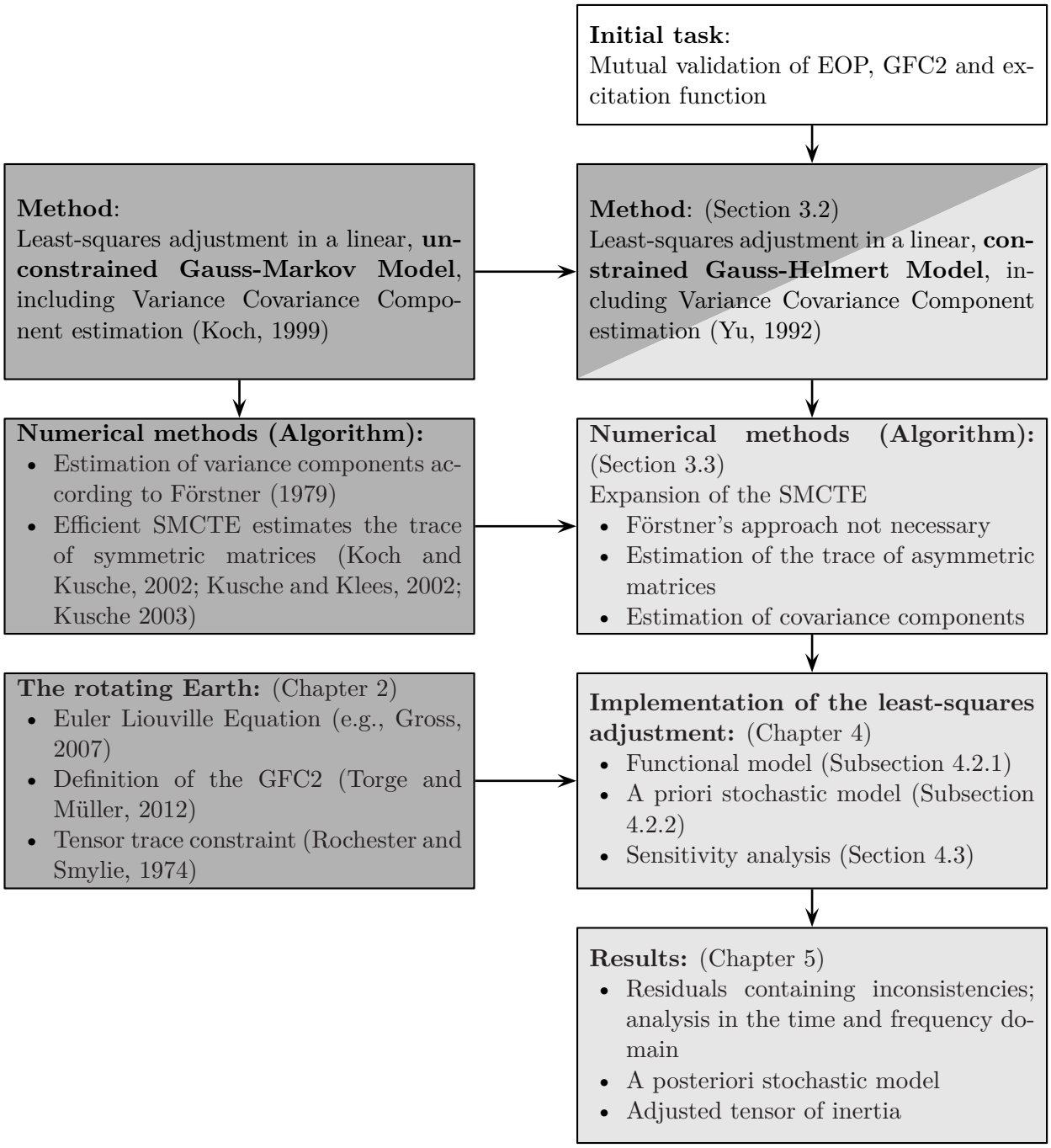

Figure 1.2: Beginning with the initial task of the mutual validation, the graph describes the content of this dissertation. Models and ideas found in literature are denoted with gray boxes. The own contributions to the solution of the initial task are indicated by light gray boxes.

tation. Models and ideas found in literature are denoted with gray boxes. The own contributions to the solution of the initial task are indicated by light gray boxes.
Briefly summarized, this dissertation is focused on two different aspects:

- A sophisticated, universal, efficient, linear least-squares adjustment solver is developed, which includes an estimation of VCC. The dissertation extents previously known methods regarding to additional constraints and an efficient estimation of covariance components. The proposed universal, efficient, linear least-squares adjustment model is suitable for each adjustment problem, which can be handled by linearization with sufficient accuracy.

- The mutual validation of EOP, GFC2 and geophysical excitation functions is performed by the proposed least-squares solver. The residuals of each time series contain those parts of the signal not present in the other time series and contain therefore the inconsistencies of the data. They are

analyzed in the time and frequency domain. Furthermore, the adjustment provides the adjusted tensor of inertia and the a posteriori VCM, describing the relative accuracy of the time series. The scientific community is supported with a valuable insight on the quality of the measured data and models.

The dissertation is outlined as follows: Chapter 2 models the rotating Earth and presents the functional relations between the time series and the tensor of inertia. Figure 1.1 describes graphically the dependencies within the functional model. Chapter 3 develops the universal, efficient, linear least-squares adjustment solver, which allows the estimation of variance components as well as covariance components. The development of the linear least-squares solver is performed in several steps. As a preparatory step, Section 3.1 considers a known stochastic model and solves a constrained least-squares GHM. Section 3.2 derives the BIQUE of the VCC. Section 3.3 proposes the numerical methods and provides a pseudocode for the universal least-squares solver. The least-squares solver is applied to the specific problem of the mutual validation of EOP, GFC2 and excitation functions in Chapter 4. This chapter links the Chapters 2 and 3 and includes a description of preprocessing steps and a sensitivity analysis. The sensitivity analysis investigates the effect of different functional models on the results. Chapter 5 contains a short description of the used time series and presents the results of the mutual validation of the time series. The residuals are extensively analyzed in the time and frequency domain, and the a priori and a posteriori VCM are compared. Additionally, this chapter answers some questions, arising during the work on this dissertation. Finally, Chapter 6 summarizes the results and gives an outlook.

2. Model of the rotating Earth

2.1. Reference systems and reference frames

2.1.1. Celestial and terrestrial reference systems and frames

The Earth is observed on global and local scales by means of numerous global and local techniques. Each measurement has to be performed within a reference system defined by conventions. A reference frame realizes a predefined reference system by measurements. If the rotating Earth is observed by global techniques, two reference systems are required, a non-rotating, celestial, inertial reference system and a rotating, Earth-fixed reference system. The International Earth Rotation and References Systems Service (IERS) maintains the conventional inertial and terrestrial reference systems and frames by means of the IERS Conventions (2010).
The International Astronomical Union recommends for the International Celestial Reference System (ICRS) that the origin of the ICRS is centered in the barycenter of the solar system. The directions of the axes should be fixed with respect to distant extra galactic quasars, whose motions are negligible small. This recommendation further stipulates that the celestial reference system should have its principal plane as close as possible to the mean equator at January 1st 2000, 12:00 Coordinated Universal Time (UTC). This date is denoted by the epoch identifier J2000.0. The origin of this principal plane should be as close as possible to the dynamical equinox of J2000.0. The ICRS is realized by the International Celestial Reference Frame (ICRF) (IERS Conventions, 2010, Chapter 2). The realization consists of a set of precise coordinates of extra galactic radio sources, which are observed by VLBI. Chapter 2 of the IERS Conventions (2010) provides further information and references about the ICRS and the ICRF.
The International Union of Geodesy and Geophysics and the International Association of Geodesy define the International Terrestrial Reference System (ITRS) as a right-handed, geocentric reference system. Its origin is the Earth's center of mass, including oceanic and atmospheric masses. The unit length is the meter. The orientation of the ITRS is initially given by the Bureau International de l'Heure orientation of J1984.0. The temporal stability of the orientation is ensured by using the no-net-rotation condition, which regards the motion of tectonic plates (Kreemer et al., 2006). The ITRS is realized by the International Terrestrial Reference Frame (ITRF). The positions of the IERS network stations and their velocities are determined by combining VLBI, SLR, GNSS and DORIS. Due to enhancement in both, measuring equipment and modeling, twelve versions of the ITRF were published over the years. The current reference frame is the ITRF2008. Further information and the transformation parameters between the current ITRF and previous references frames are published in IERS Conventions (2010, Chapter 4). The Geocentric Celestial Reference System (GCRS), introduced in Chapter 5 of the IERS Conventions (2010), has the same orientation as the ICRS and its origin equals the origin of the ITRS.

2.1.2. Transformation between the International Terrestrial Reference System and Geocentric Celestial Reference System

Geophysical processes change the distribution of masses of the entire Earth including atmosphere and oceans and induce variations of the Earth's pole and the rotation velocity. Additionally, the gravitational torques of the Sun, the Moon and the planets cause precession and nutation of the Earth's rotation axis. Thus, the instantaneous rotation axis varies in the ITRS as well as in the GCRS. The Celestial Intermediate Pole (CIP) divides by conventions the motion of the pole into a terrestrial and a celestial part. Since the Earth rotates in one sidereal day about its own axis, the frequency of a motion observed in the ITRS is one cycle per sidereal day (cpsd) higher than the frequency of the same motion observed in the GCRS. The precession and nutation describe the celestial motion of the CIP and include periods larger than two days, observed in the GCRS. These periods correspond to the retrograde diurnal band in the ITRS. In contrast, the polar motion describes the terrestrial motion of the CIP and includes frequencies outside of the retrograde diurnal band in the ITRS. Figure 2.1 illustrates the definition of the CIP (IERS Conventions, 2010).
The EOP, provided by the IERS, contain daily values for

- the observed coordinates of the CIP in the ITRS (polar motion),

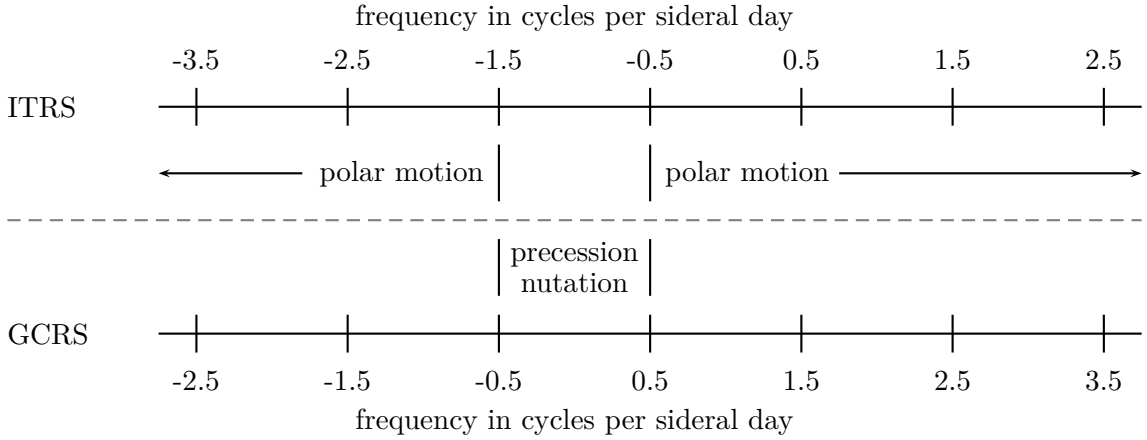

Figure 2.1: The chart illustrates the conventional frequency separation between the precession/nutation and the polar motion, either viewed in the ITRS (top), or the GCRS (bottom), with a 1 cpsd shift due to the rotation of the ITRS with respect to the GCRS. (IERS Conventions, 2010, page 46).

- the observed variation of the Earth's rotation velocity, measured by the difference between the universal time UT1 and UTC and Length Of Day (LOD) respectively, and
- the observed corrections to the precession/nutation model, which describe the motion of the CIP in the GCRS.

The transformation of a position vector $\boldsymbol{x}_{\mathrm{ITRS}}$ in the ITRS to a position vector $\boldsymbol{x}_{\mathrm{GCRS}}$ in the GCRS is performed at a given date t with

$$\boldsymbol{x}_{\mathrm{GCRS}}(t) \quad = \quad \boldsymbol{Q}(t)\,\boldsymbol{R}(t)\,\boldsymbol{W}(t)\,\boldsymbol{x}_{\mathrm{ITRS}}(t) \tag{2.1}$$

where the transformation matrices $\boldsymbol{Q}$, $\boldsymbol{R}$ and $\boldsymbol{W}$ arise from

$\boldsymbol{Q}(t)$: the motion of the CIP in the GCRS (precession/nutation),
$\boldsymbol{R}(t)$: the Earth's rotation about its own rotation axis and
$\boldsymbol{W}(t)$: the motion of the CIP in the ITRS (polar motion).

The transformation matrices depend on the EOP and are described in detail in IERS Conventions (2010, Chapter 5). Due to the definition of the CIP, the polar motion excludes daily and subdaily tidal variations and includes long periodic tidal signals and the secular trend due to the postglacial rebound. The IERS Conventions (2010, Sections 5.5.1, 5.5.3, and 8.2) provides models which add daily and subdaily tides to polar motion, LOD and the difference UT1–UTC. Additionally, the IERS Conventions (2010, Sections 8.1 and 8.3) and Appendix A provide models which remove long periodic tidal signals. The corrections of Appendix A have to be subtracted from the observed polar motion, LOD and the difference UT1–UTC, to obtain values free from tidal variations.

2.2. Theory of the Earth's rotation

2.2.1. Euler Liouville Equation

The Earth's rotation and its excitation are studied by various authors. Munk and MacDonald (1960, 1975) is probably the most cited textbooks regarding the rotation of the Earth. Further textbooks are Lambeck (1980) and Moritz and Mueller (1987). The latter textbook gives a very detailed and comprehensible overview. Gross (2007) and Dehant and Mathews (2007) wrote compact papers regarding the rotation of the Earth. Gross (2007) limited his paper to long periodic rotation variations caused by geophysical processes, and Dehant and Mathews (2007) focused on nutation effects caused by gravitational torques of Sun and Moon. This section summarizes the mechanic of a rotating Earth with a deformable body. The derivations presented here are similar to the textbook of Moritz and Mueller (1987) and the paper of Gross (2007). First, the rotation of rigid Earth is described. Later, this simple model is refined in two steps accounting for a deformable Earth model:
Assume an inertial and a rotating terrestrial reference system, both with the same origin. Assume further, a point mass on the Earth is viewed from a fixed point in the inertial reference system. Then, the observed

motion of the point mass in the inertial system is composed of the sum of two motions. The first motion is due to the deformation of the Earth's body. If the body were rigid, this motion with respect to the rotating reference system would be zero. The second motion of the point mass is due to the rotation itself and is obtained from the crossproduct of the rotation vector $\boldsymbol{\omega}$ and the position vector $\boldsymbol{x}$ of the point mass. The rotation vector $\boldsymbol{\omega}$ points along the instantaneous rotation axis, and its length quantifies the rotation velocity. Hence, the time derivative of a point mass with respect to a fixed inertial reference system is

$$\frac{\mathsf{d}\,\boldsymbol{x}_\mathrm{I}}{\mathsf{d}\,t} = \frac{\mathsf{d}\,\boldsymbol{x}_\mathrm{T}}{\mathsf{d}\,t} + \boldsymbol{\omega} \times \boldsymbol{x}_\mathrm{T}. \tag{2.2}$$

The indices I and T denote the position vector of the point mass in the inertial and the terrestrial reference system. The angular momentum of a point mass is defined by the crossproduct of the position vector and its time derivative. The angular momentum $\boldsymbol{H}_\mathrm{I}$ of the Earth's body, consisting of continuously distributed point masses $\mathsf{d}M$, is according to Moritz and Mueller (1987, formula 2-37)

$$\boldsymbol{H}_\mathrm{I} = \iiint\limits_{\mathrm{Earth}} \boldsymbol{x}_\mathrm{I} \times \frac{\mathsf{d}\,\boldsymbol{x}_\mathrm{I}}{\mathsf{d}\,t}\,\mathsf{d}M. \tag{2.3}$$

If the inertial position vector $\boldsymbol{x}_\mathrm{I}$ and the angular momentum $\boldsymbol{H}_\mathrm{I}$ are transformed in the terrestrial position vector $\boldsymbol{x}_\mathrm{T}$ and the angular momentum $\boldsymbol{H}_\mathrm{T}$ respectively and if Equation 2.2 is substituted into Equation 2.3, it yields

$$\boldsymbol{H}_\mathrm{T} = \iiint\limits_{\mathrm{Earth}} \boldsymbol{x}_\mathrm{T} \times (\boldsymbol{\omega} \times \boldsymbol{x}_\mathrm{T})\,\mathsf{d}M + \iiint\limits_{\mathrm{Earth}} \boldsymbol{x}_\mathrm{T} \times \frac{\mathsf{d}\,\boldsymbol{x}_\mathrm{T}}{\mathsf{d}\,t}\,\mathsf{d}M. \tag{2.4}$$

The definition of the tensor of inertia $\boldsymbol{I}$ results from the first summand of the last equation

$$\iiint\limits_{\mathrm{Earth}} \boldsymbol{x}_\mathrm{T} \times (\boldsymbol{\omega} \times \boldsymbol{x}_\mathrm{T})\,\mathsf{d}M = \left(\iiint\limits_{\mathrm{Earth}} \begin{bmatrix} y^2+z^2 & xy & xz \\ xy & x^2+z^2 & yz \\ xz & yz & x^2+y^2 \end{bmatrix} \mathsf{d}M \right) \boldsymbol{\omega} = \boldsymbol{I}\boldsymbol{\omega} \tag{2.5}$$

where x, y and z denote the Cartesian coordinates of the terrestrial position vector. The relative angular momentum $\boldsymbol{h}$ is defined with

$$\boldsymbol{h} = \iiint\limits_{\mathrm{Earth}} \boldsymbol{x}_\mathrm{T} \times \frac{\mathsf{d}\,\boldsymbol{x}_\mathrm{T}}{\mathsf{d}\,t}\,\mathsf{d}M. \tag{2.6}$$

It follows from the Equations 2.5 and 2.6 that the Earth's angular momentum $\boldsymbol{H}_\mathrm{T}$ is

$$\boldsymbol{H}_\mathrm{T} = \boldsymbol{I}\boldsymbol{\omega} + \boldsymbol{h}. \tag{2.7}$$

The Earth's reaction on external torques, mainly gravitational torques of the Moon and the Sun, has to be taken into account. The angular momentum is constant in closed systems. If an external torque $\boldsymbol{L}$ acts on the rotating Earth, the angular momentum changes. According to Moritz and Mueller (1987, pp. 42f and 118), the conservation of the angular momentum is described by

$$\frac{\mathsf{d}\,\boldsymbol{H}_\mathrm{I}}{\mathsf{d}\,t} = \boldsymbol{L}. \tag{2.8}$$

This equation is commonly called the Eulerian Equation of motion or simply Euler Equation. According to (Moritz and Mueller, 1987, formula 2-35), the time derivative of any arbitrary vector with respect to the inertial system consists of the sum of the time derivative with respect to the rotating system and the temporal changes due to the rotation. The time derivative of the inertial angular momentum vector is determined analogous to Equation 2.2 and it holds

$$\frac{\mathsf{d}\,\boldsymbol{H}_\mathrm{T}}{\mathsf{d}\,t} + \boldsymbol{\omega} \times \boldsymbol{H}_\mathrm{T} = \boldsymbol{L}. \tag{2.9}$$

If $\boldsymbol{H}_\mathrm{T}$ in Equation 2.7 is substituted into Equation 2.9, it holds

$$\frac{\mathsf{d}}{\mathsf{d}\,t}\left(\boldsymbol{I}\boldsymbol{\omega} + \boldsymbol{h}\right) + \boldsymbol{\omega} \times \left(\boldsymbol{I}\boldsymbol{\omega} + \boldsymbol{h}\right) = \boldsymbol{L}. \tag{2.10}$$

This form of the Euler Equation, defined in the terrestrial reference system, is called Liouville Equation (Munk and MacDonald, 1960, 1975) or Euler Liouville Equation (ELE) (Moritz and Mueller, 1987). The motion of the rotation axis with respect to the inertial system is called precession and nutation, whereas the motion of the rotation axis with respect to the terrestrial frame is denoted wobble (Dehant and Mathews, 2007). The rotation varies due to mass redistributions, changing the tensor of inertia and the relative angular momentum. External forces of Moon, Sun and planets cause additional rotation variations. Free modes consider mass redistributions due to internal geophysical processes only, and the external torques are set to zero. Forced modes describe the rotation variations caused by external torques. Since this dissertation is limited to Earth rotation variations due to geophysical processes, it holds $\boldsymbol{L} = \boldsymbol{0}$. The time derivative with respect to the terrestrial reference system is hereafter replaced with a dot, in order to make the following derivations more legible. Equation 2.10 results then in

$$\dot{\boldsymbol{I}}\boldsymbol{\omega} + \boldsymbol{I}\dot{\boldsymbol{\omega}} + \dot{\boldsymbol{h}} + \boldsymbol{\omega} \times \boldsymbol{I}\boldsymbol{\omega} + \boldsymbol{\omega} \times \boldsymbol{h} = \boldsymbol{0}. \tag{2.11}$$

The tensor of inertia is split in a mean, time-invariant, biaxial tensor of inertia and a time-dependent part, described by comparatively small deviations c_{jk} (with $j,k = x,y,z$) from the mean tensor

$$\boldsymbol{I} = \begin{bmatrix} A' & 0 & 0 \\ 0 & A' & 0 \\ 0 & 0 & C \end{bmatrix} + \begin{bmatrix} c_{xx} & c_{xy} & c_{xz} \\ c_{xy} & c_{yy} & c_{yz} \\ c_{xz} & c_{yz} & c_{zz} \end{bmatrix} \quad \text{with} \quad A' = \frac{A+B}{2}. \tag{2.12}$$

The parameters A, B and C denote the Earth's principal moments of the tensor of inertia.
The Earth approximately rotates about the z-axis of the terrestrial reference system with a mean rotation velocity Ω. The rotation vector $\boldsymbol{\omega}$ is described by a sum of the mean rotation vector and small time-dependent variations Ωm_j (with $j = x,y,z$)

$$\boldsymbol{\omega} = \begin{bmatrix} 0 \\ 0 \\ \Omega \end{bmatrix} + \Omega \begin{bmatrix} m_x \\ m_y \\ m_z \end{bmatrix} = \Omega \begin{bmatrix} m_x \\ m_y \\ 1 + m_z \end{bmatrix}. \tag{2.13}$$

The tensor of inertia and the rotation vector in Equations 2.12 and 2.13 are substituted into Equation 2.11. It holds for all deviations $c_{jk} \ll A', C$ and all $m_j \ll 1$. If products of two or more small quantities c_{jk} and m_j are neglected, it yields the linear approximation of the ELE with (Gross, 2007; Moritz and Mueller, 1987, pp.123f)

$$\frac{A'}{\Omega\,(C-A')}\dot{m}_x + m_y = \frac{1}{\Omega\,(C-A')}\left(\Omega c_{yz} - \dot{c}_{xz} + h_y - \frac{1}{\Omega}\dot{h}v\right), \tag{2.14a}$$

$$\frac{A'}{\Omega\,(C-A')}\dot{m}_y - m_x = \frac{1}{\Omega\,(C-A')}\left(-\Omega c_{xz} - \dot{c}_{yz} - h_x - \frac{1}{\Omega}\dot{h}_y\right), \tag{2.14b}$$

$$\dot{m}_z = \frac{1}{\Omega C}\left(-\Omega \dot{c}_{zz} - \dot{h}_z\right). \tag{2.14c}$$

The linear approximation decouples the equatorial part in Equations 2.14a and 2.14b from the axial part in Equation 2.14c. Furthermore, the tensor elements c_{xx}, c_{xy} and c_{yy} vanish due to linearization. The Equations 2.14 are simplified by defining excitation functions

$$\chi_x = \frac{\Omega c_{xz} + h_x}{\Omega\,(C-A')}, \qquad \chi_y = \frac{\Omega c_{yz} + h_y}{\Omega\,(C-A')} \qquad \text{and} \qquad \chi_z = \frac{\Omega c_{zz} + h_z}{\Omega C}. \tag{2.15}$$

Using the excitation functions, the equatorial ELE is described by

$$\frac{A'}{\Omega\,(C-A')}\dot{m}_x + m_y = \chi_y - \frac{1}{\Omega}\dot{\chi}_x, \tag{2.16a}$$

$$\frac{A'}{\Omega\,(C-A')}\dot{m}_y - m_x = -\chi_x - \frac{1}{\Omega}\dot{\chi}_y. \tag{2.16b}$$

The integration of the axial Equation 2.14c results in

$$m_z = -\chi_z. \tag{2.16c}$$

The two equatorial ELE are usually summarized in one complex equation. Complex equatorial quantities are defined by using the imaginary number $\mathrm{i} = \sqrt{-1}$ with

$$\tilde{m} = m_x + \mathrm{i}\, m_y, \qquad \tilde{c} = c_{xz} + \mathrm{i}\, c_{yz}, \qquad \tilde{h} = h_x + \mathrm{i}\, h_y \qquad \text{and} \qquad \tilde{\chi} = \chi_x + \mathrm{i}\, \chi_y. \tag{2.17}$$

Then, the complex equatorial ELE reads

$$\tilde{m} + \mathrm{i}\frac{A'}{\Omega\,(C - A')}\dot{\tilde{m}} = \tilde{\chi} - \mathrm{i}\frac{1}{\Omega}\dot{\tilde{\chi}}. \tag{2.18}$$

If the Earth were rigid, the mass distribution would remain constant. Hence, the right-hand side of the Equation 2.18 would be zero. Then, the solution of the complex differential Equation 2.18 would be

$$\tilde{m} = \tilde{m}_0 \, \exp\left(\mathrm{i}\,\frac{C - A'}{A'}\,\Omega t\right) \tag{2.19}$$

where $\tilde{m}_0$ is an initial value required for the unique solution of the differential equation. The pole would describe a prograde undamped circular motion. The radius of the circular polar motion can be obtained from $\tilde{m}_0$. Based on the known flattening of the Earth, Euler (1765) predicted the frequency of the wobble with

$$\sigma_E = \frac{C - A'}{A'}\Omega, \tag{2.20}$$

which corresponds to a period of about 10 months. However, the Earth wobbles with a longer period of 14 months. This wobble was first detected by Chandler (1891) more than 100 years later. Newcomb (1902) explained the large deviation between the Euler and the Chandler frequency with a deformable Earth body.

2.2.2. Euler Liouville Equation for a deformable Earth

As mentioned before, the Earth's body, including atmosphere and oceans, is not rigid. Tides and atmospheric and oceanic loading effects deform the Earth's mantle and crust. The change of the rotation itself induce deformations. The variation of the mass distribution in the Earth's core leads to rotation variations. The distribution of water in atmosphere, oceans, continental lakes and rivers and ice changes continuously. The motions of the tectonic plates cause earthquakes and volcanic eruptions. Each subsystem contributes to the total tensor of inertia and the total relative angular momentum and it holds

$$\boldsymbol{h} = \boldsymbol{h}_{Core} + \boldsymbol{h}_{Tides} + \boldsymbol{h}_{Rot} + \boldsymbol{h}_{Load} + \boldsymbol{h}_{Atmo} + \boldsymbol{h}_{Ocean} + \boldsymbol{h}_{Hydro} + \boldsymbol{h}_{Ice} + \boldsymbol{h}_{Tectonic} + \ldots \tag{2.21}$$

$$\boldsymbol{c} = \begin{bmatrix} c_{xz} \\ c_{yz} \\ c_{zz} \end{bmatrix} = \boldsymbol{c}_{Core} + \boldsymbol{c}_{Tides} + \boldsymbol{c}_{Rot} + \boldsymbol{c}_{Load} + \boldsymbol{c}_{Atmo} + \boldsymbol{c}_{Ocean} + \boldsymbol{c}_{Hydro} + \boldsymbol{c}_{Ice} + \boldsymbol{c}_{Tectonic} + \ldots \quad . \tag{2.22}$$

The vector $\boldsymbol{c}$ contains the three tensor elements c_{xz}, c_{yz} and c_{zz}. The tensor elements c_{xx}, c_{yy} and c_{xy} are not considered in vector $\boldsymbol{c}$, as they vanish due to the linearization of the ELE.
Some terms in Equations 2.21 and 2.22 are approximated by models. The core is assumed to be ellipsoidal and to be of a homogeneous, incompressible fluid. As the fluid is homogeneous and incompressible, the mass distribution and therefore the tensor of inertia of the core remains constant. Thus, it holds $\boldsymbol{c}_{Core} = \boldsymbol{0}$. Based on the work of Hough (1895), Smith and Dahlen (1981) models the changes of relative angular momentum due to rotation variations. If the rotation axis of the core varies with a frequency $\sigma \ll \Omega$ (so that $\sigma/\Omega \approx 0$), it holds

$$\boldsymbol{h}_{Core} = \begin{bmatrix} -\left(1 - \epsilon_C\right) A_C \dot{m}_y \\ \left(1 - \epsilon_C\right) A_C \dot{m}_x \\ -\Omega C_C m_z \end{bmatrix} \tag{2.23}$$

where A_C and C_C denote the principal moments of inertia of the biaxial, ellipsoidal core. ϵ_C describes the ellipticity of the surface of the core.
The terrestrial reference system is assumed to be oriented in a manner that the relative angular momentum caused by motions of the Earth's crust and mantle vanishes. The assumed reference system is the Tisserand mean-mantle reference system. The Tisserand mean-mantle reference system is equivalent to

orienting the Earth's rotation axis $\boldsymbol{\omega}$ along the mean rotation axis of the mantle (Munk and MacDonald, 1975). Then, motions of crust and mantle do not contribute to the total relative angular momentum $\boldsymbol{h}$, and it holds $\boldsymbol{h}_{Rot} = \mathbf{0}$ and $\boldsymbol{h}_{Load} = \mathbf{0}$ (Gross, 2007). Dahlen (1976) studied the effect of the rotation deformation on the Earth. Rotation variations change the centripetal potential of the Earth and cause elastic deformation of its body. Reactions to changes of the centripetal potential are assumed to be equal to reactions that a non-rotating Earth would show to changes of a static potential of the same amplitude and type. Then, the contribution to the tensor of inertia due to rotation variations is modeled by

$$\begin{aligned} \boldsymbol{c}_{Rot} &= \begin{bmatrix} D_e & 0 & 0 \\ 0 & D_e & 0 \\ 0 & 0 & D_a \end{bmatrix} \begin{bmatrix} m_x \\ m_y \\ m_z \end{bmatrix} = \boldsymbol{D}\boldsymbol{m} \\ \text{with} \quad D_e &= \frac{a^5\Omega^2}{3G}\left(k_2 + \Delta k_{ocn,w}\right) \quad \text{and} \quad D_a = \frac{a^5\Omega^2}{3G}\left(n_0 + \frac{4}{3}\left(k_2 + \Delta k_{ocn,s}\right)\right) \end{aligned} \tag{2.24}$$

where a is the mean radius of the Earth and G is the Newtonian gravitational constant. The second-degree body tide Love number k_2 is a dimensionless parameter, describing the elastic deformation of the Earth's body. Assuming equilibrium oceans, the oceans also undergo centrifugal deformations. Oceanic Love numbers modify the body tide Love number k_2 to account for oceanic deformations. As the oceans are non-uniformly distributed over the Earth, two different oceanic Love numbers $\Delta k_{ocn,w}$ and $\Delta k_{ocn,s}$ for the Earth's wobble and spin are considered. The non-uniform distribution of the oceans couples the equatorial and axial components. That leads to off-diagonal elements of the matrix $\boldsymbol{D}$ which are unequal to zero. Based on older Earth models 1066A and 1066B (Gilbert and Dziewonski, 1975), Dahlen (1976) investigated the off-diagonal elements and found a weak coupling. This finding is extrapolated to the current Preliminary Reference Earth Model (PREM) (Dziewonski and Anderson, 1981). The coupling due to non-uniform distribution of the oceans is neglected as well. The parameter n_0 arises from the change of the mean moment of inertia caused by purely radial deformation of the Earth (Dahlen, 1976; Gross, 2007).

The loads of atmosphere and oceans are assumed to deform the Earth radially. The deformation due to loading changes the tensor of inertia with

$$\boldsymbol{c}_{Load} = k_2' \boldsymbol{c} \tag{2.25}$$

where k_2' denotes the load Love number. The assumed radial deformation is a rough approximation, which does not consider local deformations of the Earth's crust, caused by pressure variations of the atmosphere and oceans. Dill (2002) and Seitz (2004) developed a model accounting for regional deformations of the Earth's crust.

As mentioned previously, the frequency of the Earth rotation variations is assumed to be low. Then, the second time derivative of the polar motion is approximately zero ($\ddot{\tilde{m}} \approx 0$). The Equations 2.23, 2.24 and 2.25 are substituted into the equatorial ELE in Equation 2.18

$$\begin{aligned} &\tilde{m} + \mathrm{i}\frac{A'}{\Omega\left(C - A'\right)}\dot{\tilde{m}} = \frac{\Omega D_e \tilde{m} + \mathrm{i}\left(1 - \epsilon_C\right) A_C \dot{\tilde{m}} - \mathrm{i} D_e \dot{\tilde{m}} + \Omega\left(1 + k_2'\right)\tilde{c} + \tilde{h} - \left(1 + k_2'\right)\dot{\tilde{c}} - \frac{1}{\Omega}\dot{\tilde{h}}}{\Omega\left(C - A'\right)} \\ \Rightarrow &\Omega\left(C - A' - D_e\right)\tilde{m} + \mathrm{i}\left(A' - \left(1 - \epsilon_C\right) A_C + D_e\right)\dot{\tilde{m}} = \Omega\left(1 + k_2'\right)\tilde{c} + \tilde{h} - \left(1 + k_2'\right)\dot{\tilde{c}} - \frac{1}{\Omega}\dot{\tilde{h}} \\ \Rightarrow &\tilde{m} + \mathrm{i}\frac{A' - \left(1 - \epsilon_C\right) A_C + D_e}{\Omega\left(C - A' - D_e\right)}\dot{\tilde{m}} = \tilde{\chi} - \mathrm{i}\frac{1}{\Omega}\dot{\tilde{\chi}} \end{aligned} \tag{2.26}$$

with a refined complex valued equatorial excitation function

$$\tilde{\chi} = \frac{\Omega\left(1 + k_2'\right)\tilde{c} + \tilde{h}}{\Omega\left(C - A' - D_e\right)}. \tag{2.27}$$

If the Earth is approximated by an axisymmetric body with a fluid core, an elastically deformable mantle and equilibrium oceans, the Earth rotates with a refined theoretical Chandler frequency of

$$\sigma_C = \frac{C - A' - D_e}{A' - \left(1 - \epsilon_C\right) A_C + D_e}\Omega. \tag{2.28}$$

The axial component of the ELE is similarly refined. The total principal moment of inertia consists of the sum of the principal moments of the mantle C_M and the core C_C. Hence, it holds $C_M = C - C_C$. According to the Equations 2.23, 2.24 and 2.25, the axial Euler Liouville Equation follows as

$$\begin{aligned} m_z &= -\frac{-\Omega C_C m_z + \Omega D_a m_z + \Omega\,(1+k_2')\,c_{zz} + h_z}{\Omega C} \\ \Rightarrow \left(1 - \frac{C_C}{C} + \frac{D_a}{C}\right) m_z &= -\frac{\Omega\,(1+k_2')\,c_{zz} + h_z}{\Omega C} \\ \Rightarrow (C - C_C + D_a)\, m_z &= -\frac{\Omega\,(1+k_2')\,c_{zz} + h_z}{\Omega} \\ \Rightarrow \left(1 + \frac{D_a}{C_M}\right) m_z &= -\frac{\Omega\,(1+k_2')\,c_{zz} + h_z}{\Omega C_M}. \end{aligned} \tag{2.29}$$

However, the theoretical value for the Chandler period in Equation 2.28 is more than one week shorter than the observed Chandler period (Gross, 2007). This difference is caused by the anelastic reaction of the Earth's body. Viscose, electromagnetic or topographic core-mantle coupling processes and dissipation in the Earth's mantle and oceans lead to the anelastic reaction of the Earth (Smith and Dahlen, 1981). If the Chandler wobble were not excited, the figure axis and rotation axis of the Earth would coincide over time due to the anelasticity. The Chandler wobble would be damped and the polar motion would describe an inward spiral. However, the excitation of the Earth rotation is still not completely understood. A damped Chandler wobble is reflected by a complex-valued Chandler frequency σ_0. The anelasticity modifies the body tide and load Love numbers by complex values. According to Gross (2007), accurate models for the anelastic Earth do not exist for the frequencies of interest ($\sigma < \Omega$). Therefore, the ELE is refined by replacing the theoretical Chandler frequency σ_C with the empirical Chandler frequency σ_0 in Equations 2.26 and 2.28. If σ_C in Equation 2.28 is replaced, a refined complex-valued parameter D_e can be derived. If the parameter D_e and the empirical Chandler frequency σ_0 are substituted into Equation 2.26 the refined ELE is obtained (Gross, 2007)

$$\tilde{m} + \mathrm{i}\frac{1}{\sigma_0}\dot{\tilde{m}} = \tilde{\chi} - \mathrm{i}\frac{1}{\Omega}\dot{\tilde{\chi}} \qquad \text{with} \qquad \tilde{\chi} = \frac{\Omega\,(1 + k_2' + \Delta k_a')\,\tilde{c} + \tilde{h}}{\sigma_0\,(C - A' + A_M + \epsilon_C A_C)} \tag{2.30a}$$

$$m_z = -\chi_z \qquad\qquad \chi_z = \left(1 + \frac{D_a}{C_M}\right)^{-1} \frac{\Omega\,(1 + k_2' + \Delta k_a')\,c_{zz} + h_z}{\Omega C_M} \tag{2.30b}$$

where the complex-valued factor $\Delta k_a'$ accounts for the effects of the mantle elasticity on the load Love number and where $A' - A_C = A_M$ holds. This refined ELE models an Earth with an axisymmetric body, a fluid core, an elastically deformable mantle and equilibrium oceans. The imaginary parts describe the damping of the Chandler wobble caused by dissipative processes. The dimensionless excitation functions $\tilde{\chi}$ and χ_z are denoted as Effective Angular Momentum Functions (EAMF). Since the empirical complex-valued Chandler frequency is used to constrain the anelastic behavior of the Earth's mantle, Equation 2.30a only holds for frequencies close to the Chandler frequency (Wahr, 2005). The numerical values derived from the refined Equation 2.30a differ by 1%–3% from the values obtained by Equation 2.26. Wahr (2005) and Smith and Dahlen (1981) tried to estimate the quality of the models by quantifying the model errors as far as possible. The model errors cause perturbations of the Chandler frequency of $^1/_{800}$ cycles per day maximum.

According to literature, different numerical values for the complex-valued Love numbers and the Chandler frequency exist. They are derived from Earth models, seismological measurements and from the observed polar motion. The real parts slightly differ about a few percent. In contrast to the real parts, the imaginary parts are determined with low accuracy. The sensitivity analysis in Subsection 4.3.3 analyzes the effect of the different numerical values for the Love numbers and the Chandler frequency.

A further open question is the extent to which the Earth's core and mantle are coupled. The effects of core viscosity, electromagnetic and topographic coupling processes are still unknown. A completely decoupled core is not affected by mantle deformation, whereas a fully coupled core completely deforms. According to Dickman (2003), the core is hardly affected by mantle deformations. Therefore, he recommended to replace the body tide Love number k_2 and the load Love number k_2' for the entire Earth with mantle-only Love numbers. However, the core-mantle coupling is differently treated in literature. Barnes et al. (1983) modeled a coreless Earth. Several publications assumed inconsistent zero coupling of core and

mantle for the axial component but full coupling in the equatorial component (Wahr, 1983; Eubanks, 1993; Aoyama and Naito, 2000; Gross, 2007). Dickman (2003) compared the various EAMF with respect to the core-mantle coupling. Based on available data, Subsection 5.1.4 shortly discusses the core-mantle coupling.

2.2.3. IERS Earth Orientation Parameters and the rotation vector of the Earth

The rotation vector $\boldsymbol{\omega}$ linearly depends on small perturbations m_x, m_y and m_z according to Equation 2.13. The parameters m_x and m_y describe the angular offset of the instantaneous rotation vector from the z-axis of the terrestrial reference system. However, the IERS does not report the angles m_x and m_y. Instead, it reports the coordinates of the instantaneous CIP (cf. Subsection 2.1.2). The CIP represents an intermediate reference system, separating the precession/nutation from the polar motion by conventions (cf. Figure 2.1). As the instantaneous rotation vector $\boldsymbol{\omega}$ is not given by the IERS, it has to be derived from the transformation matrix between the terrestrial and celestial reference system. The here presented derivation of the rotation vector follows according to Gross (1992, 2007).
First, assume an arbitrary inertial and an arbitrary terrestrial reference system. The inertial system is fixed and the terrestrial system rotates. The origins of these systems coincide and the relative orientation is arbitrary. The transformation of the inertial system (denoted with index 'I') in the terrestrial system (denoted with index 'T') is performed by a transformation matrix $\boldsymbol{A}$ which considers the relative orientation of the two systems

$$\boldsymbol{x}_\mathrm{T} = \boldsymbol{A}\boldsymbol{x}_\mathrm{I}. \tag{2.31}$$

Since the orientation of the terrestrial system is continuously changing, $\boldsymbol{A}$ is time-dependent. Furthermore, $\boldsymbol{A}$ is an orthogonal transformation matrix and therefore its inverse is its transpose. Hence, it holds

$$\boldsymbol{x}_\mathrm{I} = \boldsymbol{A}^\mathsf{T}\boldsymbol{x}_\mathrm{T}. \tag{2.32}$$

The time derivative of the position vector $\boldsymbol{x}_\mathrm{I}$ in the inertial system is obtained by the product rule for derivatives. The multiplication of the time derivative of the position vector $\boldsymbol{x}_\mathrm{I}$ and the matrix $\boldsymbol{A}$ leads to

$$\begin{aligned} \boldsymbol{A}\frac{\mathsf{d}\,\boldsymbol{x}_\mathrm{I}}{\mathsf{d}\,t} &= \boldsymbol{A}\frac{\mathsf{d}\,\boldsymbol{A}^\mathsf{T}}{\mathsf{d}\,t}\boldsymbol{x}_\mathrm{T} + \boldsymbol{A}\boldsymbol{A}^\mathsf{T}\frac{\mathsf{d}\,\boldsymbol{x}_\mathrm{T}}{\mathsf{d}\,t} \\ &= \frac{\mathsf{d}\,\boldsymbol{x}_\mathrm{T}}{\mathsf{d}\,t} + \boldsymbol{A}\frac{\mathsf{d}\,\boldsymbol{A}^\mathsf{T}}{\mathsf{d}\,t}\boldsymbol{x}_\mathrm{T}. \end{aligned} \tag{2.33}$$

The terrestrial and inertial systems are assumed to coincide momentarily. Then, the left hand side of this expression represents the time derivative of a vector with respect to the inertial system (cf. Equation 2.2). The right hand side is the sum of the time derivative with respect to the terrestrial system and a summand linearly dependent on $\boldsymbol{x}_\mathrm{T}$. According to Equation 2.2, the second summand in Equation 2.33 has to be equal to the crossproduct of the Earth rotation vector and the position vector $\boldsymbol{x}_\mathrm{T}$. If the definition of the crossproduct is considered, it holds (Gross, 1992, 2007)

$$\begin{aligned} \boldsymbol{A}\frac{\mathsf{d}\,\boldsymbol{x}_\mathrm{I}}{\mathsf{d}\,t} &= \frac{\mathsf{d}\,\boldsymbol{x}_\mathrm{T}}{\mathsf{d}\,t} + \boldsymbol{\omega} \times \boldsymbol{x}_\mathrm{T} \\ &= \frac{\mathsf{d}\,\boldsymbol{x}_\mathrm{T}}{\mathsf{d}\,t} + \begin{bmatrix} 0 & -\omega_z & \omega_y \\ \omega_z & 0 & -\omega_x \\ -\omega_y & \omega_x & 0 \end{bmatrix} \boldsymbol{x}_\mathrm{T} \end{aligned} \tag{2.34}$$

where ω_x, ω_y and ω_z denote the coordinates of the Earth's rotation vector. A comparison of Equations 2.33 and 2.34 relates the coordinates of the Earth's rotation vector to the transformation matrix $\boldsymbol{A}$ with

$$\begin{bmatrix} 0 & -\omega_z & \omega_y \\ \omega_z & 0 & -\omega_x \\ -\omega_y & \omega_x & 0 \end{bmatrix} = \boldsymbol{A}\frac{\mathsf{d}\,\boldsymbol{A}^\mathsf{T}}{\mathsf{d}\,t}. \tag{2.35}$$

Thus, the Earth's rotation vector $\boldsymbol{\omega}$ is derived from the transformation matrix $\boldsymbol{A}$ between the terrestrial and the celestial reference systems and its time derivative. Chapter 5 of the IERS Conventions (2010) provides the transformation matrix between the ITRS and the GCRS. Three transformation matrices

arise according to Equation 2.1, one due to precession/nutation, one due to the Earth's spin and one due to the polar motion. As the precession/nutation causes daily and subdaily variations of the Earth rotation vector $\boldsymbol{\omega}$ (cf. Figure 2.1) and since this dissertation is limited to long periods, the transformation matrix due to precession/nutation is neglected here. The variation of the Earth rotation velocity is given by the time difference ΔUT=UT1–UTC. The Universal Time (UT1) is the mean solar time at 0° longitude and is proportional to the rotation angle of the Earth with respect to distant quasars. UTC is the time measured by atomic clocks. The spin of the Earth is considered by a rotation of the Earth Rotation Angle (ERA) about the z-axis with

$$\mathrm{ERA} \approx \Omega \left(t + \Delta UT\left(t\right)\right). \tag{2.36}$$

The transformation matrix due to the polar motion consists of two rotations about the x- and y-axes. Subsection 5.4.1 of the IERS Conventions (2010) considers a third rotation about the z-axis, called the 'TIO locator'. This angle has a value of a few microarcseconds in the period considered within this dissertation. Therefore, it is omitted as well as the precession/nutation matrix. The angles p_x and $-p_y$ describe the coordinates of the instantaneous CIP in the ITRF. The angle $-p_y$ has a negative sign as traditionally the positive direction of p_y is taken towards the 90°W longitude, whereas the positive y-axis of the terrestrial system points to the 90°E longitude. The angle $p_z = \Omega \Delta UT\left(t\right)$ is related to the perturbation of the mean rotation velocity. The transformation between the terrestrial system and the inertial system is performed by using following three rotation matrices

$$\begin{aligned}
\boldsymbol{R}_x &= \begin{bmatrix} \cos p_x & 0 & -\sin p_x \\ 0 & 1 & 0 \\ \sin p_x & 0 & \cos p_x \end{bmatrix} \\
\boldsymbol{R}_y &= \begin{bmatrix} 1 & 0 & 0 \\ 0 & \cos p_y & \sin p_y \\ 0 & -\sin p_y & \cos p_y \end{bmatrix} \\
\boldsymbol{R}_z &= \begin{bmatrix} \cos\left(\Omega t + p_z\right) & -\sin\left(\Omega t + p_z\right) & 0 \\ \sin\left(\Omega t + p_z\right) & \cos\left(\Omega t + p_z\right) & 0 \\ 0 & 0 & 1 \end{bmatrix}.
\end{aligned} \tag{2.37}$$

The three rotation matrices are summarized to the transformation matrix

$$\boldsymbol{A}^{\mathsf{T}} = \boldsymbol{R}_z \boldsymbol{R}_x \boldsymbol{R}_y. \tag{2.38}$$

The rotation vector $\boldsymbol{\omega}$ is obtained by Equation 2.35 and the given transformation matrix $\boldsymbol{A}$ with

$$\boldsymbol{\omega} = \begin{bmatrix} \left(\Omega + \dot{p}_z\right) \sin p_x - \dot{p}_y \\ -\left(\Omega + \dot{p}_z\right) \sin p_y \cos p_x - \dot{p}_x \cos p_y \\ \left(\Omega + \dot{p}_z\right) \cos p_x \cos p_y - \dot{p}_x \sin p_y \cos p_y \end{bmatrix}. \tag{2.39}$$

If any arbitrary angle p is small, the sine and cosine of p are approximately $\sin p \approx p$ and $\cos p \approx 1$. If small products of second order are neglected, the Earth's rotation vector and the vector $\boldsymbol{m}$ are

$$\boldsymbol{\omega} = \begin{bmatrix} \Omega p_x - \dot{p}_y \\ -\Omega p_y - \dot{p}_x \\ \Omega + \dot{p}_z \end{bmatrix} \qquad \text{and} \qquad \boldsymbol{m} = \begin{bmatrix} p_x - \frac{1}{\Omega}\dot{p}_y \\ -p_y - \frac{1}{\Omega}\dot{p}_x \\ \frac{1}{\Omega}\dot{p}_z \end{bmatrix}. \tag{2.40}$$

If the two polar motion parameters are combined into a complex notation

$$\tilde{p} = p_x - \mathrm{i} p_y, \tag{2.41}$$

the complex parameter $\tilde{m}$ is then

$$\tilde{m} = \tilde{p} - \mathrm{i}\frac{1}{\Omega}\dot{\tilde{p}}. \tag{2.42}$$

The complex-valued $\tilde{m}$ is substituted into Equation 2.30a. Then, one obtains

$$\begin{aligned}
\tilde{\chi} - \mathrm{i}\frac{1}{\Omega}\dot{\tilde{\chi}} &= \tilde{p} - \mathrm{i}\frac{1}{\Omega}\dot{\tilde{p}} + \mathrm{i}\frac{1}{\sigma_0}\left(\dot{\tilde{p}} - \mathrm{i}\frac{1}{\Omega}\ddot{\tilde{p}}\right) \\
&= \tilde{p} + \mathrm{i}\frac{1}{\sigma_0}\dot{\tilde{p}} - \mathrm{i}\frac{1}{\Omega}\left(\dot{\tilde{p}} + \mathrm{i}\frac{1}{\sigma_0}\ddot{\tilde{p}}\right).
\end{aligned} \tag{2.43}$$

The last equation relates the polar motion and the refined excitation function of Equation 2.30a

$$\tilde{p} + \mathrm{i}\frac{1}{\sigma_0}\dot{\tilde{p}} = \frac{\Omega\,(1 + k_2' + \Delta k_a)\,\tilde{c} + \tilde{h}}{\sigma_0\,(C - A' + A_M + \epsilon_C A_C)}. \tag{2.44}$$

This formulation of the equatorial ELE offers the advantage, that the transition from the quantity $\tilde{m}$ to the complex polar motion $\tilde{p}$ does not require any time derivatives of the equatorial complex excitation function $\tilde{\chi}$.
The time derivative $\dot{p}_z$ of UT1–UTC equals the negative LOD quantity Δ_{LOD} by definition. As the IERS provides the Δ_{LOD} in seconds per day, Δ_{LOD} has to be divided by the nominal length of day ($\Lambda_0 = 86400$ seconds) to reach a dimensionless quantity. Thus, it holds for m_z

$$m_z = \frac{\mathrm{d}\,(\mathrm{UT1} - \mathrm{UTC})}{\mathrm{d}t} = -\frac{\Delta_{LOD}}{\Lambda_0}. \tag{2.45}$$

According to Equations 2.30b and 2.45, the final axial component of the ELE is

$$\frac{\Delta_{LOD}}{\Lambda_0} = k_r \frac{\Omega\,(1 + k_2' + \Delta k_a)\,c_{zz} + h_z}{\Omega C_M} \quad \text{with} \quad k_r = \left(1 + \frac{D_a}{C_M}\right)^{-1}. \tag{2.46}$$

2.2.4. Excitation functions from geophysical models

According to the Equations 2.5 and 2.6, the total relative angular momentum and the total tensor of inertia are integrals over the point masses of the entire Earth's body. If the contribution of one subsystem to the total relative angular momentum and tensor of inertia is calculated, the point masses belonging to the specific subsystems are integrated. The integrals require the position vectors of the point masses and their time derivatives. The position vectors and currents are obtained by geophysical models of the subsystems. This subsection derives the atmospheric excitation functions in analogy to the Equations 2.5 and 2.6. The excitation functions of further subsystems are obtained accordingly. The atmospheric contribution to the relative angular momentum and the third column of the tensor of inertia is

$$\boldsymbol{c}_{Atmo} = \iiint\limits_{\text{Atmosphere}} \begin{bmatrix} xz \\ yz \\ x^2 + y^2 \end{bmatrix} \mathrm{d}M \tag{2.47}$$

and

$$\boldsymbol{h}_{Atmo} = \iiint\limits_{\text{Atmosphere}} \boldsymbol{x} \times \dot{\boldsymbol{x}}\ \mathrm{d}M. \tag{2.48}$$

The Cartesian coordinates of the vector $\boldsymbol{x}$ are expressed by spherical coordinates. Denoting the radius with r, the longitude with λ and the latitude with ϕ the position vector is

$$\boldsymbol{x} = \begin{bmatrix} r\cos\phi\cos\lambda \\ r\cos\phi\sin\lambda \\ r\sin\phi \end{bmatrix}. \tag{2.49}$$

The atmospheric currents are given by meteorological models, which provide a radial wind component u_r, a west-east wind component u_λ and a north-south component u_ϕ for each position. That leads to

$$\boldsymbol{u} = \begin{bmatrix} u_r \\ u_\lambda \\ u_\phi \end{bmatrix} = \begin{bmatrix} \dot{r} \\ r\dot{\lambda}\cos\phi \\ r\dot{\phi} \end{bmatrix}. \tag{2.50}$$

The time derivative of the position vector $\boldsymbol{x}$ is obtained by differentiating Equation 2.49. It yields with the definition of the wind vector $\boldsymbol{u}$

$$\dot{\boldsymbol{x}} = \begin{bmatrix} \dot{r}\cos\phi\cos\lambda - r\dot{\lambda}\cos\phi\sin\lambda - r\dot{\phi}\sin\phi\cos\lambda \\ \dot{r}\cos\phi\sin\lambda + r\dot{\lambda}\cos\phi\cos\lambda - r\dot{\phi}\sin\phi\sin\lambda \\ \dot{r}\sin\phi + r\dot{\phi}\cos\phi \end{bmatrix} = \begin{bmatrix} u_r\cos\phi\cos\lambda - u_\lambda\sin\lambda - u_\phi\sin\phi\cos\lambda \\ u_r\cos\phi\sin\lambda + u_\lambda\cos\lambda - u_\phi\sin\phi\sin\lambda \\ u_r\sin\phi + u_\phi\cos\phi \end{bmatrix}. \tag{2.51}$$

The mass element $\mathsf{d}M$ is replaced with the density ρ of the mass element multiplied by the spherical volume element. Thus, it holds

$$\mathsf{d}M = \rho r^2 \cos\phi \, \mathsf{d}r \, \mathsf{d}\phi \, \mathsf{d}\lambda. \tag{2.52}$$

The atmospheric contribution to the tensor of inertia and the relative angular momentum is obtained by the Equations 2.49, 2.51 and 2.52 as

$$\boldsymbol{c}_{Atmo} = \iiint\limits_{\text{Atmosphere}} \rho r^4 \begin{bmatrix} \cos^2\phi \sin\phi \cos\lambda \\ \cos^2\phi \sin\phi \sin\lambda \\ \cos^3\phi \end{bmatrix} \mathsf{d}r \, \mathsf{d}\phi \, \mathsf{d}\lambda \tag{2.53}$$

and

$$\boldsymbol{h}_{Atmo} = \iiint\limits_{\text{Atmosphere}} \rho r^3 \begin{bmatrix} u_\phi \cos\phi \sin\lambda - u_\lambda \sin\phi \cos\phi \cos\lambda \\ -u_\phi \cos\phi \cos\lambda - u_\lambda \sin\phi \cos\phi \sin\lambda \\ u_\lambda \cos^2\phi \end{bmatrix} \mathsf{d}r \, \mathsf{d}\phi \, \mathsf{d}\lambda. \tag{2.54}$$

The contributions of the oceans and hydrology are obtained accordingly. In practice, the models of the subsystems provide threedimensional grids with various data. Some models are shortly described in Subsection 5.1.3. Each grid cell contains, among other data, values for the time and position dependent velocity vector $\boldsymbol{u}$ and the time and position dependent density ρ. The contributions of the subsystems to the tensor of inertia and the relative angular moment are then obtained by numerical integration of the grid cells.

The modeled excitation functions are provided either in terms of dimensionless EAMF or angular momentum functions, which posses the unit $\mathrm{kg\,m^2\,s^{-1}}$. If the excitation functions are given in angular momentum functions, the motion term (sometimes called wind term) is identical to the relative angular momentum $\boldsymbol{h}$. The mass term (sometimes called pressure term) is the tensor vector $\boldsymbol{c}$ multiplied by the mean rotation velocity Ω. The EAMF reflect the dimensionless functions χ_x, χ_y and χ_z. Since differently defined EAMF exist, consistent time series have to be ensured by a transformation of the different EAMF (Dickman, 2003, discussion in Subsection 2.2.2). Here, EAMF are transformed into angular momentum functions.

2.3. Gravity field of the Earth

According to Newton's law of gravitation, the gravitational potential V of a point mass is proportional to the gravitational constant G and to the reciprocal distance between the point mass and a given point P with the spherical coordinates (r, λ, ϑ). The potential of the entire Earth is accordingly obtained by the integral over the continuously distributed point masses

$$V(r, \lambda, \vartheta) = G \iiint\limits_{\text{Earth}} \frac{\mathsf{d}M}{l} \tag{2.55}$$

where l denotes the distance from P to the differential mass element $\mathsf{d}M$ with the spherical coordinates $(r', \lambda', \vartheta')$. Figure 2.2 shows the relation between P and differential mass element $\mathsf{d}M$. The angle ψ is the angle between the differential mass element $\mathrm{d}M$ and P. The spherical law of cosines gives the relation between $\cos\psi$ and the longitudes λ and the polar distances ϑ of $\mathrm{d}M$ and P as

$$\cos\psi = \cos\vartheta \cos\vartheta' + \sin\vartheta \sin\vartheta' \cos(\lambda' - \lambda). \tag{2.56}$$

If P lies outside of the Earth's body, the reciprocal distance $1/l$ can be developed in a Taylor series. If $\cos\psi$ in Equation 2.56 is substituted into the Taylor series, the potential is expressed by following series expansion (Hofmann-Wellenhof and Moritz, 2006; Torge and Müller, 2012)

$$V(r, \lambda, \vartheta) = \frac{GM}{r} \sum_{n=0}^{\infty} \sum_{m=0}^{n} \left(\frac{a}{r}\right)^n (C_{nm} \cos m\lambda + S_{nm} \sin m\lambda) \, P_{nm}(\cos\vartheta) \tag{2.57}$$

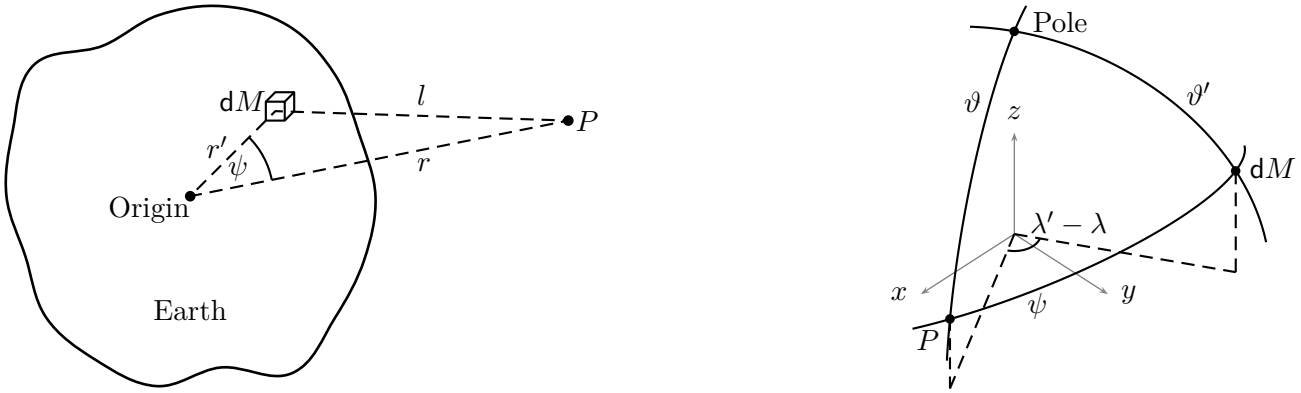

Figure 2.2: The left figure describes the relation between the differential mass element $\mathrm{d}M$ and an arbitrary point P outside of the Earth's body. The right figure illustrates the spherical coordinates of $\mathrm{d}M$ and P (Hofmann-Wellenhof and Moritz, 2006, Figures 1.7 and 2.9, modified).

where P_{nm} denotes the fully normalized associated Legendre function of degree n and order m. The fully normalized gravity field coefficients C_{nm} and S_{nm} are defined with (Torge and Müller, 2012)

$$\begin{aligned} C_{n0} &= \frac{1}{Ma^n}\,\frac{1}{2n+1}\iiint\limits_{\text{Earth}} r'^n\, P_{n0}\left(\cos\vartheta'\right)\,\mathrm{d}M && \text{if} \quad m=0 \\ C_{nm} &= \frac{1}{Ma^n}\,\frac{1}{2\,(2n+1)}\iiint\limits_{\text{Earth}} r'^n\,\cos m\lambda'\,P_{nm}\left(\cos\vartheta'\right)\,\mathrm{d}M && m\neq 0 \\ S_{nm} &= \frac{1}{Ma^n}\,\frac{1}{2\,(2n+1)}\iiint\limits_{\text{Earth}} r'^n\,\sin m\lambda'\,P_{nm}\left(\cos\vartheta'\right)\,\mathrm{d}M && m\neq 0. \end{aligned} \tag{2.58}$$

The gravity field coefficients of the degrees $n = 0, 1, 2$ are related to the Earth's center of mass and to the tensor of inertia. According to Hofmann-Wellenhof and Moritz (2006) and Torge and Müller (2012), the fully normalized associated Legendre functions P_{nm} of the low degrees are

$$\begin{aligned} &P_{00}(\cos\vartheta') = 1, \\ &P_{10}(\cos\vartheta') = \sqrt{3}\cos\vartheta', && P_{11}(\cos\vartheta') = \sqrt{3}\sin\vartheta', \\ &P_{20}(\cos\vartheta') = \frac{3\sqrt{5}}{2}\cos'^2\vartheta - \frac{\sqrt{5}}{2}, && P_{21}(\cos\vartheta') = \sqrt{15}\sin\vartheta'\cos\vartheta', \quad P_{22}(\cos\vartheta') = \frac{\sqrt{15}}{2}\sin'^2\vartheta'. \end{aligned} \tag{2.59}$$

The fully normalized gravity field coefficients of low degrees are evaluated according to Equations 2.58 and 2.59

$$\begin{aligned} C_{00} &= \frac{1}{M}\iiint\limits_{\text{Earth}}\mathrm{d}M = 1 \\ C_{10} &= \frac{1}{Ma}\frac{1}{\sqrt{3}}\iiint\limits_{\text{Earth}} r'\cos\vartheta'\,\mathrm{d}M \\ C_{11} &= \frac{1}{Ma}\frac{1}{\sqrt{3}}\iiint\limits_{\text{Earth}} r'\cos\lambda'\sin\vartheta'\,\mathrm{d}M && S_{11} = \frac{1}{Ma}\frac{1}{\sqrt{3}}\iiint\limits_{\text{Earth}} r'\sin\lambda'\sin\vartheta'\,\mathrm{d}M \\ C_{20} &= \frac{1}{Ma^2}\frac{1}{\sqrt{5}}\iiint\limits_{\text{Earth}} r'^2\left(\frac{3}{2}\cos^2\vartheta' - \frac{1}{2}\right)\mathrm{d}M \\ C_{21} &= \frac{1}{Ma^2}\sqrt{\frac{3}{5}}\iiint\limits_{\text{Earth}} r'^2\cos\lambda'\sin\vartheta'\cos\vartheta'\,\mathrm{d}M && S_{21} = \frac{1}{Ma^2}\sqrt{\frac{3}{5}}\iiint\limits_{\text{Earth}} r'^2\sin\lambda'\sin\vartheta'\cos\vartheta'\,\mathrm{d}M \\ C_{22} &= \frac{1}{Ma^2}\sqrt{\frac{3}{5}}\iiint\limits_{\text{Earth}} \frac{1}{2}r'^2\cos 2\lambda'\sin^2\vartheta'\,\mathrm{d}M && S_{22} = \frac{1}{Ma^2}\sqrt{\frac{3}{5}}\iiint\limits_{\text{Earth}} \frac{1}{2}r'^2\sin 2\lambda'\sin^2\vartheta'\,\mathrm{d}M. \end{aligned} \tag{2.60}$$

The spherical coordinates $(r', \lambda', \vartheta')$ in Equations 2.60 are replaced with Cartesian coordinates (x', y', z'). The transformation formulas are

$$x' = r' \cos\lambda' \sin\vartheta', \qquad y' = \sin\lambda' \sin\vartheta', \qquad z' = r' \cos\vartheta'. \tag{2.61}$$

The Cartesian coordinates are substituted into the fully normalized gravity field coefficients. The addition theorems for angles are applied to the terms $\cos 2\lambda'$ and $\sin 2\lambda'$. Then, it holds

$$\begin{aligned}
C_{00} &= 1 \\
C_{10} &= \frac{1}{Ma}\frac{1}{\sqrt{3}} \iiint\limits_{\text{Earth}} z' \,\mathrm{d}M \\
C_{11} &= \frac{1}{Ma}\frac{1}{\sqrt{3}} \iiint\limits_{\text{Earth}} x' \,\mathrm{d}M & S_{11} &= \frac{1}{Ma}\frac{1}{\sqrt{3}} \iiint\limits_{\text{Earth}} y' \,\mathrm{d}M \\
C_{20} &= \frac{1}{Ma^2}\frac{1}{\sqrt{5}} \iiint\limits_{\text{Earth}} z'^2 - \frac{x'^2 + y'^2}{2} \,\mathrm{d}M \\
C_{21} &= \frac{1}{Ma^2}\sqrt{\frac{3}{5}} \iiint\limits_{\text{Earth}} x' z' \,\mathrm{d}M & S_{21} &= \frac{1}{Ma^2}\sqrt{\frac{3}{5}} \iiint\limits_{\text{Earth}} y' z' \,\mathrm{d}M \\
C_{22} &= \frac{1}{Ma^2}\sqrt{\frac{3}{5}} \iiint\limits_{\text{Earth}} \frac{x'^2 - y'^2}{2} \,\mathrm{d}M & S_{22} &= \frac{1}{Ma^2}\sqrt{\frac{3}{5}} \iiint\limits_{\text{Earth}} x' y' \,\mathrm{d}M.
\end{aligned} \tag{2.62}$$

The integrals $\iiint x' \,\mathrm{d}M/M$, $\iiint y' \,\mathrm{d}M/M$ and $\iiint z' \,\mathrm{d}M/M$ are the coordinates of the Earth's center of mass. Since the origin of the geocentric ITRS coincides with the center of mass, these integrals are zero

$$C_{10} = 0, \qquad C_{11} = 0 \qquad \text{and} \qquad S_{11} = 0. \tag{2.63}$$

According to Equation 2.5, the GFC2 are related to Earth's tensor of inertia by

$$\begin{aligned}
C_{20} &= \frac{1}{Ma^2}\frac{1}{\sqrt{5}}\left(\frac{i_{xx} + i_{yy}}{2} - i_{zz}\right) \\
C_{21} &= \frac{1}{Ma^2}\sqrt{\frac{3}{5}} i_{yz} & S_{21} &= \frac{1}{Ma^2}\sqrt{\frac{3}{5}} i_{xz} \\
C_{22} &= \frac{1}{Ma^2}\sqrt{\frac{3}{5}} \frac{i_{yy} - i_{xx}}{2} & S_{22} &= \frac{1}{Ma^2}\sqrt{\frac{3}{5}} i_{xy}.
\end{aligned} \tag{2.64}$$

where i_{xx}, i_{xy}, i_{xz}, i_{yy}, i_{xz} and i_{zz} denote the elements of the Earth's tensor of inertia. Equation 2.12 splits the tensor of inertia in a constant and in a time-variable part. Substituting Equation 2.12 into Equation 2.64 leads to

$$\begin{aligned}
\Delta C_{20} &= C_{20} - \frac{1}{Ma^2}\frac{1}{\sqrt{5}}(A' - C) = \frac{1}{Ma^2}\frac{1}{\sqrt{5}}\left(\frac{c_{xx} + c_{yy}}{2} - c_{zz}\right) \\
\Delta C_{21} &= \frac{1}{Ma^2}\sqrt{\frac{3}{5}} c_{yz} & \Delta S_{21} &= \frac{1}{Ma^2}\sqrt{\frac{3}{5}} c_{xz} \\
\Delta C_{22} &= \frac{1}{Ma^2}\sqrt{\frac{3}{5}} \frac{c_{yy} - c_{xx}}{2} & \Delta S_{22} &= \frac{1}{Ma^2}\sqrt{\frac{3}{5}} c_{xy}.
\end{aligned} \tag{2.65}$$

The last equations relate five gravity field coefficients to six elements of the tensor of inertia. The off-diagonal elements of the tensor of inertia can be uniquely determined, whereas the trace of the tensor of inertia is underdetermined. According to Rochester and Smylie (1974), the trace of the tensor of inertia is invariant to any deformations as long as the principle of mass conservation is valid. Their result allows to solve the otherwise underdetermined system by applying following additional tensor trace constraint

$$c_{xx} + c_{yy} + c_{zz} = 0. \tag{2.66}$$

The potentials of Moon and Sun cause tidal variations of the Earth's potential. Chapter 1 of the IERS Conventions (2010) gives a short overview over the tidal effects on the potential and positions observed

on the Earth's crust. The observed gravitational potential is effected by the combination of the tidal gravitational potential of external bodies (Moon, Sun and planets) and the Earth's own (indirect) potential, which is additionally perturbed by the action of the tidal potential. The external and the indirect potential contain both permanent and time-dependent parts.
The gravity field coefficients are given either as conventional tide free or as zero tide gravity field coefficients. If all tidal signals are removed from the potential, it is a conventional tide free potential. EGM2008 (`http://earth-info.nga.mil/GandG/wgs84/gravitymod/egm2008/`) is an example for a conventional tide free potential. Accordingly, ITRF coordinates describe positions on a conventional tide free crust. Chapter 6 of IERS Conventions (2010) provides a model which removes tidal signals from the gravity field coefficients by means of the Love numbers. The zero tide potential is obtained by restoring the indirect, permanent part of the tide potential. The degree two zonal tide generating potential has a non-zero mean (average in time) value. The time-independent potential produces a permanent deformation and consequently a time-independent contribution to the potential coefficient C_{20}. Therefore, the zero tide and conventional tide free values for C_{20} differ by a constant factor (IERS Conventions, 2010, Subsection 6.2.2), whereas the other GFC2 have the same value in the zero tide and conventional tide free system.

3. Estimation of Variance and Covariance Components in a constrained Gauss-Helmert Model

3.1. Least-squares adjustment in a constrained Gauss-Helmert Model

As mentioned before, the mutual validation is performed by a universal, linear least-squares solver, which includes the estimation of VCC. The development of the least-squares solver is performed in several steps. As a preparatory step, the first Subsection 3.1 solves a constrained least-squares adjustment problem considering a known stochastic model. Subsection 3.2 derives the necessary formulas for the BIQUE of the VCC in a constrained GHM. Subsection 3.3 proposes the numerical methods for the calculation of the VCC and suggests a pseudocode for an efficient universal least-squares solver. The development of the BIQUE of the VCC in a constrained GHM requires some theorems, provided by Koch (1999) with proofs. The used theorems are listed in Appendix B. The development of the least-squares solver is described by Figure 1.2 graphically.
The method of least-squares is a standard approach to solve overdetermined systems. The goal of least-squares adjustment is to determine unknown parameters, functionally related to observed quantities. The observations are collected in a $n \times 1$ vector $\boldsymbol{l}$. The observation vector has an expectation value $\boldsymbol{\mu_l}$ and a positive-definite variance covariance matrix $\boldsymbol{D_{ll}}$

$$\mathrm{E}(\boldsymbol{l}) = \boldsymbol{\mu_l} \qquad \text{and} \qquad \mathrm{Var}(\boldsymbol{l}) = \boldsymbol{D_{ll}}. \tag{3.1}$$

The unknown parameters are collected in a $u \times 1$ vector $\boldsymbol{\beta}$. The unknowns and the observations are related by b_1 independent functional relations $\boldsymbol{\phi}_H$. The unknowns are restricted by b_2 additional independent functional relations $\boldsymbol{\phi}_C$. For example, the unknowns might be constrained by physical laws, or datum defects might be solved by applying constraints. The non-linear functional relations between $\boldsymbol{\mu_l}$ and $\boldsymbol{\beta}$ are generally described by

$$\boldsymbol{\phi}_H(\boldsymbol{\mu_l}, \boldsymbol{\beta}) = \mathbf{0}. \tag{3.2a}$$

The additional constraints are given by

$$\boldsymbol{\phi}_C(\boldsymbol{\beta}) \quad = \mathbf{0}. \tag{3.2b}$$

Equation 3.2b contains no stochastic quantity. Therefore, the constraints have a high impact on the estimation of the unknowns. If the zero-vector on the right hand side in Equation 3.2b is interpreted as a pseudo-observation vector with a corresponding VCM, the impact of the constraints decrease in dependency on the chosen VCM. In that case, both Equations 3.2 are stochastic, and they can be summarized into one unconstrained functional model.
The non-linear Equations 3.2 are linearized by the Taylor expansion with respect to an approximated vector of unknowns $\boldsymbol{\beta}_0$ and the vector of the observations $\boldsymbol{l}$. The Taylor expansion is truncated after the linear term. That leads to

$$\boldsymbol{A}_H \Delta\boldsymbol{\beta} = \boldsymbol{w}_H + \boldsymbol{B}\boldsymbol{\epsilon} \tag{3.3a}$$
$$\boldsymbol{A}_C \Delta\boldsymbol{\beta} = \boldsymbol{w}_C \tag{3.3b}$$

with the residual vector: $\boldsymbol{\epsilon} = \boldsymbol{l} - \boldsymbol{\mu_l}$,
reduced unknowns: $\Delta\boldsymbol{\beta} = \boldsymbol{\beta} - \boldsymbol{\beta}_0$,
misclosure vectors: $\boldsymbol{w}_H = -\boldsymbol{\phi}_H(\boldsymbol{l}, \boldsymbol{\beta}_0)$, $\boldsymbol{w}_C = -\boldsymbol{\phi}_C(\boldsymbol{\beta}_0)$,
design matrices: $\boldsymbol{A}_H = \frac{\mathsf{d}\,\boldsymbol{\phi}_H}{\mathsf{d}\,\boldsymbol{\beta}}(\boldsymbol{l}, \boldsymbol{\beta}_0)$, $\boldsymbol{A}_C = \frac{\mathsf{d}\,\boldsymbol{\phi}_C}{\mathsf{d}\,\boldsymbol{\beta}}(\boldsymbol{\beta}_0)$, $\boldsymbol{B} = -\frac{\mathsf{d}\,\boldsymbol{\phi}_H}{\mathsf{d}\,\boldsymbol{l}}(\boldsymbol{l}, \boldsymbol{\beta}_0)$.

According to the definition of the residuals $\boldsymbol{\epsilon}$, the expectation value of $\boldsymbol{\epsilon}$ is zero and it holds for the expectation value of $\boldsymbol{w}_H$

$$\mathrm{E}(\boldsymbol{w}_H) = \boldsymbol{A}_H \Delta\boldsymbol{\beta}. \tag{3.4}$$

A least-squares adjustment minimizes the weighted squared sum of the residuals

$$\Omega = \boldsymbol{\epsilon}^\mathsf{T} \boldsymbol{D}_{ll}^{-1} \boldsymbol{\epsilon} \rightarrow \min . \tag{3.5}$$

A constrained optimization problem can be solved by Lagrange functions. The minimization problem constrained by the Equations 3.3 leads to the Lagrange function

$$\boldsymbol{\phi}_{LG} = \boldsymbol{\epsilon}^\mathsf{T} \boldsymbol{D}_{ll}^{-1} \boldsymbol{\epsilon} + 2\boldsymbol{k}_H^\mathsf{T} \left(\boldsymbol{A}_H \Delta\boldsymbol{\beta} - \boldsymbol{B}\boldsymbol{\epsilon} - \boldsymbol{w}_H \right) + 2\boldsymbol{k}_C^\mathsf{T} \left(\boldsymbol{A}_C \Delta\boldsymbol{\beta} - \boldsymbol{w}_C \right) \tag{3.6}$$

where $\boldsymbol{k}_H$ and $\boldsymbol{k}_C$ denote the Lagrange multipliers. The minimum is found by setting the derivatives of the Lagrange function with respect to each unknown parameter to zero. Adjusted unknown parameters are denoted with a hat over the parameters. The differentiation leads to

$$\frac{\mathsf{d}\,\boldsymbol{\phi}_{LG}}{\mathsf{d}\,\boldsymbol{\epsilon}} = 2\boldsymbol{D}_{ll}^{-1}\hat{\boldsymbol{\epsilon}} - 2\boldsymbol{B}^\mathsf{T}\hat{\boldsymbol{k}}_H \overset{!}{=} \boldsymbol{0} \quad \Rightarrow \quad \hat{\boldsymbol{\epsilon}} = \boldsymbol{D}_{ll}\boldsymbol{B}^\mathsf{T}\hat{\boldsymbol{k}}_H, \tag{3.7a}$$

$$\frac{\mathsf{d}\,\boldsymbol{\phi}_{LG}}{\mathsf{d}\,\Delta\boldsymbol{\beta}} = 2\boldsymbol{A}_H^\mathsf{T}\hat{\boldsymbol{k}}_H + 2\boldsymbol{A}_C^\mathsf{T}\hat{\boldsymbol{k}}_C \overset{!}{=} \boldsymbol{0} \quad \Rightarrow \quad \boldsymbol{A}_H^\mathsf{T}\hat{\boldsymbol{k}}_H = -\boldsymbol{A}_C^\mathsf{T}\hat{\boldsymbol{k}}_C. \tag{3.7b}$$

If $\hat{\boldsymbol{\epsilon}}$ in Equation 3.7a is substituted into Equation 3.3a, it yields

$$\boldsymbol{A}_H\Delta\hat{\boldsymbol{\beta}} = \boldsymbol{w}_H + \boldsymbol{B}\boldsymbol{D}_{ll}\boldsymbol{B}^\mathsf{T}\hat{\boldsymbol{k}}_H \quad \Rightarrow \quad \hat{\boldsymbol{k}}_H = \left(\boldsymbol{B}\boldsymbol{D}_{ll}\boldsymbol{B}^\mathsf{T}\right)^{-1}\left(\boldsymbol{A}_H\Delta\hat{\boldsymbol{\beta}} - \boldsymbol{w}_H\right). \tag{3.8}$$

Substituting $\hat{\boldsymbol{k}}_H$ into Equation 3.7b leads to

$$\begin{aligned} & \boldsymbol{A}_H^\mathsf{T}\left(\boldsymbol{B}\boldsymbol{D}_{ll}\boldsymbol{B}^\mathsf{T}\right)^{-1}\left(\boldsymbol{A}_H\Delta\hat{\boldsymbol{\beta}} - \boldsymbol{w}_H\right) = -\boldsymbol{A}_C^\mathsf{T}\hat{\boldsymbol{k}}_C \\ \Rightarrow \quad & \boldsymbol{A}_H^\mathsf{T}\left(\boldsymbol{B}\boldsymbol{D}_{ll}\boldsymbol{B}^\mathsf{T}\right)^{-1}\boldsymbol{A}_H\Delta\hat{\boldsymbol{\beta}} + \boldsymbol{A}_C^\mathsf{T}\hat{\boldsymbol{k}}_C = \boldsymbol{A}_H^\mathsf{T}\left(\boldsymbol{B}\boldsymbol{D}_{ll}\boldsymbol{B}^\mathsf{T}\right)^{-1}\boldsymbol{w}_H. \end{aligned} \tag{3.9}$$

Defining the matrix

$$\boldsymbol{D}_{ww} = \boldsymbol{B}\boldsymbol{D}_{ll}\boldsymbol{B}^\mathsf{T} \tag{3.10}$$

the Equations 3.9 and 3.3b are summarized to the system of normal equations

$$\begin{bmatrix} \boldsymbol{A}_H^\mathsf{T}\boldsymbol{D}_{ww}^{-1}\boldsymbol{A}_H & \boldsymbol{A}_C^\mathsf{T} \\ \boldsymbol{A}_C & \boldsymbol{0} \end{bmatrix} \begin{bmatrix} \Delta\hat{\boldsymbol{\beta}} \\ \hat{\boldsymbol{k}}_C \end{bmatrix} = \begin{bmatrix} \boldsymbol{A}_H^\mathsf{T}\boldsymbol{D}_{ww}^{-1}\boldsymbol{w}_H \\ \boldsymbol{w}_C \end{bmatrix}. \tag{3.11}$$

The system of normal equations is similar to the solution of a constrained GMM. In fact, each GHM can be transformed into a GMM. The misclosure vector $\boldsymbol{w}_H$ is the transformed observation vector and the matrix $\boldsymbol{D}_{ww}$ is the VCM of the transformed observation vector. The vector $\boldsymbol{B}\boldsymbol{\epsilon}$ is interpreted as the transformed residual vector. It might be easier for some readers to follow the derivations in this chapter, if she or he imagines a transformed GMM instead of the GHM.
The system of normal equations is assumed to describe a well-posed problem. Ill-posed problems (caused by e.g. datum defects) are assumed to be solved by the application of appropriate constraints. Then, a unique inverse of the normal equation matrix exists. The normal equation matrix and its inverse $\boldsymbol{Q}$, which contains the submatrices $\boldsymbol{Q}_{11}$, $\boldsymbol{Q}_{12}$ and $\boldsymbol{Q}_{22}$, are related by

$$\begin{bmatrix} \boldsymbol{A}_H^\mathsf{T}\boldsymbol{D}_{ww}^{-1}\boldsymbol{A}_H & \boldsymbol{A}_C^\mathsf{T} \\ \boldsymbol{A}_C & \boldsymbol{0} \end{bmatrix} \begin{bmatrix} \boldsymbol{Q}_{11} & \boldsymbol{Q}_{12} \\ \boldsymbol{Q}_{12}^\mathsf{T} & \boldsymbol{Q}_{22} \end{bmatrix} = \begin{bmatrix} \boldsymbol{I} & \boldsymbol{0} \\ \boldsymbol{0} & \boldsymbol{I} \end{bmatrix}. \tag{3.12}$$

Four subequations are derived from Equation 3.12

$$\boldsymbol{A}_H^\mathsf{T}\boldsymbol{D}_{ww}^{-1}\boldsymbol{A}_H\boldsymbol{Q}_{11} + \boldsymbol{A}_C^\mathsf{T}\boldsymbol{Q}_{12}^\mathsf{T} = \boldsymbol{I}, \tag{3.13a}$$

$$\boldsymbol{A}_H^\mathsf{T}\boldsymbol{D}_{ww}^{-1}\boldsymbol{A}_H\boldsymbol{Q}_{12} + \boldsymbol{A}_C^\mathsf{T}\boldsymbol{Q}_{22} = \boldsymbol{0}, \tag{3.13b}$$

$$\boldsymbol{A}_C\boldsymbol{Q}_{11} = \boldsymbol{0}, \tag{3.13c}$$

$$\boldsymbol{A}_C\boldsymbol{Q}_{12} = \boldsymbol{I}. \tag{3.13d}$$

The submatrices of the inverse $\boldsymbol{Q}$ can be determined at once by Equation 3.12. Alternatively, if the matrix $\boldsymbol{A}_H^\mathsf{T}\boldsymbol{D}_{ww}^{-1}\boldsymbol{A}_H$ has a unique inverse, the submatrices can be determined by a sequential inversion (Koch, 1999, Formula 1.111, p. 33).

The adjusted vector of unknowns $\Delta\hat{\boldsymbol{\beta}}$ is

$$\Delta\hat{\boldsymbol{\beta}} = \boldsymbol{Q}_{11}\boldsymbol{A}_H^{\mathsf{T}}\boldsymbol{D}_{\boldsymbol{ww}}^{-1}\boldsymbol{w}_H + \boldsymbol{Q}_{12}\boldsymbol{w}_C. \tag{3.14}$$

The product $\boldsymbol{B}\hat{\boldsymbol{\epsilon}}$ is obtained by Equations 3.14 and 3.3a with

$$\boldsymbol{B}\hat{\boldsymbol{\epsilon}} = \boldsymbol{A}_H\Delta\hat{\boldsymbol{\beta}} - \boldsymbol{w}_H = \left(\boldsymbol{A}_H\boldsymbol{Q}_{11}\boldsymbol{A}_H^{\mathsf{T}}\boldsymbol{D}_{\boldsymbol{ww}}^{-1} - \boldsymbol{I}\right)\boldsymbol{w}_H + \boldsymbol{A}_H\boldsymbol{Q}_{12}\boldsymbol{w}_C. \tag{3.15}$$

The adjusted residual vector $\hat{\boldsymbol{\epsilon}}$ is according to the Equations 3.7a, 3.8 and 3.15

$$\hat{\boldsymbol{\epsilon}} = \boldsymbol{D}_{\boldsymbol{ll}}\boldsymbol{B}^{\mathsf{T}}\boldsymbol{D}_{\boldsymbol{ww}}^{-1}\left(\left(\boldsymbol{A}_H\boldsymbol{Q}_{11}\boldsymbol{A}_H^{\mathsf{T}}\boldsymbol{D}_{\boldsymbol{ww}}^{-1} - \boldsymbol{I}\right)\boldsymbol{w}_H + \boldsymbol{A}_H\boldsymbol{Q}_{12}\boldsymbol{w}_C\right). \tag{3.16}$$

The expectation value of the adjusted residuals $\hat{\boldsymbol{\epsilon}}$ has to be zero. Otherwise, the functional model is biased. Unbiasness is proven with Equations 3.4 and 3.13a

$$\begin{aligned}
\mathrm{E}\left(\hat{\boldsymbol{\epsilon}}\right) &= \boldsymbol{D}_{\boldsymbol{ll}}\boldsymbol{B}^{\mathsf{T}}\boldsymbol{D}_{\boldsymbol{ww}}^{-1}\left(\left(\boldsymbol{A}_H\boldsymbol{Q}_{11}\boldsymbol{A}_H^{\mathsf{T}}\boldsymbol{D}_{\boldsymbol{ww}}^{-1} - \boldsymbol{I}\right)\mathrm{E}\left(\boldsymbol{w}_H\right) + \boldsymbol{A}_H\boldsymbol{Q}_{12}\boldsymbol{w}_C\right) \\
&= \boldsymbol{D}_{\boldsymbol{ll}}\boldsymbol{B}^{\mathsf{T}}\boldsymbol{D}_{\boldsymbol{ww}}^{-1}\left(\boldsymbol{A}_H\boldsymbol{Q}_{11}\boldsymbol{A}_H^{\mathsf{T}}\boldsymbol{D}_{\boldsymbol{ww}}^{-1}\boldsymbol{A}_H\Delta\boldsymbol{\beta} - \boldsymbol{A}_H\Delta\boldsymbol{\beta} + \boldsymbol{A}_H\boldsymbol{Q}_{12}\boldsymbol{A}_C\Delta\boldsymbol{\beta}\right) \\
&= \boldsymbol{D}_{\boldsymbol{ll}}\boldsymbol{B}^{\mathsf{T}}\boldsymbol{D}_{\boldsymbol{ww}}^{-1}\left(\boldsymbol{A}_H\left(\boldsymbol{I} - \boldsymbol{Q}_{12}\boldsymbol{A}_C\right) - \boldsymbol{A}_H + \boldsymbol{A}_H\boldsymbol{Q}_{12}\boldsymbol{A}_C\right)\Delta\boldsymbol{\beta} \\
&= \boldsymbol{0}.
\end{aligned} \tag{3.17}$$

The VCM of the unknowns and residuals are obtained by variance covariance propagation. In contrast to the stochastic vector $\boldsymbol{w}_H$, the deterministic vector $\boldsymbol{w}_C$ does not contribute to the VCM. It holds with the Equations 3.13, 3.14 and 3.16

$$\boldsymbol{D}_{\hat{\boldsymbol{\beta}}\hat{\boldsymbol{\beta}}} = \boldsymbol{Q}_{11} \tag{3.18}$$

$$\boldsymbol{D}_{\hat{\boldsymbol{\epsilon}}\hat{\boldsymbol{\epsilon}}} = \boldsymbol{D}_{\boldsymbol{ll}}\boldsymbol{B}^{\mathsf{T}}\boldsymbol{D}_{\boldsymbol{ww}}^{-1}\left(\boldsymbol{D}_{\boldsymbol{ww}} - \boldsymbol{A}_H\boldsymbol{Q}_{11}\boldsymbol{A}_H^{\mathsf{T}}\right)\boldsymbol{D}_{\boldsymbol{ww}}^{-1}\boldsymbol{B}\boldsymbol{D}_{\boldsymbol{ll}}. \tag{3.19}$$

The adjusted residual squares sum $\hat{\Omega}$ is obtained by Equations 3.15 and 3.16 with

$$\hat{\Omega} = \hat{\boldsymbol{\epsilon}}^{\mathsf{T}}\boldsymbol{D}_{\boldsymbol{ll}}^{-1}\hat{\boldsymbol{\epsilon}} = \hat{\boldsymbol{\epsilon}}^{\mathsf{T}}\boldsymbol{B}^{\mathsf{T}}\boldsymbol{D}_{\boldsymbol{ww}}^{-1}\boldsymbol{B}\hat{\boldsymbol{\epsilon}}. \tag{3.20}$$

Koch (1999, Theorem 2.175, p. 134) gave the expectation value of quadratic forms. According to this theorem, $\mathrm{E}\left(\hat{\boldsymbol{\epsilon}}\right) = \boldsymbol{0}$ and Equations 3.13, it holds for the expectation value of $\hat{\Omega}$

$$\begin{aligned}
\mathrm{E}\left(\hat{\Omega}\right) &= \mathrm{tr}\left(\boldsymbol{D}_{\hat{\boldsymbol{\epsilon}}\hat{\boldsymbol{\epsilon}}}\boldsymbol{D}_{\boldsymbol{ll}}^{-1}\right) \\
&= \mathrm{tr}\left(\boldsymbol{D}_{\boldsymbol{ll}}\boldsymbol{B}^{\mathsf{T}}\boldsymbol{D}_{\boldsymbol{ww}}^{-1}\left(\boldsymbol{D}_{\boldsymbol{ww}} - \boldsymbol{A}_H\boldsymbol{Q}_{11}\boldsymbol{A}_H^{\mathsf{T}}\right)\boldsymbol{D}_{\boldsymbol{ww}}^{-1}\boldsymbol{B}\right) \\
&= \mathrm{tr}\left(\boldsymbol{I} - \boldsymbol{A}_H\boldsymbol{Q}_{11}\boldsymbol{A}_H^{\mathsf{T}}\boldsymbol{D}_{\boldsymbol{ww}}^{-1}\right) \\
&= b_1 - \mathrm{tr}\left(\boldsymbol{A}_H^{\mathsf{T}}\boldsymbol{D}_{\boldsymbol{ww}}^{-1}\boldsymbol{A}_H\boldsymbol{Q}_{11}\right) \\
&= b_1 - \mathrm{tr}\left(\boldsymbol{I} - \boldsymbol{A}_C^{\mathsf{T}}\boldsymbol{Q}_{12}^{\mathsf{T}}\right) \\
&= b_1 - u + \mathrm{tr}\left(\boldsymbol{Q}_{12}^{\mathsf{T}}\boldsymbol{A}_C^{\mathsf{T}}\right) \\
&= b_1 + b_2 - u = r.
\end{aligned} \tag{3.21}$$

The expectation value of the adjusted residual squares sum $\hat{\Omega}$ equals the redundancy r. The elements on the main diagonal of the matrix $\boldsymbol{D}_{\hat{\boldsymbol{\epsilon}}\hat{\boldsymbol{\epsilon}}}\boldsymbol{D}_{\boldsymbol{ll}}^{-1}$ are the partial redundancies of the specific observations. The partial redundancies are reliability measures for the observations (Baarda, 1968). If the observations are uncorrelated, the partial redundancies amount to values within the unit-interval [0, 1]. A partial redundancy of zero indicates that the specific observation is not controlled by any other observation. An error in this observation cannot be detected, and the error has furthermore a high impact on the estimation of the unknowns. A partial redundancy of one suggests that this specific observation is fully controlled by other observations and does therefore not contribute to the estimation of the unknowns. If the observations are correlated, the partial redundancies sporadically amount to values outside of the unit-interval. Schaffrin (1997) suggested a transformation of partial redundancies of correlated observations, in order to reach partial redundancies within the unit-interval, which are open to interpretation.

3.2. Best Invariant Quadratic Estimation of Variance and Covariance Components

The integration of heterogeneous observations into a common linear adjustment model requires the determination of the unknown relative weights of these data. They are usually determined by a variance component estimation. Additionally, the estimation of covariances might be of interest. Helmert (1924) was the first who introduced the idea of VCC estimation assuming an unconstrained GMM. Rao (1973) developed the Minimum Norm Quadratic Unbiased Estimation (MINQUE) of VCC in an unconstrained GMM. Sjöberg (1983) extended the MINQUE approach to unconstrained GHM. According to Koch (1986), the Maximum-Likelihood estimation of VCC is identical to a local BIQUE and MINQUE, if an unconstrained GMM and normally distributed observations are assumed. Yu (1992) derived the BIQUE of VCC in a constrained GHM and showed that the MINQUE of Rao (1973) and the BIQUE of Sjöberg (1983) are special cases of his estimator. The estimator of Yu (1992) is a universal estimator, capable to deal with each well-posed linear model. This section derives the BIQUE of VCC in a constrained GHM. The development differs from Yu (1992) but results in the same formulas. The presented derivation expands the approach of Koch (1999), who derived the BIQUE of VCC in an unconstrained GMM.
Let the variance covariance matrix of all observations consists of a sum of z a priori known matrices $\boldsymbol{V}_i$ multiplied by unknown VCC σ_i

$$\boldsymbol{D}_{ll} = \sum_{i=1}^{z} \sigma_i \boldsymbol{V}_i. \tag{3.22}$$

According to Xu et al. (2007), the number of independently estimable VCC is limited by the redundancy to $z \leq r(r+1)/2$. Note, the σ_i denote variance components as well as covariance components. The VCM of the misclosure $\boldsymbol{w}_H$ vector is obtained accordingly (cf. Equation 3.10)

$$\boldsymbol{D}_{\boldsymbol{ww}} = \sum_{i=1}^{z} \sigma_i \boldsymbol{B}\boldsymbol{V}_i\boldsymbol{B}^{\mathsf{T}}. \tag{3.23}$$

A best estimation of the unknown VCC is obtained, if the variance of the weighted residuals squared sum Ω is minimal

$$\mathrm{Var}\,(\Omega) \rightarrow \min. \tag{3.24}$$

The estimation is unbiased, if the expectation value of Ω is a linear combination of the VCC

$$\mathrm{E}\,(\Omega) = \boldsymbol{p}^{\mathsf{T}}\boldsymbol{\sigma} \tag{3.25}$$

where $\boldsymbol{\sigma} = \begin{bmatrix}\sigma_1 & \sigma_2 & \dots & \sigma_z\end{bmatrix}^{\mathsf{T}}$ and $\boldsymbol{p}$ denote unknown vectors. According to Equation 3.20, the adjusted residual squares sum is obtained by a quadratic form of the adjusted residual vector $\hat{\boldsymbol{\epsilon}}$, which depends on both misclosure vectors $\boldsymbol{w}_H$ and $\boldsymbol{w}_C$. Hence, the expectation value is a quadratic form

$$\mathrm{E}\,(\Omega) = \mathrm{E}\left(\begin{bmatrix}\boldsymbol{w}_H^{\mathsf{T}} & \boldsymbol{w}_C^{\mathsf{T}}\end{bmatrix}\begin{bmatrix}\boldsymbol{M}_{11} & \boldsymbol{M}_{12}\\ \boldsymbol{M}_{12}^{\mathsf{T}} & \boldsymbol{M}_{22}\end{bmatrix}\begin{bmatrix}\boldsymbol{w}_H\\ \boldsymbol{w}_C\end{bmatrix}\right) \tag{3.26}$$

where $\boldsymbol{M}$ is an unknown symmetric matrix which depends on the VCC. If the deterministic vector $\boldsymbol{w}_C = \boldsymbol{A}_C\Delta\boldsymbol{\beta}$ is considered, Equation 3.26 yields

$$\mathrm{E}\,(\Omega) = \mathrm{E}\left(\boldsymbol{w}_H^{\mathsf{T}}\boldsymbol{M}_{11}\boldsymbol{w}_H\right) + 2\,\mathrm{E}\,(\boldsymbol{w}_H)\,\boldsymbol{M}_{11}\boldsymbol{A}_C\Delta\boldsymbol{\beta} + \Delta\boldsymbol{\beta}^{\mathsf{T}}\boldsymbol{A}_C^{\mathsf{T}}\boldsymbol{M}_{22}\boldsymbol{A}_C\Delta\boldsymbol{\beta}. \tag{3.27}$$

The expectation value of the quadratic form $\mathrm{E}\left(\boldsymbol{w}_H^{\mathsf{T}}\boldsymbol{M}_{11}\boldsymbol{w}_H\right)$ is given by Koch (1999, Theorem 2.174, p. 134). Then, the expectation value of Ω yields with Equation 3.4

$$\mathrm{E}\,(\Omega) = \mathrm{tr}\,(\boldsymbol{M}_{11}\boldsymbol{D}_{\boldsymbol{ww}}) + \Delta\boldsymbol{\beta}^{\mathsf{T}}\left(\boldsymbol{A}_H^{\mathsf{T}}\boldsymbol{M}_{11}\boldsymbol{A}_H + 2\boldsymbol{A}_H^{\mathsf{T}}\boldsymbol{M}_{12}\boldsymbol{A}_C + \boldsymbol{A}_C^{\mathsf{T}}\boldsymbol{M}_{22}\boldsymbol{A}_C\right)\Delta\boldsymbol{\beta}. \tag{3.28}$$

Since the vector $\boldsymbol{w}_H$ is stochastic and the vector $\boldsymbol{w}_C$ is deterministic, the variance of Ω is obtained according to Koch (1999, theorem 2.175, p. 134)

$$\begin{aligned}
\mathrm{Var}\,(\Omega) &= \mathrm{Var}\left(\begin{bmatrix}\boldsymbol{w}_H^{\mathsf{T}} & \boldsymbol{w}_C^{\mathsf{T}}\end{bmatrix}\begin{bmatrix}\boldsymbol{M}_{11} & \boldsymbol{M}_{12}\\ \boldsymbol{M}_{12}^{\mathsf{T}} & \boldsymbol{M}_{22}\end{bmatrix}\begin{bmatrix}\boldsymbol{w}_H\\ \boldsymbol{w}_C\end{bmatrix}\right)\\
&= \mathrm{E}\left(\left(\boldsymbol{w}_H^{\mathsf{T}}\boldsymbol{M}_{11}\boldsymbol{w}_H + 2\boldsymbol{w}_H^{\mathsf{T}}\boldsymbol{M}_{12}\boldsymbol{w}_C + \boldsymbol{w}_C^{\mathsf{T}}\boldsymbol{M}_{22}\boldsymbol{w}_C - \mathrm{E}\,(\Omega)\right)^2\right)\\
&= 2\,\mathrm{tr}\,(\boldsymbol{M}_{11}\boldsymbol{D}_{\boldsymbol{ww}}\boldsymbol{M}_{11}\boldsymbol{D}_{\boldsymbol{ww}}) +\\
&\quad 4\Delta\boldsymbol{\beta}^{\mathsf{T}}\left(\boldsymbol{A}_H^{\mathsf{T}}\boldsymbol{M}_{11}\boldsymbol{D}_{\boldsymbol{ww}}\boldsymbol{M}_{11}\boldsymbol{A}_H + 2\boldsymbol{A}_H^{\mathsf{T}}\boldsymbol{M}_{11}\boldsymbol{D}_{\boldsymbol{ww}}\boldsymbol{M}_{12}\boldsymbol{A}_C + \boldsymbol{A}_C^{\mathsf{T}}\boldsymbol{M}_{12}^{\mathsf{T}}\boldsymbol{D}_{\boldsymbol{ww}}\boldsymbol{M}_{12}\boldsymbol{A}_C\right)\Delta\boldsymbol{\beta}.
\end{aligned} \tag{3.29}$$

The estimation of the VCC is requested to be invariant to any arbitrary estimation of the unknowns $\Delta\boldsymbol{\beta}$. Hence, it must hold

$$\mathrm{E}(\Omega) = \mathrm{tr}(\boldsymbol{M}_{11}\boldsymbol{D}_{\boldsymbol{ww}}) \tag{3.30}$$
$$\mathrm{Var}(\Omega) = 2\,\mathrm{tr}(\boldsymbol{M}_{11}\boldsymbol{D}_{\boldsymbol{ww}}\boldsymbol{M}_{11}\boldsymbol{D}_{\boldsymbol{ww}})\,. \tag{3.31}$$

Therefore, the terms in the brackets between $\Delta\boldsymbol{\beta}^{\mathsf{T}}$ and $\Delta\boldsymbol{\beta}$ in Equations 3.28 and 3.29 have to be zero. Invariance of any arbitrary estimation of $\Delta\boldsymbol{\beta}$ is achieved, if it holds

$$\boldsymbol{A}_H^{\mathsf{T}}\boldsymbol{M}_{12} = -\boldsymbol{A}_C^{\mathsf{T}}\boldsymbol{M}_{22} \tag{3.32a}$$
$$\boldsymbol{M}_{12}\boldsymbol{A}_C = -\boldsymbol{M}_{11}\boldsymbol{A}_H. \tag{3.32b}$$

According to Equations 3.23 and 3.30,it follows

$$\mathrm{E}(\Omega) = \sum_{i=1}^{z}\sigma_i\,\mathrm{tr}\left(\boldsymbol{M}_{11}\boldsymbol{B}\boldsymbol{V}_i\boldsymbol{B}^{\mathsf{T}}\right) = \boldsymbol{p}^{\mathsf{T}}\boldsymbol{\sigma} \quad \Rightarrow \quad p_i = \mathrm{tr}\left(\boldsymbol{M}_{11}\boldsymbol{B}\boldsymbol{V}_i\boldsymbol{B}^{\mathsf{T}}\right). \tag{3.33}$$

Again, a constrained optimization problem arises. The Lagrange multipliers of the constraints in the Equations 3.32 and 3.33 are denoted with $\boldsymbol{K}_1$, $\boldsymbol{K}_2$ and $\boldsymbol{k}^{\mathsf{T}} = \begin{bmatrix}k_1 & k_2 & \dots & k_z\end{bmatrix}$. The minimal variance of Ω is determined with the Lagrange function

$$\begin{aligned}\phi_{LG} = {} & 2\,\mathrm{tr}(\boldsymbol{M}_{11}\boldsymbol{D}_{\boldsymbol{ww}}\boldsymbol{M}_{11}\boldsymbol{D}_{\boldsymbol{ww}}) - 4\,\mathrm{tr}\left(\left(\boldsymbol{A}_H^{\mathsf{T}}\boldsymbol{M}_{12} + \boldsymbol{A}_C^{\mathsf{T}}\boldsymbol{M}_{22}\right)\boldsymbol{K}_1\right) \\ & - 4\,\mathrm{tr}\left(\left(\boldsymbol{M}_{12}\boldsymbol{A}_C + \boldsymbol{M}_{11}\boldsymbol{A}_H\right)\boldsymbol{K}_2\right) - \sum_{i=1}^{z}k_i\left(\mathrm{tr}\left(\boldsymbol{M}_{11}\boldsymbol{B}\boldsymbol{V}_i\boldsymbol{B}^{\mathsf{T}}\right) - p_i\right).\end{aligned} \tag{3.34}$$

The minimum is found by setting the derivatives of the Lagrange function with respect to each unknown parameter to zero. According to Koch (1999, Theorem 1.269 and 1.270, p. 70), the derivatives of the Lagrange function with respect to the submatrices $\boldsymbol{M}_{11}$, $\boldsymbol{M}_{12}$ and $\boldsymbol{M}_{22}$ lead to

$$\frac{\mathsf{d}\,\phi_{LG}}{\mathsf{d}\,\boldsymbol{M}_{11}} \stackrel{!}{=} \boldsymbol{0} \quad \Rightarrow \quad \boldsymbol{D}_{\boldsymbol{ww}}\hat{\boldsymbol{M}}_{11}\boldsymbol{D}_{\boldsymbol{ww}} = \hat{\boldsymbol{K}}_2^{\mathsf{T}}\boldsymbol{A}_H^{\mathsf{T}} + \sum_{i=1}^{z}\hat{k}_i\boldsymbol{B}\boldsymbol{V}_i\boldsymbol{B}^{\mathsf{T}} \tag{3.35a}$$
$$\frac{\mathsf{d}\,\phi_{LG}}{\mathsf{d}\,\boldsymbol{M}_{12}} \stackrel{!}{=} \boldsymbol{0} \quad \Rightarrow \quad \boldsymbol{A}_H\hat{\boldsymbol{K}}_1^{\mathsf{T}} = -\hat{\boldsymbol{K}}_2^{\mathsf{T}}\boldsymbol{A}_C^{\mathsf{T}} \tag{3.35b}$$
$$\frac{\mathsf{d}\,\phi_{LG}}{\mathsf{d}\,\boldsymbol{M}_{22}} \stackrel{!}{=} \boldsymbol{0} \quad \Rightarrow \quad \boldsymbol{A}_C\hat{\boldsymbol{K}}_1^{\mathsf{T}} = \boldsymbol{0}. \tag{3.35c}$$

The BIQUE of the VCC is obtained by an iterative process (Koch, 1999, p. 233ff). Based on a 'first-guess' stochastic model

$$\boldsymbol{D}_{\boldsymbol{ww}}^{0} = \sum_{i=1}^{z}\boldsymbol{B}\boldsymbol{V}_i^{0}\boldsymbol{B}^{\mathsf{T}} \tag{3.36}$$

the system of normal equations (Equation 3.11) is solved. In order to clarify that this local estimation of the VCC is dependent on the approximated a priori stochastic model, an additional index 0 is used. A symmetric matrix $\boldsymbol{W}$ is defined by

$$\boldsymbol{W} = \boldsymbol{D}_{\boldsymbol{ww}}^{0^{-1}} - \boldsymbol{D}_{\boldsymbol{ww}}^{0^{-1}}\boldsymbol{A}_H\boldsymbol{Q}_{11}^{0}\boldsymbol{A}_H^{\mathsf{T}}\boldsymbol{D}_{\boldsymbol{ww}}^{0^{-1}}. \tag{3.37}$$

Equation 3.35a contains the matrix $\hat{\boldsymbol{M}}_{11}$ on the left hand side. The matrix $\hat{\boldsymbol{M}}_{11}$ is separated by using following two auxiliary relations. Equations 3.32b, 3.13c and 3.13a yield

$$\hat{\boldsymbol{M}}_{11}\boldsymbol{A}_H\boldsymbol{Q}_{11}^{0} = -\hat{\boldsymbol{M}}_{12}\boldsymbol{A}_C\boldsymbol{Q}_{11}^{0} = \boldsymbol{0} \tag{3.38a}$$
$$\boldsymbol{A}_H^{\mathsf{T}}\boldsymbol{W} = \boldsymbol{A}^{\mathsf{T}}\boldsymbol{D}_{\boldsymbol{ww}}^{0^{-1}} - \left(\boldsymbol{I} - \boldsymbol{A}_C^{\mathsf{T}}\boldsymbol{Q}_{12}^{0^{\mathsf{T}}}\right)\boldsymbol{A}_H^{\mathsf{T}}\boldsymbol{D}_{\boldsymbol{ww}}^{0^{-1}} = \boldsymbol{A}_C^{\mathsf{T}}\boldsymbol{Q}_{12}^{0^{\mathsf{T}}}\boldsymbol{A}_H^{\mathsf{T}}\boldsymbol{D}_{\boldsymbol{ww}}^{0^{-1}}. \tag{3.38b}$$

Equation 3.35a is multiplied on the left and on the right by $\boldsymbol{W}$. Then, it holds with Equations 3.35b, 3.35c, 3.37 and 3.38

$$\boldsymbol{W}\boldsymbol{D}_{\boldsymbol{ww}}\hat{\boldsymbol{M}}_{11}\boldsymbol{D}_{\boldsymbol{ww}}\boldsymbol{W} = \boldsymbol{W}\hat{\boldsymbol{K}}_2^{\mathsf{T}}\boldsymbol{A}_H^{\mathsf{T}}\boldsymbol{W} + \sum_{i=1}^{z}\hat{k}_i\boldsymbol{W}\boldsymbol{B}\boldsymbol{V}_i^0\boldsymbol{B}^{\mathsf{T}}\boldsymbol{W}$$

(cf. Eq. 3.37) $$\Rightarrow \quad \left(\boldsymbol{I} - \boldsymbol{D}_{\boldsymbol{ww}}^{0^{-1}}\boldsymbol{A}_H\boldsymbol{Q}_{11}^0\boldsymbol{A}_H^{\mathsf{T}}\right)\hat{\boldsymbol{M}}_{11}\left(\boldsymbol{I} - \boldsymbol{A}_H\boldsymbol{Q}_{11}^0\boldsymbol{A}_H^{\mathsf{T}}\boldsymbol{D}_{\boldsymbol{ww}}^{0^{-1}}\right) = \boldsymbol{W}\hat{\boldsymbol{K}}_2^{\mathsf{T}}\boldsymbol{A}_C^{\mathsf{T}}\boldsymbol{Q}_{12}^{0^{\mathsf{T}}}\boldsymbol{A}_H^{\mathsf{T}}\boldsymbol{D}_{\boldsymbol{ww}}^{0^{-1}} + \sum_{i=1}^{z}\hat{k}_i\boldsymbol{W}\boldsymbol{B}\boldsymbol{V}_i^0\boldsymbol{B}^{\mathsf{T}}\boldsymbol{W}$$

(cf. Eq. 3.38) $$\Rightarrow \quad \hat{\boldsymbol{M}}_{11} = \boldsymbol{W}\boldsymbol{A}_H\hat{\boldsymbol{K}}_1^{\mathsf{T}}\boldsymbol{A}_C^{\mathsf{T}}\boldsymbol{Q}_{12}^{0^{\mathsf{T}}}\boldsymbol{A}_H^{\mathsf{T}}\boldsymbol{D}_{\boldsymbol{ww}}^{0^{-1}} + \sum_{i=1}^{z}\hat{k}_i\boldsymbol{W}\boldsymbol{B}\boldsymbol{V}_i^0\boldsymbol{B}^{\mathsf{T}}\boldsymbol{W}$$

(cf. Eq. 3.35b) $$\Rightarrow \quad \hat{\boldsymbol{M}}_{11} = -\boldsymbol{D}_{\boldsymbol{ww}}^{0^{-1}}\boldsymbol{A}_H\boldsymbol{Q}_{12}^0\boldsymbol{A}_C\hat{\boldsymbol{K}}_1^{\mathsf{T}}\boldsymbol{A}_C^{\mathsf{T}}\boldsymbol{Q}_{12}^{0^{\mathsf{T}}}\boldsymbol{A}_H^{\mathsf{T}}\boldsymbol{D}_{\boldsymbol{ww}}^{0^{-1}} + \sum_{i=1}^{z}\hat{k}_i\boldsymbol{W}\boldsymbol{B}\boldsymbol{V}_i^0\boldsymbol{B}^{\mathsf{T}}\boldsymbol{W}$$

(cf. Eq. 3.35c) $$\Rightarrow \quad \hat{\boldsymbol{M}}_{11} = \sum_{i=1}^{z}\hat{k}_i\boldsymbol{W}\boldsymbol{B}\boldsymbol{V}_i^0\boldsymbol{B}^{\mathsf{T}}\boldsymbol{W}. \tag{3.39a}$$

The adjusted $\hat{\boldsymbol{M}}_{11}$ is substituted into the Equations 3.32. Then, it holds according to Equations 3.38

$$\hat{\boldsymbol{M}}_{12}\boldsymbol{A}_C = -\sum_{i=1}^{z}\hat{k}_i\boldsymbol{W}\boldsymbol{B}\boldsymbol{V}_i^0\boldsymbol{B}^{\mathsf{T}}\boldsymbol{W}\boldsymbol{A}_H = -\sum_{i=1}^{z}\hat{k}_i\boldsymbol{W}\boldsymbol{B}\boldsymbol{V}_i^0\boldsymbol{B}^{\mathsf{T}}\boldsymbol{D}_{\boldsymbol{ww}}^{0^{-1}}\boldsymbol{A}_H\boldsymbol{Q}_{12}^0\boldsymbol{A}_C$$

$$\Rightarrow \quad \hat{\boldsymbol{M}}_{12} = -\sum_{i=1}^{z}\hat{k}_i\boldsymbol{W}\boldsymbol{B}\boldsymbol{V}_i^0\boldsymbol{B}^{\mathsf{T}}\boldsymbol{D}_{\boldsymbol{ww}}^{0^{-1}}\boldsymbol{A}_H\boldsymbol{Q}_{12}^0 \tag{3.39b}$$

$$\boldsymbol{A}_C^{\mathsf{T}}\hat{\boldsymbol{M}}_{22} = \sum_{i=1}^{z}\hat{k}_i\boldsymbol{A}_H^{\mathsf{T}}\boldsymbol{W}\boldsymbol{B}\boldsymbol{V}_i^0\boldsymbol{B}^{\mathsf{T}}\boldsymbol{D}_{\boldsymbol{ww}}^{0^{-1}}\boldsymbol{A}_H\boldsymbol{Q}_{12}^0 = \sum_{i=1}^{z}\hat{k}_i\boldsymbol{A}_C^{\mathsf{T}}\boldsymbol{Q}_{12}^{0^{\mathsf{T}}}\boldsymbol{A}_H^{\mathsf{T}}\boldsymbol{D}_{\boldsymbol{ww}}^{0^{-1}}\boldsymbol{B}\boldsymbol{V}_i^0\boldsymbol{B}^{\mathsf{T}}\boldsymbol{D}_{\boldsymbol{ww}}^{0^{-1}}\boldsymbol{A}_H\boldsymbol{Q}_{12}^0$$

$$\Rightarrow \quad \hat{\boldsymbol{M}}_{22} = \sum_{i=1}^{z}\hat{k}_i\boldsymbol{Q}_{12}^{0^{\mathsf{T}}}\boldsymbol{A}_H^{\mathsf{T}}\boldsymbol{D}_{\boldsymbol{ww}}^{0^{-1}}\boldsymbol{B}\boldsymbol{V}_i^0\boldsymbol{B}^{\mathsf{T}}\boldsymbol{D}_{\boldsymbol{ww}}^{0^{-1}}\boldsymbol{A}_H\boldsymbol{Q}_{12}^0. \tag{3.39c}$$

The submatrices $\hat{\boldsymbol{M}}_{11}$, $\hat{\boldsymbol{M}}_{12}$ and $\hat{\boldsymbol{M}}_{22}$ in the Equations 3.39 are rearranged to the block matrix $\hat{\boldsymbol{M}}$

$$\hat{\boldsymbol{M}} = \begin{bmatrix}\boldsymbol{W}\boldsymbol{D}_{\boldsymbol{ww}}^0 \\ -\boldsymbol{Q}_{12}^{0^{\mathsf{T}}}\boldsymbol{A}_H^{\mathsf{T}}\end{bmatrix}\left(\sum_{i=1}^{z}\hat{k}_i\boldsymbol{D}_{\boldsymbol{ww}}^{0^{-1}}\boldsymbol{B}\boldsymbol{V}_i^0\boldsymbol{B}^{\mathsf{T}}\boldsymbol{D}_{\boldsymbol{ww}}^{0^{-1}}\right)\begin{bmatrix}\boldsymbol{D}_{\boldsymbol{ww}}^0\boldsymbol{W} & -\boldsymbol{A}_H\boldsymbol{Q}_{12}^0\end{bmatrix}. \tag{3.40}$$

$\hat{\boldsymbol{M}}$ is substituted into Equation 3.26. The adjusted weighted squares sum of the residuals is according to Equation 3.15

$$\begin{aligned}\hat{\Omega} &= \begin{bmatrix}\boldsymbol{w}_H^{\mathsf{T}} & \boldsymbol{w}_C^{\mathsf{T}}\end{bmatrix}\hat{\boldsymbol{M}}\begin{bmatrix}\boldsymbol{w}_H \\ \boldsymbol{w}_C\end{bmatrix} \\ &= \left(\boldsymbol{w}_H^{\mathsf{T}}\boldsymbol{W}\boldsymbol{D}_{\boldsymbol{ww}}^0 - \boldsymbol{w}_C^{\mathsf{T}}\boldsymbol{Q}_{12}^{0^{\mathsf{T}}}\boldsymbol{A}_H^{\mathsf{T}}\right)\left(\sum_{i=1}^{z}\hat{k}_i\boldsymbol{D}_{\boldsymbol{ww}}^{0^{-1}}\boldsymbol{B}\boldsymbol{V}_i^0\boldsymbol{B}^{\mathsf{T}}\boldsymbol{D}_{\boldsymbol{ww}}^{0^{-1}}\right)\left(\boldsymbol{D}_{\boldsymbol{ww}}^0\boldsymbol{W}\boldsymbol{w}_H - \boldsymbol{A}_H\boldsymbol{Q}_{12}^0\boldsymbol{w}_C\right) \\ &= \left(-\boldsymbol{w}_H^{\mathsf{T}}\left(\boldsymbol{D}_{\boldsymbol{ww}}^{0^{-1}}\boldsymbol{A}_H\boldsymbol{Q}_{11}^0\boldsymbol{A}_H^{\mathsf{T}} - \boldsymbol{I}\right) - \boldsymbol{w}_C^{\mathsf{T}}\boldsymbol{Q}_{12}^{0^{\mathsf{T}}}\boldsymbol{A}_H^{\mathsf{T}}\right)\left(\sum_{i=1}^{z}\hat{k}_i\boldsymbol{D}_{\boldsymbol{ww}}^{0^{-1}}\boldsymbol{B}\boldsymbol{V}_i^0\boldsymbol{B}^{\mathsf{T}}\boldsymbol{D}_{\boldsymbol{ww}}^{0^{-1}}\right) \\ &\qquad\qquad \left(-\left(\boldsymbol{A}_H\boldsymbol{Q}_{11}^0\boldsymbol{A}_H^{\mathsf{T}}\boldsymbol{D}_{\boldsymbol{ww}}^{0^{-1}} - \boldsymbol{I}\right)\boldsymbol{w}_H - \boldsymbol{A}_H\boldsymbol{Q}_{12}^0\boldsymbol{w}_C\right) \\ &= \sum_{i=1}^{z}\hat{k}_i\hat{\boldsymbol{\epsilon}}_0^{\mathsf{T}}\boldsymbol{B}^{\mathsf{T}}\boldsymbol{D}_{\boldsymbol{ww}}^{0^{-1}}\boldsymbol{B}\boldsymbol{V}_i^0\boldsymbol{B}^{\mathsf{T}}\boldsymbol{D}_{\boldsymbol{ww}}^{0^{-1}}\boldsymbol{B}\hat{\boldsymbol{\epsilon}}_0 \\ &= \hat{\boldsymbol{k}}^{\mathsf{T}}\boldsymbol{q} \qquad\qquad \text{with} \quad q_i = \hat{\boldsymbol{\epsilon}}_0^{\mathsf{T}}\boldsymbol{B}^{\mathsf{T}}\boldsymbol{D}_{\boldsymbol{ww}}^{0^{-1}}\boldsymbol{B}\boldsymbol{V}_i^0\boldsymbol{B}^{\mathsf{T}}\boldsymbol{D}_{\boldsymbol{ww}}^{0^{-1}}\boldsymbol{B}\hat{\boldsymbol{\epsilon}}_0.\end{aligned} \tag{3.41}$$

If $\hat{\boldsymbol{M}}_{11}$ in Equation 3.39a is substituted into Equation 3.33, it yields

$$\begin{aligned}\hat{p}_i &= \operatorname{tr}\left(\sum_j k_j\boldsymbol{W}\boldsymbol{B}\boldsymbol{V}_j^0\boldsymbol{B}^{\mathsf{T}}\boldsymbol{W}\boldsymbol{B}\boldsymbol{V}_i^0\boldsymbol{B}^{\mathsf{T}}\right) \\ \Rightarrow \quad \hat{\Omega} &= \hat{\boldsymbol{k}}^{\mathsf{T}}\boldsymbol{S}\hat{\boldsymbol{\sigma}} \qquad\qquad \text{with} \quad s_{ij} = \operatorname{tr}\left(\boldsymbol{W}\boldsymbol{B}\boldsymbol{V}_j^0\boldsymbol{B}^{\mathsf{T}}\boldsymbol{W}\boldsymbol{B}\boldsymbol{V}_i^0\boldsymbol{B}^{\mathsf{T}}\right).\end{aligned} \tag{3.42}$$

The matrix

$$\sum_{i=1}^{z}\sum_{j=1}^{z} \boldsymbol{W}\boldsymbol{B}\boldsymbol{V}_i^0\boldsymbol{B}^\mathsf{T}\boldsymbol{W}\boldsymbol{B}\boldsymbol{V}_j^0\boldsymbol{B}^\mathsf{T} = \boldsymbol{W}\boldsymbol{D}_{\boldsymbol{ww}}^0\boldsymbol{W}\boldsymbol{D}_{\boldsymbol{ww}}^0 = \boldsymbol{W}\boldsymbol{D}_{\boldsymbol{ww}}^0 \tag{3.43}$$

is an idempotent matrix (proof: Equations 3.13). According to Equation 3.21, the trace of this idempotent matrix is equal to the redundancy r of the adjustment problem. Therefore, a useful relation to control the correct estimation of the traces is

$$\sum_{i=1}^{z}\sum_{j=1}^{z} s_{ij} = r. \tag{3.44}$$

A comparison of the Equations 3.41 and 3.42 results in

$$\boldsymbol{S}\hat{\boldsymbol{\sigma}} = \boldsymbol{q}. \tag{3.45}$$

If the symmetric matrix $\boldsymbol{S}$ is regular, the adjusted VCC are

$$\hat{\boldsymbol{\sigma}} = \boldsymbol{S}^{-1}\boldsymbol{q}. \tag{3.46}$$

If a singular matrix $\boldsymbol{S}$ arises, at least two variance or covariance components depend on each other. As mentioned before, the number of independently estimable VCC is restricted to $r\,(r+1)\,/2$ components (Xu et al., 2007). If $\boldsymbol{S}$ is singular, one might consider a reformulation of the stochastic model with a reduced number of VCC.
The matrix $\boldsymbol{M}$ is postulated to be symmetric, but a positive-definite matrix $\boldsymbol{M}$ is not postulated. Therefore, negative variance components might occur (Koch, 1999). Negative variance components are a strong indication for too few observations or an incorrect functional or stochastic model (Crocetto et al., 2000). Thus, if negative variance components occur, a reformulation of the problem should be considered. However, Sjöberg (1984) derived a variance component estimator, which provides positive variance components, but unbiasedness is not ensured by his estimator.
The VCC are obtained within an iterative process, until all σ_i converge to $\sigma_i = 1$. $z\,(z+1)\,/2$ trace operations are required in each iteration step. Each trace operation $\mathrm{tr}\left(\boldsymbol{W}\boldsymbol{B}\boldsymbol{V}_j^0\boldsymbol{B}^\mathsf{T}\boldsymbol{W}\boldsymbol{B}\boldsymbol{V}_i^0\boldsymbol{B}^\mathsf{T}\right)$ calculates the trace of a product of several matrices. Therefore, even medium scaled problems require a large number of floating point operations. Förstner (1979) modified the matrix $\boldsymbol{S}$ in Equation 3.42 to a diagonal matrix. Then, the main diagonal of $\boldsymbol{S}$ contains trace operations of the type $\mathrm{tr}\left(\boldsymbol{W}\boldsymbol{B}\boldsymbol{V}_i^0\boldsymbol{B}^\mathsf{T}\right)$. Förstner's approach reduces the number of floating point operations significantly about approximately the factor zn (with n denoting here the size of the quadratic matrix $\boldsymbol{W}$). Nevertheless, doubt arises during the work on this dissertation that Förstner's approach is suitable for the estimation of covariance components in any case. Appendix C contains an example in which the estimation of a covariance component fails using Förstner's approach, whereas the approach developed here leads to a meaningful result. Therefore, Förstner's approach is not considered here.

3.3. Stochastic Monte-Carlo Trace Estimator

According to the previous section, the matrix $\boldsymbol{S}$ requires the calculation of the traces of matrix products. These calculations require large computer capacities, if a large number of observations and unknowns have to be considered. The trace can be efficiently obtained by a SMCTE. The Monte-Carlo sampler determines the trace by generating several samples of a random vector. Since the SMCTE replaces each matrix-matrix multiplication by a matrix-vector multiplication, the number of floating points operations are reduced to a minimum and the SMCTE is highly efficient. In particular, the SMCTE avoids the explicit calculation of the matrix $\boldsymbol{W}$ and the calculation of any inverse. Koch and Kusche (2002), Kusche and Klees (2002) and Kusche (2003) proposed a SMCTE for Förstner's approach. Their SMCTE estimates the trace of non-stochastic, symmetric matrices. Symmetry is provided by a Cholesky decomposition of the matrices $\boldsymbol{V}_i$. Since a Cholesky decomposition is not possible, if covariance components are estimated, their SMCTE has to be expanded to deal with the trace estimation of asymmetric matrices. This section motivates the chosen probability distribution for the random vector, compares the variance of the trace estimation of symmetric and asymmetric matrices and proposes an algorithm for the universal least-squares solver.

Assume a non-stochastic, asymmetric $n \times n$ matrix $\boldsymbol{T}$, whose trace is estimated by a SMCTE. The SMCTE generates several samples of the $n \times 1$ stochastic vector $\boldsymbol{u}$. Two probability distributions are analyzed, first $\boldsymbol{u}$ is normally distributed with the expectation value $\mathrm{E}(\boldsymbol{u}) = \mathbf{0}$ and the assigned VCM is the identity matrix (cf. Equation 3.47a). The second probability distribution provides a random vector $\boldsymbol{u}$ with a discrete distribution. Each element u_i has either the value -1 or $+1$, each with the probability of 0.5 (cf. Equation 3.47b)

$$\boldsymbol{u} \sim \mathcal{N}(\mathbf{0}, \boldsymbol{I}) \tag{3.47a}$$

$$\boldsymbol{u} \sim \begin{cases} p(u_i = -1) & = 0.5 \\ p(u_i = +1) & = 0.5 \end{cases} \quad \text{for } i = 1, \ldots, n. \tag{3.47b}$$

The quadratic form $\boldsymbol{u}^\mathsf{T}\boldsymbol{T}\boldsymbol{u}$ is calculated by

$$\boldsymbol{u}^\mathsf{T}\boldsymbol{T}\boldsymbol{u} = \sum_{i=1}^{n}\sum_{j=1}^{n} u_i u_j t_{ij}. \tag{3.48}$$

Then, the expectation value $\mathrm{E}\left(\boldsymbol{u}^\mathsf{T}\boldsymbol{T}\boldsymbol{u}\right)$ of the quadratic form is

$$\mathrm{E}\left(\boldsymbol{u}^\mathsf{T}\boldsymbol{T}\boldsymbol{u}\right) = \mathrm{E}\left(\sum_{i=1}^{n}\sum_{j=1}^{n} u_i u_j t_{ij}\right) = \sum_{i=1}^{n}\sum_{j=1}^{n} \mathrm{E}(u_i u_j)\, t_{ij}. \tag{3.49}$$

The elements of the vector $\boldsymbol{u}$ are uncorrelated in both distributions. Hence, if $i \neq j$, the expectation value $\mathrm{E}(u_i u_j)$ is zero. If $i = j$, the expectation value is $\mathrm{E}(u_i^2) = 1$ in both distributions. Thus, it holds

$$\mathrm{E}\left(\boldsymbol{u}^\mathsf{T}\boldsymbol{T}\boldsymbol{u}\right) = \sum_{i=1}^{n} t_{ii} = \mathrm{tr}(\boldsymbol{T}). \tag{3.50}$$

The variance of the quadratic form is

$$\begin{aligned} \mathrm{Var}\left(\boldsymbol{u}^\mathsf{T}\boldsymbol{T}\boldsymbol{u}\right) &= \mathrm{E}\left(\left(\boldsymbol{u}^\mathsf{T}\boldsymbol{T}\boldsymbol{u} - \mathrm{E}\left(\boldsymbol{u}^\mathsf{T}\boldsymbol{T}\boldsymbol{u}\right)\right)^2\right) \\ &= \mathrm{E}\left(\left(\sum_{i=1}^{n}\sum_{j=1}^{n} u_i u_j t_{ij} - \mathrm{tr}(\boldsymbol{T})\right)^2\right) \\ &= (\mathrm{tr}(\boldsymbol{T}))^2 - 2\,\mathrm{tr}(\boldsymbol{T})\sum_{i=1}^{n}\sum_{j=1}^{n}\mathrm{E}(u_i u_j)\, t_{ij} + \sum_{i=1}^{n}\sum_{j=1}^{n}\sum_{k=1}^{n}\sum_{l=1}^{n}\mathrm{E}(u_i u_j u_k u_l)\, t_{ij} t_{kl}. \end{aligned} \tag{3.51}$$

The expectation values $\mathrm{E}(u_i u_j u_k u_l)$ are given in Table 3.1. In case of a normally distributed vector $\boldsymbol{u}$ the variance of the quadratic form is

$$\begin{aligned} \mathrm{Var}\left(\boldsymbol{u}^\mathsf{T}\boldsymbol{T}\boldsymbol{u}\right) &= -(\mathrm{tr}(\boldsymbol{T}))^2 + \sum_{i=1}^{n}\sum_{j=1}^{n} t_{ij}^2 + t_{ii}t_{jj} + t_{ij}t_{ji} \\ &= \sum_{i=1}^{n}\sum_{j=1}^{n} t_{ij}^2 + t_{ij}t_{ji} \\ &= \mathrm{tr}\left(\mathbf{T}^\mathsf{T}\mathbf{T}\right) + \mathrm{tr}(\mathbf{T}\mathbf{T}). \end{aligned} \tag{3.52}$$

Table 3.1: Expectation values of the summands in Equation 3.51

		normal distribution	discrete distribution
$\mathrm{E}(u_i^4)$		3	1
$\mathrm{E}(u_i^3 u_j)$	$i \neq j$	0	0
$\mathrm{E}\left(u_i^2 u_j^2\right)$	$i \neq j$	1	1
$\mathrm{E}(u_i^2 u_j u_k)$	$i \neq j \neq k$	0	0
$\mathrm{E}(u_i u_j u_k u_l)$	$i \neq j \neq k \neq l$	0	0

If the vector $\boldsymbol{u}$ has the discrete distribution, it holds

$$\begin{aligned}\operatorname{Var}\left(\boldsymbol{u}^{\mathsf{T}}\boldsymbol{T}\boldsymbol{u}\right) &= -\left(\operatorname{tr}\left(\boldsymbol{T}\right)\right)^2 + \sum_{i=1}^{n}\sum_{j=1}^{n} t_{ii}t_{jj} + \sum_{i=1}^{n}\sum_{j=1,j\neq i}^{n} t_{ij}^2 + t_{ij}t_{ji} \\ &= \sum_{i=1}^{n}\sum_{j=1,j\neq i}^{n} t_{ij}^2 + t_{ij}t_{ji} \\ &= \operatorname{tr}\left(\boldsymbol{T}^{\mathsf{T}}\boldsymbol{T}\right) + \operatorname{tr}\left(\boldsymbol{T}\boldsymbol{T}\right) - 2\sum_{i=1}^{z} t_{ii}^2.\end{aligned} \tag{3.53}$$

The variance in Equation 3.53 is $2\sum_{i=1}^{n} t_{ii}^2$ smaller than the variance in Equation 3.52. Since the discrete distributed random vector needs fewer samples to obtain a comparable variance than a normally distributed random vector, the SMCTE draws samples from the discrete distribution.
The SMCTE of Koch and Kusche (2002), Kusche and Klees (2002) and Kusche (2003) estimates the trace of symmetric matrices. Symmetry might be a crucial factor for an efficient trace estimation. Therefore, bounds for the variance of the traces of symmetric and asymmetric matrices are derived, in order to evaluate the influence of the symmetry. Hutchinson (1989) found bounds for the variance of the trace estimation of symmetric matrices, determined by a discrete distributed random vector $\boldsymbol{u}$. The bounds depend on the eigen values of $\boldsymbol{T}$. Motivated by Hutchinson (1989), bounds for the trace of asymmetric matrices are estimated by using the singular value decomposition. The singular value decomposition of $\boldsymbol{T}$ is

$$\boldsymbol{T} = \boldsymbol{U}\boldsymbol{\Lambda}\boldsymbol{V}^{\mathsf{T}}. \tag{3.54}$$

$\boldsymbol{\Lambda}$ is a diagonal matrix with non-negative real singular values. If the matrix $\boldsymbol{T}$ is real, the matrices $\boldsymbol{U}$ and $\boldsymbol{V}$ are orthogonal matrices. The inverse of an orthogonal matrix is its transpose. Hence, it holds

$$\begin{aligned}\operatorname{tr}\left(\boldsymbol{T}^{\mathsf{T}}\boldsymbol{T}\right) &= \operatorname{tr}\left(\boldsymbol{V}\boldsymbol{\Lambda}\boldsymbol{U}^{\mathsf{T}}\boldsymbol{U}\boldsymbol{\Lambda}\boldsymbol{V}^{\mathsf{T}}\right) \\ &= \operatorname{tr}\left(\boldsymbol{\Lambda}\boldsymbol{V}^{\mathsf{T}}\boldsymbol{V}\boldsymbol{\Lambda}\boldsymbol{U}^{\mathsf{T}}\boldsymbol{U}\right) \\ &= \operatorname{tr}\left(\boldsymbol{\Lambda}^2\right).\end{aligned} \tag{3.55}$$

Since the product of two orthogonal matrices is as well orthogonal, each column and row respectively of the product $\boldsymbol{V}^{\mathsf{T}}\boldsymbol{U}$ has the length 1 and the maximal value of each matrix element is also 1. Therefore, it holds

$$\begin{aligned}\operatorname{tr}\left(\boldsymbol{T}\boldsymbol{T}\right) &= \operatorname{tr}\left(\boldsymbol{U}\boldsymbol{\Lambda}\boldsymbol{V}^{\mathsf{T}}\boldsymbol{U}\boldsymbol{\Lambda}\boldsymbol{V}^{\mathsf{T}}\right) \\ &= \operatorname{tr}\left(\boldsymbol{\Lambda}\boldsymbol{V}^{\mathsf{T}}\boldsymbol{U}\boldsymbol{\Lambda}\boldsymbol{V}^{\mathsf{T}}\boldsymbol{U}\right) \\ &< \operatorname{tr}\left(\boldsymbol{\Lambda}\begin{bmatrix}1 & \dots & 1\\ \vdots & \ddots & \vdots\\ 1 & \dots & 1\end{bmatrix}\boldsymbol{\Lambda}\begin{bmatrix}1 & \dots & 1\\ \vdots & \ddots & \vdots\\ 1 & \dots & 1\end{bmatrix}\right) \\ &< \operatorname{tr}\left(\boldsymbol{\Lambda}\right)\operatorname{tr}\left(\boldsymbol{\Lambda}\right).\end{aligned} \tag{3.56}$$

Thus, the variance is bounded by the singular values with

$$\operatorname{Var}\left(\boldsymbol{u}^{\mathsf{T}}\boldsymbol{T}\boldsymbol{u}\right) < \operatorname{tr}\left(\boldsymbol{\Lambda}^2\right) + \operatorname{tr}\left(\boldsymbol{\Lambda}\right)\operatorname{tr}\left(\boldsymbol{\Lambda}\right) - 2\sum_{i=1}^{z} t_{ii}^2. \tag{3.57}$$

This bound is still highly overestimated, as most elements of the matrix product $\boldsymbol{V}^{\mathsf{T}}\boldsymbol{U}$ are significantly smaller than one.
If $\boldsymbol{T}$ is a symmetric matrix, $\boldsymbol{U}$ equals $\boldsymbol{V}$ and the bound is described with

$$\operatorname{Var}\left(\boldsymbol{u}^{\mathsf{T}}\boldsymbol{T}\boldsymbol{u}\right) \leq 2\operatorname{tr}\left(\boldsymbol{\Lambda}^2\right) - 2\sum_{i=1}^{z} t_{ii}^2. \tag{3.58}$$

As the singular values are non-negative, the variance is tighter bounded in the symmetric case than in the asymmetric case. Therefore, the SMCTE estimates the trace of asymmetric matrices with a larger variance than the trace of a symmetric matrix.
According to Equation 3.42, a typical trace estimation calculates $s_{ij} = \operatorname{tr}\left(\boldsymbol{W}\boldsymbol{B}\boldsymbol{V}_j^0\boldsymbol{B}^\mathsf{T}\boldsymbol{W}\boldsymbol{B}\boldsymbol{V}_i^0\boldsymbol{B}^\mathsf{T}\right)$. The matrix product within the trace operator lacks symmetry. Koch and Kusche (2002), Kusche and Klees (2002) and Kusche (2003) ensured the symmetry of the matrices by a Cholesky decomposition. If a Cholesky decomposition of at least one of the matrices $\boldsymbol{V}_i^0 = \boldsymbol{R}^\mathsf{T}\boldsymbol{R}$ or $\boldsymbol{V}_j^0 = \boldsymbol{R}^\mathsf{T}\boldsymbol{R}$ exists, it holds

$$\begin{aligned}\operatorname{tr}\left(\boldsymbol{W}\boldsymbol{B}\boldsymbol{V}_j^0\boldsymbol{B}^\mathsf{T}\boldsymbol{W}\boldsymbol{B}\boldsymbol{V}_i^0\boldsymbol{B}^\mathsf{T}\right) &= \operatorname{tr}\left(\boldsymbol{R}\boldsymbol{B}^\mathsf{T}\boldsymbol{W}\boldsymbol{B}\boldsymbol{V}_j^0\boldsymbol{B}^\mathsf{T}\boldsymbol{W}\boldsymbol{B}\boldsymbol{R}^\mathsf{T}\right) \quad \text{or}\\ \operatorname{tr}\left(\boldsymbol{W}\boldsymbol{B}\boldsymbol{V}_j^0\boldsymbol{B}^\mathsf{T}\boldsymbol{W}\boldsymbol{B}\boldsymbol{V}_i^0\boldsymbol{B}^\mathsf{T}\right) &= \operatorname{tr}\left(\boldsymbol{R}\boldsymbol{B}^\mathsf{T}\boldsymbol{W}\boldsymbol{B}\boldsymbol{V}_i^0\boldsymbol{B}^\mathsf{T}\boldsymbol{W}\boldsymbol{B}\boldsymbol{R}^\mathsf{T}\right).\end{aligned} \tag{3.59}$$

If both matrices $\boldsymbol{V}_i^0$ and $\boldsymbol{V}_j^0$ describe covariances, a Cholesky decomposition does not exist, and symmetry cannot be provided. Therefore, the trace estimation of asymmetric matrices remains necessary. The variance of the trace estimation is improved by drawing several samples of the vector $\boldsymbol{u}$ and calculating the arithmetic average of the samples. Then, the elements of the matrix $\boldsymbol{S}$ are

$$s_{ij} = \frac{1}{n_s}\sum_{k=1}^{n_s}\boldsymbol{u}_k^\mathsf{T}\boldsymbol{W}\boldsymbol{B}\boldsymbol{V}_j^0\boldsymbol{B}^\mathsf{T}\boldsymbol{W}\boldsymbol{B}\boldsymbol{V}_i^0\boldsymbol{B}^\mathsf{T}\boldsymbol{u}_k \tag{3.60}$$

where n_s is the number of the drawn samples. Koch and Kusche (2002), Kusche and Klees (2002) and Kusche (2003) estimated the trace of symmetric matrices. According to them, it is sufficient to draw one single sample in most cases. According to empirical experience, this statement also is true for the trace estimation of asymmetric matrices, although the trace of asymmetric matrices is estimated with a larger variance than the trace of symmetric matrices. This experience additionally indicates that the bound in Equation 3.57 is highly overestimated. The variance of the trace estimation can be evaluated by analyzing the convergence during the iterations. The variations of the VCC around the point of convergence indicate the accuracy of the stochastic trace estimation. If the variations are too large, they can be decreased by increasing the number of samples. However, the convergence is additionally affected by the partial redundancies of the specific observations. This aspect is discussed in more detail in Section 5.2. Note, if a covariance component of zero is estimated by the SMCTE, the associated σ_i continuously changes the sign during the iterations and does not converge. In that case, a reformulation of the stochastic model is recommended.
The matrix $\boldsymbol{W}$ is determined by repeated inversions and multiplications of sometimes large VCM and normal equation matrices. The algorithm is optimized significantly in computation time and memory requirements, if inversions are avoided and matrix-matrix multiplications are replaced with matrix-vector multiplications (Koch and Kusche, 2002; Kusche and Klees, 2002; Kusche, 2003). If the trace is estimated by the SMCTE, it holds for the kth sample of $\boldsymbol{u}$:

$$\boldsymbol{u}_k^\mathsf{T}\boldsymbol{W}\boldsymbol{B}\boldsymbol{V}_j^0\boldsymbol{B}^\mathsf{T}\boldsymbol{W}\boldsymbol{B}\boldsymbol{V}_i^0\boldsymbol{B}^\mathsf{T}\boldsymbol{u}_k = \boldsymbol{u}_k^\mathsf{T}\boldsymbol{W}_E\boldsymbol{B}\boldsymbol{V}_j^0\boldsymbol{B}^\mathsf{T}\boldsymbol{W}_E\boldsymbol{B}\boldsymbol{V}_i^0\boldsymbol{B}^\mathsf{T}\boldsymbol{u}_k \tag{3.61}$$

$$\text{with} \qquad \boldsymbol{W}_E = \boldsymbol{D}_H^{0\,-1} - \boldsymbol{D}_H^{0\,-1}\begin{bmatrix}\boldsymbol{A}_H & \boldsymbol{0}\end{bmatrix}\boldsymbol{N}^{0-1}\begin{bmatrix}\boldsymbol{A}_H^\mathsf{T}\\ \boldsymbol{0}\end{bmatrix}\boldsymbol{D}_H^{0\,-1}.$$

The matrix $\boldsymbol{A}_H$ is extended by zeros in order to include the inverse of the entire normal equation matrix $\boldsymbol{N}^0$ instead of the submatrix $\boldsymbol{Q}_{11}^0$. The matrix $\boldsymbol{W}_E$ is not explicitly calculated. The products $\boldsymbol{W}_E\boldsymbol{u}_k$ and $\boldsymbol{W}_E\left(\boldsymbol{B}\boldsymbol{V}_i^0\boldsymbol{B}^\mathsf{T}\boldsymbol{u}_k\right)$ are obtained by matrix-vector multiplications, which requires significantly fewer floating point operations than matrix-matrix multiplications. The matrix $\boldsymbol{W}_E$ contains the inverses of the matrices $\boldsymbol{D}_H^0$ and $\boldsymbol{N}^0$. The explicit calculations of these inverses are avoided by using suitable fast linear solvers, e.g. Gaussian elimination algorithms. Since the unknown vector $\Delta\boldsymbol{\beta}$ can be determined by fast linear solvers as well, inversions are not necessary. Nevertheless, if the complete VCM of the unknown parameters is requested, the normal equation matrix has to be inverted at least in the last iteration step. Alkhatib (2007) described a Monte-Carlo sampler which inverts large matrices.
Appendix D describes a pseudocode for the iterative estimation of unknown parameters and VCC in a constrained GHM. The suggested algorithm for the estimation of VCC was verified by several simulated examples. For example, threedimensional coordinates on a surface of a sphere were simulated, and its radius and three variance and three covariance components were estimated. The expected results were obtained and the VCC converged rapidly toward $\sigma_i = 1$.

4. Combined analysis of Earth Orientation Parameters, Gravity Field Coefficients of second degree and geophysical excitation functions in a constrained Gauss-Helmert Model

4.1. Preprocessing of the data: Filter

The combined analysis of the different time series is complicated by the different temporal resolution of the time series. The EOP and the excitation functions are given by daily time series. In contrast, the GRACE and SLR provide gravity field solutions with a significantly lower temporal resolution. The gravity field coefficients are available with a temporal resolution between ten days and one month. Therefore, the daily time series contain high frequencies which are not present in the gravity field coefficients. The excitation functions model the atmospheric, oceanic and hydrological contributions to the Earth rotation variations. Greiner-Mai (1987), Martinec and Hagedoorn (2005), Greiner-Mai and Hagedoorn (2008) and Hagedoorn and Greiner-Mai (2008) model the contribution of the core to Earth rotation variations. The core causes decadal variations of the EOP. As the available time series span less than a decade, the core models are not considered here. Thus, the EOP contain low frequencies which are not modeled by excitation functions. As the time series contain different frequencies, they have to be filtered, before the combined analysis is performed. The filters remove those frequencies not present in all time series. The daily time series are filtered with a bandpass filter to remove low and high frequencies, and the gravity field coefficients are treated with a highpass filter.
Ideal filters completely eliminate frequencies smaller or larger than the cutoff frequencies (stop band), while frequencies passing remain unchanged. However, ideal filters cannot be realized, since the response of a filter on an impulse is infinitely long in time (Meyer, 2011, page 125). Thus, the design of a digital filter is generally concerned with realizing an optimal approximation to an ideal filter. Numerous filters with different characteristics were proposed in literature. However, all filters feature a more or less large attenuation of the amplitude and a phase shift (Schlittgen and Streitberg, 1997, page 165ff). It is necessary to use the same filter for all time series, in order to avoid artifacts resulting from amplitude attenuation and phase shifts. Since the temporal resolution of the time series is different, exact filters cannot be realized for all time series. However, the filters of the daily and monthly time series need to be as similar as possible.
Using an approach similar to the Fourier transformation, a simple filter is proposed for the preprocessing of data. The filter assumes equidistant observations. Some of the GFC2 time series contain a few gaps due to suboptimal satellite orbits. The gaps are filled by linear interpolation, before the filter is applied. The observation vector $\boldsymbol{l}_o = \begin{bmatrix} l_o^1 & l_o^2 & \dots & l_o^n \end{bmatrix}^\mathsf{T}$ contains n equidistant original observations in total. The proposed filter removes a linear trend and frequencies smaller than the cutoff frequency f_l. In case of the bandpass filter, additional frequencies larger than the second cutoff frequency f_h are removed. The filtered time series $\boldsymbol{l}_f = \begin{bmatrix} l_f^1 & l_f^2 & \dots & l_f^n \end{bmatrix}^\mathsf{T}$ is obtained from the difference between the observed time series $\boldsymbol{l}^o$ and the removed signal $\boldsymbol{l}_r = \begin{bmatrix} l_r^1 & l_r^2 & \dots & l_r^n \end{bmatrix}^\mathsf{T}$. The removed part of the jth observation ($j = 1, \dots, n$) is approximated by following equation

$$l_r^j = a_0 + a_1\tau_j + \sum_{k=1}^{k\leq nf_l} \left(b_k \cos 2\pi k\tau_j + c_k \sin 2\pi k\tau_j\right) + \sum_{k\geq nf_h}^{n_{max}} \left(b_k \cos 2\pi k\tau_j + c_k \sin 2\pi k\tau_j\right) \qquad 4.1$$

with the normed time $\tau_j = (j-1)/n$ and $n_{max} = \text{floor}\,(n/2)$. The second sum only exists in case of a bandpass filter. The coefficients a_0, a_1, b_k and c_k are determined by a least-squares adjustment in an unconstrained GMM. The observations are assumed to be uncorrelated and determined with equal accuracy. The design matrix $\boldsymbol{A}$ contains the partial derivatives of Equation 4.1 with respect to the unknown coefficients. Since the filtered signal is obtained from the difference between the original observations and the removed signal, the filtered signal corresponds to the residuals of the least-squares adjustment. Therefore, the filtered signal is obtained by

$$\boldsymbol{l}_f = \boldsymbol{l}_o - \boldsymbol{A}\left(\boldsymbol{A}^\mathsf{T}\boldsymbol{A}\right)^{-1}\boldsymbol{A}^\mathsf{T}\boldsymbol{l}_o. \qquad 4.2$$

Figure 4.1 provides examples for the bandpass filter and the highpass filter. The figure depicts the original signal, the removed signal and the resulting filtered signal of the daily LOD and of a monthly

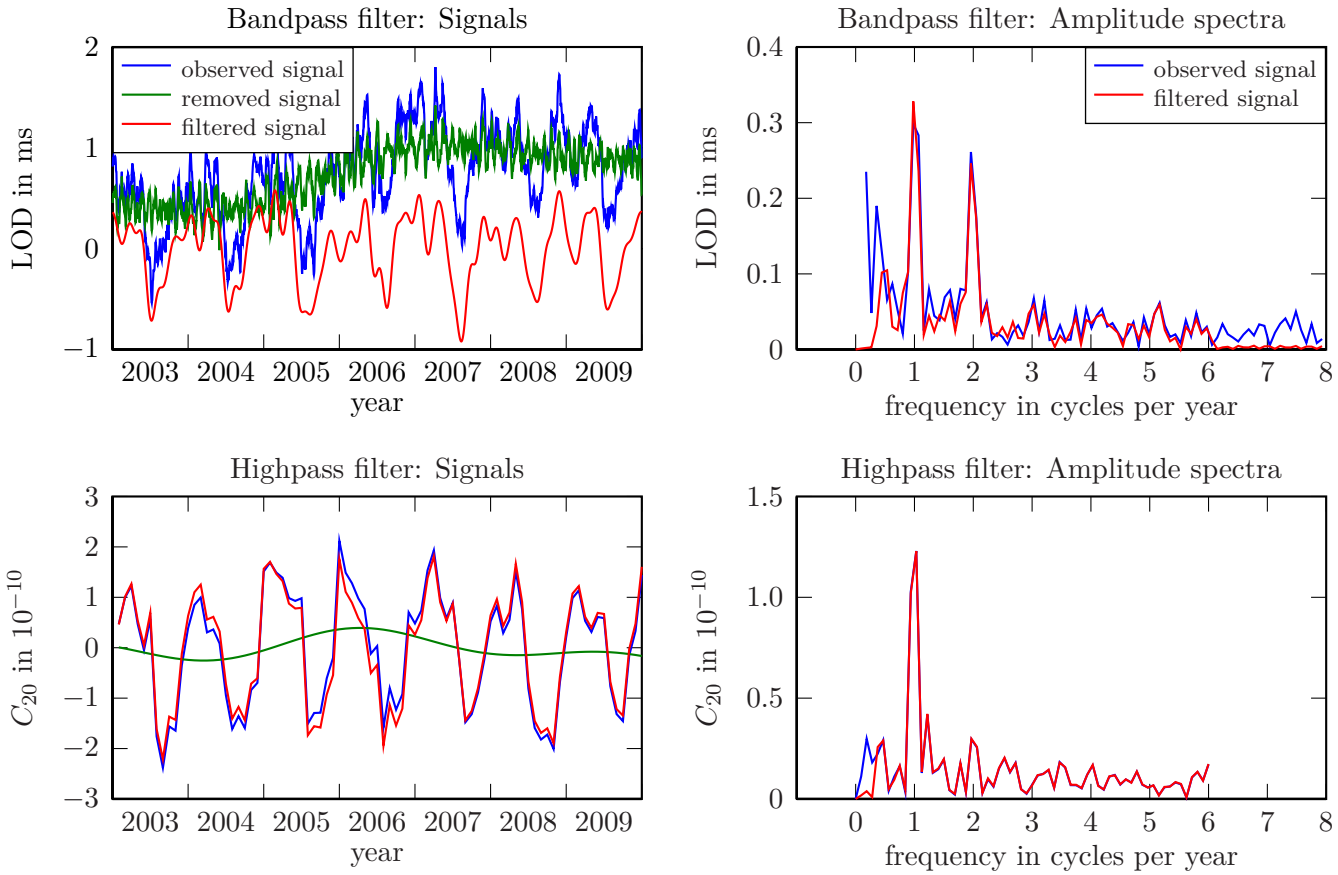

Figure 4.1: The figures show the observed original signal (blue), the removed signal (green) and the filtered signal (red) of LOD (upper row) and the gravity field coefficents C_{20} (lower row). The signals are shown in the time domain (left column) and in the frequency domain (right column).

C_{20} time series. A constant offset was removed from C_{20}, before the filter is applied. LOD is bandpass-filtered with the cutoff frequencies $f_l = 1/(3 \cdot 365 \text{ days})$ and $f_h = 1/60$ days. C_{20} is highpass-filtered with the cutoff frequency $f_l = 1/(3 \cdot 12 \text{ months})$. According to the amplitude spectra, the amplitudes in the stopbands are approximately zero in both time series. The characteristic annual and semiannual peaks in the passbands remain present in the filtered time series. The filtered semiannual amplitude in LOD shows a small attenuation. Therefore, the proposed filter is sufficient for the further analysis of the data. However, since the time series feature different temporal resolutions, the passbands do not consider exactly the same frequencies. Thus, filter artifacts might arise near the cutoff frequencies.

4.2. Realisation of the Gauss-Helmert Model

4.2.1. Functional model

According to Chapter 2, the EOP, GFC2 and the excitation function are linearly related to the tensor of inertia. Since the equations are linear and since three of six elements of the tensor inertia can be redundantly determined by the different time series, a constrained linear least-squares adjustment model is chosen for the mutual validation. The least-squares adjustment is performed by considering the EOP, GFC2 and geophysical excitation functions as observations. The functional model of the least-squares adjustment problem is based on the geophysical models in Chapter 2. This subsection generates the vectors and matrices used within the least-squares adjustment, whereas the a priori stochastic models are described by Subsection 4.2.2.

In principle, the time series are mutually validated by comparisons of the tensors of inertia, obtained from time series with different temporal resolutions. Therefore, the tensors have to be related to the same epochs. Thus, the daily observations have to be downsampled to the lower temporal resolution of the GFC2. The simplest method of downsampling is the calculation of monthly arithmetic averages of the daily time series. The equatorial part of the ELE in Equation 2.30a requires the unavailable time derivatives of the polar motion. Therefore, the time derivatives have to be approximated by the polar

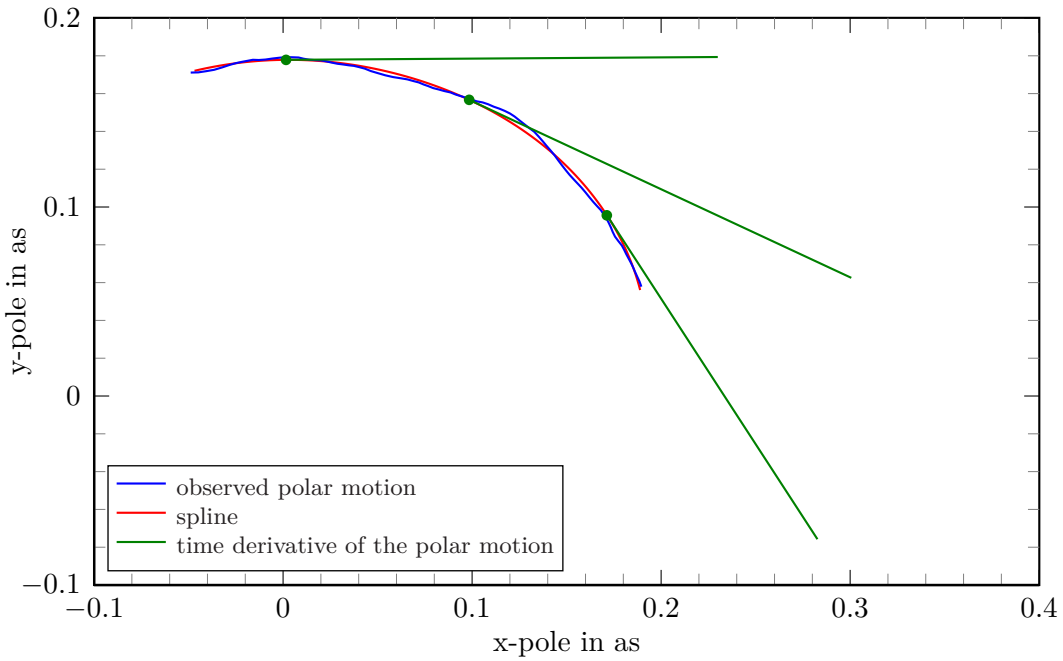

Figure 4.2: The observed polar motion of June, July and August 2009 are pictured in blue. The polar motion is approximated by the red splines. The green dots denote the representative monthly values obtained by the spline coefficients. The green lines are the time derivatives of the polar motion, obtained from the analytic differentiation of the splines, multiplied by the reciprocal Chandler frequency $1/\sigma_0$.

motion itself. The simplest approximation of the time derivative is the differential quotient. Then, the time derivative of the jth epoch is obtained by the polar motion of the previous epoch $j-1$ and the subsequent epoch $j+1$ with

$$\dot{\tilde{p}}^j = \frac{\tilde{p}^{j+1} - \tilde{p}^{j-1}}{2\Delta t} \tag{4.3}$$

where Δt denotes the time span of one epoch. The numerical differentiation causes linear dependencies of the epochs. The first and the last epoch cannot be validated by a linear least-squares adjustment, if the epochs are linearly dependent on each others. Then, the polar motion of the first and last epoch are hardly controlled by other observations, as they only are present in the time derivatives of the second and the next-to-last epoch. Errors in the first and last epoch would not be detected and would impact the entire validation. Though, this simple approach is discussed within the sensitivity analyses in Section 4.3. Another approach is proposed, in order avoid the disadvantage of the numeric differentiation. Each epoch (e.g. one month) is modeled by one cubic spline. The downsampled representative monthly epoch values are obtained by evaluating the splines at the mid of the month. Cubic splines have the advantage that the time derivatives can be easily obtained by analytic differentiation. According to Mayer-Gürr (2006), the approximation of a time series by piecewise defined functions, e.g. splines, is superior to blockwise calculated averages, since the piecewise defined functions are in contrast to the averages continuous over time. Figure 4.2 illustrates the approximation of the polar motion by cubic splines.
If the time series involve n epochs, $n+1$ moments in time T_j (with $j = 1, \ldots, n+1$) exist which denote the begin and end of each spline. If the k-th daily observation, belonging to the jth spline, is observed at the time t_k, the observation l_k is described by

$$f_j(\tau_k) = l_k + \epsilon_k = a_j\tau_k^3 + b_j\tau_k^2 + c_j\tau_k + d_j. \tag{4.4}$$

with $\tau_k = (t_k - T_j)/(T_{j+1} - T_j)$. The normed time τ_k (with $0 \leq \tau_k \leq 1$) is introduced to reach a good numerical condition. The $4n$ unknown spline coefficients a_j, b_j, c_j and d_j are estimated within the least-squares adjustment. The first and second time derivative of the observation l_k are according to Equation 4.4

$$\dot{f}_j(\tau_k) = \dot{l}_k = \frac{1}{T_{j+1} - T_j}\left(3a_j\tau_k^2 + 2b_j\tau_k + c_j\right), \tag{4.5}$$

$$\ddot{f}_j(\tau_k) = \ddot{l}_k = \frac{1}{(T_{j+1} - T_j)^2}\left(6a_j\tau_k + 2b_j\right). \tag{4.6}$$

Additionally, it is required that the splines are twice continuously differentiable in the transition points between two splines. $3\,(n-1)$ constraints result from this request

$$f_j(1) = f_{j+1}(0) \quad \Rightarrow \quad a_j + b_j + c_j + d_j = d_{j+1} \tag{4.7a}$$

$$\dot{f}_j(1) = \dot{f}_{j+1}(0) \quad \Rightarrow \quad 3a_j + 2b_j + c_j = \frac{T_{j+1} - T_j}{T_{j+2} - T_{j+1}} c_{j+1} \tag{4.7b}$$

$$\ddot{f}_j(1) = \ddot{f}_{j+1}(0) \quad \Rightarrow \quad 3a_j + b_j = \left(\frac{T_{j+1} - T_j}{T_{j+2} - T_{j+1}} \right)^2 b_{j+1}. \tag{4.7c}$$

The constraints in Equations 4.7 are used to reduce the number of the unknown parameters from $4n$ parameters to $n+3$ parameters per time series. The reduction of the unknown parameters improves the efficiency of the least-squares adjustment. Since the necessary computer capacity increases by the order three of the size of the normal equation system, the reduction is essential for efficient coding. Reductions lead to smaller but denser normal equation systems. Here, the $4n$ splines coefficients are reduced to following $n+3$ spline coefficients

$$\boldsymbol{\beta}_{sp} = \begin{bmatrix} a_n & b_1 & b_n & d_1 & d_2 & \dots & d_n \end{bmatrix}^{\mathsf{T}}. \tag{4.8}$$

The coefficients in the vector $\boldsymbol{\beta}_{sp}$ are chosen with respect to sufficient numerical condition numbers. Appendix E performs the reduction of the unknown parameter. The resulting system of normal equations is reduced to approximately 30% of the original size. Appendix E delivers design matrices $\boldsymbol{A}_{sp}$ and $\boldsymbol{B}_{sp}$ relating daily time series and their time derivatives to the chosen $n+3$ spline coefficients. Then, it holds for the observations $\boldsymbol{l}_{daily}$ and their time derivatives

$$\boldsymbol{l}_{daily} + \boldsymbol{\epsilon}_{daily} = \boldsymbol{A}_{sp}\boldsymbol{\beta}_{sp} \tag{4.9}$$

$$\dot{\boldsymbol{l}}_{daily} \qquad\quad = \boldsymbol{B}_{sp}\boldsymbol{\beta}_{sp}. \tag{4.10}$$

The vector $\boldsymbol{\epsilon}_{daily}$ denotes the residuals. The EOP contain three daily time series (p_x, p_y and Λ_{LOD}) in total and the excitation functions contain six daily time series (Ωc_{xz}, Ωc_{yz}, Ωc_{zz}, h_x, h_y, h_z). The daily observations are related to the $9\,(n+3)$ spline coefficients by

$$\begin{bmatrix} \boldsymbol{l}_{EOP} \\ \boldsymbol{l}_{EF} \end{bmatrix} + \begin{bmatrix} \boldsymbol{\epsilon}_{EOP} \\ \boldsymbol{\epsilon}_{EF} \end{bmatrix} = \underbrace{\begin{bmatrix} \boldsymbol{A}_{sp} & \boldsymbol{0} & \boldsymbol{0} & \boldsymbol{0} & \boldsymbol{0} & \boldsymbol{0} & \boldsymbol{0} & \boldsymbol{0} & \boldsymbol{0} \\ \boldsymbol{0} & \boldsymbol{A}_{sp} & \boldsymbol{0} & \boldsymbol{0} & \boldsymbol{0} & \boldsymbol{0} & \boldsymbol{0} & \boldsymbol{0} & \boldsymbol{0} \\ \boldsymbol{0} & \boldsymbol{0} & \boldsymbol{A}_{sp} & \boldsymbol{0} & \boldsymbol{0} & \boldsymbol{0} & \boldsymbol{0} & \boldsymbol{0} & \boldsymbol{0} \\ \boldsymbol{0} & \boldsymbol{0} & \boldsymbol{0} & \boldsymbol{A}_{sp} & \boldsymbol{0} & \boldsymbol{0} & \boldsymbol{0} & \boldsymbol{0} & \boldsymbol{0} \\ \boldsymbol{0} & \boldsymbol{0} & \boldsymbol{0} & \boldsymbol{0} & \boldsymbol{A}_{sp} & \boldsymbol{0} & \boldsymbol{0} & \boldsymbol{0} & \boldsymbol{0} \\ \boldsymbol{0} & \boldsymbol{0} & \boldsymbol{0} & \boldsymbol{0} & \boldsymbol{0} & \boldsymbol{A}_{sp} & \boldsymbol{0} & \boldsymbol{0} & \boldsymbol{0} \\ \boldsymbol{0} & \boldsymbol{0} & \boldsymbol{0} & \boldsymbol{0} & \boldsymbol{0} & \boldsymbol{0} & \boldsymbol{A}_{sp} & \boldsymbol{0} & \boldsymbol{0} \\ \boldsymbol{0} & \boldsymbol{0} & \boldsymbol{0} & \boldsymbol{0} & \boldsymbol{0} & \boldsymbol{0} & \boldsymbol{0} & \boldsymbol{A}_{sp} & \boldsymbol{0} \\ \boldsymbol{0} & \boldsymbol{0} & \boldsymbol{0} & \boldsymbol{0} & \boldsymbol{0} & \boldsymbol{0} & \boldsymbol{0} & \boldsymbol{0} & \boldsymbol{A}_{sp} \end{bmatrix}}_{\boldsymbol{A}_{daily}} \underbrace{\begin{bmatrix} \boldsymbol{\beta}_{p_x} \\ \boldsymbol{\beta}_{p_y} \\ \boldsymbol{\beta}_{\Lambda_{LOD}} \\ \boldsymbol{\beta}_{\Omega c_{xz}} \\ \boldsymbol{\beta}_{\Omega c_{yz}} \\ \boldsymbol{\beta}_{\Omega c_{zz}} \\ \boldsymbol{\beta}_{h_x} \\ \boldsymbol{\beta}_{h_y} \\ \boldsymbol{\beta}_{h_z} \end{bmatrix}}_{\boldsymbol{\beta}_{daily}}. \tag{4.11}$$

Equation 2.65 describes the linear functional relation between GFC2 variations and the unknown tensor in inertia. The observed GFC2 variations of the jth epoch depend on the variations of the tensor of inertia by

$$\underbrace{\begin{bmatrix} \Delta C^j_{20} \\ \Delta C^j_{21} \\ \Delta S^j_{21} \\ \Delta C^j_{22} \\ \Delta S^j_{22} \end{bmatrix}}_{\boldsymbol{l}^j_{GFC}} + \boldsymbol{\epsilon}^j_{GFC} = \frac{1}{Ma^2} \underbrace{\begin{bmatrix} \frac{1}{2\sqrt{5}} & 0 & 0 & \frac{1}{2\sqrt{5}} & 0 & -\frac{1}{\sqrt{5}} \\ 0 & 0 & 0 & 0 & \sqrt{\frac{3}{5}} & 0 \\ 0 & 0 & \sqrt{\frac{3}{5}} & 0 & 0 & 0 \\ -\frac{1}{2}\sqrt{\frac{3}{5}} & 0 & 0 & \frac{1}{2}\sqrt{\frac{3}{5}} & 0 & 0 \\ 0 & \sqrt{\frac{3}{5}} & 0 & 0 & 0 & 0 \end{bmatrix}}_{\boldsymbol{A}^j_{GFC}} \underbrace{\begin{bmatrix} c^j_{xx} \\ c^j_{xy} \\ c^j_{xz} \\ c^j_{yy} \\ c^j_{yz} \\ c^j_{zz} \end{bmatrix}}_{\boldsymbol{\beta}^j_T} \tag{4.12}$$

where the vector $\boldsymbol{\beta}^j_T$ contains the unknown tensor elements of the jth epoch ($j = 1, \dots, n$). This equation relates five gravity field coefficients to six elements of the tensor of inertia. The trace of the tensor of

inertia is underdetermined. According to the tensor trace constraint in Equation 2.66, the trace of the tensor of inertia is invariant to any deformations. The tensor trace constraint of the jth epoch is

$$\underbrace{\begin{bmatrix}1 & 0 & 0 & 1 & 0 & 1\end{bmatrix}}_{\boldsymbol{A}_{C12}^{j}} \boldsymbol{\beta}_T^j = 0. \tag{4.13}$$

The last two equations describe the relations between the GFC2 and the tensor elements of one epoch. Summarizing all epochs leads to

$$\underbrace{\begin{bmatrix}\boldsymbol{l}_{GFC}^1 \\ \vdots \\ \boldsymbol{l}_{GFC}^n\end{bmatrix}}_{\boldsymbol{l}_{GFC}} + \underbrace{\begin{bmatrix}\boldsymbol{\epsilon}_{GFC}^1 \\ \vdots \\ \boldsymbol{\epsilon}_{GFC}^n\end{bmatrix}}_{\boldsymbol{\epsilon}_{GFC}} = \underbrace{\operatorname{diag}\left(\boldsymbol{A}_{GFC}^1, \ldots, \boldsymbol{A}_{GFC}^n\right)}_{\boldsymbol{A}_{GFC}} \underbrace{\begin{bmatrix}\boldsymbol{\beta}_T^1 \\ \vdots \\ \boldsymbol{\beta}_T^n\end{bmatrix}}_{\boldsymbol{\beta}_T} \quad \Rightarrow \quad \boldsymbol{l}_{GFC} + \boldsymbol{\epsilon}_{GFC} = \boldsymbol{A}_{GFC}\boldsymbol{\beta}_T \tag{4.14}$$

$$\underbrace{\operatorname{diag}\left(\boldsymbol{A}_{C12}^1, \ldots, \boldsymbol{A}_{C12}^n\right)}_{\boldsymbol{A}_{C12}} \underbrace{\begin{bmatrix}\boldsymbol{\beta}_T^1 \\ \vdots \\ \boldsymbol{\beta}_T^n\end{bmatrix}}_{\boldsymbol{\beta}_T} = \boldsymbol{0} \quad \Rightarrow \quad \boldsymbol{A}_{C12}\boldsymbol{\beta}_T = \boldsymbol{0}. \tag{4.15}$$

The operator 'diag' provides block-diagonal matrices. Equation 4.15 contains n constraints.
Subsection 2.2.3 derives the linear approximation of the ELE, which relates the EOP, the mass and motion terms of the excitation functions and the tensor of inertia to each other. The motion terms equal the relative angular momentum h_x, h_y and h_z, whereas the mass terms Ωc_{xz}, Ωc_{yz} and Ωc_{zz} contain three tensor elements multiplied by the mean rotation velocity Ω. The mass and the motion terms have the unit $\mathrm{kg\,m^2\,s^{-1}}$. As mentioned before, the daily observations have to be downsampled to one value per epoch. The downsampled epoch values and their time derivatives are obtained by the spline coefficients. The design matrices $\boldsymbol{A}_m$ and $\boldsymbol{B}_m$ are evaluated according to Appendix E by considering $\tau = 0.5$. The relation between the EOP, the motion terms and the tensor of inertia are given by the Equations 2.44 and 2.46. These equations lead to following $3n$ constraints

$$\underbrace{\begin{bmatrix} \boldsymbol{A}_m & \frac{1}{\sigma_0}\boldsymbol{B}_m & \boldsymbol{0} & \boldsymbol{0} & \boldsymbol{0} & \boldsymbol{0} & -\frac{1}{\sigma_0(C-A_C+\epsilon_C A_C)}\boldsymbol{A}_m & \boldsymbol{0} & \boldsymbol{0} \\ -\frac{1}{\sigma_0}\boldsymbol{B}_m & \boldsymbol{A}_m & \boldsymbol{0} & \boldsymbol{0} & \boldsymbol{0} & \boldsymbol{0} & \boldsymbol{0} & -\frac{1}{\sigma_0(C-A_C+\epsilon_C A_C)}\boldsymbol{A}_m & \boldsymbol{0} \\ \boldsymbol{0} & \boldsymbol{0} & \frac{1}{\Lambda_0}\boldsymbol{A}_m & \boldsymbol{0} & \boldsymbol{0} & \boldsymbol{0} & \boldsymbol{0} & \boldsymbol{0} & -\frac{k_r}{\Omega C_M}\boldsymbol{A}_m \end{bmatrix}}_{\boldsymbol{A}_{C21}} \boldsymbol{\beta}_{daily}$$

$$- \underbrace{\begin{bmatrix} \frac{\Omega\left(1+k_2'+\Delta k_a\right)}{\sigma_0(C-A_C+\epsilon_C A_C)}\boldsymbol{A}_{xz} \\ \frac{\Omega\left(1+k_2'+\Delta k_a\right)}{\sigma_0(C-A_C+\epsilon_C A_C)}\boldsymbol{A}_{yz} \\ k_r\frac{\Omega\left(1+k_2'+\Delta k_a\right)}{\Omega C_M}\boldsymbol{A}_{zz} \end{bmatrix}}_{\boldsymbol{A}_{C22}} \boldsymbol{\beta_T} = \boldsymbol{0}. \tag{4.16}$$

The design matrices $\boldsymbol{A}_{xz}$, $\boldsymbol{A}_{yz}$ and $\boldsymbol{A}_{zz}$ contain the value one for the c_{xz}, c_{yz} and c_{zz}, respectively, and zeros for all remaining tensor elements (compare Equations 2.44 and 2.46). As the mass terms contain the tensor elements multiplied by the mean rotation velocity, further $3n$ constraints arise with

$$\underbrace{\begin{bmatrix} \boldsymbol{0} & \boldsymbol{0} & \boldsymbol{0} & \boldsymbol{A}_m & \boldsymbol{0} & \boldsymbol{0} & \boldsymbol{0} & \boldsymbol{0} & \boldsymbol{0} \\ \boldsymbol{0} & \boldsymbol{0} & \boldsymbol{0} & \boldsymbol{0} & \boldsymbol{A}_m & \boldsymbol{0} & \boldsymbol{0} & \boldsymbol{0} & \boldsymbol{0} \\ \boldsymbol{0} & \boldsymbol{0} & \boldsymbol{0} & \boldsymbol{0} & \boldsymbol{0} & \boldsymbol{A}_m & \boldsymbol{0} & \boldsymbol{0} & \boldsymbol{0} \end{bmatrix}}_{\boldsymbol{A}_{C31}} \boldsymbol{\beta}_{daily} - \underbrace{\begin{bmatrix} \Omega\boldsymbol{A}_{xz} \\ \Omega\boldsymbol{A}_{yz} \\ \Omega\boldsymbol{A}_{zz} \end{bmatrix}}_{\boldsymbol{A}_{C32}} \boldsymbol{\beta_T} = \boldsymbol{0}. \tag{4.17}$$

The equations derived in this section describe a functional model according to Chapter 3. The Equations 4.11 and 4.14 contain stochastic observations, whereas the Equations 4.15, 4.16 and 4.17 describe $7n$ nonstochastic constraints. The stochastic equations are summarized to

$$\underbrace{\begin{bmatrix}\boldsymbol{l}_{EOP} \\ \boldsymbol{l}_{EF} \\ \boldsymbol{l}_{GFC}\end{bmatrix}}_{\boldsymbol{l}} + \underbrace{\begin{bmatrix}\boldsymbol{\epsilon}_{EOP} \\ \boldsymbol{\epsilon}_{EF} \\ \boldsymbol{\epsilon}_{GFC}\end{bmatrix}}_{\boldsymbol{\epsilon}} = \underbrace{\begin{bmatrix}\boldsymbol{A}_{daily} & \boldsymbol{0} \\ \boldsymbol{0} & \boldsymbol{A}_{GFC}\end{bmatrix}}_{\boldsymbol{A}_H} \underbrace{\begin{bmatrix}\boldsymbol{\beta}_{daily} \\ \boldsymbol{\beta}_T\end{bmatrix}}_{\boldsymbol{\beta}} \quad \Rightarrow \quad \boldsymbol{l} + \boldsymbol{\epsilon} = \boldsymbol{A}_H\boldsymbol{\beta} \tag{4.18a}$$

and the constraints to

$$\underbrace{\begin{bmatrix} \boldsymbol{0} & \boldsymbol{A}_{C12} \\ \boldsymbol{A}_{C21} & -\boldsymbol{A}_{C22} \\ \boldsymbol{A}_{C31} & -\boldsymbol{A}_{C32} \end{bmatrix}}_{\boldsymbol{A}_C} \underbrace{\begin{bmatrix} \boldsymbol{\beta}_{daily} \\ \boldsymbol{\beta}_T \end{bmatrix}}_{\boldsymbol{\beta}} = \boldsymbol{0} \qquad \Rightarrow \quad \boldsymbol{A}_C\boldsymbol{\beta} = \boldsymbol{0}. \tag{4.18b}$$

The last two equations describe a constrained GHM, which can be solved by the algorithm shown in Appendix D. To be precise, the functional model describes a constrained GMM, since the design matrix $\boldsymbol{B}$ is the identity matrix (compare Equations 3.3a and 4.18a).

4.2.2. Stochastic model

The data validated within this dissertation partly results from previous measurements (EOP and GFC2) and partly from models (excitation functions). Here, the excitation functions are introduced as stochastic pseudo-observations. Data resulting from models do not contain any stochastic information. The EOP and GFC2 are provided with standard deviations and therefore with variances. However, information on covariances is not delivered from the data provider, except one GFC2 time series. This subsection proposes the approximation of unknown variances and covariances by empirical auto- and crosscorrelation functions.

Assume two arbitrary equidistant time series $\boldsymbol{x}$ and $\boldsymbol{y}$, which observe stochastic processes. Each time series contains n observations. The empirical autocorrelation function σ_{xx} and the crosscorrelation function σ_{xy} are defined as (Koch and Schmidt, 1994, page 218)

$$\sigma_{xx}(d) = \begin{cases} \dfrac{1}{n-d} \displaystyle\sum_{i=1}^{n-d} (x_i - \mu_{x_i})\,(x_{i+d} - \mu_{x_{i+d}}) & \text{for} \quad d \geq 0 \\ \sigma_{xx}(-d) & \text{for} \quad d < 0 \end{cases} \tag{4.19a}$$

$$\sigma_{xy}(d) = \begin{cases} \dfrac{1}{n-d} \displaystyle\sum_{i=1}^{n-d} (x_i - \mu_{x_i})\,(y_{i+d} - \mu_{y_{i+d}}) & \text{for} \quad d \geq 0 \\ \dfrac{1}{n+d} \displaystyle\sum_{i=1}^{n+d} (x_{i-d} - \mu_{x_{i-d}})\,(y_i - \mu_{y_i}) & \text{for} \quad d < 0 \end{cases} \tag{4.19b}$$

where d denotes the time difference. The expectation values μ are considered due to stationarity. Since the auto- and crosscorrelations functions have to reflect stochastic variations, deterministic parts of the signal are removed by the expectation values. Then, the differences between the observations and the expectation values are time-invariant, and the stochastic process is stationary (Koch and Schmidt, 1994, page 166). For example, since the polar motion is modeled by splines, the splines reflect the deterministic part of the signal. Thus, a preliminary spline adjustment is performed. The adjusted splines are removed from the original signal. Then, the empirical auto- and crosscorrelations functions are calculated by the residual signal. Koch et al. (2010) suggested to generate Toeplitz-structured VCM using the empirical auto- and crosscorrelation functions. Toeplitz matrices contain the same values on the diagonals.

If stochastic processes are ergodic, the auto- and crosscorrelations functions tend to zero for large time differences d. However, since only a few summands contribute to the empirical variances and covariances of large d, the empirical auto- and crosscorrelations in Equations 4.19 are usually comparatively large. Ergodic VCM can be reached by defining zero correlations for large d, e.g. for all $|d| > n/10$, or by using biased empirical auto- and crosscorrelations functions instead of the auto- and crosscorrelations functions in the Equations 4.19. Koch et al. (2010) proposed the latter approach.

Toeplitz-structured VCM, composed of empirical auto- and crosscorrelation functions, are positive semidefinite (Koch et al., 2010). According to experience, made during the work on this dissertation, the VCM resulting from empirically derived auto- and crosscorrelations functions tend to be semidefinite. Then, the VCM are poorly conditioned. The condition numbers of the VCM are improved by approximating the empirical auto- and crosscorrelation functions by analytical functions. Sansò and Schuh (1987), Gaspari and Cohn (1999) and Koch et al. (2010) propose piecewise analytical functions. However, the analytical

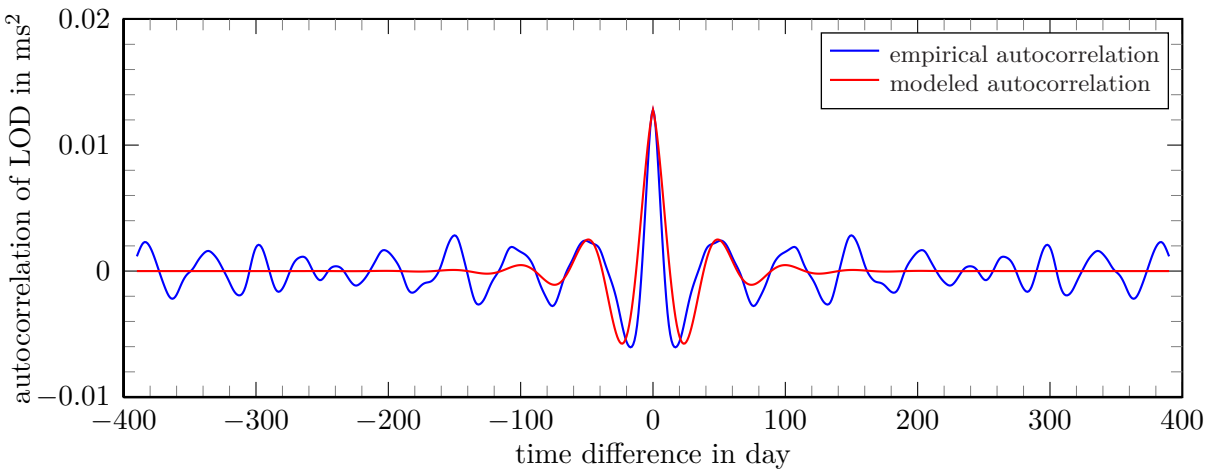

Figure 4.3: The empirical autocorrelation function in blue is modeled by a damped oscillation function in red.

functions do not necessarily provide positive semidefinite VCM (Koch et al., 2010). Positive-definiteness has to be verified, e.g., by Cholesky decomposition.
The a priori VCM for daily time series are obtained as follows: Empirical auto- and crosscorrelation functions are calculated in each possible combination. The crosscorrelation functions between the equatorial (polar motion, h_x/h_y, $\Omega c_{xz}/\Omega c_{yz}$) and axial components (LOD, h_z, Ωc_{zz}) do not indicate systematic effects but rather noise. Therefore, the correlations between equatorial and axial components of the daily time series are set to zero. The autocorrelation and the remaining crosscorrelation functions are similar to damped oscillation functions. Therefore the empirical auto- and crosscorrelations functions are approximated by

$$s_{xy}(d) = s_{xy_0} \exp(\delta|d - d_0|) \cos(2\pi f|d - d_0|) \tag{4.20}$$

where s_{xy_0} denotes the maximal value of the empirical auto- and crosscorrelation function. The parameter d_0 is time difference of the maximal value. It holds $d_0 = 0$ in case of autocorrelation functions. The parameter δ is the damping factor and f is the frequency of the damped oscillation. The damping factor and the frequency are determined by a nonlinear least-squares solver. Figure 4.3 gives an example for the empirical and approximated autocorrelation function of LOD.
The correlations decrease for large time differences d. The correlations for large time differences d are set to zero as long as the values are below a threshold level. The threshold level is set to 0.1% of the maximal value of the empirical auto- or crosscorrelation functions here. The achieved zeros in the margins of the auto- or crosscorrelation functions ensure sparse a priori VCM and optimize therefore the efficiency of the estimation (regarding computer storages). The resulting Toeplitz-structured VCM are band-diagonal and positive-definiteness is proven by Cholesky decomposition.
As the monthly gravity field time series are too short, meaningful empirical auto- and crosscorrelations functions cannot be calculated. One gravity field solution is delivered with full VCM. The VCM of the other gravity field solutions are diagonal matrices composed of the given formal errors. Further information on the available GFC2 time series is given in Subsection 5.1.2.

4.3. Sensitivity analysis

4.3.1. Comparison of time series with different units

Two methods for the approximation of the time derivative of the polar motion are proposed in Subsection 4.2.1. Furthermore, different values exist for some of the geophysical quantities in Chapter 2. The sensitivity analysis investigates the influence of the different functional approaches and numerical values. In order to make the different units of the time series comparable, a common Tensor Unit (TU) is defined as

$$1 \text{ TU } [\text{dimensionless}] = \frac{10^{10}\,\text{kg}\,\text{m}^2}{a^2 M} \tag{4.21}$$

where a and M denote the Earth's radius and mass. The values for a and M are given in Table 4.4. The variations of the time series cause variations of the tensor elements. The values in Table 4.1 change

Table 4.1: The values change the associated tensor element about 1 TU.

	equatorial			axial		
EOP	Δp_x, Δp_y	$\approx$	20.8 mas	$\Delta\Lambda$	$\approx$	0.02 ms
	$\Delta\dot{p}_x$, $\Delta\dot{p}_y$	$\approx$	0.3 mas day^{-1}			
Motion terms	Δh_x, Δh_y	$\approx$	$1.21 \cdot 10^{24}$ kg m^2 s^{-1}	Δh_z	$\approx$	$1.33 \cdot 10^{24}$ kg m^2 s^{-1}
Mass terms	$\Omega\Delta c_{xz}$, $\Omega\Delta c_{yz}$	$\approx$	$1.77 \cdot 10^{24}$ kg m^2 s^{-1}	$\Omega\Delta c_{zz}$	$\approx$	$1.77 \cdot 10^{24}$ kg m^2 s^{-1}
GFC2	ΔC_{21}, ΔS_{21}	$\approx$	$0.77 \cdot 10^{-10}$	ΔC_{20}	$\approx$	$0.67 \cdot 10^{-10}$

the associated tensor element about 1 TU. For example, if LOD changes about 0.02 ms, the tensor element c_{zz} varies about 1 TU. If the polar motion varies, the time derivative of the polar motion also varies. The influence of polar motion variations on the time derivative and vice versa cannot be separated from each other without taking further assumptions into account. The polar motion values in Table 4.1 are obtained by assuming that polar motion variations do not cause variations of the time derivative and vice versa. Though this assumption does not describe reality, the values in Table 4.1 are used to relate different units to each other.

As mentioned before, three unknown tensor elements are redundantly determinable first by the difference of the EOP and motion terms, second by the mass terms and third by the GFC2. Figure 4.4 shows the tensor elements resulting from the difference between the EOP and motion terms. The contributions of the EOP (blue), the time derivatives of the polar motion (green) and the motion terms (red) to the total tensor elements are shown separately. The resulting tensor element is drawn in gray. The graphs are obtained from the IERS C04 time series and from atmospheric and oceanic excitation functions from the GeoForschungsZentrum Potsdam (GFZ). A more detailed description of the time series is given in Section 5.1. The left and the middle figures show the contributions to the equatorial tensor component c_{xz} and c_{yz}. The influence of the motion term is significantly smaller than the influence of the polar motion and its time derivative. The contributions of the polar motion and the polar motion time derivatives have similar absolute values but impact in opposite directions. Thus, the equatorial tensor elements are comparatively small quantities resulting from the differences of two larger values. According to the right figure, the contributions of the axial motion term h_z are significantly larger than the contributions of the equatorial motion terms. The axial tensor elements result as well from the difference of two large quantities, namely LOD and the motion term h_z. Figure 5.1 presents additional tensor elements calculated from further time series.

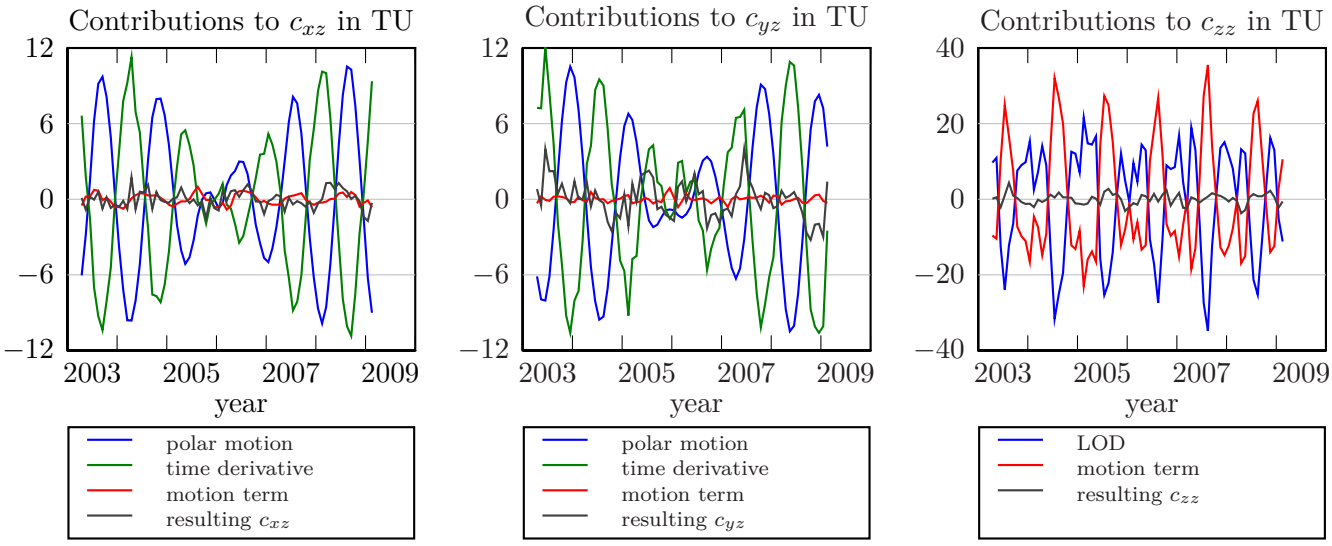

Figure 4.4: Graphs show the contribution of the EOP and motion terms to the resulting tensor of inertia.

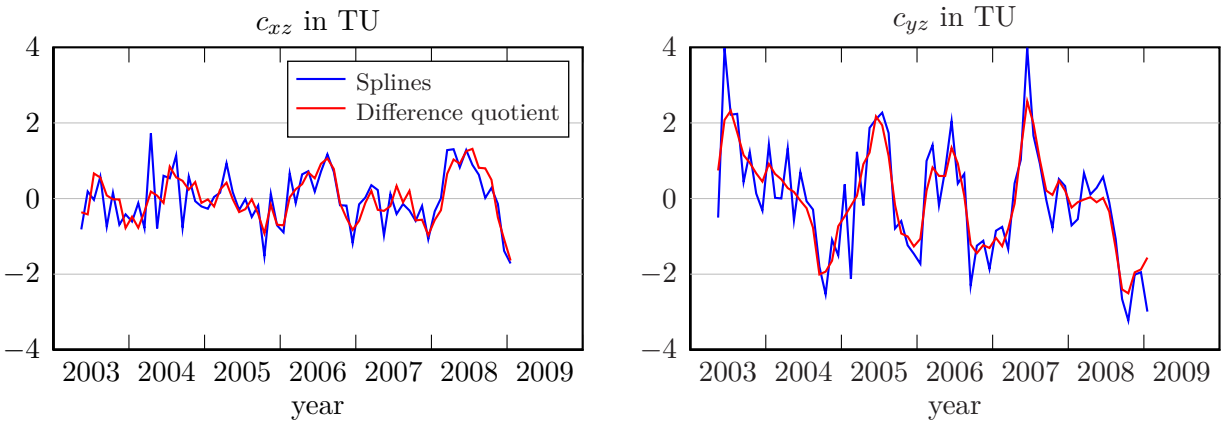

Figure 4.5: Graphs show the equatorial tensor elements resulting from the EOP and the motion terms. The blue lines are obtained by the splines approach and the red lines result from monthly arithmetic averages and numerical differentiation.

4.3.2. Splines versus numerical differentiation

According to Subsection 4.2.1, the time derivatives of the polar motion are not observed directly and are approximated by the observed polar motion. Additionally, the daily time series are downsampled to epoch values due to the different temporal resolution of the time series. Two approaches for the downsampling and the approximation of the time derivatives are discussed. The first approach models the representative epoch values and the time derivatives by cubic splines (cf. Subsection 4.2.1). The splines have the advantage that the time derivatives can be obtained by analytic differentiation. The second approach calculates the monthly arithmetic average and determines the time derivative by simple numeric differentiation of monthly averages (cf. Equation 4.3).
The effect of the two approaches on the tensor of inertia is analyzed by calculating the equatorial tensor elements from the polar motion and the motion terms using both approaches. Figure 4.5 shows the resulting tensor elements. Both approaches deliver mostly similar results. Comparatively large deviations of maximal 1.8 TU occur in some epochs. The spline approach obviously shows a noisier pattern than the second approach. According to further analysis, the differences between these two approaches are caused by the time derivatives. The representative epoch values for the polar motion and the motion terms differ barely. However, the differences between the two approaches do not reveal any systematic behavior. Therefore it is concluded, that the equatorial tensor solution resulting from the polar motion and the motion terms shows large but stochastic variations due to the chosen approximation of the time derivatives.

4.3.3. Effect of different numerical values for geophysical constants

The ELE contains several geophysical constants describing a model of the Earth. Different numerical values exist for some of the constants. If the tensor elements are obtained from the difference between the EOP and the motion terms, the different constants affect the resulting tensor elements. Therefore, the effect of the different values are analyzed.

Effect of the complex-valued Chandler frequency on the equatorial ELE:

The anelastic reaction of the Earth leads to energy dissipation and consequently to a damped Chandler wobble. The body tide Love number is modified by a complex-valued number to account for the anelasticity. That leads via the parameter D_e (cf. Subsection 2.2.2) to a modified complex-valued Chandler frequency (Wahr, 2005)

$$\sigma_0 = \frac{2\pi}{T_{CW}} \left(1 + \frac{1}{2Q_{CW}}\mathrm{i}\right) \tag{4.22}$$

where T_{CW} denotes the period of the Chandler wobble and Q_{CW} the damping factor. Gross (2007) and Seitz (2004) listed values for T_{CW} and Q_{CW}. Table 4.2 contains these values and the resulting complex-valued Chandler frequency. Since the imaginary part of the Chandler frequency is smaller than 2% of the real part and since it is determined with high uncertainty (Gross, 2007), the imaginary part is neglected.

Table 4.2: Period and damping factor of the Chandler wobble

T_{CW} in solar days	Q_{CW}	σ_0 in radiant per day	References
433.2	63	$0.014\,504 + 0.000\,115$i	Jeffreys (1972)
434.0	100	$0.014\,477 + 0.000\,072$i	Wilson and Haubrich (1976)
434.8	96	$0.014\,451 + 0.000\,075$i	Ooe (1978)
433.3	170	$0.014\,501 + 0.000\,043$i	Wilson and Vicente (1980)
431.7	24	$0.014\,555 + 0.000\,303$i	Lenhardt and Groten (1985)
433.0	179	$0.014\,511 + 0.000\,041$i	Wilson and Vicente (1990)
439.5	72	$0.014\,296 + 0.000\,099$i	Kuehne et al. (1996)
433.7	49	$0.014\,487 + 0.000\,148$i	Furuya and Chao (1996)
[413.0 439.0]		[0.014 312 0.015 214]	Schuh et al. (2001)
433.1	83	$0.014\,507 + 0.000\,087$i	Gross (2004)
431.9	82	$0.014\,548 + 0.000\,089$i	Seitz (2004)

Gross (2007) suggested to use a Chandler period of 433.0 solar days proposed by Wilson and Vicente (1990), as this value results from long time series and a sophisticated maximum Likelihood Monte-Carlo estimator.

Effect of the complex-valued body tide Love number on the axial ELE:

The complex modification of the body tide Love number changes among the Chandler frequency the parameter D_a and therefore the factor k_r. The effective axial body tide Love number $k_{2,s}^{eff}$ is defined as

$$k_{2,s}^{eff} = k_2 + \Delta k_{an} + \Delta k_{ocn,s} \tag{4.23}$$

where Δk_{an} and $\Delta k_{ocn,s}$ account for the anelasticity of the Earth's body and for the oceans. Δk_{an} is complex-valued. Göttl (2013) listed four different effective Love numbers. The factors k_r in Table 4.3 are obtained from the effective Love numbers according to Equations 2.24 and 2.46.
The real parts of the complexed-valued axial factors k_r agree in four decimal places and the imaginary parts are as well negligible. Therefore, the choice of the effective body tide axial Love number has an infinitesimal influence on the estimation of the tensor of inertia. However, neglecting the imaginary parts of Δk_{an} and the Chandler frequency means that the ELE models an Earth having an undamped polar motion.

Effect of core-mantle coupling:

Dickman (2003) pointed out that the core-mantle coupling is handled inhomogeneously in literature (cf. discussion in Subsection 2.2.2). According to Wahr (1983), the effective body tide and load Love numbers have to be multiplied by a factor $\alpha_3 = 0.792$, if mantle-only Love numbers are considered. The theoretical body tide Love number is replaced with the empirical Chandler frequency in the equatorial ELE. The axial factor k_r changes about 0.1%, if a decoupled core is assumed. Therefore, the influence of the core-mantle coupling on the body tide Love number is insignificant. Though, the influence of

Table 4.3: Effect of the complex-valued body tide Love number on the axial ELE

axial $k_{2,s}^{eff}$	complex-valued k_r	References
$0.3566 - 0.0034$i	$0.995\,747 + 0.000\,018$i	Smith and Dahlen (1981), Mathews et al. (2002), Gross (2007)
$0.3537 - 0.0034$i	$0.995\,762 + 0.000\,018$i	Dickman (2003), Mathews et al. (2002), Gross (2007)
$0.3504 - 0.0036$i	$0.995\,779 + 0.000\,019$i	IERS Conventions (2003), Gross (2007)
$0.3520 - 0.0042$i	$0.995\,771 + 0.000\,022$i	Seitz (2004)

the core-mantle coupling on the load Love number has a larger influence. If a fully decoupled core is considered, the tensor elements are about the factor 1.09 larger than the tensor elements resulting from a fully coupled core-mantle model. As a difference of approximately 10% is worth taking a closer look, Subsection 5.1.4 discusses the effects of the core-mantle coupling with respect to available time series.

Brief summary of the sensitivity analysis:

The approximation of the polar motion time derivatives by two different models leads to tensor elements which differ up to 1.8 TU. However, the partly large differences between the two approximations do not show obvious systematics. The factor due to the core-mantle coupling has the second largest effects. In contrast to the approximation of the time derivatives, the assumed core-mantle coupling model has a systematic influence, since the tensor elements, resulting from the difference of the EOP and motion terms, depend linearly on the chosen core-mantle model. Further influences due to different numerical values and models are small and are therefore neglected.
The least-squares adjustment additionally takes the GFC2 and the mass terms into account. The tensor elements resulting from the GFC2 and the mass terms are independent on polar motion time derivatives and the core-mantle coupling. Therefore, the effects of the time derivatives and the core-mantle coupling on the adjusted tensor elements are limited. The finally chosen numerical values for the geophysical constants are listed in Table 4.4.

Table 4.4: Geodetic parameters of the Earth

Constant	Value	Description	Ref.
G	$6.674\,28 \times 10^{-11}\,\mathrm{m^3\,kg^{-1}\,s^{-2}}$	Constant of gravitation	(a)
GM	$3.986\,004\,418 \times 10^{14}\,\mathrm{m^3\,s^{-2}}$	Geocentric gravitational constant	(b)
a	$6\,378\,136.6\,\mathrm{m}$	Equatorial radius of the Earth	(c)
Ω	$7.292\,115 \times 10^{-5}\,\mathrm{rad\,s^{-1}}$	Mean angular velocity	(c)
Λ_0	$86\,400\,\mathrm{s}$	Nominal Length of Day	
$C-A$	$2.6398 \times 10^{35}\,\mathrm{kg\,m^2}$	Difference between largest and smallest principal moments of inertia	(c)
$C-B$	$2.6221 \times 10^{35}\,\mathrm{kg\,m^2}$	Difference between largest and intermediate principal moments of inertia	(c)
A_m	$7.0999 \times 10^{37}\,\mathrm{kg\,m^2}$	Smallest principal moment of inertia of crust and mantle	(d)
C_m	$7.1236 \times 10^{37}\,\mathrm{kg\,m^2}$	Largest principal moment of inertia of crust and mantle	(d)
C_c	$9.1401 \times 10^{36}\,\mathrm{kg\,m^2}$	Largest principal moment of inertia of the core	(d)
ϵ_c	2.546×10^{-3}	Ellipicity of the core's surface	(d)
n_0	0.155 05	Factor due to change in the moment of inertia caused by the purely radial component of the rotational potential	(e)
k_2	0.298	Degree-2 body tide Love number of the Earth	(f)
k_2'	-0.305	Degree-2 load Love number of the Earth	(f)
Δk_{an}	-0.011	Modification of the degree-2 Love numbers due to mantle anelasticity; (imaginary part is neglected)	(f)
$\Delta k_{ocn,s}$	0.043 228	Modification of the degree-2 body Tide Love number due to ocean (axial component)	(g)
α_3	0.792	Factor modifying the degree-2 load Love number of the Earth due to core-mantle coupling	(h)
T_{CW}	433.0 days	Chandler period	(i)

References: (a) Mohr et al. (2008), (b) Ries et al. (1992), (c) Groten (2004), (d) Mathews et al. (1991), (e) Dahlen (1976), (f) Wahr (2005), (g) Gross (2007), (h) Wahr (1983), (i) Wilson and Vicente (1990)

5. Results

5.1. Data description

5.1.1. Earth Orientation Parameters

The IERS provides the *EOP 08 C04* time series, which describes the coordinates of the CIP in the ICRF and in the ITRF2008. *EOP 08 C04* also contains the deviations of the instantaneous rotation velocity from the mean rotation velocity by providing the difference UT1–UTC and LOD, respectively. Bizouard and Gambis (2010) described the derivation of *EOP 08 C04* and listed the used models. According to Subsection 2.1.2, the CIP separates by definition the daily and subdaily precession/nutation from polar motion (cf. Figure 2.1). Since this dissertation is limited to long periodic movements, precession/nutation parameters are not considered, and the Earth rotation vector is described by LOD and polar motion. The EOP include long periodic tidal signals. As the validation is performed in a tide free system, the tidal influences are removed according to Appendix A (IERS Conventions, 2010).
Two other EOP time series exist. The Institut Géographique National provides the ITRF together with consistent *EOP ITRF* time series on behalf of the IERS. Altamimi et al. (2007) described the determination of the ITRF2005 extensively. This description was updated for the ITRF2008 in Altamimi et al. (2011). Here, LOD values are determined by VLBI only. The limitation on VLBI avoids contamination of the VLBI estimates by biases caused by GNSS (Altamimi et al., 2011; Ray, 2009). As VLBI measurements are not performed continuously, *EOP ITRF* does not contain daily LOD values and is not considered for further analyses in this dissertation. The differences between *EOP ITRF* and *EOP 08 C04* polar motion do not exceed ±0.2 mas in the years from 2000 to 2008. This corresponds to ±0.01 TU according to Table 4.1.
The Deutsches Geodätisches Forschungsinstitut (DGFI) proposes the *EOP DTRF2008* time series (Seitz et al., 2012). This time series is based on the models of the older IERS Conventions (2003) and is obtained similar to the ITRF2005D reference frame, proposed in Angermann et al. (2009). The differences between *EOP DTRF2008* and *EOP 08 C04* have been analyzed in the years from 2000 to 2008. The differences do not exceed ±0.4 mas (±0.02 TU) in polar motion and ±0.05 ms per day (±2.5 TU) in LOD. The differences are due to different input data, different weighting of the contributing techniques and different parametrization of the ITRF station coordinates (personal communication with M. Seitz, July 2012). If the differences of the two time series are analyzed in the frequency domain, the largest LOD amplitudes are at periods of approximately 59 days, one year, 44 days and 14 days. If the LOD time series are bandpass-filtered (cutoff periods of 60 days and three years, c.f. Section 4.1) before the comparisons, the differences between the LOD time series do not contain the 44 days and 14 days periods. Then, the differences of the filtered LOD time series remain below ±0.02 ms (±1 TU). Göttl (2013) gave a more detailed description of the three EOP time series and included more background information.

5.1.2. Gravity field coefficients

Gravity Recovery and Climate Experiment (GRACE)

GRACE is a joint project of the National Aeronautics and Space Administration (NASA) in the United States and the Deutsches Zentrum für Luft- und Raumfahrt (DLR) in Germany and determines the time variable gravity field. The project management and system engineering activities are carried out by the Jet Propulsion Laboratory (JPL). GRACE consists of two identical low Earth orbiters launched in March 2002 and orbiting about 220 km apart in a nearly spherical, polar orbit of initially 500 km above the Earth. Despite of the previously intended life time of five years, the tenth anniversary of GRACE has been celebrated in March 2012. A K-Band-microwave beam tracks the distance between the two satellites with micrometer accuracy. The satellites are additionally equipped with Global Positioning System (GPS) antennas and accelerometers to measure non-gravitational accelerations. If the gravity changes beneath the satellites, the orbital motion of each satellite is changed causing variations of the distance between the satellites. A combined processing of the measured non-gravitational accelerations, the GPS data, the K-Band ranges and further sensors leads to a time variable gravity field with a high spatial resolution up to degree/order 120. The GRACE data are processed in three centers, at the University of Texas Center for Space Research (CSR), the JPL and the GFZ. Further information on GRACE can be found in Tapley et al. (2004) and Schmidt (2007).

The time variable gravity field coefficients are determined by a least-squares adjustment with respect to a background gravity field which considers

- a static background gravity field,
- tidal acceleration caused by Sun, Moon and planets and obtained from models (including atmospheric and oceanic tides, tidal deformation of the Earth and loading effects),
- rotational deformation,
- non-tidal, aperiodic mass variations of atmosphere and oceans, the Atmospheric-Ocean-De-Aliasing-products (Flechtner, 2007b),
- non-gravitational forces (friction of the higher atmosphere, the solar radiation pressure and the Earth albedo), measured by the accelerometers and
- relativistic corrections, accounting for the deviation of Newton's mechanics from Einstein's relativity theory.

Based on the background gravity field, the orbits of the two satellites are precisely obtained by numerical integration. According to Mayer-Gürr (2006), the numerical integration of Newton's dynamic equation is formulated either as initial value problem (Volterra's integral equation) or as boundary value problem (Fredholm's integral equation of second art). Since the micrometer accuracy of the K-Band measurements is significantly more accurate than the centimeter accuracy of the GPS-positions, the functional model of the least-squares adjustment has to separate these two types of measurements (Mayer-Gürr, 2006). The high accuracy of the K-Band ranges allows to determine the gravity field with a high spatial resolution. Since the satellites approximately orbit along the meridians, the microwave sensor errors act in north-south direction. Thus, the sensor errors, combined with the mission geometry, cause north-south stripes in the potential maps and derived equivalent water height maps. Various authors proposed filters for the reduction of the stripes with respect to the smallest possible loss of signals, e.g. Kusche (2007), Wouters and Schrama (2007), Davis et al. (2008) and Klees et al. (2008). As the two satellites orbit a short distance apart on a global scale, GRACE is less sensitive to gravity field coefficients of low degrees. However, the coefficients of low degrees can still be determined, as the GPS-positions of the satellites are available. Though, the delivered formal errors for coefficients of low degrees do usually not reflect the lesser accuracy of the GPS-positions and are therefore too optimistic in most cases.
The non-tidal redistribution of atmospheric and oceanic masses is considered by the Atmospheric-Ocean-De-Aliasing-products (AOD1B). The atmospheric contribution is obtained from the European Center for Medium-range Weather Forecast (ECMWF) and the oceanic mass redistribution is modeled by the Ocean Model for Circulation and Tides (OMCT). Subsection 5.1.3 describes the atmospheric and oceanic models in more detail. The GRACE data centers provide gravity field coefficients, which describe an Earth without the non-tidal, aperiodic masses of atmosphere and oceans (GSM products). The non-tidal, aperiodic masses of atmosphere and oceans are additionally provided in form of further gravity field coefficients (GAC products). The sum of the GSM und GAC products describes a gravity field which includes the complete atmospheric and oceanic masses. The sum of the GRACE GSM and GAC products is validated here.
Apart from the three official GRACE data centers, two further groups, the Institut für Geodäsie und Geoinformation (ITG) and the Groupe de Recherche de Géodésie Spatiale (GRGS), deliver GRACE gravity fields. The five solutions differ in various details. The main differences are shortly recapitulated as follows: The gravity field solution *CSR R04* is unconstrained, but the GRACE Technical Note No 5 suggests to replace the C_{20} coefficient with SLR coefficients. The gravity field solution *JPL R04* is obtained by a two step approach. First, a subset of orbit and GPS clock parameters is solved without adjusting gravity. In the next step, the subset constrains a second adjustment which determines the gravity field coefficients. This approach aims to the reduction of the stripes and to a more reliable determination of C_{20}, but leads to leakage effects in regions where a large signal is near areas with low signals, e.g. North Atlantic near Greenland (personal communication M. Watkins, April 2012). The gravity field solution *GFZ R04* is unconstrained. *GRGS R02* uses the barotropic MOG2D ocean model instead of the baroclinic AOD1B ocean model and provides a higher temporal resolution as the other

Table 5.1: Overview over background models and processing of GRACE and SLR gravity fields

	CSR R04	*JPL R04*	*GFZ R04*	*GRGS R02*	*ITG 2010*	*CSR SLR R04*
Static gravity field						
Static gravity field	GIF22a	GIF22a	EIGEN-GL04C	EIGEN-GRGS.RL02.MEAN-FIELD	Grace ITG03s	GGM02C
Tidal reference	zero tide	zero tide	tide free	tide free	zero tide	zero tide
Tidal forces of Sun, Moon and planets						
Solid Earth tides	IERS 2003	IERS 2003	IERS 2003	IERS 2003	IERS 2003	IERS 2003
Planetary ephemerides	DE-405	DE-405	DE-405	DE-403	DE-405	unknown
Oceanic tides	FES 2004	FES 2004	FES 2004	FES 2004	EOT08a	FES 2004
Atmospheric tides	none	none	Biancale and Bode (2006)	none	none	none
Polar tides (rotational deformation)						
Solid Earth	IERS 2003	IERS 2003	IERS 2003	IERS 2003	IERS 2003	IERS 2003
Oceans	Desai (2002)	Desai (2002)	Desai (2002)	Desai (2002)	Desai (2002)	Desai (2002)
Short periodic mass variations						
Atmosphere	AOD1B	AOD1B	AOD1B	ECMWF	AOD1B	AOD1B
Oceans	AOD1B	AOD1B	AOD1B	MOG2D	AOD1B	AOD1B
Non-tidal accelerations						
Non-tidal accelerations	GRACE accelerometer	GRACE accelerometer	GRACE accelerometer	GRACE accelerometer	GRACE accelerometer	models
Relativistic effects						
Relativistic effects	IERS 2003	IERS 2003	IERS 2003	IERS 2003	IERS 2003	IERS 2003
Reference frames						
Transformation from inertial to Earth-fixed reference frames	IERS 2003	IERS 1996	IERS 2003	IERS 2003	IERS 2003	IERS 2003
Processing of the data						
numerical orbit integration	initial value problem	initial value problem	initial value problem	initial value problem	boundary value problem	unknown
Constraints and remarks	replacement of GRACE C_{20} coefficients by SLR coefficients recommended (Technical Note No. 5)	GPS clocks and orbits are solved first and constrain the gravity field determination	none	constrained gravity field and stabilization by LAGEOS-1 and 2	none	SLR only (LAGEOS-1 and 2, Starlette, Stella and Ajisai)
Temporal resolution	monthly	monthly	monthly	10 days	monthly	monthly
References to the gravity field solution						
References	Bettadpur (2007)	Watkin and Dah Ning (2007)	Flechtner (2007a)	Bruinsma et al. (2010)	Mayer-Gürr (2006)	Cheng and Tapley (2004)

Further references: IERS 1996: IERS Conventions (1996); IERS 2003: IERS Conventions (2003); IERS 2010: IERS Conventions (2010); EIGEN-GL04C: Förste et al. (2008); Grace ITG03s: Mayer-Gürr et al. (2010); GGM02C: Tapley et al. (2005); FES 2004: Lyard et al. (2006); EOT08a: Savcenko and Bosch (2008); AOD1B: Flechtner (2007b); MOG2D: Carrére and Lyard (2003)

groups. Since the higher temporal resolution means that a reduced number of satellite ground tracks is available, the solution is constrained. The background gravity field coefficients of degrees and orders larger than 30 are introduced as pseudo-observations with given degree- and order-dependent variances. Furthermore, the gravity field coefficients of low degrees are stabilized by taking SLR range observations into account (cf. next paragraph). The gravity field solution *ITG 2010* is determined with the EOT08a ocean tide model instead of the FES2004 model. Beyond that, no special constraints are taken into account. The background models, the references to the models and some further details of the five GRACE solutions are summarized in Table 5.1.
The official GRACE data centers have recently published new releases of the gravity fields (Release 05). The new releases are based on improved AOD1B products and improved knowledge of the relative alignment of the different satellite sensors. The new releases 05 show reduced north-south stripes and an improved estimation of C_{20} (Bettadpur, 2012). Nevertheless, the SLR estimation of C_{20} is still better than the new *CSR R05*, whereas *CSR R05* provides a better estimation of C_{21}, S_{21}, C_{22} and S_{22} (Bettadpur, 2012). The releases 05 are not considered, as the background models of the older releases 04 are more consistent to the background models of *ITG 2010* and *GRGS R02*. The Institut für Geodäsie und Geoinformation additionally provides daily gravity fields by using a smoothing Kalman filter which considers spatial and temporal correlations (Kurtenbach et al., 2012). The GFZ additionally delivers weekly gravity fields with a smaller spatial resolution (Schmidt et al., 2007). Both daily and weekly gravity fields are disregarded. The limitation to one time series per data center avoids the double weight of processing strategies on the combined adjustment.

Satellite Laser Ranging (SLR)

SLR determines gravity fields of low temporal resolution by range measurements from globally distributed, Earth-fixed ground stations to satellites. The satellites are passive spherical satellites with a dense core and retroreflectors on their surface. The range is measured with millimeter accuracy by the travel time of laser pulses to the reflectors and back. The LAGEOS-1 and 2 satellites were launched in 1976 and 1992, in orbits with an altitude of approximately 5900 km and inclinations of 110° and 54°. The smaller satellites Starlette and Stella orbit in an lower altitude of approximately 800 km since 1975 and 1993. They have inclinations of 50° and 99°. The Japanese satellite Ajisai orbits in an altitude of 1500 km with an inclination of 50° since 1986. Further information can be found on `http://ilrs.gsfc.nasa.gov/`.
The gravity field is determined analogously to GRACE. The satellite orbits are integrated numerically with respect to a background gravity field. Since the spherical satellites have an optimal surface-mass ratio, the non-gravitational accelerations are described with sufficient accuracy by models (Cheng and Tapley, 2004). As the SLR satellites orbit the Earth in higher altitudes than the GRACE twin-satellites, a lower spatial resolution of the gravity fields is reached. Table 5.1 summarizes the background models and processing details of the GRACE gravity fields and *CSR SLR R04*. *CSR SLR R04* is obtained by using the same background models as *CSR R04*. The C_{20} values in the GRACE Technical Note No 5 results from *CSR SLR R04*.

5.1.3. Excitation functions

The mass redistributions of the Earth's atmosphere, oceans and hydrology are calculated by geophysical models. Based on the models, data fields with a large number of parameters, e.g. velocity, temperature and pressure, are calculated in threedimensional grids covering the Earth. The models differ in the spatial resolution of the grids and in the temporal resolution. Most models are constrained by other models and/or assimilate observed data.
The excitation functions of the specific subsystem and model are obtained by the numerical integration of the grid data according to Equations 2.53 and 2.54. If the excitation functions are given as dimensionless EAMF, they are transformed into angular momentum functions (unit: $\mathrm{kg\,m^2\,s^{-1}}$). The transformation is necessary, as the EAMF from different sources might differ in details (Dickman, 2003). Consistent transformations are ensured by evaluating the definitions of the EAMF and the used numerical values of the geophysical constants. The motion terms of the excitation functions equal the relative angular momentum h_x, h_y and h_z. The mass terms contain the tensor variations c_{xz}, c_{yz} and c_{zz} multiplied by the mean rotation velocity Ω. Some models are briefly described in following paragraphs.

Atmospheric NCEP/NCAR Reanalysis model

The National Centers for Environmental Prediction (NCEP) and the National Center for Atmospheric Research (NCAR) have established the NCEP/NCAR Reanalysis project to produce atmospheric fields which support the needs of research and climate communities (Kalnay et al., 1996). The NCEP/NCAR Reanalysis project collects atmospheric data from various sources, e.g. from sensors on ships, weather stations, buoys, airplanes and satellites. The quality of the data is analyzed, and the data are assimilated into a model which remains constant over the entire reanalysis period. This results in a threedimensional grid of data with a horizontal resolution of 210 km and 28 vertical layers and with a temporal resolution of six hours (Salstein et al., 1993; Zhou et al., 2006).
The atmospheric excitation functions depend on assumptions of oceanic reactions on pressure variations. The so called Inverted Barometer (IB) hypothesis assumes that the oceans react with sealevel depressions in areas with high atmospheric pressure and with sealevel rise in areas with low pressure. Oceans and atmosphere are assumed to be in an equilibrium state. If the IB hypothesis is assumed, the Earth's rotation does not react on local pressure changes, but rather on changes of the mean pressure over the oceans of the entire Earth (Salstein et al., 1993). The NCEP/NCAR excitation functions are calculated assuming both the IB and the Non-IB hypothesis. The ocean model ECCO implies the IB hypothesis (Gross, 2009).

Atmospheric ECMWF model

The European Center for Medium-range Weather Forecast (ECMWF) provides atmospheric models which assimilate measured data. The ERA-Interim reanalysis model provides grids with a horizontal resolution of 79 km and 60 vertical layers. A detailed description of ERA-Interim is found in Dee et al. (2011). Although ERA-Interim data are provided with a short latency, the delay is unacceptable for some applications. Therefore, the ECMWF also provides operational forecast data with a spatial resolution of 79 km and 91 vertical layers. Dee et al. (2011) described the differences between the operational forecast model and ERA-Interim. Since the forecast model is occasionally updated and the data are not reprocessed after updates, they are in contrast to ERA-Interim not strictly consistent over time. However, the GRACE AOD1B products are based on the operational ECMWF forecast data (Flechtner, 2007b).

Oceanic ECCO model

Oceanic currents and the resulting bottom pressure of the oceans are modeled by Estimating the Circulation and Climate of the Ocean (ECCO). ECCO is based on the MIT ocean general circulation model Marshall et al. (1997a,b). It spans the globe between 80° S to 80° N. The latitudinal grid spacing differs from 0.3° at the equator to 1° at the poles and the longitudinal grid is spaced with 1°. The model possesses 46 vertical layers and is forced with wind stress, surface heat flux and evaporation-precipitation fields from the NCEP/NCAR Reanalysis project. Atmospheric surface pressure fields do not force the model (baroclinic model). Further information on ECCO is available in Stammer et al. (2003).
The Special Bureau for the Oceans of the IERS Geophysical fluids center provides two different excitation functions, ECCO_kf079 and ECCO_kf080. In contrast to ECCO_kf079, altimetric sea surface height measurements are assimilated into ECCO_kf080. Beyond that, both time series are obtained from the same model configuration and the same forces.

Oceanic OMCT model

The Ocean Model for Circulation and Tides (OMCT) (Thomas, 2002) is an advancement of the climatological Hamburg Ocean Primitive Equation Model (Drijfhout et al., 1996; Wolff et al., 1997). The ocean model has a lower spatial resolution than ECCO (horizontal resolution of 1.875 degree in latitude and longitude and 13 vertical layers). The atmospheric forcing of OMCT includes wind stress, surface pressure as well as heat and freshwater fluxes. Continental freshwater fluxes, provided by e.g. LSDM, can optionally be taken into account. OMCT is alternatively forced by ERA-Interim or by operational ECMWF forecast data and does not assimilate altimeter data. Dobslaw et al. (2010) gave a compact overview over consistent ECMWF, OMCT and LSDM models.

Table 5.2: Definitions of the integral excitation functions

Integral excitation function	=	Atmospheric Angular Momentum functions	+	Oceanic Angular Momentum functions	+	Hydrological Angular Momentum functions
Interim GFZ	=	ERA-Interim	+	OMCT driven by ERA-Interim and LSDM	+	LSDM driven by ERA-Interim
op. GFZ	=	operational ECMWF	+	OMCT driven by operational ECMWF and LSDM	+	LSDM driven by operational ECMWF
non-ass. JPL	=	NCEP/NCAR Reanalysis model	+	ECCO driven by NCEP/NCAR Reanalysis model, no further data assimilation	+	none
ass. JPL	=	NCEP/NCAR Reanalysis model	+	ECCO driven by NCEP/NCAR Reanalysis model, assimilation of altimeter measurements	+	none

Hydrological LSDM model

The continental hydrology is simulated by the Land Surface Discharge Model (LSDM) (Dill, 2008). The model simulates global water storage variations of surface water in rivers, lakes, wetlands, groundwater, and soil moisture as well as water stored in snow and ice. The model is discretized on a regular 0.5° global grid and is integrated with a 24 hour timestep. LSDM is forced with precipitation, evaporation and temperature from ERA-Interim and operational ECMWF forecast data, respectively. LSDM is not part of the GRACE AOD1B products, as an inclusion of the continental hydrology is not expected to improve monthly GRACE gravity solutions (Dobslaw and Thomas, 2007). The hydrological signal remains present in the GRACE GSM products. Therefore, the GSM+GAC product contains the total masses of all subsystems.

Integral excitation functions

The observed EOP and gravity field coefficients reflect the sum of mass redistributions in all subsystems. Therefore, only the sum of consistent excitation functions can be validated. The described models provide four possible consistent integral excitation functions, defined in Table 5.2.
The integral excitation functions of the GFZ consider hydrology, in contrast to the JPL excitation functions. *Interim GFZ* is forced by ERA-Interim and *op. GFZ* by operational ECMWF data. The differences of both bandpass-filtered integral GFZ excitation functions do not exceed ±0.5 TU in the equatorial mass and motion terms and ±2 TU in the axial mass and motion terms. Both bandpass-filtered integral JPL excitation functions show differences of ±0.5 TU maximum in the equatorial and axial mass and motion terms.
A comparison of all four possible integral excitation functions reveals differences but no significant pattern in the mass terms. Whereas both equatorial JPL motion terms clearly show larger variations than both GFZ excitation functions. Both axial GFZ motion terms show larger annual variations than both JPL excitation functions. The motion terms of GFZ and JPL differ more than the two GFZ and the two JPL time series among each other.

5.1.4. Comparison of preliminary tensor elements obtained from the time series

Three of the six elements of the tensor of inertia can be redundantly determined either by the difference of the EOP and the motion terms, by the mass terms or by the GFC2. Preliminary values for the tensor of inertia are calculated from each time series, in order to obtain a first, summarizing overview over the time series. Representative, monthly epoch values for the daily time series (EOP and excitation functions) are obtained by cubic splines. The spline coefficients are adjusted by assuming uncorrelated observations with equal standard deviations. Note, since this subsection aims to a first overview, a sophisticated adjustment is not necessary at this point. The preliminary spline adjustment does not take relations between different time series into account. The adjustment model described in the previous chapter is applied in Section 5.2. Monthly epoch values of the daily time series are calculated by evaluating the

adjusted spline coefficients at the midpoint of each spline. The six tensor elements cannot be uniquely determined by five GFC2. Therefore, the underdetermined trace of the tensor of inertia is solved by taking the tensor trace constraint in Equation 2.66 into account. Due to this constraint, the tensor element c_{zz} solely depends on the gravity field coefficient C_{20}.
Figure 5.1 illustrates the preliminary tensor elements. The first column shows the tensor elements resulting from the difference of the EOP and motion terms. The tensor elements obtained from the mass terms are given in the second column. The third column presents the tensor elements resulting from the GFC2. The tensor elements c_{xz} (first row) show an annual period with a small amplitude in some of the time series (mass terms and some of the gravity field coefficients), whereas other preliminary solutions (EOP minus motion terms, *ITG 2010*) do not show obvious annual periods in c_{xz}. In contrast to c_{xz}, the tensor elements c_{yz} (second row) and c_{zz} (third row) clearly contain annual periods. The smaller variations of the equatorial tensor element c_{xz} compared to the tensor element c_{yz} are mainly caused by the unequal distribution of continents and oceans masses over the Earth.

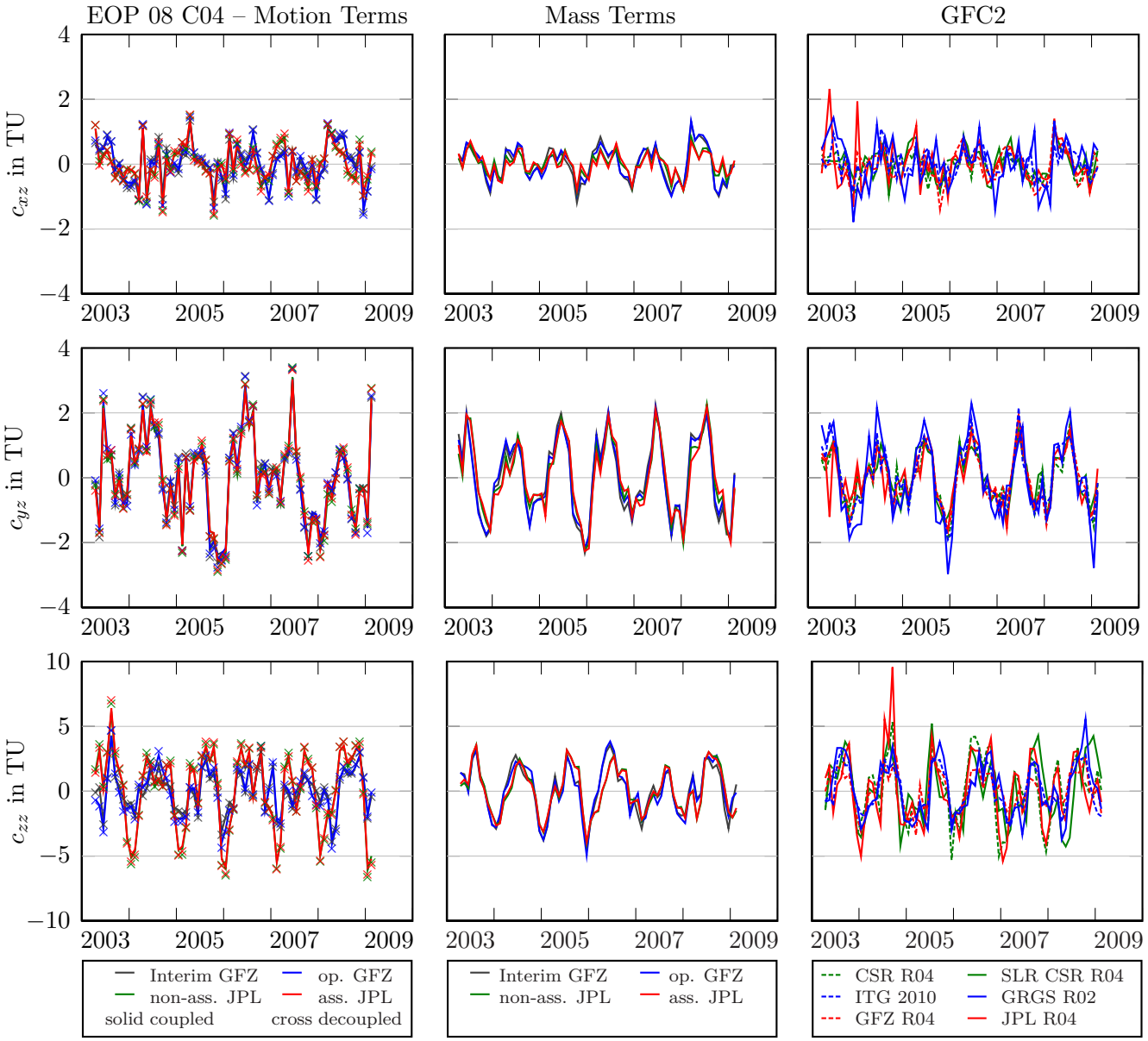

Figure 5.1: Preliminary elements of the tensor of inertia are presented (c_{xz} first row, c_{yz} second row and c_{zz} third row). The first column contains the tensor elements resulting from the difference of the EOP 08 C04 and the motion terms. The solid lines display the tensor elements obtained by assuming a coupled core and mantle, whereas the crosses denote tensor elements obtained from a decoupled Earth model. The second column illustrates the tensor elements calculated from the mass terms. Tensor elements resulting from the GFC2 are given in the third column.

The tensor elements resulting from the difference of the EOP and motion terms show a significantly noisier behavior compared to the tensor elements obtained from the mass terms. The noisy behavior is caused by the spline approximation of the polar motion time derivatives (cf. Figure 4.5 and discussion in Subsection 4.3.2). The two GFZ excitation functions and the two JPL excitation functions show small differences in the resulting tensor elements. The axial tensor elements resulting from the differences between LOD and both GFZ motion terms contain smaller annual amplitudes than those tensor elements resulting from both JPL motion terms.
Dickman (2003) discussed the effect of the core-mantle coupling. Depending on the assumed core-mantle coupling, the tensor of inertia obtained from the EOP and the motion terms differ about approximately 10% (cf. Subsection 4.3.3). The tensor elements in the first column of Figure 5.1 are calculated by assuming both, the fully coupled and the completely decoupled model. The solid lines describe the coupled Earth model and the crosses denote the uncoupled model. The equatorial tensor elements obviously support the coupled model more than the decoupled model. The axial tensor elements resulting from the difference of LOD and the axial JPL motion terms support the coupled model as well. In contrast to that, the axial tensor elements resulting from GFZ motion terms do not indicate a specific coupling model. As mentioned before, the chosen model for the core-mantle coupling changes the tensor elements by a multiplicative factor and is therefore a potential source for inconsistencies. The tensor elements resulting from the mass terms agree well. The time series resulting from the GFC2 generally agree with the mass terms but show larger variations than the mass terms.

5.2. Mutual validation of EOP, excitation functions and GFC2

5.2.1. A priori setting of the adjustment model and adjustment

Preprocessing of the data

This section performs the mutual validation of one EOP time series, two different excitation functions and six different GFC2 time series. As mentioned before, the three available polar motion time series show small differences. If all three EOP time series are considered, the differences between the EOP and motion terms obtain a high weight, which is not in relation to the comparatively small accuracy of the motion terms. Note, only the difference between the EOP and the motion terms can be validated. Therefore, only one EOP time series is considered. The tides are removed from the chosen *EOP 08 C04* time series before the filter is applied (cf. Appendix A). The four excitation functions defined in Table 5.2 depend on two geophysical models. To avoid that the geophysical models are weighted twice, one set of excitation functions is considered per each geophysical model. The GRACE AOD1B products are obtained from the operational atmospheric ECMWF forecast data and consistent OMCT data (Flechtner, 2007b). Therefore, the excitation functions *op. GFZ* are chosen. As *op. GFZ* do not assimilate altimeter data, the excitation functions *non-ass. JPL* are additionally considered.
Though the six different gravity solutions are obtained from the same original data and/or models, the GFC2 obviously differ due to various details in the models and weighting (Figure 5.1). As the differences are comparatively large, the six GFC2 time series in Table 5.1 are considered. The time series have a temporal resolution of one month except *GRGS R02* with a temporal resolution of ten days. *GRGS R02* is downsampled to a monthly temporal resolution by calculating weighted averages. The weights are determined according to the number of days belonging to the month. Some gaps arise in the monthly GRACE time series due to satellite orbits causing repeated ground tracks. The poor orbit configurations impede the determination of the gravity field. The gaps are filled by linear interpolation before the filter is applied.
The time series are filtered according to Section 4.1 to reduce known inconsistencies before the adjustment. The daily EOP and excitation functions are bandpass-filtered with the cutoff frequencies of $1/(60 \text{ days})$ and $1/(3 \cdot 365 \text{ days})$. The monthly GFC2 time series are highpass-filtered with the cutoff frequencies of $1/(3 \cdot 12 \text{ months})$. Note, absolute values of the time series cannot be validated due to the filter. The validation is limited to relative variations. The data of the six first and the six last months are discarded to avoid effects caused by run-in effects of the filter. The remaining time series cover a period of 71 months between April 2003 and February 2009. If the filters are not applied before, the tensor elements obtained by different time series are biased and the results are deteriorated. Heiker et al. (2012) did not apply the filter before the mutual validation. The unknown parameter vector in Heiker

et al. (2012) was extended to account for biases between the time series, which were estimated within the least-squares adjustment. The influence of the filters is discussed more detailed in Subsection 5.3.1.

Least-squares adjustment

The functional model is set up according to Subsection 4.2.1. The ELE assumes a fully coupled core-mantle model. Six unknown elements of the tensor of inertia and one spline per daily time series are estimated per each of the 71 epoch. Each of the 15 daily time series ($3 \times$ *EOP 08 C04*, $6 \times$ *op. GFZ*, $6 \times$ *non-ass. JPL*) is modeled by 74 unknown spline coefficients (equivalent to $74 \cdot 15 = 1110$ unknowns). The daily time series contain 32 445 observations in total. The observed $71 \cdot 5 = 355$ GFC2 directly depend on the tensor of inertia with $71 \cdot 6 = 426$ unknown tensor elements. The model is constrained by the ELE ($71 \cdot 3 = 213$ constraints), by the relation between the mass term and the tensor of inertia ($71 \cdot 3 = 213$ constraints) and by the 71 tensor trace constraints (Rochester and Smylie, 1974). The least-squares adjustment considers 32800 observations, 497 constraints and 1536 unknowns in total. Hence, the redundancy amounts to 31 761.
The a priori stochastic model for the daily EOP and excitation functions is obtained according to Subsection 4.2.2. The VCM of the daily parameters are described by band-diagonal Toeplitz matrices, composed of analytical auto- and crosscorrelation functions. As the monthly time series of the GFC2 are too short for the calculation of meaningful auto- and crosscorrelation functions, the a priori stochastic model is composed of given stochastic information. *ITG 2010* is delivered with a complete VCM. The other GFC2 are provided with formal errors / standard deviations without any information about covariances. Therefore, their a priori VCM are diagonal matrices assuming uncorrelated observations.
Nine equatorial variance components ($1 \times$ polar motion, $2 \times h_x/h_y/\Omega c_{xz}/\Omega c_{yz}$, $6 \times C_{21}/S_{21}/C_{22}/S_{22}$) and nine axial variance components ($1 \times$ LOD, $2 \times h_z/\Omega c_{zz}$, $6 \times C_{20}$) are estimated. Additionally, one covariance component is estimated for the covariance between C_{20} and $C_{21}/S_{21}/C_{22}/S_{22}$ of the *ITG 2010* time series.

Iterations

The least-squares adjustment algorithm, described in Figure D, delivers adjusted residuals for all time series and a posterori stochastic models. The matrix $\boldsymbol{S}$ (cf. Equation 3.42) is estimated by the SMCTE, which draws one single sample for each trace. Koch and Kusche (2002), Kusche and Klees (2002) and Kusche (2003) proposed a Cholesky decomposition. Since the extended SMCTE allows the estimation of traces of asymmetric matrices and since inversions are replaced by a fast linear solver, provided by the used computer software Matlab, a Cholesky decomposition is not necessary here (cf. Section 3.3). Figure 5.2 illustrates the adjusted VCC. The VCC of the first two iterations are not shown, as they partly have values larger than 100. If the VCC are estimated correctly, they converge to $\sigma_j = 1$ with $j = 1, \ldots, 19$. The adjusted σ_j vary around one in each iteration step, due to the stochastic characteristic of the SMCTE. 50 iterations are calculated in total, in order to illustrate the stochastic effect of the SMCTE.
The variance components of the daily time series show smaller variations than the variance components of the GFC2 and the covariance component of the *ITG 2010* time series. Furthermore, the variations of the axial C_{20} variance components are larger than the variations of the equatorial $C_{21}/S_{21}/C_{22}/S_{22}$ variance components. According to Equation 3.61, the vector $\boldsymbol{B}\boldsymbol{V}_i\boldsymbol{B}^\mathsf{T}\boldsymbol{u}_k$ contains one non-zero vector element per month in case of a C_{20} time series, whereas this vector contains approximately four non-zero vector elements per month in case of $C_{21}/S_{21}/C_{22}/S_{22}$ time series and approximately 30 non-zero vector elements per month in case of daily time series. (Note, here holds: $\boldsymbol{B} = \boldsymbol{I}$.) The variations of the adjusted variance components obviously depend on the number of the elements in the stochastic vector $\boldsymbol{B}\boldsymbol{V}_i\boldsymbol{B}^\mathsf{T}\boldsymbol{u}_k$ which are unequal to zero. Nevertheless, the covariance component surprisingly shows a clearly larger variation than the C_{20} variance components. The reason for this behavior is not completely understood. The condition number of the a priori matrices $\boldsymbol{V}_i$ might play a role. The matrix $\boldsymbol{V}_{Covariance}$, describing

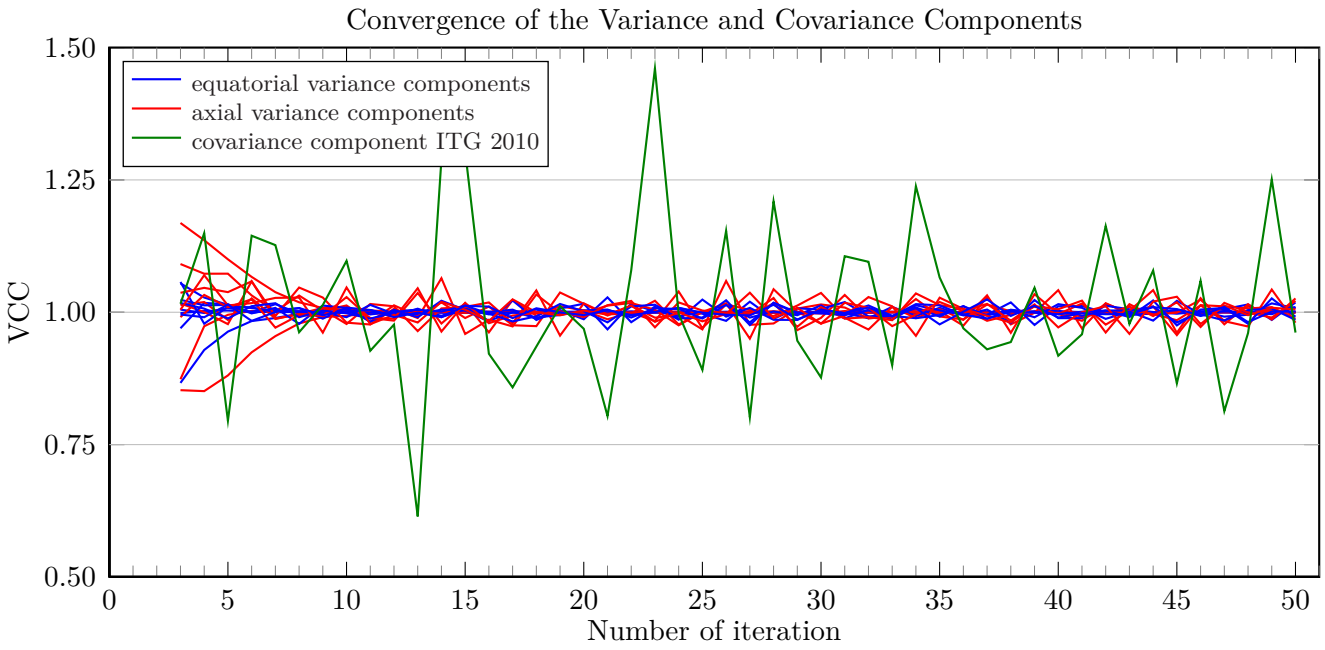

Figure 5.2: The estimated VCC since the third iteration are shown.

the correlation between C_{20} and $C_{21}/S_{21}/C_{22}/S_{22}$, has following structure in each epoch j

$$\boldsymbol{V}^{j}_{Covariance} = \begin{bmatrix} 0 & \sigma^{j}_{C_{20}\,C_{21}} & \sigma^{j}_{C_{20}\,S_{21}} & \sigma^{j}_{C_{20}\,C_{22}} & \sigma^{j}_{C_{20}\,S_{22}} \\ \sigma^{j}_{C_{20}\,C_{21}} & 0 & 0 & 0 & 0 \\ \sigma^{j}_{C_{20}\,S_{21}} & 0 & 0 & 0 & 0 \\ \sigma^{j}_{C_{20}\,C_{22}} & 0 & 0 & 0 & 0 \\ \sigma^{j}_{C_{20}\,S_{22}} & 0 & 0 & 0 & 0 \end{bmatrix}. \tag{5.1}$$

According to the last equation, a rank defect of three occurs per each epoch. A second possible reason for the poorer convergence is discussed in Subsection 5.2.3.

5.2.2. Adjusted residuals

The least-squares adjustment results in consistent, adjusted time series. The residuals describe the difference between the original observations and the adjusted observations. Therefore, the residuals contain the inconsistencies of the time series. The residuals of the EOP, the excitation functions and the GFC2 are analyzed by means of amplitude spectra to reveal systematic periods. Furthermore, the residuals affect the adjusted VCC via the vector $\boldsymbol{q}$ (cf. Equation 3.41). Large residuals lead to large a posteriori standard deviations and indicate a poorer degree of consistency.

Residuals of the EOP

Figure 5.3 shows the residuals of the EOP in the time domain and the frequency domain. The EOP residuals are small compared to the residuals of the other time series. The polar motion residuals have a maximal value of ±3 mas, which corresponds to ±0.14 TU, according to Table 4.1. The maximal LOD residuals amount to ±0.1 ms (±0.5 TU). The largest amplitudes of the EOP residuals are associated with periods of about two months corresponding to the cutoff frequency of the filter. These periods are artifacts, caused by the filter and leakage effects. The Nyquist-Shannon theorem (Shannon, 1984) states that a signal with a given frequency f can be reconstructed from an infinite sequence of samples, if the sampling rate exceeds $2f$ samples. That means an annual signal can be detected, if it is measured at least twice per year. Thus, as monthly GFC2 are considered, frequencies about six cycles per year and higher cannot be validated mutually. That is the reason, that the daily time series are filtered with a cutoff period of 60 days. Since the months contain a different number of days and the filters for daily and monthly time series are therefore not exactly equal, additional leakage effects contribute to the artifacts.

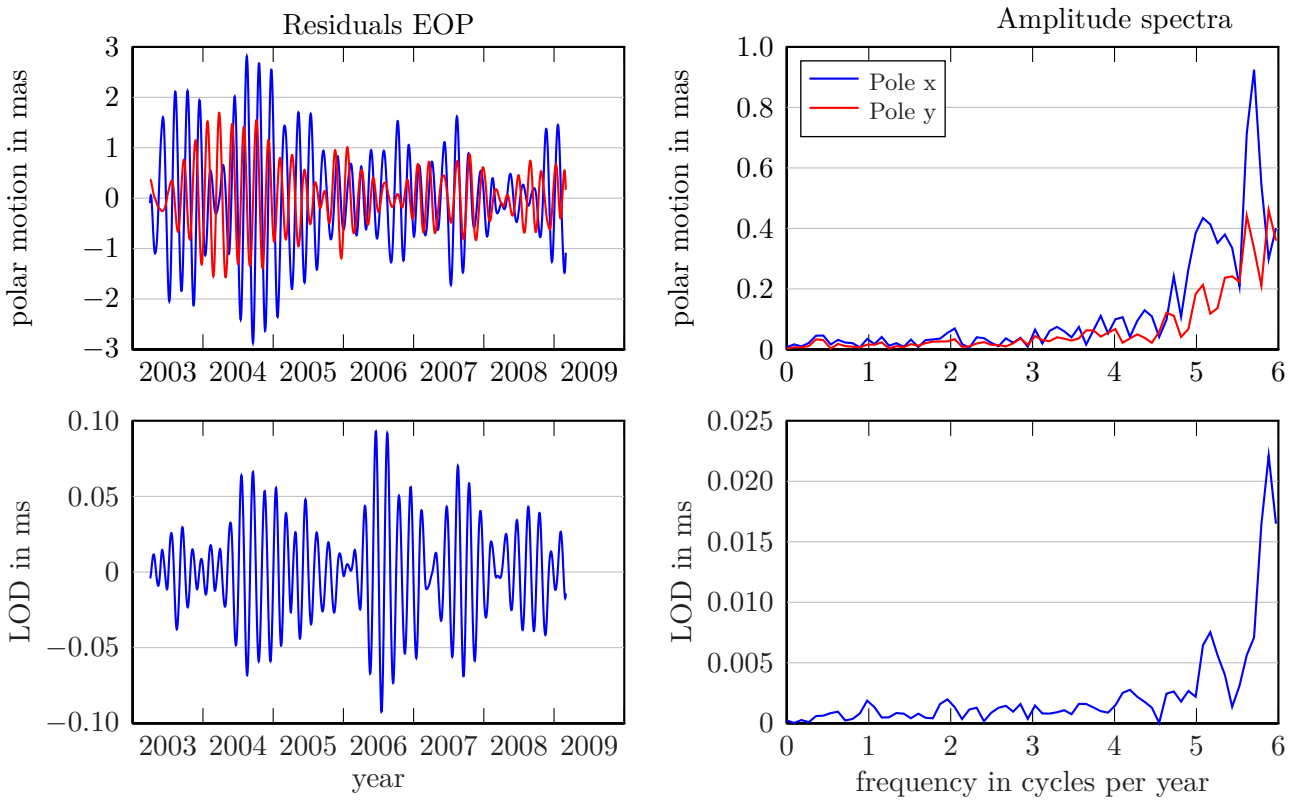

Figure 5.3: The residuals of the EOP are depicted in the time domain (left column) and the frequency domain (right column).

Residuals of the motion terms

The residuals of the motion terms are shown in Figure 5.4. The equatorial residuals do not exceed $\pm 1.5 \times 10^{24}\,\mathrm{kg\,m^2\,s^{-1}}$ (± 1.2 TU), and the axial motion term residuals remain below $\pm 8 \times 10^{24}\,\mathrm{kg\,m^2\,s^{-1}}$ (± 6 TU). The equatorial residuals partly are larger than their associated observations. This aspect is discussed in the next paragraph. Both h_x residuals are mainly dominated by noise. Both h_y amplitude spectra contain large peaks at the long period of 2 years and ten months. This period is slightly shorter than the cutoff period of three years. On one hand, this long period might be a filter artifact, resulting from slightly different filters for daily and monthly times series. On the other hand, this period might be a remainder of a real long period not completely filtered out. This aspect is discussed in Subsection 5.3.1. Both h_y amplitude spectra additionally show small annual and semiannual peaks. Both h_z amplitude spectra show, like the EOP amplitude spectra, filter artifacts with periods about two months. The annual signal in the *non-ass. JPL* h_z amplitude spectrum is larger than the *op. GFZ* annual signal. *non-ass. JPL* presents furthermore an additional semiannual signal in h_z, which does not exist in the *op. GFZ* motion term.

As the ELE determines the tensor elements by differences between EOP and motion terms, these differences instead of absolute values are validated by the mass terms and the GFC2. According to Subsection 4.3.2, inconsistencies in the differences might arise due to three reasons: first from the EOP, second from the approximation of the polar motion time derivatives and third from the motion terms. The splines allow to separate the combined residuals into EOP residuals and motion term residuals. However, the inconsistencies due to the approximation of the time derivatives are not quantified and contaminate either the polar motion or the motion term residuals. Thus, the large residuals of the equatorial motion terms are likely caused by the approximation of the time derivatives.

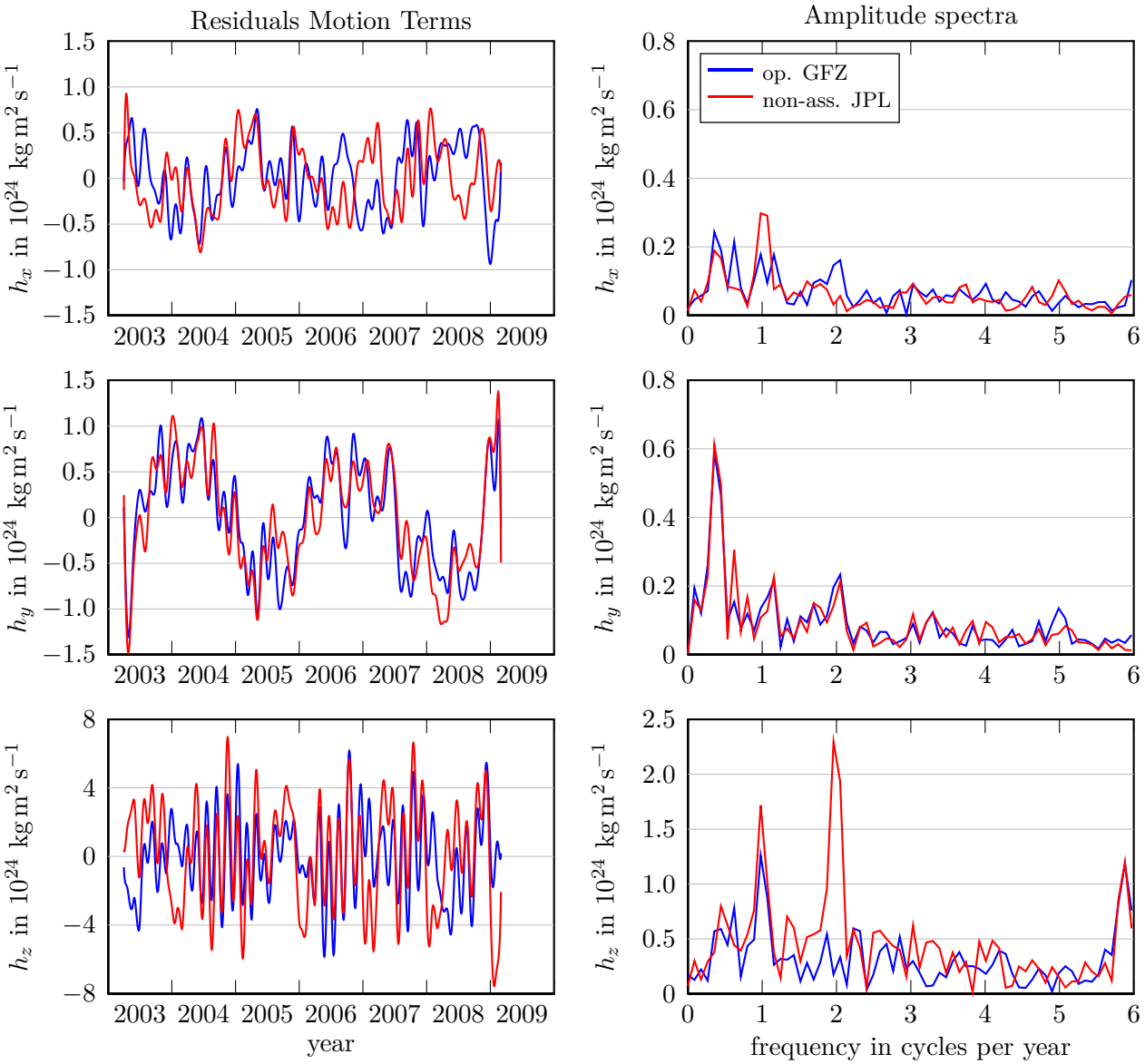

Figure 5.4: The residuals of the motion terms are shown in the time domain (left column) and the frequency domain (right column). Blue lines denote residuals of the op. GFZ and red lines the residuals of non-ass. JPL.

Residuals of the mass terms

Figure 5.5 shows the residuals of the mass terms in the time domain and the frequency domain. The equatorial residuals do not exceed $\pm 3 \times 10^{24}\,\mathrm{kg\,m^2\,s^{-1}}$ (± 1.7 TU), and the maximal axial mass term residuals amount to $\pm 4 \times 10^{24}\,\mathrm{kg\,m^2\,s^{-1}}$ (± 2.2 TU). The equatorial graphs show a picture similar to the motion term residuals. Both Ωc_{xz} residuals show small annual peaks in the amplitude spectra. The *op. GFZ* annual amplitude is slightly larger than the *non-ass. JPL* annual signal. The long period of two years and ten month also is present and possesses large amplitudes in both Ωc_{yz} amplitude spectra. The two Ωc_{zz} residuals show large differences. The *op. GFZ* amplitude spectrum is dominated by the artifact period of two months and two smaller amplitudes, denoting periods of one and two years. The axial *non-ass. JPL* residuals show larger variations than the *op. GFZ* residuals. The amplitude spectrum of the axial *non-ass. JPL* is dominated by a large annual amplitude and a longer period of two years. However, as the GRACE gravity fields are determined with respect to a background model which incorporates the operational ECMWF atmosphere model and OMCT driven by operational ECMWF data, it is expected that *op. GFZ* mass and motion terms show a higher degree of consistency to the EOP and GFC2 and therefore smaller residuals than *non-ass. JPL*. The axial residuals satisfy this expectation, whereas the equatorial residuals of both analyzed excitation functions have the same dimensions and mostly contain the same periods.

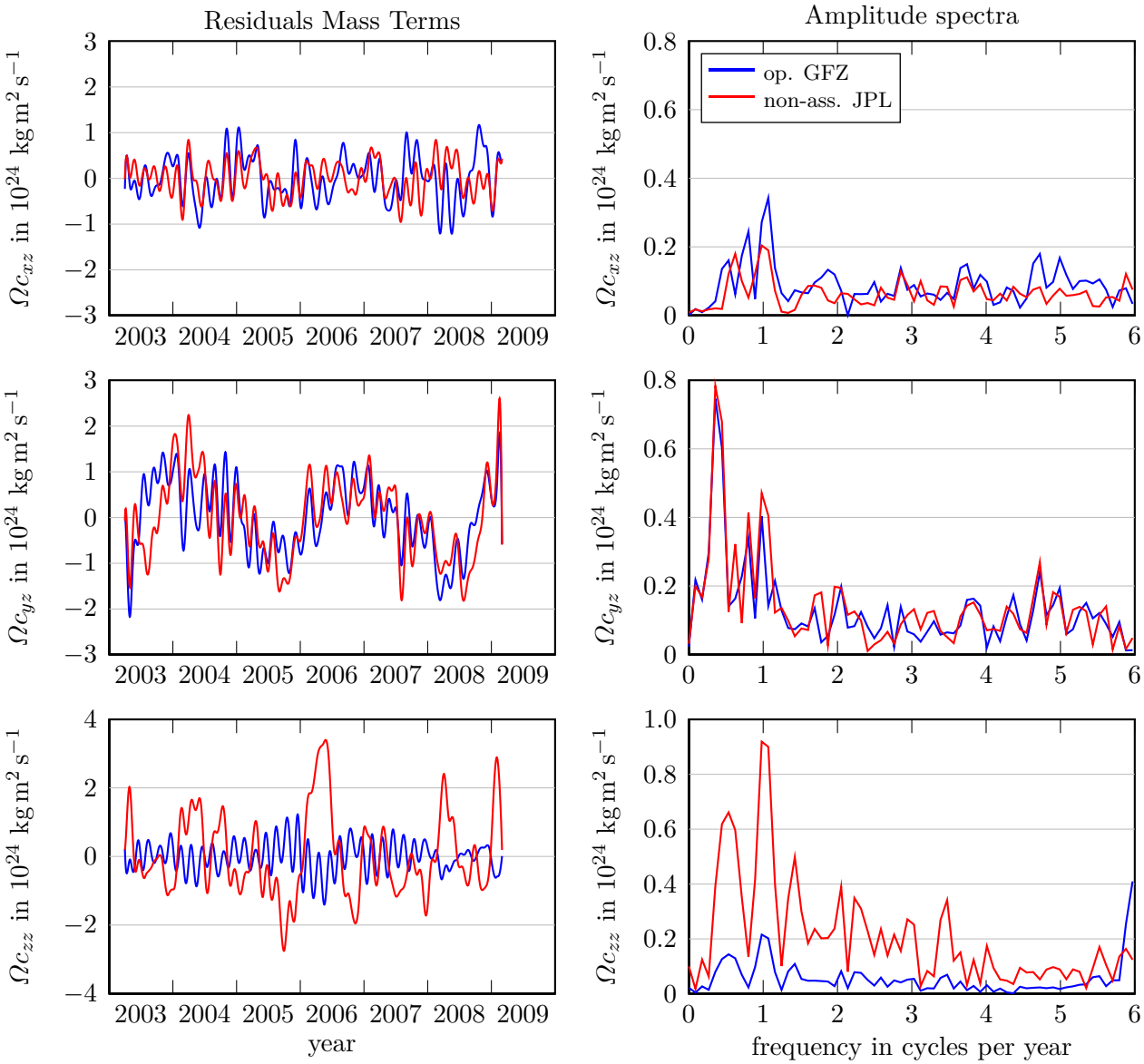

Figure 5.5: The residuals of the mass terms are shown in the time domain (left column) and the frequency domain (right column). Blue lines denote residuals of the op. GFZ and red lines the residuals of non-ass. JPL.

Residuals of the GFC2

Figure 5.6 presents the GFC2 residuals in the time domain and the frequency domain. The equatorial C_{21}/S_{21} residuals have maximal values of $\pm 2.5 \times 10^{-10}$ (± 3.2 TU). The C_{20} residuals contain values of $\pm 6 \times 10^{-10}$ (± 9 TU) maximum. Hence, the GFC2 residuals are larger than the EOP residuals and the residuals of the excitation functions. All C_{20} amplitude spectra contain an annual period. Three of the six C_{20} time series, namely *CRS R04*, *GFZ R04* and *ITG 2010*, additionally comprise amplitudes with a frequency of 2.25 cycles per year, corresponding to a period of approximately 161 days. This period results from errors in high-frequency ocean tide models. The period of 161 days is an alias period of the S2 semidiurnal solar tide (Chen et al., 2009). The remaining C_{20} time series do not contain the S2 tide alias. Since SLR C_{20} coefficients are not sensitive to this tide error, *CSR SLR R04* and *GRGS R02* C_{20} coefficients are not affected. The two step approach of *JPL R04* successfully prevents a contamination with this tide error as well.

The C_{21} residuals mainly contain noise apart from *GRGS R02*, which contains an additional annual period. In contrast to C_{21}, the S_{21} residuals possess amplitudes with periods of one year and two years. The linear approximation of the ELE leads to the consequence that the C_{22} and S_{22} coefficients cannot be validated by the EOP and excitation functions. Therefore, the residuals of C_{22} and S_{22} arise from the redundant observation of six GFC2 time series. However, the four time series *GRGS R02* C_{22}, *GRGS R02* S_{22}, *CSR SLR R04* C_{22} and *JPL R04* S_{22} time series contain an annual signal.

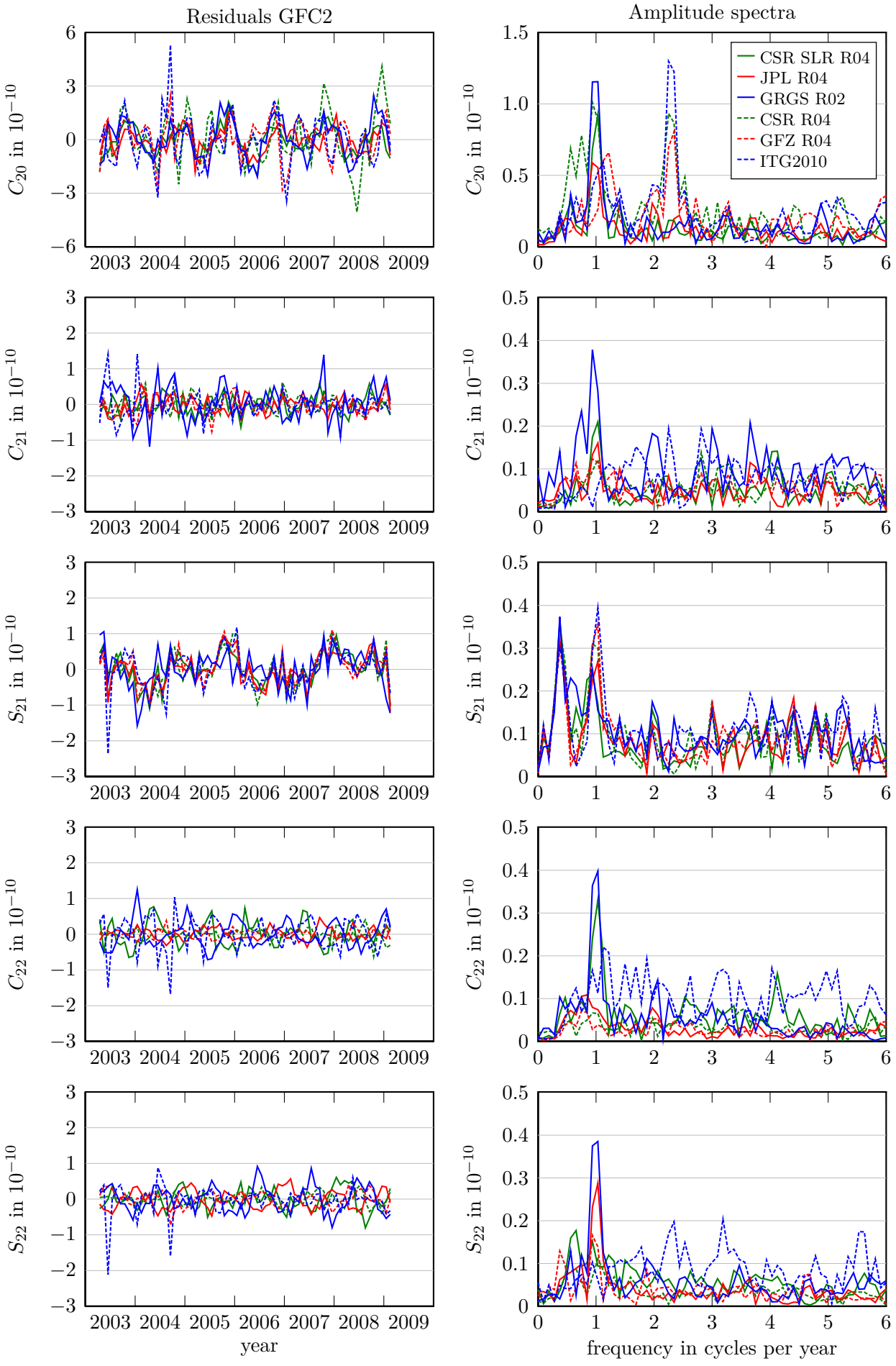

Figure 5.6: The residuals of the six GFC2 time series are shown in the time domain (left column) and the frequency domain (right column).

5.2.3. Partial redundancies and a posteriori stochastic model

Subsection 3.1 discusses the partial redundancies as a measure of reliability. The partial redundancy of an observation informs to which extent the specific observation is controlled by other observations. A small partial redundancy of $r_i \approx 0$ indicates a weakly controlled observation. An error in a weekly controlled observation has a high impact on the results. A large partial redundancy of $r_i \approx 1$ means a highly controlled observation. Here, the combined least-squares adjustment problem has a total redundancy of $r = 31\,761$. The total redundancy is distributed over 32 800 observations. The adjustment problem is therefore highly overdetermined. The partial redundancies of observations of the first and last epochs are smaller than the partial redundancies of the observations in median epochs. However, the partial redundancy of observations belonging to the same time series are basically homogeneous. Therefore, the arithmetic averages of the partial redundancies of each time series are calculated and shown in Figure 5.7. Apart from the C_{22}/S_{22} time series, the averaged partial redundancies slightly differ and are larger than 0.95. The smaller partial redundancies of the C_{22}/S_{22} coefficients are caused by the linearization of the ELE. The linearization decouples C_{22}/S_{22} from the other time series. Therefore, the partial redundancies of the C_{22}/S_{22} coefficients solely arise from the multiple observation of the gravity field.
According to Heiker et al. (2008) the polar motion and C_{22}/S_{22} are not controlled by other observations, and C_{21}/S_{21} have partial redundancies of one. Since Heiker et al. (2008) considered only one GFC2 time series, the C_{22}/S_{22} coefficients were not controlled by other observations. Furthermore, Heiker et al. (2008) considered the excitation functions as deterministic parameters and did not estimate VCC, which caused the extreme partial redundancies of the polar motion and C_{21}/S_{21}.
The a posteriori standard deviations reflect the agreement of the time series and depend on the residuals. Large residuals cause large VCC and standard deviations and therefore indicate a low agreement of the specific time series with other time series. Since the a priori VCM of the daily time series are modeled by Toeplitz matrices, the variances of the daily time series are time-invariant. Table 5.3 lists the adjusted a posteriori standard deviations of the daily parameters. The standard deviations are additionally transformed into TU according to Table 4.1. The a posteriori standard deviation of the polar motion is approximately three to four times larger than the mean standard deviations of 0.07 mas given by the IERS. Whereas the a posteriori standard deviation of LOD amounts to 7 µs and is slightly smaller than the mean IERS standard deviation of 10 µs. The mean IERS standard deviations are calculated by the arithmetic averages of the *EOP 08 C04* standard deviations of the years 2002 to 2009.

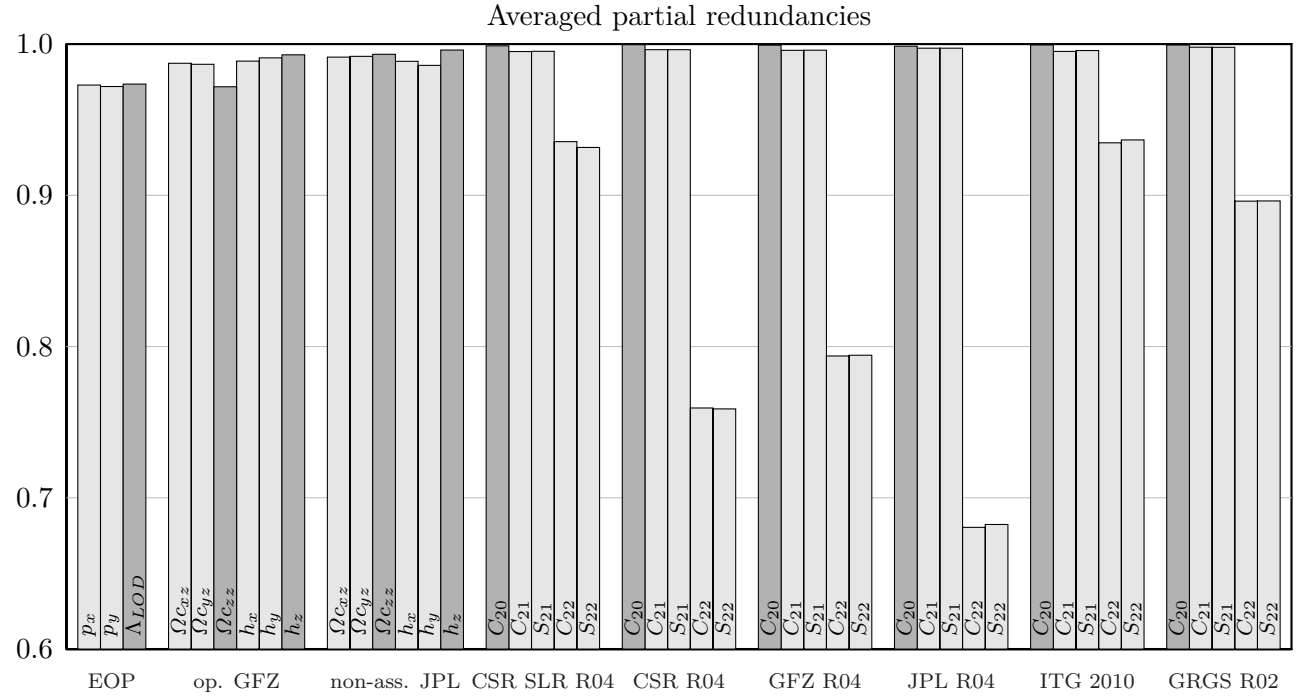

Figure 5.7: The averaged partial redundancies are shown. Light gray bars denote equatorial observations and gray bars axial observations.

Table 5.3: a posteriori standard deviation of the daily time series

time series		standard deviation $\hat{\sigma}$	standard deviation $\hat{\sigma}$ in TU
EOP 08 C04	p_x	0.3 mas	0.0132
EOP 08 C04	p_y	0.2 mas	0.0087
EOP 08 C04	Λ_{LOD}	7 µs	0.2982
op. GFZ	Ωc_{xz}	$3.5 \cdot 10^{23}$ kg m^2 s^{-1}	0.1948
op. GFZ	Ωc_{yz}	$4.2 \cdot 10^{23}$ kg m^2 s^{-1}	0.2348
op. GFZ	Ωc_{zz}	$2.2 \cdot 10^{23}$ kg m^2 s^{-1}	0.1231
op. GFZ	h_x	$2.3 \cdot 10^{23}$ kg m^2 s^{-1}	0.1890
op. GFZ	h_y	$2.3 \cdot 10^{23}$ kg m^2 s^{-1}	0.1914
op. GFZ	h_z	$6.3 \cdot 10^{23}$ kg m^2 s^{-1}	0.4741
non-ass. JPL	Ωc_{xz}	$3.3 \cdot 10^{23}$ kg m^2 s^{-1}	0.1867
non-ass. JPL	Ωc_{yz}	$4.6 \cdot 10^{23}$ kg m^2 s^{-1}	0.2590
non-ass. JPL	Ωc_{zz}	$4.0 \cdot 10^{23}$ kg m^2 s^{-1}	0.2236
non-ass. JPL	h_x	$2.4 \cdot 10^{23}$ kg m^2 s^{-1}	0.1942
non-ass. JPL	h_y	$2.5 \cdot 10^{23}$ kg m^2 s^{-1}	0.2052
non-ass. JPL	h_z	$9.6 \cdot 10^{23}$ kg m^2 s^{-1}	0.7209

The time-variable a posteriori standard deviations of the gravity field coefficients are shown in Figure 5.8. The a posteriori standard deviations of *GFZ R04*, *JPL R04* and *ITG 2010* are significantly larger in June 2003, January 2004 and August to October 2004 than in the other months. The large values are caused by suboptimal satellites orbits of the GRACE satellites. *CSR R04*, *GFZ R04* *JPL R04* and *GRGS R02* even do not provide a gravity field solution in June 2003. The gaps are filled by linear interpolation. The C_{20} a priori and a posteriori standard deviations of *CSR R04* are in contrast to the other time series increasing with time due to unknown reasons.
The standard deviations are averaged and transformed into TU according to Table 4.1, in order to compare standard deviations with different units. Since the GFC2 of the years 2003 and 2004 are affected by suboptimal satellite orbits, the years 2003 and 2004 are not considered for the calculation of the arithmetic averages. The averaged a posteriori standard deviations are described by two bar charts in Figure 5.9. The bar chart on the left separates the standard deviations of the equatorial observations from the standard deviations of the axial components on the right. The equatorial standard deviations are smaller than the axial standard deviations.
As mentioned in Subsection 5.2.2, the inconsistencies in the differences between the EOP and the motion terms are mainly assigned to the motion terms, although the approximation of the polar motion time derivatives likely is the reason for large h_x/h_y residuals. Therefore, the EOP have the smallest standard deviations. Since the GRACE AOD1B products result from the same geophysical models as *op. GFZ* and

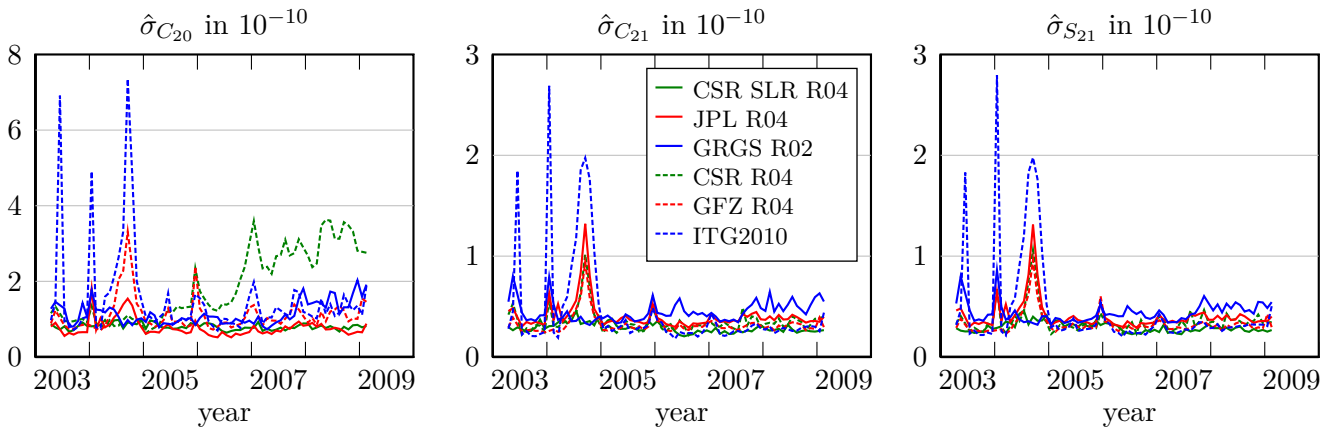

Figure 5.8: The left figure shows the adjusted standard deviations of C_{20}, the middle figure describes the a posteriori standard deviations of C_{21} and the right figure of S_{21}.

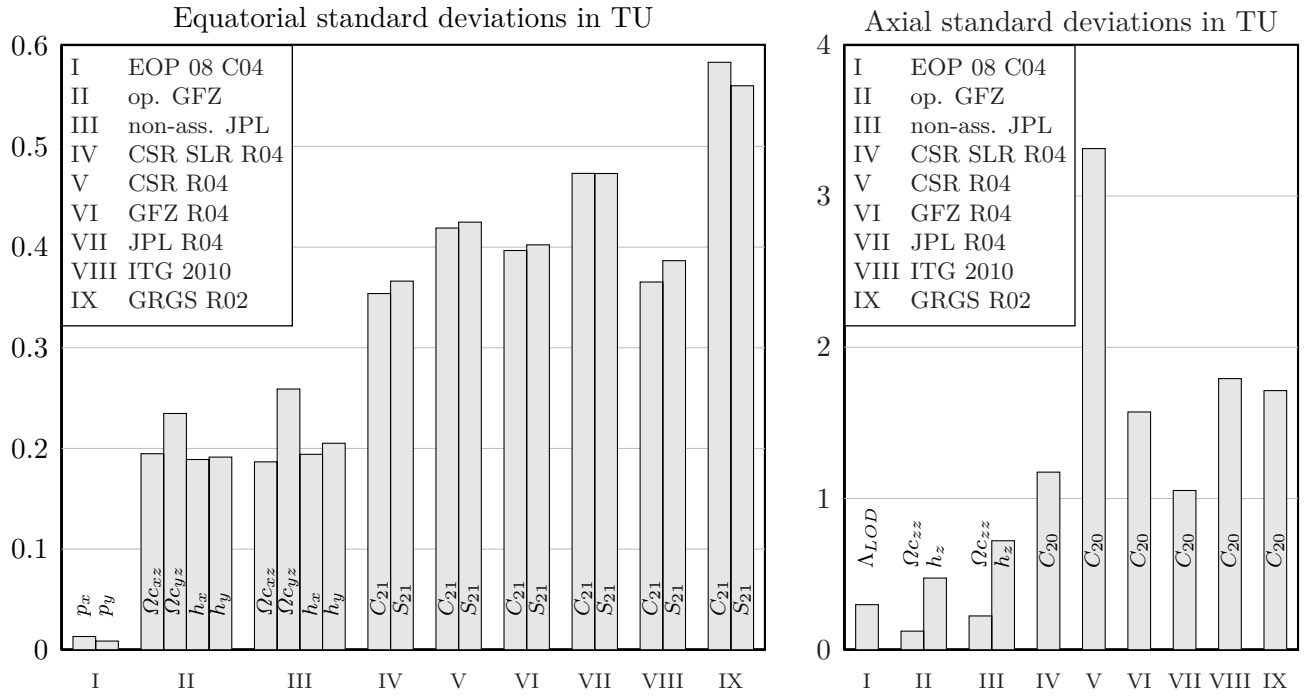

Figure 5.9: The bars in the left chart shows the averaged equatorial a posteriori standard deviations whereas the bar chart on the right side illustrates the averaged axial a posteriori standard deviations.

since *non-ass. JPL* do not model the continental hydrology, it is expected that the *op. GFZ* excitation functions show a higher consistency and therefore a lower standard deviations than *non-ass. JPL*. The axial excitation functions satisfy this expectation, whereas the equatorial *op. GFZ* standard deviations exhibit marginally smaller standard deviations than the *non-ass. JPL* excitation functions. Both axial mass terms clearly show the smallest standard deviations and therefore contribute the largest weight to the estimation of the tensor element c_{zz}. However, the equatorial mass terms and the combined standard deviation for the difference of the polar motion and the motion terms have roughly similar standard deviations.

The GFC2 time series generally show larger standard deviations than the EOP and excitation functions. *GRGS R02* provides the largest C_{21}/S_{21} standard deviations. Since *CSR SLR R04* possesses the smallest standard deviations and since *GRGS R02* considers also SLR, this result is surprising on one hand. On the other hand, Bettadpur (2012) stated that the new GRACE CSR release 05 provides better estimations of C_{21}/S_{21} than SLR. The combined GRACE-SLR approach does not lead to improved C_{21}/S_{21} coefficients in *GRGS R02*. The standard deviations of *ITG 2010* C_{21}/S_{21} coefficients are slightly larger than the standard deviations of the *CSR SLR R04* coefficients. The C_{21}/S_{21} coefficients of the official GRACE data centers (*CSR R04*, *GFZ R04* and *JPL R04*) possess larger standard deviations than *CSR SLR R04* and *ITG 2010*.

The averaged standard deviation of the *CSR R04* C_{20} coefficients is nearly twice as large as the other C_{20} standard deviations. *JPL R04* possesses the smallest C_{20} standard deviations. This result is surprising, since *JPL R04* is a pure GRACE solution and since GRACE is less sensitive to C_{20} variations than SLR. Therefore, the two step approach of the JPL reduces the errors in C_{20} quite successfully. A second conclusion arises due to this result. Since *CSR SLR R04* is expected to deliver the smallest residuals, since it is based on the same background models as *CSR R04* and since *CSR R04* provides the largest standard deviation, the CSR background models and processing strategies might be inferior compared to the other groups.

The last two paragraphs discuss the a posteriori standard deviations of the GFC2. They do not analyze the quality of the a priori formal errors. This paragraph relates the a priori and the a posteriori standard deviations to each other. The a priori VCM of the GFC2 are composed of the formal errors provided by the data centers. According to Wahr et al. (2006), the formal errors of GRACE time series are too optimistic. To provide more realistic accuracy measures, CSR and GFZ add calibrated errors to their results, which are obtained from comparisons of different gravity field solutions. The calibrated errors of the GFC2 are approximately 13 times larger than the formal errors. Table 5.4 lists factors obtained

Table 5.4: A posteriori standard deviations and calibrated errors divided by formal errors

GFC2 time series	equatorial factor	axial factor	calibrated factor
CSR SLR R04	2.28	1.13	
CSR R04	11.23	17.29	13.65
GFZ R04	40.56	30.33	13.56
JPL R04	36.98	44.95	
ITG 2010	20.15	5.12	
GRGS R02	58.36	33.46	

by dividing the averaged a posteriori standard deviations and the calibrated errors by the formal errors. These factors equal the squared roots of the adjusted VCC. The factors of the *CSR SLR R04* solution are slightly larger than one. Therefore, the formal errors of *CSR SLR R04* describe a more or less realistic accuracy. In contrast to SLR, the formal errors of all GRACE time series clearly are too optimistic. The calibrated errors of *CSR R04* approximately correspond to the a posteriori standard deviations and therefore describe a realistic accuracy. The calibrated errors of *GFZ R04* still are about a factor of three too optimistic. The formal errors of *GFZ R04*, *JPL R04* and *GRGS R02* have to be multiplied by factors between 30 and 60 to obtain realistic standard deviations. *ITG 2010* also is too optimistic, but has smaller factors than *GFZ R04*, *JPL R04* and *GRGS R02*.
Apart from the variance components, the covariance between C_{20} and $C_{21}/S_{21}/C_{22}/S_{22}$ of *ITG 2010* is estimated. Figure 5.10 shows the a priori and a posteriori correlation coefficients. The a posteriori correlation coefficients are 2.1 times larger than the a priori correlation coefficients. Nonetheless, as the maximal correlation coefficients amounts to ± 0.3, the correlation coefficients remain small. However, it is assumed, that the correlations between C_{20} and $C_{21}/S_{21}/C_{22}/S_{22}$ of all other GFC2 time series are zero. The neglected correlations of five time GFC2 time series might cause the small correlation coefficients of the *ITG 2010* time series.
In order to analyze the influence of neglected covariances, the adjustment is repeated by taking only *ITG 2010* into account. Surprisingly, the convergence of the covariance component deteriorates and varies between $0.01 < \sigma_{\text{Covariance}} < 4$. Therefore, a reliable estimation of the covariance component is not possible due to the large variations. Increasing the number of samples drawn by the SMCTE does not improve the convergence substantially. Since the covariance component is successfully estimated during the first adjustment, which takes six gravity field solutions into account, the algorithm likely is not the reason for the poor convergence. According to Xu et al. (2007), the total number of VCC is limited by the total redundancy of the adjustment problem. However, the poor convergence leads to the suspicion that the estimation of an individual variance or covariance component is not limited by the total redundancy but rather by the partial redundancies of the involved observations. As only one gravity field solution is considered in the second adjustment, C_{21} and S_{21} show reduced partial redundancies and C_{22} and S_{22} partial redundancies of zero. Therefore, the C_{22} and S_{22} residuals also are near zero and do not

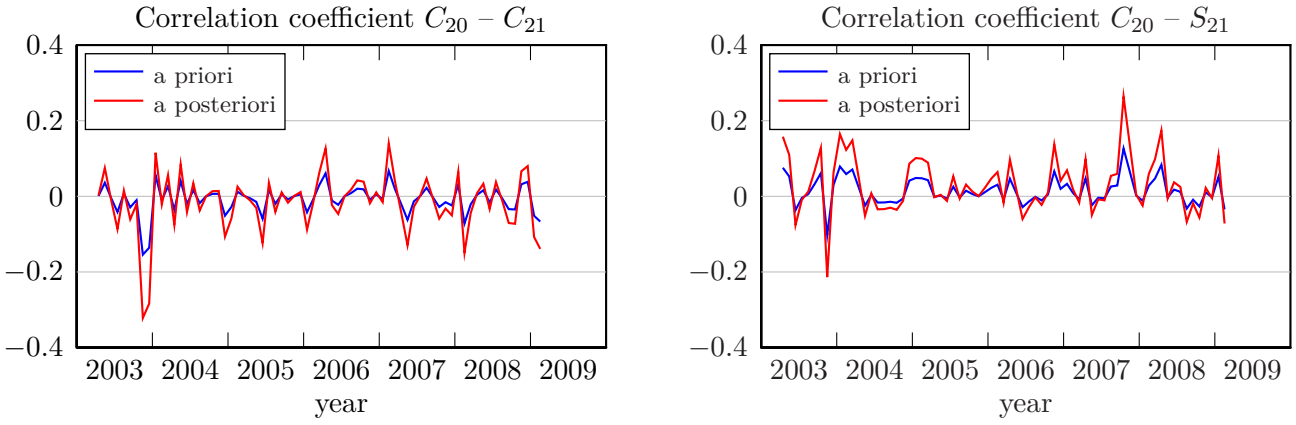

Figure 5.10: The a priori and a posteriori correlations coefficients between C_{20} and C_{21} (left graph) and between C_{20} and S_{21} (right graph) of ITG 2010 are illustrated.

contribute to the estimation of VCC (cf. vector $\boldsymbol{q}$ in Equation 3.41). Therefore, the reliability of the estimation of VCC likely depends on the partial redundancies of the associated observations.

5.2.4. Summary and open questions

The least-squares adjustment delivers residuals for each time series, VCC and the adjusted tensor of inertia. The residuals contain the inconsistencies of the data, caused by measurements errors or inaccurate models. Therefore, a thorough analysis of the residuals provides a valuable insight into the quality of the validated data. The adjusted VCC depend on the residuals and determine the a posteriori VCM of the time series. A transformation of the a posteriori standard deviations into a common TU facilitates comparisons of time series with different units. The larger the transformed standard deviations, the less the associated time series contribute to the adjusted tensor of inertia. The adjusted tensor of inertia is a weighted average of the tensors resulting from the individual time series. However, the results obtained in this section arise further open questions that are investigated within the following Section 5.3. The results and the open questions are summarized by following list.

- Most residuals show an annual signal. The annual signal results from inconsistencies of considered data and models. The residuals of h_y and Ωc_{yz} additionally contain a long period, which is either caused by filter artifacts or by existing inconsistencies. This aspect is investigated in Subsection 5.3.1.

- The equatorial *op. GFZ* excitation functions show a marginally higher degree of consistency with the EOP and GFC2 than the *non-ass. JPL* excitation functions. The axial *op. GFZ* excitation functions clearly are more consistent to LOD and C_{20} time series than the *non-ass. JPL* excitation functions.

- The inconsistencies arising from the difference between the polar motion and the equatorial motion terms are mainly caused by the approximation of the polar motion time derivatives. The least-squares adjustment is not able to separate inconsistencies due to the polar motion, the approximation of the time derivative and the motion terms. The inconsistencies due to the time derivatives do not deteriorate the polar motion residuals but rather enlarge the motion term residuals. Therefore, a reliable validation of the equatorial motion terms h_x/h_y is not possible.

- The axial mass terms of the excitation functions contribute the largest weights to the adjusted tensor element c_{zz}. The equatorial mass terms and the difference between the polar motion and the motion terms contribute roughly the same weight to the determination of the adjusted tensor elements c_{xz}/c_{yz}. The GFC2 time series contribute the smallest weights.

- The known S2 tide alias is successfully identified in those GRACE C_{20} time series which are not stabilized by further appropriate measures.

- JPL uses a two step approach for the estimation of the GRACE gravity field solution *JPL R04*. This approach reduces the C_{20} errors efficiently. Therefore, the *JPL R04* C_{20} values even show a slightly higher degree of consistency than the *CSR SLR R04* C_{20} values.

- The GRACE GFC2 formal errors clearly are too optimistic, whereas the formal errors of *CSR SLR R04* seem to be realistic.

- The adjusted correlations between C_{20} and $C_{21}/S_{21}/C_{22}/S_{22}$ of the *ITG 2010* time series are small.

- The results are obtained by assuming the tensor trace constraint in Equation 2.66. Since the tensor element c_{zz} can be redundantly determined by LOD and the axial excitation functions, the tensor trace constraint is not necessary to obtain a unique solution of the system of normal equations. The tensor trace constraint is a strict constraint, which influences the estimation of the tensor elements essentially. In order to analyze the effect of this constraint, the tensor trace constraint is neglected in Subsection 5.3.2.

- The GFC2 and the gravity field coefficients of higher degrees are linked by correlations. If the GFC2 change due to the least-squares adjustment, the gravity field coefficients of higher degrees have to change likewise. Thus, the least-squares adjustment model is extended in Subsection 5.3.3, to take the gravity field coefficients of higher degrees into account.

5.3. Investigation of further open questions

5.3.1. Effect of the filter on the least-squares adjustment

The results presented in the previous section are based on filtered data. The filters remove frequencies which are not present in all time series. For example, geophysical processes in the Earth's core cause long periodical variations of LOD, which are not modeled by the excitation functions. On one hand, the filters increase the consistency of the data before the adjustment is performed and therefore lead to decreased residuals. On the other hand, the filters alter the original data and filter artifacts might arise. Hence, suspicion arises in Section 5.2 that long periods detected in the equatorial mass and motion term residuals are caused by filter artifacts. In order to analyze the effect of the filters, the least-squares adjustment in Section 5.2 is repeated with unfiltered data. However, linear trends are removed from the data before the adjustment to account for biases and secular trends. Heiker et al. (2012) suggested an alternative approach which considers unaltered data by estimating the biases and trend parameters within the least-squares adjustment.
The resulting residuals of the time series are significantly larger than the residuals in Section 5.2, because they additionally contain inconsistent frequencies not filtered out before. Figure 5.11 illustrates the residuals of LOD. A comparison with Figure 5.3 reveals significantly larger residuals. The long periods in the residuals are caused by the Earth's core, which is not modeled by excitation functions. Furthermore, the residuals contain increased amplitudes in frequency between six and twelve cycles per years. As monthly cubic splines model unfiltered daily time series, frequencies larger than six times per year are expected here.
Figure 5.12 presents the residuals of the mass terms. They also are larger than the residuals in Figure 5.5. The long period in the Ωc_{yz} residuals is still present. Therefore, the long period in Figure 5.5 is not caused by a filter artifact but is rather a residual signal which is not completely filtered out. However, since the times series only cover six years, the specific long period cannot be identified more precisely. Therefore, further conclusions regarding underlying geophysical processes cannot be drawn here. According to Figure 5.5, the axial *op. GFZ* mass term residuals show a better agreement with LOD and the C_{20} time series than *non-ass. JPL*. Surprisingly, this finding is not verified by Figure 5.12, where the axial *op. GFZ* residuals even show a larger annual amplitude than the *non-ass. JPL* residuals.
The motion term residuals show a similar pattern as the mass term residuals. Therefore, they are not presented here. The residuals of the GFC2 are barely changed by the neglected filter. Since the daily time series show significantly larger residuals due to the unfiltered high frequencies, the averaged standard deviations increase likewise. In contrast to Figure 5.9, the transformed averaged standard deviations of the excitation functions are larger than the standard deviations of the GFC2.

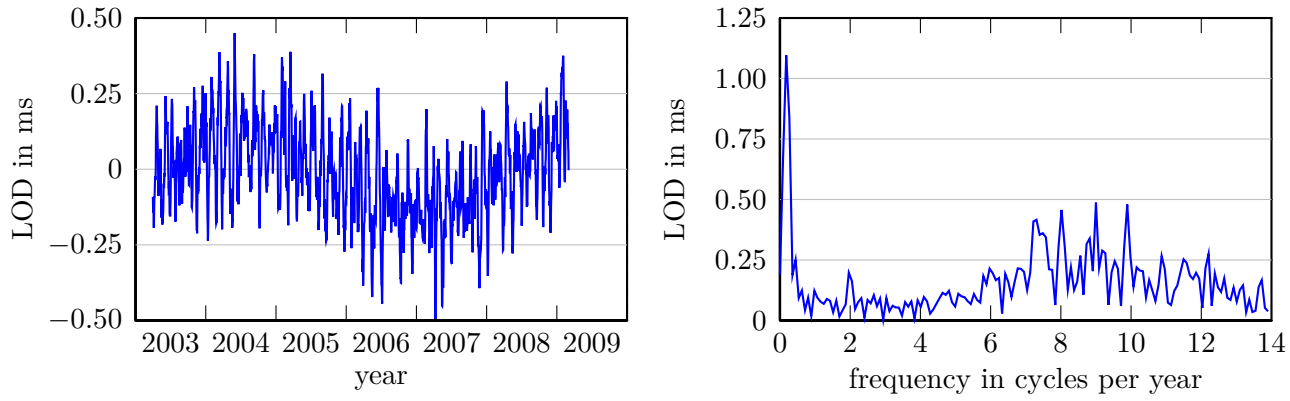

Figure 5.11: The residuals of the LOD are shown in the time domain (left column) and the frequency domain (right column).

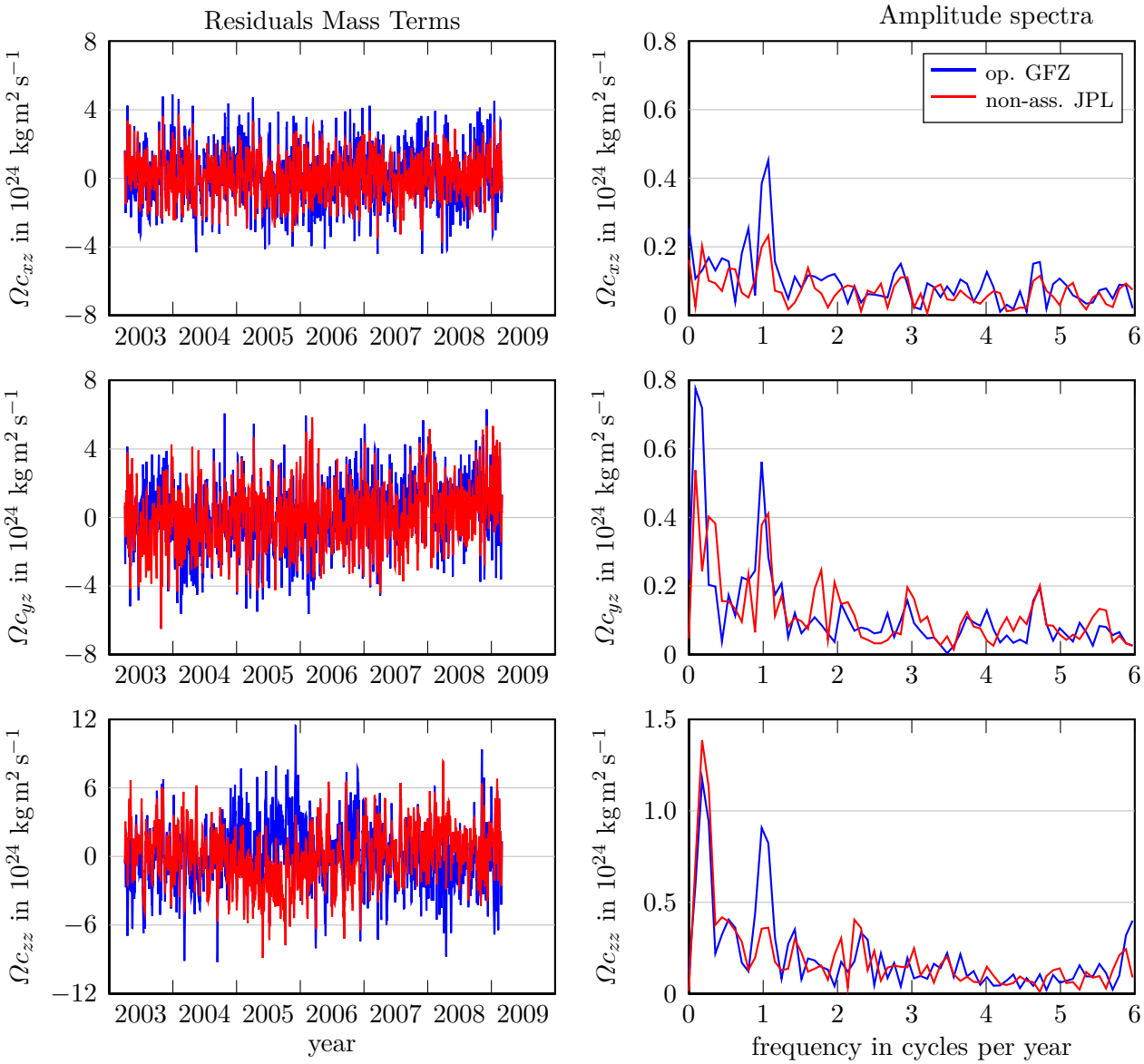

Figure 5.12: The residuals of the mass terms are shown in the time domain (left column) and the frequency domain (right column). Blue lines denote residuals of the op. GFZ and red lines the residuals of non-ass. JPL.

This subsection leads to the conclusion that the reduction of previously known inconsistencies improves the results and the interpretation of the results significantly. Additionally, this subsection reveals that the inconsistent long periods obtained in Section 5.2 are not caused by filter artifacts.

5.3.2. Effect of the tensor trace constraint

According to Rochester and Smylie (1974) the trace of the tensor of inertia is invariant to any redistribution of masses as long as the principle of mass conversation holds. The gravity field solutions consider the Earth's total masses. In contrast to the gravity field coefficients, the excitation functions do not model the masses of all subsystems. For example, water in glaciers, ice shelfs and partly in the continental hydrology is not modeled. Therefore, the excitation functions violate the principle of mass conversation. However, the tensor trace constraint is justified by assuming that the masses of the neglected subsystems are small compared to the atmospheric and oceanic masses.
The tensor trace constraint in Equation 2.66 stabilizes the estimation of the tensor of inertia by the EOP, GFC2 and the excitation functions. It relates the tensor element c_{zz} linearly to C_{20}, and the elements c_{xx} and c_{yy} are linearly dependent on C_{20} and C_{22}. As the tensor element c_{zz} can be redundantly determined by LOD and the axial excitation functions, the tensor trace constraint is not necessary to obtain a unique solution of the system of normal equations. If the tensor trace constraint is neglected, the C_{20} gravity field coefficients are not validated by the EOP and the excitation functions. Then, C_{20} observations are

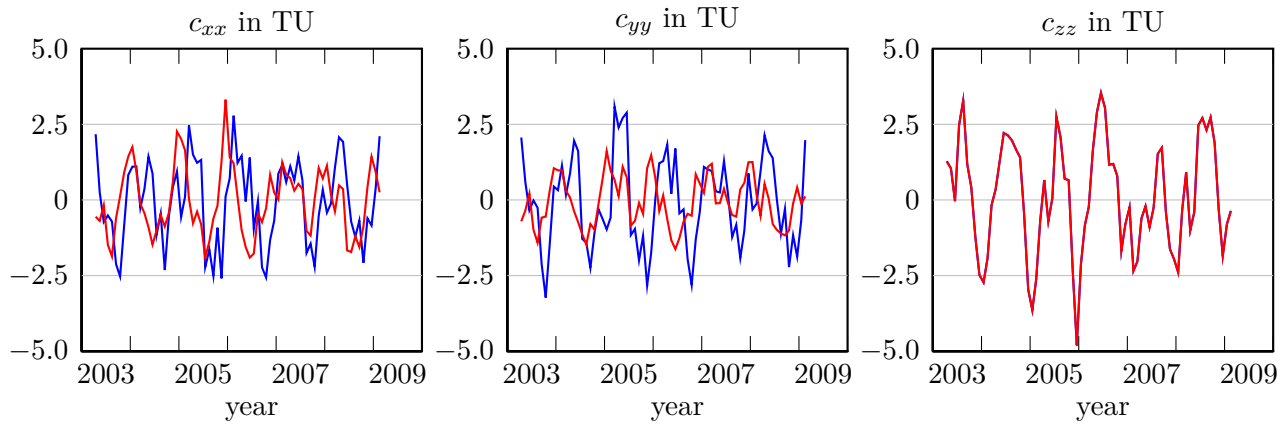

Figure 5.13: The adjusted tensor elements on the main diagonal of the tensor of inertia are plotted. Red lines illustrate the tensor elements resulting from an adjustment which considers the tensor trace constraint. The blue lines are obtained from an adjustment which neglects the tensor trace constraint.

only validated by the multiple observation of the gravity field coefficients, and the tensor elements c_{xx} and c_{yy} are determined by the gravity field coefficients C_{20}, C_{22}, LOD and the axial excitation functions. The least-squares adjustment described in Section 5.2 is repeated with identical functional and stochastic models, except that the tensor trace constraint is not considered. The adjusted tensor elements c_{xx}, c_{yy} and c_{zz} differ from the results obtained in Subsection 5.2. Figure 5.13 shows the tensor elements. The red lines are obtained from the adjustment which considers the tensor trace constraint. The blue lines result from the adjustment which neglects the tensor trace constraint. The right graph shows nearly identical tensor elements c_{zz}. The difference between both c_{zz} solutions does not exceed ±0.02 TU. Small differences between the two c_{zz} solutions are expected, as according to Section 5.2 the axial mass terms contribute the largest weights to the adjusted tensor element c_{zz}. However, the tensor elements c_{xx} and c_{yy} show significantly larger differences than c_{zz}. If the tensor trace constraint is considered, the c_{xx} and c_{yy} depend on C_{20} and C_{22}. In contrast, if the tensor trace constraint is neglected, the tensor elements c_{xx} and c_{yy} additionally depend on LOD and the axial excitation functions, which leads to different values for c_{xx} and c_{yy}.

On one hand, the tensor trace constraint is a meaningful assumption, as it reflects the physical law of the mass conservation (Rochester and Smylie, 1974). On the other hand, the tensor trace constraint highly impact the estimation of the unknown tensor of inertia. However, Rochester and Smylie (1974) do not give a numerical value for the trace of the tensor of inertia. Figure 5.14 shows the trace of the tensor of inertia, which is obtained by neglecting the tensor trace constraint. The trace of the tensor of inertia varies around zero and shows an annual period with maximal values of about ±8 TU. The assumption that the constant trace equals the sum of the principal moments of inertia is confirmed by the variations around zero. The trace cumulates the inconsistencies in LOD, the axial excitation functions, C_{20} and C_{22}. The residuals of the axial time series mostly have annual periods, according to Subsection 5.2.2. The individual contributions of the time series to the inconsistent trace cannot be identified. An amplitude of approximately ±8 TU is expected, as the averaged axial standard deviations in Figure 5.9 amounts up to 3.2 TU.

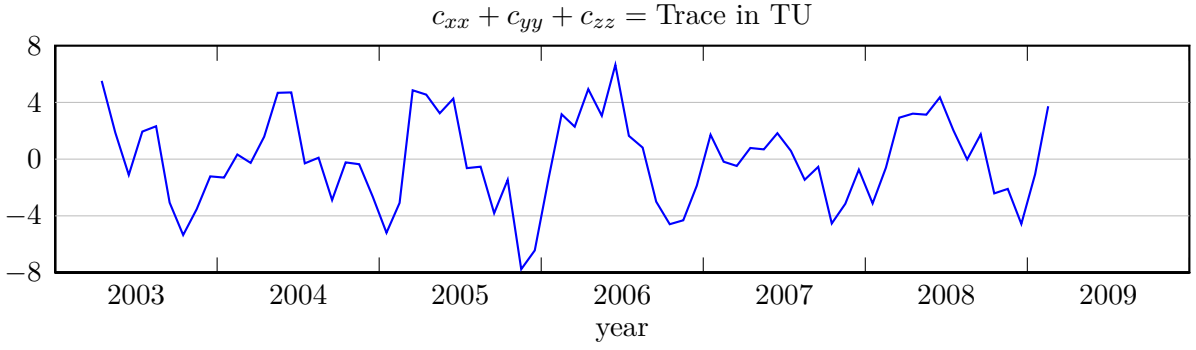

Figure 5.14: The trace of the tensor of inertia is shown, which is obtained by neglecting the tensor trace constraint.

According to this subsection, the tensor trace constraint is necessary to assign inconsistencies to the individual time series. Furthermore, it is confirmed that the constant trace equals the sum of the principal moments of inertia.

5.3.3. Effect of covariances on the gravity field coefficients of higher degrees

As mentioned before, the raw GRACE gravity field coefficients deliver potential maps with north-south stripes due to the satellite geometry. The stripes are accompanied by high correlations between the gravity field coefficients of even and odd degrees (Swenson and Wahr, 2006). Figure 5.15 illustrates the correlation coefficients of the *ITG 2010* gravity field coefficients up to degree/order ten of June 2008. The correlation coefficients are summarized in a correlation matrix. The correlation matrix is sorted by degrees and within the degrees by orders. The high correlation coefficients of even and odd degrees are visible clearly.
If the GFC2 change due to the combined adjustment, the gravity field coefficients of higher degrees also change due to correlations. Uncorrelated gravity field coefficients of higher degrees are not effected whereas highly correlated observations show large residuals. The correlations between the GFC2 and the gravity field coefficients of higher degrees are small (compare first row and left column of Figure 5.15). Therefore, one can assume that the impact of the correlations is small, too. To analyze the effect of the correlations, the least-squares adjustment model of Section 5.2 is modified. The gravity field coefficients up to degree/order ten are introduced as additional observations on the one hand and as additional unknown parameters on the other hand. The total redundancy of the adjustment problem is not changed by this modification.
The modified adjustment model only considers *ITG 2010*, as this time series is the sole gravity field solution with covariances information. According to Subsection 5.2.3, the correlation coefficients between C_{20} and C_{21}/S_{21} are enlarged by the factor 2.1 due to the covariance component estimation. Figure 5.15 shows that correlation coefficients exist, which are larger than ± 0.5. The duplication of the correlation coefficients would lead to values larger than ± 1 and consequently to incorrect negative definite VCM. Therefore, covariance components are not estimated. The extended adjustment model estimates one common variance component for *ITG 2010*.

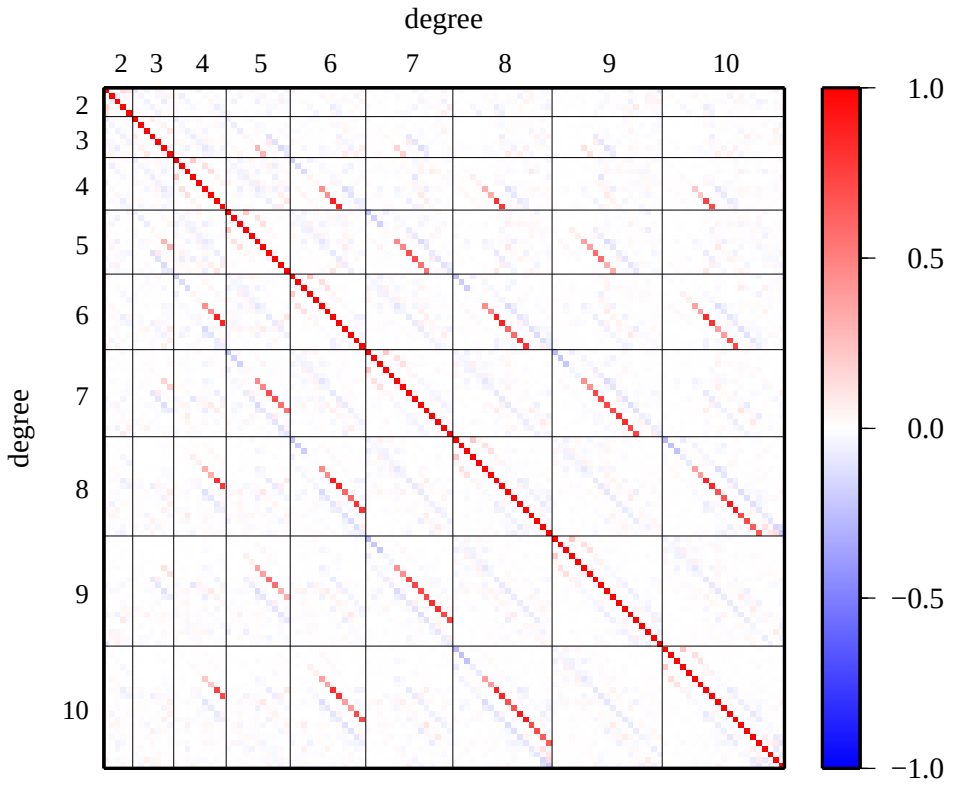

Figure 5.15: The figure illustrates the correlation coefficients of the ITG 2010 gravity field coefficients up to degree/order ten. The correlation matrix of June 2008 is shown.

The obtained C_{20}, C_{21} and S_{21} residuals are similar to the residuals in Figure 5.6. Since the C_{22} and S_{22} coefficients are not controlled by other gravity field coefficients, the residuals of C_{22}/S_{22} and the residuals of coefficients of higher degrees mostly are significantly smaller than the C_{20}, C_{21} and S_{21} residuals. The residuals correspond to the correlation matrix in Figure 5.15. Residuals of gravity field coefficients of odd and even degrees and high orders have larger absolute values than the residuals of gravity field coefficient of low orders, because gravity field coefficients of high orders show larger correlations than gravity field coefficients of low orders.
The adjusted residuals are used to calculate residual potential maps according to Equation 2.57. The residual potential is calculated for $r = a$, where a denotes the Earth's radius. The resulting residual potential maps of the year 2005 are plotted in Figure 5.16. If the absolute C_{20} residuals are larger than zero and all other residuals are zero, the residual potential maps show a horizontal stripe. If only C_{21}/S_{21} residuals are considered, the residual potential maps show a checkerboard pattern. If the effects of C_{20} and C_{21}/S_{21} residuals are added, a typical S-shaped structure is visible in the residual potential maps. The maps in Figure 5.16 are dominated by C_{20}, C_{21} and S_{21} residuals. The maps of most months (e.g.

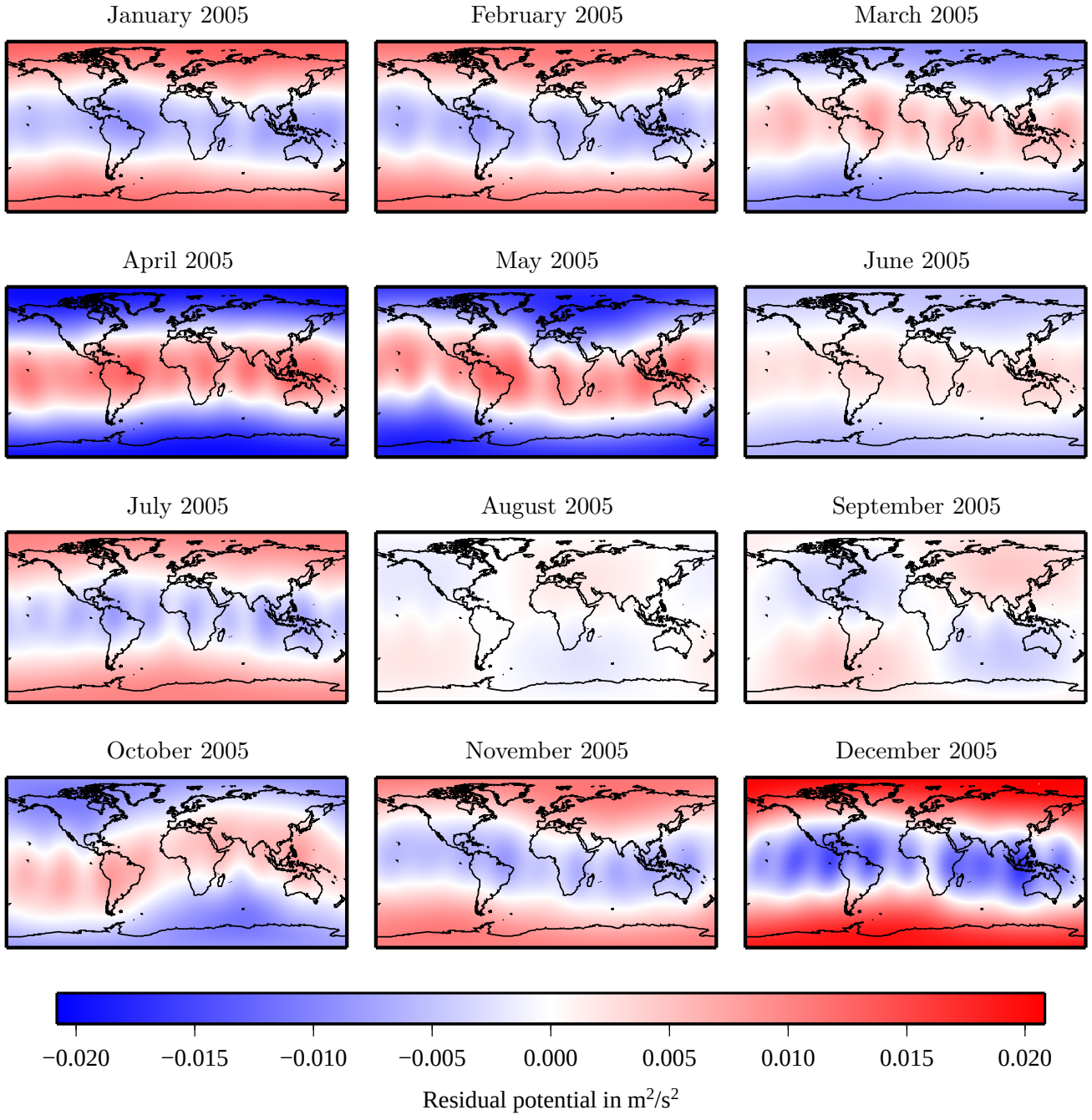

Figure 5.16: The maps show the residual potential obtained from the residuals of the ITG 2010 gravity field coefficients.

May 2005 and December 2005) show smaller structures within the S-band, caused by residuals of higher degrees. As gravity field coefficients of higher degrees are hardly correlated with GFC2, the effect of the correlations is surprisingly large. The high systematic correlations between even and odd degrees likely amplify the influence of the originally small correlations between the GFC2 and the gravity field coefficients of higher degrees.
The approach described in this subsection is relevant. Correlations between the GFC2 and the gravity field coefficients of higher degrees cannot be neglected. Therefore, the release of more covariance information is recommended. If potential maps are drawn by means of the results obtained within this dissertation, the effect of the correlations has to be considered.

6. Summary and outlook

6.1. Summary

The main goal of this dissertation was the mutual validation of EOP, GFC2 and the geophysical excitation functions. The common link between these time series was the Earth's tensor of inertia. As this common link was not taken into account during the derivations of the different time series, it allowed the mutual validation of the time series. Since the functional relation between the time series and the tensor of inertia was linear, a linear least-squares adjustment in a constrained GHM was chosen as a suitable approach for the mutual validation. The time series resulted from different sources, therefore the least-squares adjustment had to include an estimation of VCC to account for the different relative accuracy of the time series. The main results of the dissertation are summarized as follows:

- A universal least-squares solver has been developed within this dissertation. This solver is suitable for each linear least-squares adjustment problem. The SMCTE developed by Koch and Kusche (2002), Kusche and Klees (2002) and Kusche (2003) has been extended in a manner that the SMCTE is able to estimate not only variance components but also covariance components in a constrained GHM. That has resulted in an efficient algorithm, whose pseudocode is presented in this dissertation.

- The daily times series had to be downsampled to representative monthly epoch values due to the different temporal resolution of the time series. Furthermore, the ELE required the time derivatives of the polar motion. Since the time derivatives were not accessible by observations, they were approximated by polar motion observations. Two approaches were discussed, both approaches had significant disadvantages. Therefore, it was concluded that the direct observation of polar motion time derivatives would have improve the validation. However, the polar motion time derivatives currently are not included in the IERS time series.

- The least-squares adjustment was performed by taking into account the *EOP 08 C04* from the IERS, the two excitation functions *op. GFZ* and *non-ass. JPL* and six gravity field solutions (*CSR SLR R04*, *CSR R04*, *GFZ R04*, *JPL R04*, *ITG 2010* and *GRGS R02*). The data were filtered before the adjustment, in order to reduce a priori known inconsistencies. The time series covered approximately six years between April 2003 and February 2009. In total, 18 variance components and one covariance component were estimated by the suggested adjustment algorithm. The mutual validation of nine different time series resulted in residuals, containing the inconsistencies, and adjusted VCM, reflecting the agreement of the time series. The results are summarized as:
  - Most residuals showed annual periods. The EOP residuals were generally small. The residuals of the equatorial motion terms partly were larger than the observed motion terms. These large residuals were caused by the approximation of the polar motion time derivatives by analytic functions. Both Ωc_{xz} residuals mainly contained noise, whereas both Ωc_{yz} residuals showed a low periodical signal, whose frequency could not be identified precisely due to the short time series. The axial *op. GFZ* excitation functions had a higher degree of consistency than the axial *non-ass. JPL* excitation functions. Those three GRACE gravity field solutions, whose C_{20} coefficients were not stabilized by further appropriate measures, were identified by the S2 tide alias in the C_{20} residuals. The C_{21} residuals mainly contained noise, whereas the S_{21} residuals showed an annual period and a long period, both periods with small amplitudes. The C_{22}/S_{22} coefficients were not validated by the EOP and excitation functions due to the linear approximation of the ELE.
  - The variations of the adjusted VCC around the point of convergence differed. The extent of the variations depended on the number of the residuals considered for the estimation of the individual variance or covariance components. The second impact factor was the partial redundancy of the associated observations. Additionally, the condition of the a priori VCM was assumed to play a role, since the adjusted covariance component for the covariance between C_{20} and $C_{21}/S_{21}/C_{22}/S_{22}$ varied more than C_{20} variance components.
  - The a posteriori standard deviations were obtained from the VCC, transformed into a common TU and averaged over the time. The smaller the mean standard deviations were, the larger

were the weights contributed to the adjusted tensor elements by the associated time series. The EOP and the motion terms jointly contributed to the adjusted tensor of inertia. The mass terms and the difference between the EOP and the motion terms roughly contributed with equal weights to the adjusted equatorial tensor elements, whereas the axial mass terms clearly showed the largest weights. The GFC2 contributed the smallest weights to the equatorial and axial tensor elements. However, the *JPL R04* C_{20} coefficients possessed a larger weight than *CSR SLR R04* coefficients, although *JPL R04* was a pure GRACE solution. Thus, the two step approach (cf. Subsection 5.1.2) of the JPL was highly convincing. The results indicated further that the CSR background models or processing strategies might be inferior compared to the other data centers, particularly because the *CSR R04* C_{20} gravity field coefficients had an averaged standard deviation twice as large as the other data centers. However, if the adjusted averaged standard deviations of the GFC2 were compared to the a priori formal and calibrated errors, CSR was the only data provider delivering realistic standard deviations for *CSR R04* and *CSR SLR R04*. The other GFC2 were delivered with too optimistic formal errors. The adjusted covariance component doubled the a priori correlation coefficients between C_{20} and $C_{21}/S_{21}/C_{22}/S_{22}$ of *ITG 2010*. Nevertheless, the adjusted covariances remained small.

- Finally, the least-squares adjustment was repeated with different conditions, in order to address three specific questions: First, the adjustment was repeated with unfiltered data. Then, the residuals of the daily time series were enlarged significantly, as high-frequent variations remained present. This adjustment also revealed that the long period identified in the first adjustment did not result from filter artifacts but was rather present in reality. The second adjustment were performed without the tensor trace condition. Then, C_{20}, C_{22} and S_{22} were not validated by the EOP and the excitation functions. Their residuals resulted from the multiple observation of the gravity field. The resulting trace of the tensor of inertia was not zero and showed annual variations, caused by inconsistent axial time series. The third adjustment model investigated the effect of the covariances between the GFC2 and the gravity field coefficients of higher degrees. The gravity field coefficients of higher degree were introduced on one hand as observations and as unknown parameters on the other hand. This extension did not change the total redundancy. The resulting residuals of the gravity field coefficients of higher degree were smaller than the residuals of C_{20}, C_{21} and S_{21}. However, the higher a gravity field coefficient was correlated with other coefficients, the larger was its residual. The resulting residual potential maps were dominated by the residuals of C_{20}, C_{21} and S_{21} coefficients, but the effect of the gravity field coefficients of higher degrees also were visible. Thus, if the adjusted GFC2 are used for further applications, the changes of gravity field coefficients of higher degrees, caused by correlations, have to be considered, too.

6.2. Outlook

Time series covering nearly six years were mutually validated within this dissertation. The length of the time series is currently limited by *ITG 2010*, which is the only time series delivered with complete stochastic information. Longer time series are required to identify long periodical inconsistencies in the time series. Unfortunately, the outdated GRACE satellites are expected to last not longer than 2013 or 2014, since their batteries are already running low. The GRACE follow-on mission is scheduled for 2017. Therefore, a gap between the current GRACE mission and the follow-on mission has to be expected, which impedes an analysis of long GRACE time series. Time variable gravity fields can be obtained from SLR with a low spatial resolution. However, the results of this dissertation show that C_{22} and S_{22} cannot be validated and reliable covariance components cannot be estimated, if only one gravity field time series is considered. The longest period, in which several gravity field solutions are available, will span approximately eleven years in near future.

The available data mostly have a temporal resolution of one month. As the months have a different number of days, the gravity field solutions are not exactly equidistant and a time series analysis is more effected by leakage effects than necessary. Therefore, it is recommended to process strictly equidistant gravity field solutions. A higher temporal resolution of the GFC2 would allow to validate shorter periods than the two month period. Gravity field solutions exist, which have a temporal resolution of 10 days or one week. These solutions are constrained, as the GRACE satellites provide too few ground tracks to

allow unconstrained gravity field solutions with a high temporal resolution. If several pairs of GRACE satellites were in the orbit, unconstrained gravity field solutions with a higher temporal resolution would be available.
Covariance components are estimated correctly and showed the same convergence as variance components in simple simulated examples. In contrast to that, the covariance components between C_{20} and $C_{21}/S_{21}/C_{22}/S_{22}$ of *ITG 2010* showed comparatively large variations around the point of convergence, if six gravity field time series was considered. If only *ITG 2010* was considered, the convergence decreased such that a reliable estimation of the covariance component were not possible. Therefore it was concluded that the partial redundancies might play a major role. Though the estimation of covariance components is described on a theoretical basis in literature, no further numerical examples for the estimation of covariance components are available so far. The reason for the deteriorated convergence of the covariance components is not completely understood up to now. Further theoretical and experimental investigations are necessary. Two reasons might cause the insufficient convergence of the covariance components: First the SMCTE might not estimate the traces with sufficient accuracy. Finding tighter bounds for the trace estimation of asymmetric matrices (Equation 3.57) might clarify the effect of the SMCTE. The second, more likely reason for inaccurate covariance components might be an ill-conditioned matrix $\boldsymbol{S}$ (Equation 3.42), which is probably caused by too small partial redundancies of the associated observations.
The proposed linear least-squares solver is proven to be an adequate approach for the mutual validation. However, other approaches also might be suitable. The Kalman and Bayes filter are highly efficient, recursive analysis methods. Two steps are performed in each filter epoch. First, based on previous epochs and a mathematical model, the filters predict the state vector, containing the unknown parameters, for the current epoch. In the second step, the observations of the current epoch are taken into account and are used to improve the predicted state vector. Then, the improved state vector is the basis for the next prediction. However, as the time derivatives of the polar motion are unavailable, they have to be approximated. If the time derivative of the current epoch is approximated by a difference quotient, the current epoch depends on measurements of the previous and the next epoch. Thus, the measurements of the epochs are not independent on each other and three different residuals occur for the same observation in three consecutive epochs. If the temporal correlations are stretched over several epochs, the application of recursive filters is additionally complicated. However, despite of the difficulties due to the epoch dependencies, the Kalman filter is currently investigated, in order to estimate Love numbers (personal communication S. Kirschner and F. Seitz, September 2012).
This dissertation validated integral time series. The validation did not allow a spatial separation of specific effects. However, the spatial resolution of gravity fields is described by the maximal degree and order of the gravity field coefficients. If gravity field coefficients of higher degrees can be validated, a spatial mapping of inconsistencies is possible. The geophysical models deliver masses and motions of the Earth subsystems in threedimensional grids. The grid values can be used to integrate modeled gravity field coefficients of degree n and order m according to the Equations 2.58. A comparison of the resulting modeled gravity field coefficients with gravity field coefficients resulting from measurements would allow the spatial mapping of inconsistencies. Thus, this dissertation might be a first step towards the spatial validation of geophysical models and gravity field coefficients of higher degrees. The spatial validation should be a further fascinating research project.

Appendix A Removing long periodic tidal variations from EOP

The polar motion is usually expressed by a complex-valued quantity

$$\tilde{p} = p_x - \mathrm{i}\, p_y, \tag{A.1}$$

where by conventions the p_x points towards the 0° longitude and p_y towards the 90°W longitude.
The complex-valued corrections $\delta_{\tilde{p}}$ due to long periodic oceanic tides (10 periods from 9 days to 18.6 years) in the polar motion are according to IERS Conventions (2010, chapter 8)

$$\delta_{\tilde{p}} = \delta_{p_x} - \mathrm{i}\,\delta_{p_y} = \sum_{j=1}^{10} A_{p_j} \exp\left(\phi_{p_j}\right) \exp\left(\mathrm{i}\xi_j\right) + A_{rj} \exp\left(\phi_{rj}\right) \exp\left(-\mathrm{i}\xi_j\right). \tag{A.2}$$

The prograde and retrograde amplitudes A_{p_j} and A_{rj} and the prograde and retrograde phases ϕ_{p_j} and ϕ_{rj} are given in IERS Conventions (2010, table 8.4). The arguments ξ_j are time-dependent values given in Equation A.5. These corrections result from the Dickman and Nam (1995) and Dickman and Gross (2010).
The correction for long periodic, lunisolar, tidal effects (62 periods from 5 days to 18.6 years) in the polar motion and LOD / UT1-UTC are obtained from

$$\delta_{\mathrm{UT1}} = \sum_{j=1}^{62} B_j \sin\xi_j + C_j \cos\xi_j \tag{A.3}$$

$$\delta_{\mathrm{LOD}} = \sum_{j=1}^{62} B'_j \sin\xi_j + C'_j \cos\xi_j. \tag{A.4}$$

B_j, C_j, B'_j and C'_j are given in IERS Conventions (2010, table 8.1). The values in this table result from Yoder et al. (1981), Wahr and Bergen (1986) and Kantha et al. (1998). The arguments ξ_j are calculated from the fundamental arguments α_k of the nutation theory by

$$\xi_j = \sum_{k=1}^{5} a_{jk}\alpha_k. \tag{A.5}$$

The integer multipliers a_{jk} for the k^{th} tide are given in the tables 8.1 and 8.4 of the IERS Conventions (2010). The fundamental arguments α_k are according to IERS Conventions (2010, section 5.7.2)

$$\begin{aligned}
\alpha_1 = l &= 134.96340251^\circ + 1717915923.2178''t' + 31.8792''t'^2 + 0.051635''t'^3 - 0.00024470''t'^4 \\
\alpha_2 = l' &= 357.52910918^\circ + 129596581.0481''t' - 0.5532''t'^2 + 0.000136''t'^3 - 0.00001149''t'^4 \\
\alpha_3 = F &= L - \Omega \\
&= 93.27209062^\circ + 1739527262.8478''t' - 12.7512''t'^2 - 0.001037''t'^3 + 0.00000417''t'^4 \\
\alpha_4 = D &= 297.85019547^\circ + 1602961601.2090''t' - 6.3706''t'^2 + 0.006593''t'^3 - 0.00003169''t'^4 \\
\alpha_5 = \Omega &= 125.04455501^\circ - 6962890.5431''t' + 7.4722''t'^2 + 0.007702''t'^3 - 0.00005939''t'^4
\end{aligned} \tag{A.6}$$

where t' denotes the Julian centuries since the J2000.0

$$t' = \frac{(t - \mathrm{J2000.0}) \text{ in days}}{36525}. \tag{A.7}$$

The fundamental arguments are linear combinations of

- l: mean anomaly of the Moon,
- l': mean anomaly of the Sun,
- L: mean longitude of the Moon,
- Ω: mean longitude of the ascending node of the Moon and
- D: mean elongation of the Moon from the Sun.

The corrections in Equations A.2, A.3 and A.4 have to be subtracted from the observed EOP, in order to obtain EOP free from long periodic tidal variations.

Appendix B Theorems from Koch (1999)

Koch (1999) provided several theorems including their proofs which are used for the derivations in Chapter 3. This appendix lists the most important theorems without proofs.

Theorems 1.143 and 1.144, page 40: Trace operations

Let $\boldsymbol{A}$ and $\boldsymbol{B}$ be two $n \times n$ matrices. Then it holds

$$\operatorname{tr}(\boldsymbol{A} + \boldsymbol{B}) = \operatorname{tr}(\boldsymbol{A}) + \operatorname{tr}(\boldsymbol{B}). \tag{B.1}$$

Further let $\boldsymbol{A}$ be a $n \times r$ and $\boldsymbol{B}$ a $r \times n$ matrix. Then it holds

$$\operatorname{tr}(\boldsymbol{AB}) = \operatorname{tr}(\boldsymbol{BA}). \tag{B.2}$$

Theorem 1.267, page 69: Differentiation of quadratic forms

Let $\boldsymbol{x}$ be a $n \times 1$ vector and $\boldsymbol{A}$ a $n \times n$ matrix. Then it holds

$$\frac{\mathsf{d}\, \boldsymbol{x}^{\mathsf{T}} \boldsymbol{A} \boldsymbol{x}}{\mathsf{d}\, \boldsymbol{x}} = 2\boldsymbol{A}\boldsymbol{x}. \tag{B.3}$$

Theorem 1.269, page 70: Differentiation of the trace of a matrix product

Let $\boldsymbol{A}$ be a $m \times n$ and $\boldsymbol{B}$ a $n \times m$ matrix. Then it holds

$$\frac{\mathsf{d}\, \operatorname{tr}(\boldsymbol{AB})}{\mathsf{d}\, \boldsymbol{A}} = \boldsymbol{B}^{\mathsf{T}}. \tag{B.4}$$

Theorem 1.270, page 70: Differentiation of the trace of a matrix product of the type $\boldsymbol{ABAC}$

Let $\boldsymbol{A}$ be a $m \times n$ and $\boldsymbol{B}$ and $\boldsymbol{C}$ two $n \times m$ matrices. Then it holds

$$\frac{\mathsf{d}\, \operatorname{tr}(\boldsymbol{ABAC})}{\mathsf{d}\, \boldsymbol{A}} = (\boldsymbol{BAC} + \boldsymbol{CAB})^{\mathsf{T}}. \tag{B.5}$$

If $\boldsymbol{B} = \boldsymbol{C}$ and $\boldsymbol{A}$ and $\boldsymbol{B}$ are symmetric, it follows from this theorem

$$\frac{\mathsf{d}\, \operatorname{tr}(\boldsymbol{ABAB})}{\mathsf{d}\, \boldsymbol{A}} = 2\boldsymbol{BAB}. \tag{B.6}$$

Theorem 2.174, page 134: Expectation value of a quadratic form

Let $\boldsymbol{x}$ be a $n \times 1$ stochastic vector with the expectation value $\mathrm{E}(\boldsymbol{x}) = \boldsymbol{\mu}_{\boldsymbol{x}}$ and the VCM $\boldsymbol{D}_{\boldsymbol{xx}}$. Then it holds

$$\mathrm{E}\left(\boldsymbol{x}^{\mathsf{T}} \boldsymbol{A} \boldsymbol{x}\right) = \operatorname{tr}(\boldsymbol{A}\boldsymbol{D}_{\boldsymbol{xx}}) + \boldsymbol{\mu}_{\boldsymbol{x}}^{\mathsf{T}} \boldsymbol{A} \boldsymbol{\mu}_{\boldsymbol{x}}. \tag{B.7}$$

Theorem 2.175, page 134: Covariance of two quadratic forms

The $n \times 1$ stochastic vector $\boldsymbol{x}$ is assumed to be normally distributed with $\boldsymbol{x} \sim \mathcal{N}(\boldsymbol{\mu}_{\boldsymbol{x}}, \boldsymbol{D}_{\boldsymbol{xx}})$. Then it holds for the covariance of the two quadratic forms $\boldsymbol{x}^{\mathsf{T}}\boldsymbol{A}\boldsymbol{x}$ and $\boldsymbol{x}^{\mathsf{T}}\boldsymbol{B}\boldsymbol{x}$

$$\operatorname{Cov}\left(\boldsymbol{x}^{\mathsf{T}} \boldsymbol{A} \boldsymbol{x}, \boldsymbol{x}^{\mathsf{T}} \boldsymbol{B} \boldsymbol{x}\right) = 2\operatorname{tr}(\boldsymbol{A}\boldsymbol{D}_{\boldsymbol{xx}}\boldsymbol{B}\boldsymbol{D}_{\boldsymbol{xx}}) + 4\boldsymbol{\mu}_{\boldsymbol{x}}^{\mathsf{T}} \boldsymbol{A} \boldsymbol{D}_{\boldsymbol{xx}} \boldsymbol{B} \boldsymbol{\mu}_{\boldsymbol{x}}. \tag{B.8}$$

The variance of a quadratic form follows from this theorem with

$$\operatorname{Var}\left(\boldsymbol{x}^{\mathsf{T}} \boldsymbol{A} \boldsymbol{x}\right) = 2\operatorname{tr}(\boldsymbol{A}\boldsymbol{D}_{\boldsymbol{xx}}\boldsymbol{A}\boldsymbol{D}_{\boldsymbol{xx}}) + 4\boldsymbol{\mu}_{\boldsymbol{x}}^{\mathsf{T}} \boldsymbol{A} \boldsymbol{D}_{\boldsymbol{xx}} \boldsymbol{A} \boldsymbol{\mu}_{\boldsymbol{x}}. \tag{B.9}$$

Appendix C Förstner's approach and the estimation of covariance components

Assume, that the x- and y-coordinate of one point in a 2D-reference system is observed n times with equal but unknown accuracy. The x- and y-coordinates of each observation are correlated and the n observations of this point are not correlated which each other. The adjusted coordinates of the point and the variances σ_x^2 and σ_y^2 and the covariance σ_{xy} are estimated according to Section 3.2. This problem is an unconstrained GMM. Since the coordinates of the point are observed with equal accuracy, one would expect that the adjusted point coordinates are the arithmetic average of the observations and the adjusted variances and covariance are equal to the empirical variances and covariance. This appendix proves two facts: First, the results of the variance covariance estimation are as expected and second, Förstner's approach fails, if covariances have to be considered.
If the observations and unknown parameters are sorted as follows, the design matrix $\boldsymbol{A}$ is

$$\boldsymbol{l} = \begin{bmatrix} x_1 \\ x_2 \\ \vdots \\ x_n \\ y_1 \\ y_2 \\ \vdots \\ y_n \end{bmatrix}, \qquad \boldsymbol{\beta} = \begin{bmatrix} x \\ y \end{bmatrix}, \qquad \text{and} \quad \boldsymbol{A} = \begin{bmatrix} 1 & 0 \\ 1 & 0 \\ \vdots & \vdots \\ 1 & 0 \\ 0 & 1 \\ 0 & 1 \\ \vdots & \vdots \\ 0 & 1 \end{bmatrix}. \tag{C.1}$$

The VCM of the observation is obtained from the 'first-guessed' variances σ_{x0}^2 and σ_{y0}^2 and the covariance σ_{xy0}

$$\boldsymbol{\Sigma}_{ll0} = \begin{bmatrix} \sigma_{x0}^2\boldsymbol{I} & \sigma_{xy0}\boldsymbol{I} \\ \sigma_{xy0}\boldsymbol{I} & \sigma_{y0}^2\boldsymbol{I} \end{bmatrix} \quad \text{with} \quad \boldsymbol{I} = n \times n \text{ identity matrix.} \tag{C.2}$$

Then, the system of normal equations is

$$\frac{n}{\sigma_{x0}^2\sigma_{y0}^2 - \sigma_{xy0}^2} \begin{bmatrix} \sigma_{y0}^2 & -\sigma_{xy0} \\ -\sigma_{xy0} & \sigma_{x0}^2 \end{bmatrix} \boldsymbol{\beta} = \frac{1}{\sigma_{x0}^2\sigma_{y0}^2 - \sigma_{xy0}^2} \begin{bmatrix} \sigma_{y0}^2 \sum_{i=1}^n x_i - \sigma_{xy0}^2 \sum_{i=1}^n y_i \\ -\sigma_{xy0} \sum_{i=1}^n x_i + \sigma_{x0}^2 \sum_{i=1}^n y_i \end{bmatrix}. \tag{C.3}$$

This system of normal equations leads to the adjusted point coordinates, which are independent of the chosen a priori VCM

$$\hat{\boldsymbol{\beta}} = \begin{bmatrix} \hat{x} \\ \hat{y} \end{bmatrix} = \frac{1}{n} \begin{bmatrix} \sum_{i=1}^n x_i \\ \sum_{i=1}^n y_i \end{bmatrix}. \tag{C.4}$$

As expected, the adjusted point coordinates are the arithmetic average of the observations. The residuals are the deviations of the observations from the arithmetic average with

$$\boldsymbol{\epsilon}_x = \begin{bmatrix} x_1 - \hat{x} \\ x_2 - \hat{x} \\ \vdots \\ x_n - \hat{x} \end{bmatrix} \quad \text{and} \quad \boldsymbol{\epsilon}_y = \begin{bmatrix} y_1 - \hat{y} \\ y_2 - \hat{y} \\ \vdots \\ y_n - \hat{y} \end{bmatrix}. \tag{C.5}$$

The VCC σ_x^2, σ_y^2 and σ_{xy} are estimated based on following stochastic model

$$\boldsymbol{\Sigma}_{ll} = \sigma_x^2 \underbrace{\sigma_{x0}^2 \begin{bmatrix} \boldsymbol{I} & \boldsymbol{0} \\ \boldsymbol{0} & \boldsymbol{0} \end{bmatrix}}_{\boldsymbol{V}_x} + \sigma_y^2 \underbrace{\sigma_{y0}^2 \begin{bmatrix} \boldsymbol{0} & \boldsymbol{0} \\ \boldsymbol{0} & \boldsymbol{I} \end{bmatrix}}_{\boldsymbol{V}_y} + \sigma_{xy} \underbrace{\sigma_{xy0} \begin{bmatrix} \boldsymbol{0} & \boldsymbol{I} \\ \boldsymbol{I} & \boldsymbol{0} \end{bmatrix}}_{\boldsymbol{V}_{xy}}. \tag{C.6}$$

The estimation of the VCC is obtained according to Section 3.2. With the given design matrix and systems of normal equations, the matrix $\boldsymbol{W}$ is

$$\boldsymbol{W} = \frac{1}{\sigma_{x0}^2\sigma_{y0}^2 - \sigma_{xy0}^2} \begin{bmatrix} \sigma_{y0}^2 \left(\boldsymbol{I} - \frac{1}{n}\boldsymbol{E}\right) & -\sigma_{xy0} \left(\boldsymbol{I} - \frac{1}{n}\boldsymbol{E}\right) \\ -\sigma_{xy0} \left(\boldsymbol{I} - \frac{1}{n}\boldsymbol{E}\right) & \sigma_{x0}^2 \left(\boldsymbol{I} - \frac{1}{n}\boldsymbol{E}\right) \end{bmatrix} \quad \text{with} \quad \boldsymbol{E} = \begin{bmatrix} 1 & \dots & 1 \\ \vdots & \ddots & \vdots \\ 1 & \dots & 1 \end{bmatrix}. \tag{C.7}$$

Then, the matrix $\boldsymbol{S}$ and the vector $\boldsymbol{q}$ are

$$\begin{aligned}\boldsymbol{S} &= \frac{n-1}{\left(\sigma_{x_0}^2\sigma_{y_0}^2 - \sigma_{xy_0}^2\right)^2}\begin{bmatrix}\sigma_{x_0}^4\sigma_{y_0}^4 & \sigma_{x_0}^2\sigma_{y_0}^2\sigma_{xy_0}^2 & -2\sigma_{x_0}^2\sigma_{y_0}^2\sigma_{xy_0}^2\\ \sigma_{x_0}^2\sigma_{y_0}^2\sigma_{xy_0}^2 & \sigma_{x_0}^4\sigma_{y_0}^4 & -2\sigma_{x_0}^2\sigma_{y_0}^2\sigma_{xy_0}^2\\ -2\sigma_{x_0}^2\sigma_{y_0}^2\sigma_{xy_0}^2 & -2\sigma_{x_0}^2\sigma_{y_0}^2\sigma_{xy_0}^2 & 2\left(\sigma_{xy_0}^4 + \sigma_{x_0}^2\sigma_{y_0}^2\sigma_{xy_0}^2\right)\end{bmatrix},\\ \boldsymbol{q} &= \frac{1}{\left(\sigma_{x_0}^2\sigma_{y_0}^2 - \sigma_{xy_0}^2\right)^2}\begin{bmatrix}\sigma_{x_0}^2\sigma_{y_0}^4\boldsymbol{\epsilon}_x^\mathsf{T}\boldsymbol{\epsilon}_x - 2\sigma_{x_0}^2\sigma_{y_0}^2\sigma_{xy_0}\boldsymbol{\epsilon}_y^\mathsf{T}\boldsymbol{\epsilon}_x + \sigma_{x_0}^2\sigma_{xy_0}^2\boldsymbol{\epsilon}_y^\mathsf{T}\boldsymbol{\epsilon}_y\\ \sigma_{y_0}^2\sigma_{xy_0}^2\boldsymbol{\epsilon}_x^\mathsf{T}\boldsymbol{\epsilon}_x - 2\sigma_{x_0}^2\sigma_{y_0}^2\sigma_{xy_0}\boldsymbol{\epsilon}_y^\mathsf{T}\boldsymbol{\epsilon}_x + \sigma_{x_0}^4\sigma_{y_0}^2\boldsymbol{\epsilon}_y^\mathsf{T}\boldsymbol{\epsilon}_y\\ -2\sigma_{y_0}^2\sigma_{xy_0}^2\boldsymbol{\epsilon}_x^\mathsf{T}\boldsymbol{\epsilon}_x + 2\left(\sigma_{x_0}^2\sigma_{y_0}^2\sigma_{xy_0} + \sigma_{xy_0}^3\right)\boldsymbol{\epsilon}_y^\mathsf{T}\boldsymbol{\epsilon}_x - 2\sigma_{x_0}^2\sigma_{xy_0}^2\boldsymbol{\epsilon}_y^\mathsf{T}\boldsymbol{\epsilon}_y\end{bmatrix}.\end{aligned} \tag{C.8}$$

The adjusted VCC are obtained by the given matrix $\boldsymbol{S}$ and the vector $\boldsymbol{q}$ with

$$\hat{\boldsymbol{\sigma}} = \begin{bmatrix}\hat{\sigma}_x\\ \hat{\sigma}_y\\ \hat{\sigma}_{xy}\end{bmatrix} = \boldsymbol{S}^{-1}\boldsymbol{q} = \frac{1}{n-1}\begin{bmatrix}\frac{1}{\sigma_{x_0}^2}\boldsymbol{\epsilon}_x^\mathsf{T}\boldsymbol{\epsilon}_x\\ \frac{1}{\sigma_{y_0}^2}\boldsymbol{\epsilon}_y^\mathsf{T}\boldsymbol{\epsilon}_y\\ \frac{1}{\sigma_{xy_0}}\boldsymbol{\epsilon}_y^\mathsf{T}\boldsymbol{\epsilon}_x\end{bmatrix}. \tag{C.9}$$

As expected, the products $\hat{\sigma}_x\sigma_{x_0}^2$, $\hat{\sigma}_y\sigma_{y_0}^2$ and $\hat{\sigma}_{xy}\sigma_{xy_0}$ contain the empiric variance for the x-coordinate $\frac{1}{n-1}\boldsymbol{\epsilon}_x^\mathsf{T}\boldsymbol{\epsilon}_x$, the empiric variance for the y-coordinate $\frac{1}{n-1}\boldsymbol{\epsilon}_y^\mathsf{T}\boldsymbol{\epsilon}_y$ and the empiric covariance $\frac{1}{n-1}\boldsymbol{\epsilon}_y^\mathsf{T}\boldsymbol{\epsilon}_x$.
According to Förstner's approach, matrix $\boldsymbol{S}$ is modified as follows

$$\boldsymbol{S}_{\text{Förstner}} = \begin{bmatrix}\operatorname{tr}(\boldsymbol{W}\boldsymbol{V}_1) & 0 & 0\\ 0 & \operatorname{tr}(\boldsymbol{W}\boldsymbol{V}_2) & 0\\ 0 & 0 & \operatorname{tr}(\boldsymbol{W}\boldsymbol{V}_3)\end{bmatrix}. \tag{C.10}$$

The adjusted VCC of Förstner's approach are then

$$\hat{\boldsymbol{\sigma}}_{\text{Förstner}} = \frac{1}{(n-1)\left(\sigma_{x_0}^2\sigma_{y_0}^2 - \sigma_{xy_0}^2\right)}\begin{bmatrix}\sigma_{y_0}^2\boldsymbol{\epsilon}_x^\mathsf{T}\boldsymbol{\epsilon}_x - 2\sigma_{xy_0}\boldsymbol{\epsilon}_y^\mathsf{T}\boldsymbol{\epsilon}_x + \frac{\sigma_{xy_0}^2}{\sigma_{y_0}^2}\boldsymbol{\epsilon}_y^\mathsf{T}\boldsymbol{\epsilon}_y\\ \frac{\sigma_{xy_0}^2}{\sigma_{x_0}^2}\boldsymbol{\epsilon}_x^\mathsf{T}\boldsymbol{\epsilon}_x - 2\sigma_{xy_0}\boldsymbol{\epsilon}_y^\mathsf{T}\boldsymbol{\epsilon}_x + \sigma_{x_0}^2\boldsymbol{\epsilon}_y^\mathsf{T}\boldsymbol{\epsilon}_y\\ \sigma_{y_0}^2\boldsymbol{\epsilon}_x^\mathsf{T}\boldsymbol{\epsilon}_x - \left(\frac{\sigma_{x_0}^2\sigma_{y_0}^2}{\sigma_{xy_0}} + \sigma_{xy_0}\right)\boldsymbol{\epsilon}_y^\mathsf{T}\boldsymbol{\epsilon}_x + \sigma_{x_0}^2\boldsymbol{\epsilon}_y^\mathsf{T}\boldsymbol{\epsilon}_y\end{bmatrix}. \tag{C.11}$$

According to Förstner's approach, the variance component $\hat{\sigma}_x$ depends not only on the empiric variance for the x-coordinate but also on the empiric variance of the y-coordinate and the empiric covariance. According to Equation C.11, the correct variances of the x- and y-coordinates are only obtained, if the covariance σ_{xy_0} is zero. Since Förstner's approach fails in this comparatively simple example, his approach is not universally appropriate for the estimation of covariances.

Appendix D Algorithm: Pseudocode of the extended SMCTE

```
Input: observations l
       z variance covariance matrices V_i
       termination conditions for while loop e_1 and e_2
       approximated vector of the unknown parameter β_0
       number of samples n_s for the SMCTE
set σ_i^1 = 1 for i = 1,...z
set arbitrary value larger than termination condition Δβ_i > e_1
set counter c = 1
WHILE max(|Δβ̂|) > e_1 AND max(|σ_i^c − 1|) > e_2
{   linearize non-linear equations: w_H, w_C, A_H, A_C and B                (Eq. 3.3)
    calculate stoch. model: Q_i = ∏_{j=1}^{c} σ_i^j B V_i B^T and D_ww = Σ_{i=1}^{z} Q_i   (Eq. 3.23)
    set up normal equation matrix: N = [ A_H^T D_ww^{-1} A_H   A_C^T ]
                                       [ A_C                   0     ]
    solve system of normal equations: [ Δβ ]   = N^{-1} [ A^T D_ww^{-1} w_H ]   (Eq. 3.11)
                                      [ k_C ]          [ w_C                 ]

    calculate residuals: Bε = A_H Δβ − w_H                                  (Eq. 3.3)
    FOR i = 1,...,z
    {   solve: h_0 = D_ww^{-1} (Bε)
        calculate: q_i = h_0^T Q_i h_0                                      (Eq. 3.41)
        FOR j = i,...,z
        {   FOR k = 1,...,n_s
            {   draw sample: u
                solve: h_1 = D_ww^{-1} (Q_j u)
                solve: h_2 = N^{-1} [ A^T h_1 ]
                                    [ 0       ]
                solve: h_3 = D_ww^{-1} ( [A  0] h_2 )
                solve: h_4 = D_ww^{-1} (Q_k (h_1 − h_3))
                solve: h_5 = N^{-1} [ A^T h_4 ]
                                    [ 0       ]
                solve: h_6 = D_ww^{-1} ( [A  0] h_5 )
                calculate trace sample: s_ij^k = u^T (h_4 − h_6)            (Eq. 3.42)
            }
            calculate arithmetic average: s_ij = Σ_{k=1}^{n_s} s_ij^k / n_s   (Eq. 3.60)
            set: s_ji = s_ij
        }
    }
    solve: σ^{c+1} = S^{-1} q                                               (Eq. 3.46)
    update: β_0 = β_0 + Δβ
    calculate new counter: c = c + 1
}
```

Appendix E Reduction of unknown parameters (spline coefficients)

If the size of an arbitrary system of normal equations is denoted with s, approximately s^3 floating point operations are required for the solution of the system of normal equations. Thus, the reduction of the unknowns decreases the number of floating points considerably and leads to smaller but denser systems of normal equations.

A time series with an arbitrary number of observations is described by n cubic splines. Then, these splines depend on $4n$ spline coefficients. If the splines are constrained such that the splines are twice continuously differentiable in the transition points from one spline to the next spline, $3\,(n-1)$ condition equations arise. The splines and the constraints are described by Equations 4.4 and 4.7a to 4.7c. This appendix uses the constraints in Equation 4.7a to 4.7c to reduce the numbers of the unknown spline coefficients from $4n$ to $n+3$ spline coefficients.

Equation 4.7c is solved for a_i

$$a_i = \frac{\left(\frac{T_{i+1}-T_i}{T_{i+2}-T_{i+1}}\right)^2 b_{i+1} - b_i}{3}. \tag{E.1}$$

Substituting a_i into Equation 4.7a leads to

$$\begin{aligned} c_i &= d_{i+1} - d_i - \frac{\left(\frac{T_{i+1}-T_i}{T_{i+2}-T_{i+1}}\right)^2 b_{i+1} + 2b_i}{3} \qquad \text{and} \\ c_{i+1} &= d_{i+2} - d_{i+1} - \frac{\left(\frac{T_{i+2}-T_{i+1}}{T_{i+3}-T_{i+2}}\right)^2 b_{i+2} + 2b_{i+1}}{3}, \end{aligned} \tag{E.2}$$

respectively. If c_i and c_{i+1} are substituted in Equation 4.7b, it holds

$$\begin{aligned} \left(\frac{T_{i+1}-T_i}{T_{i+2}-T_{i+1}}\right)^2 b_{i+1} + b_i = \frac{T_{i+1}-T_i}{T_{i+2}-T_{i+1}} \left(d_{i+2} - d_{i+1} - \frac{\left(\frac{T_{i+2}-T_{i+1}}{T_{i+3}-T_{i+2}}\right)^2 b_{i+2} + 2b_{i+1}}{3} \right) + \\ - d_{i+1} + d_i + \frac{\left(\frac{T_{i+1}-T_i}{T_{i+2}-T_{i+1}}\right)^2 b_{i+1} + 2b_i}{3} \\ \Rightarrow \quad \frac{(T_{i+1}-T_i)\,(T_{i+2}-T_{i+1})}{(T_{i+3}-T_{i+2})^2} b_{i+2} + 2\left(\left(\frac{T_{i+1}-T_i}{T_{i+2}-T_{i+1}}\right)^2 + \frac{T_{i+1}-T_i}{T_{i+2}-T_{i+1}} \right) b_{i+1} + b_i = \\ 3\frac{T_{i+1}-T_i}{T_{i+2}-T_{i+1}} d_{i+2} - 3\left(\frac{T_{i+1}-T_i}{T_{i+2}-T_{i+1}} + 1 \right) d_{i+1} + 3d_i. \end{aligned} \tag{E.3}$$

The $4n$ spline coefficients are reduced to following $n+3$ parameters

$$\boldsymbol{\beta}_{sp} = \begin{bmatrix} a_n & b_1 & b_n & d_1 & d_2 & \dots & d_n \end{bmatrix}^{\mathsf{T}}. \tag{E.4}$$

All spline coefficients are linearly depended on the spline coefficients of the vector $\boldsymbol{\beta}_{sp}$. The parameters d_i depend on $\boldsymbol{\beta}_{sp}$ as follows

$$\begin{bmatrix} d_1 \\ d_2 \\ \vdots \\ d_n \end{bmatrix} = \underbrace{\begin{bmatrix} 0 & 0 & 0 & 1 & 0 & \dots & 0 \\ 0 & 0 & 0 & 0 & 1 & \dots & 0 \\ \vdots & \vdots & \vdots & \vdots & \vdots & \ddots & \vdots \\ 0 & 0 & 0 & 0 & 0 & \dots & 1 \end{bmatrix}}_{\boldsymbol{T}_d} \boldsymbol{\beta}_{sp}. \tag{E.5}$$

Equation E.3 results in

$$\underbrace{\begin{bmatrix} 1 & 0 & 0 & 0 & \dots & 0 \\ 1 & 2\left(\left(\frac{T_2-T_1}{T_3-T_2}\right)^2+\frac{T_2-T_1}{T_3-T_2}\right) & \frac{(T_2-T_1)(T_3-T_2)}{(T_4-T_3)^2} & 0 & \dots & 0 \\ 0 & 1 & 2\left(\left(\frac{T_3-T_2}{T_4-T_3}\right)^2+\frac{T_3-T_2}{T_4-T_3}\right) & \frac{(T_3-T_2)(T_4-T_3)}{(T_5-T_4)^2} & \dots & 0 \\ \vdots & \vdots & \ddots & \ddots & \ddots & \vdots \\ 0 & 0 & \dots & \dots & \dots & 1 \end{bmatrix}}_{\boldsymbol{H}_b} \begin{bmatrix} b_1 \\ b_2 \\ \vdots \\ b_n \end{bmatrix} =$$

$$\underbrace{\begin{bmatrix} 0 & 1 & 0 & 0 & 0 & 0 & 0 & \dots & 0 \\ 0 & 0 & 0 & 3 & -3\left(\frac{T_2-T_1}{T_3-T_2}+1\right) & 3\frac{T_2-T_1}{T_3-T_2} & 0 & \dots & 0 \\ 0 & 0 & 0 & 0 & 3 & -3\left(\frac{T_3-T_2}{T_4-T_3}+1\right) & 3\frac{T_3-T_2}{T_4-T_3} & \dots & 0 \\ \vdots & \vdots & \vdots & \vdots & \vdots & \ddots & \ddots & \ddots & \vdots \\ 0 & 0 & 1 & 0 & 0 & \dots & \dots & \dots & 0 \end{bmatrix}}_{\boldsymbol{H}_d} \boldsymbol{\beta}_{sp}. \quad \text{E.6}$$

The matrix $\boldsymbol{H}_b$ is quadratic, regular and band diagonal. Therefore, a unique inverse exists. The spline coefficients b_i are then obtained by

$$\begin{bmatrix} b_1 \\ b_2 \\ \vdots \\ b_n \end{bmatrix} = \boldsymbol{H}_b^{-1}\boldsymbol{H}_d\boldsymbol{\beta}_{sp} = \boldsymbol{T}_b\boldsymbol{\beta}_{sp}. \quad \text{E.7}$$

It follows from Equation E.1

$$\begin{bmatrix} a_1 \\ a_2 \\ \vdots \\ a_n \end{bmatrix} = \left[\begin{bmatrix} -\frac{1}{3} & \frac{1}{3}\left(\frac{T_2-T_1}{T_3-T_2}+1\right)^2 & 0 & \dots & 0 \\ 0 & -\frac{1}{3} & \frac{1}{3}\left(\frac{T_3-T_2}{T_4-T_1}+1\right)^2 & \dots & 0 \\ \vdots & \vdots & \ddots & \ddots & \vdots \\ & & \begin{bmatrix} 1 & 0 & 0 & \dots & 0 \end{bmatrix} & & \end{bmatrix} \boldsymbol{T}_b \right] \boldsymbol{\beta}_{sp} = \boldsymbol{T}_a\boldsymbol{\beta}_{sp}. \quad \text{E.8}$$

The spline coefficients c_1 to c_{n-1} are obtained from Equation E.2 by

$$\begin{bmatrix} c_1 \\ c_2 \\ \vdots \\ c_{n-1} \end{bmatrix} = \underbrace{\left(\begin{bmatrix} -1 & 1 & 0 & \dots & 0 \\ 0 & -1 & 1 & \dots & 0 \\ \vdots & \vdots & \ddots & \ddots & \vdots \end{bmatrix} \boldsymbol{T}_d - \begin{bmatrix} \frac{2}{3} & \frac{1}{3}\left(\frac{T_2-T_1}{T_3-T_2}+1\right)^2 & 0 & \dots & 0 \\ 0 & \frac{2}{3} & \frac{1}{3}\left(\frac{T_3-T_2}{T_4-T_3}+1\right)^2 & \dots & 0 \\ \vdots & \vdots & \ddots & \ddots & \vdots \end{bmatrix} \boldsymbol{T}_b \right)}_{\boldsymbol{T}_{c1}} \boldsymbol{\beta}_{sp}. \quad \text{E.9}$$

The coefficient c_n is obtained from Equation 4.7b by

$$c_n = \underbrace{\frac{T_{n+1}-T_n}{T_n-T_{n-1}}\left(3\boldsymbol{T}_a^{n-1}+2\boldsymbol{T}_b^{n-1}+\boldsymbol{H}_{c1}^{n-1}\right)}_{\boldsymbol{T}_{c2}}\boldsymbol{\beta}_{sp} \quad \text{E.10}$$

where the index $n-1$ denotes the $(n-1)$-th row of the associated matrix. A vector containing the c_i including c_n is then described by

$$\begin{bmatrix} c_1 \\ c_2 \\ \vdots \\ c_n \end{bmatrix} = \begin{bmatrix} \boldsymbol{T}_{c1} \\ \boldsymbol{T}_{c2} \end{bmatrix} \boldsymbol{\beta}_{sp} = \boldsymbol{T}_c\boldsymbol{\beta}_{sp}. \quad \text{E.11}$$

Equations E.5, E.7, E.8 and E.11 describe the linear dependency of all spline coefficients on the spline coefficients in vector $\boldsymbol{\beta}_{sp}$. Thus, the k-th observation, belonging to the i-th spline, is described by

$$l_k^i + v_k = \left(\tau_k^3 \boldsymbol{T}_a^i + \tau_k^2 \boldsymbol{T}_b^i + \tau_k \boldsymbol{T}_c^i + \boldsymbol{T}_d^i\right) \boldsymbol{\beta}_{sp} = \boldsymbol{A}_{sp}^i \boldsymbol{\beta}_{sp}. \tag{E.12}$$

Then, the time derivative of the k-th observation is

$$\dot{l}_k^i = \frac{1}{T_{i+1} - T_i} \left(3\tau_k^2 \boldsymbol{T}_a^i + 2\tau_k \boldsymbol{T}_b^i + \boldsymbol{T}_c^i\right) \boldsymbol{\beta}_{sp} = \boldsymbol{B}_{sp}^i \boldsymbol{\beta}_{sp}. \tag{E.13}$$

The matrices $\boldsymbol{A}_{sp}$ and $\boldsymbol{B}_{sp}$ depend on the time of the observations and the transition points of the splines. These matrices are introduced in the linear least-squares adjustment proposed in Subsection 4.2.1.

References

H. Alkhatib. *On Monte Carlo methods with applications to the current satellite gravity missions*. PhD thesis, University of Bonn, Institute for Geodesy and Geoinformation, 2007. URL http://hss.ulb.uni-bonn.de/2007/1078/1078.htm.

Z. Altamimi, X. Collilieux, J. Legrand, B. Garayt, and C. Boucher. ITRF2005: A new release of the International Terrestrial Reference Frame based on time series of station positions and Earth Orientation Parameters. *J. Geophys. Res.*, 112(B9):B09401–, Sept. 2007. ISSN 0148-0227. URL http://dx.doi.org/10.1029/2007JB004949.

Z. Altamimi, X. Collilieux, and L. Métivier. ITRF2008: an improved solution of the international terrestrial reference frame. *Journal of Geodesy*, 85:457–473, 2011. ISSN 0949-7714. URL http://dx.doi.org/10.1007/s00190-011-0444-4.

D. Angermann, H. Drewes, M. Gerstl, M. Krügel, and B. Meisel. DGFI Combination Methodology for ITRF2005 Computation. In H. Drewes, editor, *Geodetic Reference Frames*, volume 134 of *International Association of Geodesy Symposia*, pages 11–16. Springer Berlin Heidelberg, 2009. ISBN 978-3-642-00860-3. URL http://dx.doi.org/10.1007/978-3-642-00860-3_2.

Y. Aoyama and I. Naito. Wind contributions to the Earth's angular momentum budgets in seasonal variation. *Journal of Geophysical Research*, 105:12417–12431, 2000. URL http://www.agu.org/journals/jd/v105/iD10/2000JD900101/2000JD900101.pdf.

Y. Aoyama, I. Naito, T. Iwabuchi, and N. Yamazaki. Atmospheric quasi-14 month fluctuation and excitation of the Chandler wobble. *Earth Planets Space*, 55:e25–e28, 2003. URL http://www.terrapub.co.jp/journals/EPS/abstract/5512/5512e025.html.

W. Baarda. A testing procedure for use in geodetic networks. Technical report, Netherland Geodetic Commission, 1968. URL http://www.ncg.knaw.nl/Publicaties/Geodesy/09Baarda.html.

R. T. H. Barnes, R. Hide, A. A. White, and C. A. Wilson. Atmospheric angular momentums fluctuations, length-of-day changes and polar motion. *Proceedings of the Royal Society of London,Series A*, 387:31–78, 1983. URL http://www.jstor.org/stable/2397457.

S. Bettadpur. CSR Level-2 Processing Standards Document for Product Release 04. Technical report, 2007. URL http://isdc.gfz-potsdam.de/index.php?name=UpDownload&req=viewsdownload&sid=9.

S. Bettadpur. CSR RL05. presentation on the EGU 2012, Vienna, 2012. URL http://www.csr.utexas.edu/grace/Bettadpur_RL05.pdf.

R. Biancale and A. Bode. Mean Annual and Seasonal Atmospheric Tide Models Based on 3-hourly and 6-hourly ECMWF Surface Pressure Data. Technical Report STR 06/01, GeoForschungsZentrum Potsdam, 2006. URL http://bib.gfz-potsdam.de/pub/str0601/0601.pdf.

C. Bizouard and D. Gambis. The combined solution C04 for Earth Orientation Parameters consistent with International Terrestrial Reference Frame 2008. Online, last access July 2012, 2010. URL ftp://hpiers.obspm.fr/iers/eop/eopc04/C04.guide.pdf.

S. Bruinsma, J.-M. Lemoine, R. Biancale, and N. Valès. CNES/GRGS 10-day gravity field models (release 2) and their evaluation. *Advances in Space Research*, 45(4):587 – 601, 2010. ISSN 0273-1177. doi: 10.1016/j.asr.2009.10.012. URL http://www.sciencedirect.com/science/article/pii/S0273117709006759.

L. Carrére and F. Lyard. Modeling the barotropic response of the global ocean to atmospheric wind and pressure forcing - comparisons with observations. *Geophys. Res. Lett.*, 30 (6):1275–, Mar. 2003. ISSN 0094-8276. URL http://dx.doi.org/10.1029/2002GL016473.

S. C. Chandler. On the variation of latitude, I. *Astronomical Journal*, 11. iss. 248:59–61, 1891. URL http://adsabs.harvard.edu/full/1891AJ.....11...59C.

B. F. Chao and W.-Y. Chung. Amplitude and phase variations of Earth's Chandler wobble under continual excitation. *Journal of Geodynamics*, pages –, 2011. ISSN 0264-3707. doi: 10.1016/j.jog.2011.11.009. URL http://www.sciencedirect.com/science/article/pii/S026437071100130X.

J. Chen, C. Wilson, and K.-W. Seo. S2 tide aliasing in GRACE time-variable gravity solutions. *Journal of Geodesy*, 83:679–687, 2009. ISSN 0949-7714. URL http://dx.doi.org/10.1007/s00190-008-0282-1.

M. Cheng and B. D. Tapley. Variations in the Earth's oblateness during the past 28 years. *J. Geophys. Res.*, 109(B9):B09402–, Sept. 2004. ISSN 0148-0227. URL http://dx.doi.org/10.1029/2004JB003028.

N. Copernicus. *De revolutionibus orbium coelestium*. Petreium, J., Nürnberg, 1543. URL http://de.wikisource.org/wiki/Nicolaus_Coppernicus_aus_Thorn_%C3%BCber_die_Kreisbewegungen_der_Weltk%C3%B6rper. German translation by K.-L. Menzzer, (1879).

A. Cowell. After 350 Years, Vatican Says Galileo Was Right: It Moves. *The New York Times*, October 31 1992. URL http://www.nytimes.com/1992/10/31/world/after-350-years-vatican-says-galileo-was-right-it-moves.html.

N. Crocetto, M. Gatti, and P. Russo. Simplified formulae for the BIQUE estimation of variance components in disjunctive observation groups. *Journal of Geodesy*, 74:447–457, Sep 2000. URL http://dx.doi.org/10.1007/s001900000109.

F. A. Dahlen. The Passive Influence of the Oceans upon the Rotation of the Earth. *Geophysical Journal of the Royal Astronomical Society*, 46(2):363–406, 1976. ISSN 1365-246X. URL http://dx.doi.org/10.1111/j.1365-246X.1976.tb04163.x.

J. L. Davis, M. E. Tamisiea, P. Elósegui, J. X. Mitrovica, and E. M. Hill. A statistical filtering approach for Gravity Recovery and Climate Experiment (GRACE) gravity data. *J. Geophys. Res.*, 113(B4):B04410–, Apr. 2008. ISSN 0148-0227. URL http://dx.doi.org/10.1029/2007JB005043.

D. P. Dee, S. M. Uppala, A. J. Simmons, P. Berrisford, P. Poli, S. Kobayashi, U. Andrae, M. A. Balmaseda, G. Balsamo, P. Bauer, P. Bechtold, A. C. M. Beljaars,

L. van de Berg, J. Bidlot, N. Bormann, C. Delsol, R. Dragani, M. Fuentes, A. J. Geer, L. Haimberger, S. B. Healy, H. Hersbach, E. V. Hólm, L. Isaksen, P. Kållberg, M. Köhler, M. Matricardi, A. P. McNally, B. M. Monge-Sanz, J.-J. Morcrette, B.-K. Park, C. Peubey, P. de Rosnay, C. Tavolato, J.-N. Thépaut, and F. Vitart. The ERA-Interim reanalysis: configuration and performance of the data assimilation system. *Quarterly Journal of the Royal Meteorological Society*, 137(656):553–597, 2011. URL http://dx.doi.org/10.1002/qj.828.

V. Dehant and P. Mathews. Earth Rotation Variations . In T. Herring, editor, *Treatise on Geophysics*, volume 3, pages 295–349. Elsevier, 2007.

S. D. Desai. Observing the pole tide with satellite altimetry. *J. Geophys. Res.*, 107(C11):3186–, Nov. 2002. URL http://dx.doi.org/10.1029/2001JC001224.

S. R. Dickman. Evaluation of "effective angular momentum function" formulations with respect to core-mantle coupling. *Journal of Geophysical Research (Solid Earth)*, 108:2150, Mar. 2003. URL http://dx.doi.org/10.1029/2001JB001603.

S. R. Dickman and R. S. Gross. Rotational evaluation of a long-period spherical harmonic ocean tide model. *Journal of Geodesy*, 84:457–464, 2010. URL http://dx.doi.org/10.1007/s00190-010-0383-5.

S. R. Dickman and Y. S. Nam. Revised predictions of long-period ocean tidal effects on Earth's rotation rate. *J. Geophys. Res.*, 100(B5):8233–8243, 1995. URL http://dx.doi.org/10.1029/95JB00028.

R. Dill. *Der Einfluss von Sekundäreffekten auf die Rotation der Erde*. PhD thesis, Technische Universität München, 2002. URL http://www.iapg.bv.tum.de/Dissertationen/.

R. Dill. Hydrological model LSDM for operational earth rotation and gravity field variations. Technical Report 08/09, Helmholtz-Zentrum Potsdam Deutsches GeoForschungsZentrum, 2008. URL http://edoc.gfz-potsdam.de/gfz/11927.

H. Dobslaw and M. Thomas. Impact of river run-off on global ocean mass redistribution. *Geophysical Journal International*, 168(2):527–532, 2007. URL http://dx.doi.org/10.1111/j.1365-246X.2006.03247.x.

H. Dobslaw, R. Dill, A. Grötzsch, A. Brzeziński, and M. Thomas. Seasonal polar motion excitation from numerical models of atmosphere, ocean, and continental hydrosphere. *J. Geophys. Res.*, 115(B10):B10406–, Oct. 2010. URL http://dx.doi.org/10.1029/2009JB007127.

S. Drijfhout, C. Heinze, M. Latif, and E. Maier-Reimer. Mean Circulation and Internal Variability in an Ocean Primitive Equation Model. *Journal of Physical Oceanography*, 26(4):559–580, 1996. URL http://oceanrep.geomar.de/13046/.

A. M. Dziewonski and D. L. Anderson. Preliminary reference Earth model. *Physics of the Earth and Planetary Interiors*, 25(4):297 – 356, 1981. URL http://www.sciencedirect.com/science/article/pii/0031920181900467.

T. M. Eubanks. Variations in the Orientation of the Earth. In D. E. Smith & D. L. Turcotte, editor, *Contributions of Space Geodesy to Geodynamics: Earth Dynamics*, 1993.

L. Euler. *Theoria motus corporum solidorum seu rigidorum*. Rostochii et Gryphiswaldiae litteris et impensis, 1765. URL http://www.math.dartmouth.edu/~euler/pages/E289.html. English translation by Ian Bruce.

F. Flechtner. GFZ Level-2 Processing Standards Document for Product Release 04. Technical report, 2007a. URL http://isdc.gfz-potsdam.de/index.php?name=UpDownload&req=viewsdownload&sid=9.

F. Flechtner. AOD1B Product Description Document for Product Releases 01 to 04. Technical report, 2007b. URL http://isdc.gfz-potsdam.de/index.php?name=UpDownload&req=viewsdownload&sid=8.

C. Förste, R. Schmidt, R. Stubenvoll, F. Flechtner, U. Meyer, R. König, H. Neumayer, R. Biancale, J.-M. Lemoine, S. Bruinsma, S. Loyer, F. Barthelmes, and S. Esselborn. The GeoForschungsZentrum Potsdam/Groupe de Recherche de Géodésie Spatiale satellite-only and combined gravity field models: EIGEN-GL04S1 and EIGEN-GL04C. *Journal of Geodesy*, 82:331–346, 2008. URL http://dx.doi.org/10.1007/s00190-007-0183-8.

W. Förstner. Ein Verfahren zur Schätzung von Varianz- und Kovarianzkomponenten. *Allgemeine Vermessungs-Nachrichten*, 11-12:447–453, 1979.

M. Furuya and B. F. Chao. Estimation of period and Q of the Chandler wobble. *Geophysical Journal International*, 127 (3):693–702, 1996. URL http://dx.doi.org/10.1111/j.1365-246X.1996.tb04047.x.

G. Galilei. *Dialogo di Galileo Galilei sopra i due Massimi Sistemi del Mondo Tolemaico e Copernicano (Dialogue Concerning the Two Chief World System)*. University of California Press, 1632. URL http://archimedes.mpiwg-berlin.mpg.de/cgi-bin/toc/toc.cgi?step=thumb&dir=galil_syste_065_en_1661. translated by T. Salusbury (1661).

G. Gaspari and S. E. Cohn. Construction of correlation functions in two and three dimensions. *Quarterly Journal of the Royal Meteorological Society*, 125(554):723–757, 1999. URL http://dx.doi.org/10.1002/qj.49712555417.

D. Gibert and J.-L. Le Mouël. Inversion of polar motion data: Chandler wobble, phase jumps, and geomagnetic jerks. *J. Geophys. Res.*, 113(B10):B10405–, Oct. 2008. URL http://dx.doi.org/10.1029/2008JB005700.

F. Gilbert and A. M. Dziewonski. An Application of Normal Mode Theory to the Retrieval of Structural Parameters and Source Mechanisms from Seismic Spectra. *Philosophical Transactions of the Royal Society of London. Series A, Mathematical and Physical Sciences*, 278(1280):pp. 187–269, 1975. URL http://www.jstor.org/stable/74517.

F. Göttl. *Kombination geodätischer Raumbeobachtungen zur Bestimmung von geophysikalischen Anregungsmechanismen der Polbewegung*. PhD thesis, Technische Universität München, 2013. URL http://www.iapg.bv.tum.de/Dissertationen/.

H. Greiner-Mai. The influence of the electromagnetic core-mantle coupling torques on earth's rotation. *Astronomische Nachrichten*, 308(3):217–226, 1987. ISSN 1521-3994. doi: 10.1002/asna.2113080313. URL http://dx.doi.org/10.1002/asna.2113080313.

H. Greiner-Mai and J. M. Hagedoorn. Core-mantle coupling: Part ii: Topographic coupling torques. Technical report, Potsdam, 2008. editor : Deutsches GeoForschungsZentrum.

R. Gross. The influence of earthquakes on the Chandler wobble during 1977–1983. *Geophysical Journal of the Royal Astronomical Society*, 85(1):161–177, 1986. URL http://dx.doi.org/10.1111/j.1365-246X.1986.tb05176.x.

R. Gross. Correspondence between theory and observations of polar motion. *Geophys. J. Int.*, 109:162–170, 1992. URL http://www3.interscience.wiley.com/cgi-bin/fulltext/119334495/PDFSTART.

R. Gross. Validating Earth Orientation Series with Models of Atmospheric & Oceanic Angular Momenta. In *Presentation on American Geophysical Union 2009 Fall Meeting*, 2009. URL http://acc.igs.org/erp/igs-repro1_gross_agu09.pdf.

R. S. Gross. The excitation of the Chandler wobble. *Geophys. Res. Lett.*, 27(15):2329–2332, 2000. URL http://dx.doi.org/10.1029/2000GL011450.

R. S. Gross. The Observed Period and Q of the Chandler Wobble. In H. Plag, B. Chao, R. Gross, and T. vanDam, editors, *Proceedings of the Workshop: Forcing of polar motion in the Chandler frequency band: a contribution to understanding interannuale climate variations*, volume 24 of *Cahiers Du Centre Européen de Géodynamique et de Séismologie*, pages 31–37, 23.-21. April 2004.

R. S. Gross. Earth Rotation Variations - Long Period. In T. Herring, editor, *Treatise on Geophysics*, volume 3, chapter 239–294. Elsevier, 2007.

E. Groten. Fundamental Parameters and Current (2004) Best Estimates of the Parameters of Common Relevance to Astronomy, Geodesy, and Geodynamics. *Journal of Geodesy*, 77:724–797, 2004. ISSN 0949-7714. URL http://dx.doi.org/10.1007/s00190-003-0373-y.

J. M. Hagedoorn and H. Greiner-Mai. Core-mantle coupling: Part i: Electromagnetic coupling torques. Technical report, Potsdam, 2008. editor : Deutsches GeoForschungsZentrum.

A. Heiker, H. Kutterer, and J. Müller. Combined Analysis of Earth Orientation Parameters and Gravity Field Coefficients for Mutual Validation. In *Observing our Changing Earth*, volume 133, pages 853–859. Springer Berlin Heidelberg, 2008. URL http://dx.doi.org/10.1007/978-3-540-85426-5_98.

A. Heiker, H. Kutterer, and J. Müller. Stabilization of Satellite Derived Gravity Field Coefficients by Earth Orientation Parameters and Excitation Functions. In S. Kenyon, M. C. Pacino, and U. Marti, editors, *Geodesy for Planet Earth*, volume 136 of *International Association of Geodesy Symposia*, pages 537–543. Springer Berlin Heidelberg, 2012. URL http://dx.doi.org/10.1007/978-3-642-20338-1_65.

F. Helmert. *Die Ausgleichungsrechnung nach der Methode der kleinsten Quadrate*. Teubner Verlag, Leipzig, 3rd edition, 1924. URL http://gdz.sub.uni-goettingen.de/dms/load/img/.

B. Hofmann-Wellenhof and H. Moritz. *Physical Geodesy*. SpringerWienNewYork, second edition, 2006.

S. S. Hough. The Oscillations of a Rotating Ellipsoidal Shell Containing Fluid. *Philosophical Transactions of the Royal Society of London. A*, 186:pp. 469–506, 1895. URL http://www.jstor.org/stable/90651.

M. F. Hutchinson. A Stochastic Estimator of the Trace of the Influence Matrix for Laplacian Smoothing Splines. *Communications in Statistics - Simulation and Computation*, 18:1059–1076, 1989. URL http://www.informaworld.com/10.1080/03610918908812806.

IERS Conventions. *IERS Conventions (1996)*, volume IERS Technical Note No. 21. Central Bureau of IERS - Observatoire de Paris, 1996. URL http://www.iers.org/nn_11216/SharedDocs/Publikationen/EN/IERS/Publications/tn/TechnNote21/tn21,templateId=raw,property=publicationFile.pdf/tn21.pdf.

IERS Conventions. *IERS Conventions (2003)*, volume IERS Technical Note No. 32. Verlag des Bundesamts für Kartographie und Geodäsie, 2003. URL http://www.iers.org/nn_11216/SharedDocs/Publikationen/EN/IERS/Publications/tn/TechnNote32/tn32,templateId=raw,property=publicationFile.pdf/tn32.pdf.

IERS Conventions. *IERS Conventions (2010)*, volume IERS Technical Note No. 36. Verlag des Bundesamts für Kartographie und Geodäsie, 2010. URL http://www.iers.org/nn_11216/SharedDocs/Publikationen/EN/IERS/Publications/tn/TechnNote36/tn36,templateId=raw,property=publicationFile.pdf/tn36.pdf.

JCGM. International vocabulary of metrology – Basic and general concepts and associated terms (VIM), 2008. URL http://www.bipm.org/utils/common/documents/jcgm/JCGM_200_2008.pdf. Working Group 2 of the Joint Committee for Guides in Metrology.

H. Jeffreys. The Variation of Latitude. In P. J. Melchior and S. Yumi, editors, *Rotation of the Earth*, volume 48 of *IAU Symposium*, page 39, 1972.

E. Kalnay, M. Kanamitsu, R. Kistler, W. Collins, D. Deaven, L. Gandin, M. Iredell, S. Saha, G. White, J. Woollen, Y. Zhu, A. Leetmaa, R. Reynolds, M. Chelliah, W. Ebisuzaki, W. Higgins, J. Janowiak, K. C. Mo, C. Ropelewski, J. Wang, R. Jenne, and D. Joseph. The NCEP/NCAR 40-Year Reanalysis Project. *Bull. Amer. Meteor. Soc.*, 77(3):437–471, Mar. 1996. URL http://dx.doi.org/10.1175/1520-0477(1996)077<0437:TNYRP>2.0.CO;2.

L. H. Kantha, J. S. Stewart, and S. D. Desai. Long-period lunar fortnightly and monthly ocean tides. *J. Geophys. Res.*, 103(C6):12639–12647, 1998. URL http://dx.doi.org/10.1029/98JC00888.

R. Klees, E. A. Revtova, B. C. Gunter, P. Ditmar, E. Oudman, H. C. Winsemius, and H. H. G. Savenije. The design of an optimal filter for monthly GRACE gravity models. *Geophysical Journal International*, 175(2):417–432, 2008. URL http://dx.doi.org/10.1111/j.1365-246X.2008.03922.x.

K. Koch. Maximum likelihood estimate of variance components. *Journal of Geodesy*, 60:329–338, Dec 1986. URL http://dx.doi.org/10.1007/BF02522340.

K. Koch. *Parameter Estimation and Hypothesis Testing in Linear Models*. Springer, Berlin, second edition, 1999.

K. Koch and J. Kusche. Regularization of geopotential determination from satellite data by variance components. *Journal of Geodesy*, 76:259–268, May 2002. URL http://dx.doi.org/10.1007/s00190-002-0245-x.

K. Koch and M. Schmidt. *Deterministische und stochastische Signale*. Dümmler Verlag, Bonn, 1994. URL http://www.igg.uni-bonn.de/tg/fileadmin/publication/media/Determ_u_stoch_Signale.pdf.

K. Koch, H. Kuhlmann, and W.-D. Schuh. Approximating covariance matrices estimated in multivariate models by estimated auto- and cross-covariances. *Journal of Geodesy*, 84:383–397, 2010. URL http://dx.doi.org/10.1007/s00190-010-0375-5.

C. Kreemer, D. A. LavallÃ©e, G. Blewitt, and W. E. Holt. On the stability of a geodetic no-net-rotation frame and its implication for the International Terrestrial Reference Frame. *Geophys. Res. Lett.*, 33(17):L17306–, Sept. 2006. URL http://dx.doi.org/10.1029/2006GL027058.

J. Kuehne, C. R. Wilson, and S. Johnson. Estimates of the Chandler wobble frequency and Q. *J. Geophys. Res.*, 101 (B6):13573–13579, 1996. URL http://dx.doi.org/10.1029/96JB00663.

E. Kurtenbach, A. Eicker, T. Mayer-Gürr, M. Holschneider, M. Hayn, M. Fuhrmann, and J. Kusche. Improved daily GRACE gravity field solutions using a Kalman smoother. *Journal of Geodynamics*, 59 - 60(0):39 – 48, 2012. URL http://www.sciencedirect.com/science/article/pii/S0264370712000385.

J. Kusche. A Monte-Carlo technique for weight estimation in satellite geodesy. *Journal of Geodesy*, 76:641–652, 2003. URL http://dx.doi.org/10.1007/s00190-002-0302-5.

J. Kusche. Approximate decorrelation and non-isotropic smoothing of time-variable GRACE-type gravity field models. *Journal of Geodesy*, 81:733–749, 2007. URL http://dx.doi.org/10.1007/s00190-007-0143-3.

J. Kusche and R. Klees. Regularization of gravity field estimation from satellite gravity gradients. *Journal of Geodesy*, 76:359–368, 2002. URL http://dx.doi.org/10.1007/s00190-002-0257-6.

K. Lambeck. *The Earth's Variable Rotation: Geophysical Causes and Consequences*. Cambridge University Press, 1980.

H. Lenhardt and E. Groten. Chandler wobble parameters from BIH and ILS data. *manuscripta geodaetica*, 10(4): 296–305, 1985.

D. Liao, X. Liao, and Y. Zhou. Oceanic and atmospheric excitation of the Chandler wobble. *Geophysical Journal International*, 152(1):215–227, 2003. URL http://dx.doi.org/10.1046/j.1365-246X.2003.01843.x.

F. Lyard, F. Lefevre, T. Letellier, and O. Francis. Modelling the global ocean tides: modern insights from FES2004. *Ocean Dynamics*, 56:394–415, 2006. URL http://dx.doi.org/10.1007/s10236-006-0086-x.

J. Marshall, A. Adcroft, C. Hill, L. Perelman, and C. Heisey. A finite-volume, incompressible Navier Stokes model for studies of the ocean on parallel computers. *J. Geophys. Res.*, 102(C3):5753–5766, 1997a. URL http://dx.doi.org/10.1029/96JC02775.

J. Marshall, C. Hill, L. Perelman, and A. Adcroft. Hydrostatic, quasi-hydrostatic, and nonhydrostatic ocean modeling. *J. Geophys. Res.*, 102(C3):5733–5752, 1997b. URL http://dx.doi.org/10.1029/96JC02776.

Z. Martinec and J. Hagedoorn. Time-domain approach to linearized rotational response of a three-dimensional viscoelastic earth model induced by glacial-isostatic adjustment: I. inertia-tensor perturbations. *Geophysical Journal International*, 163(2):443–462, 2005. ISSN 1365-246X. doi: 10.1111/j.1365-246X.2005.02758.x. URL http://dx.doi.org/10.1111/j.1365-246X.2005.02758.x.

P. M. Mathews, B. A. Buffett, T. A. Herring, and I. I. Shapiro. Forced Nutations of the Earth: Influence of Inner Core Dynamics 2. Numerical Results and Comparisons. *J. Geophys. Res.*, 96(B5):8243–8257, 1991. URL http://dx.doi.org/10.1029/90JB01956.

P. M. Mathews, T. A. Herring, and B. A. Buffett. Modeling of nutation and precession: New nutation series for nonrigid Earth and insights into the Earth's interior. *Journal of Geophysical Research (Solid Earth)*, 107:2068–+, 2002. URL http://adsabs.harvard.edu/abs/2002JGRB..107.2068M.

T. Mayer-Gürr. *Gravitationsfeldbestimmung aus der Analyse kurzer Bahnbögen am Beispiel der Satellitenmissionen CHAMP und GRACE*. PhD thesis, Universität Bonn, Aug 2006. URL http://hss.ulb.uni-bonn.de/diss_online/landw_fak/2006/mayer-guerr_torsten/0904.pdf.

T. Mayer-Gürr, A. Eicker, E. Kurtenbach, and K.-H. Ilk. ITG-GRACE: Global Static and Temporal Gravity Field Models from GRACE Data. In F. M. Flechtner, T. Gruber, A. Güntner, M. Mandea, M. Rothacher, T. Schöne, J. Wickert, L. Stroink, V. Mosbrugger, and G. Wefer, editors, *System Earth via Geodetic-Geophysical Space Techniques*, Advanced Technologies in Earth Sciences, pages 159–168. Springer Berlin Heidelberg, 2010. URL http://dx.doi.org/10.1007/978-3-642-10228-8_13.

M. Meyer. *Signalverarbeitung*. Vieweg+Teubner Verlag, 6. edition, 2011. URL http://dx.doi.org/10.1007/978-3-8348-8138-0.

P. J. Mohr, B. N. Taylor, and D. B. Newell. CODATA recommended values of the fundamental physical constants: 2006. *Rev. Mod. Phys.*, 80:633–730, Jun 2008. URL http://link.aps.org/doi/10.1103/RevModPhys.80.633.

H. Moritz and I. I. Mueller. *Earth rotation*. The Ungar Publishing Company, New York, 1987.

W. Munk and G. MacDonald. *The Rotation of the Earth: A Geophysical Discussion*. Cambridge Monographs on Mechanics. Cambridge University Press, 1960. URL http://books.google.com/books?id=klDqPAAACAAJ.

W. Munk and G. MacDonald. *The Rotation of the Earth. A Geophysical Discussion*. Cambridge University Press, revised edition, 1975.

S. Newcomb. *Astronomy for Everybody.* McClure, Phillips & Co., 1902. URL http://archive.org/stream/astronomyforeve02newcgoog#page/n6/mode/2up.

I. Newton. *Philosophiae Naturalis Principia Mathematica.* 1687. URL http://books.google.de/books?id=Tm0FAAAAQAAJ&pg=PA234&redir_esc=y#v=onepage&q&f=false. Englisch translation by A. Motte (1729).

M. Ooe. An optimal complex AR.MA model of the Chandler wobble. *Geophysical Journal of the Royal Astronomical Society*, 53(3):445–457, 1978. URL http://dx.doi.org/10.1111/j.1365-246X.1978.tb03752.x.

C. Rao. *Linear Statistical Inference and its Applications.* John Wiley & Sons, 1973.

J. Ray. A Quasi-Optimal, Consistent Approach for Combination of UT1 and LOD. In H. Drewes, editor, *Geodetic Reference Frames*, volume 134 of *International Association of Geodesy Symposia*, pages 239–243. Springer Berlin Heidelberg, 2009. URL http://dx.doi.org/10.1007/978-3-642-00860-3_37.

J. C. Ries, R. J. Eanes, C. K. Shum, and M. M. Watkins. Progress in the determination of the gravitational coefficient of the Earth. *Geophys. Res. Lett.*, 19(6):529–531, 1992. URL http://dx.doi.org/10.1029/92GL00259.

M. G. Rochester and D. E. Smylie. On changes in the trace of the earth's inertia tensor. *J. Geophys. Res.*, 79:4948–4951, 1974.

D. A. Salstein, R. D. Rosen, D. M. Kann, and A. J. Miller. The Sub-bureau for Atmospheric Angular Momentum of the International Earth Rotation Service: A Meteorological Data Center with Geodetic Applications. *Bull. Amer. Meteor. Soc.*, 74(1):67–80, Jan. 1993. URL http://dx.doi.org/10.1175/1520-0477(1993)074<0067:TSBFAA>2.0.CO;2.

F. Sansò and W. Schuh. Finite covariance functions. *Journal of Geodesy*, 61:331–347, 1987. URL http://dx.doi.org/10.1007/BF02520559.

R. Savcenko and W. Bosch. EOT08a - empirical ocean tide model from multi-mission satellite altimetry. Technical report, DGFI report 81, 2008. URL http://www.dgfi.badw.de/fileadmin/docs/dgfi_reports/DGFI_Report_81.pdf.

B. Schaffrin. Reliability Measures for Correlated Observations. *Journal of Surveying Engineering*, 123(3):126–137, 1997. URL http://ascelibrary.org/doi/abs/10.1061/%28ASCE%290733-9453%281997%29123%3A3%28126%29.

R. Schlittgen and B. H. Streitberg. *Zeitreihenanalyse.* Oldenbourg, 7. edition, 1997.

R. Schmidt. *Zur Bestimmung des cm-Geoids und dessen zeitlicher Variationen mit GRACE.* PhD thesis, Rheinischen Friedrich-Wilhelms-Universität zu Bonn, 2007. URL http://hss.ulb.uni-bonn.de/2007/1059/1059-index.pdf.

R. Schmidt, U. Meyer, C. Dahle, F. Flechtner, and J. Kusche. Monthly and Weekly EIGEN-GRACE05S Gravity Field Solutions For Monitoring of Mass Variations in the Earth System. In J. Benveniste, P. Berry, S. Calmant, W. Grabs, and P. Kosuth, editors, *Proceedings of the 2nd Space for Hydrology Workshop 'Surface Water Storage and Runoff: Modeling, In-Situ Data and Remote Sensing', ESA Publication WPP-280*, 2007. URL http://earth.esa.int/hydrospace07/participants/11_07/11_07_Schmidt.pdf.

H. Schuh, S. Nagel, and F. Seitz. Linear drift and periodic variations observed in long time series of polar motion. *Journal of Geodesy*, 74:701–710, 2001. URL http://dx.doi.org/10.1007/s001900000133.

F. Seitz. *Atmosphärische und ozeanische Einflüsse auf die Rotation der Erde. Numerische Untersuchungen mit einem dynamischen Erdsystemmodell.* PhD thesis, TU München, 2004. URL http://129.187.165.2/typo3_dgk/docs/c-578.pdf.

F. Seitz. Zur Anregung der Chandler-Schwingung. *zfv - Zeitschrift für Geodäsie, Geoinformation und Landmanagement*, 130(3):166–173, 01 2005.

F. Seitz and J. Stuck. White noise Chandler wobble excitation. In H. Plag, B. Chao, R. Gross, and T. vanDam, editors, *Proceedings of the Workshop: Forcing of polar motion in the Chandler frequency band: a contribution to understanding interannuale climate variations*, volume 24 of *Cahiers Du Centre Européen de Géodynamique et de Séismologie*, pages 15–21, 23.-21. April 2004.

M. Seitz, D. Angermann, M. Bloßfeld, H. Drewes, and M. Gerstl. The 2008 DGFI realization of the ITRS: DTRF2008. *Journal of Geodesy*, pages 1–27, 2012. URL http://dx.doi.org/10.1007/s00190-012-0567-2.

C. Shannon. Communication in the presence of noise. *Proceedings of the IEEE*, 72(9):1192 – 1201, sept. 1984.

L. E. Sjöberg. Unbiased Estimation of Variance-Covariance Components in Condition Adjustment with Unknowns - a MINQUE Approach -. *zfv - Zeitschrift für Geodäsie, Geoinformation und Landmanagement*, 108: 382–387, 1983.

L. E. Sjöberg. Non-negative Variance component estimation in the Gauss-Helmert Adjustment Model. *manuscripta geodaetica*, 9:247–280, 1984.

M. L. Smith and F. Dahlen. The period and Q of the Chandler wobble. *Geophysical Journal International*, 64(1):223–281, 1981. URL http://www3.interscience.wiley.com/cgi-bin/fulltext/119579104/PDFSTART.

D. Stammer, C. Wunsch, R. Giering, C. Eckert, P. Heimbach, J. Marotzke, A. Adcroft, C. N. Hill, and J. Marshall. Volume, heat, and freshwater transports of the global ocean circulation 1993–2000, estimated from a general circulation model constrained by World Ocean Circulation Experiment (WOCE) data. *J. Geophys. Res.*, 108(C1):3007–, Jan. 2003. URL http://dx.doi.org/10.1029/2001JC001115.

S. Swenson and J. M. Wahr. Post-processing removal of correlated errors in GRACE data. *Geophys. Res. Lett.*, 33(8): L08402–, Apr. 2006. URL http://dx.doi.org/10.1029/2005GL025285.

B. Tapley, J. Ries, S. Bettadpur, D. Chambers, M. Cheng, F. Condi, B. Gunter, Z. Kang, P. Nagel, R. Pastor,

T. Pekker, S. Poole, and F. Wang. GGM02 – An improved Earth gravity field model from GRACE. *Journal of Geodesy*, 79:467–478, 2005. URL http://dx.doi.org/10.1007/s00190-005-0480-z.

B. D. Tapley, S. Bettadpur, M. Watkins, and C. Reigber. The gravity recovery and climate experiment: Mission overview and early results. *Geophys. Res. Lett.*, 31(9):L09607–, May 2004. URL http://dx.doi.org/10.1029/2004GL019920.

M. Thomas. *Ocean induced variations of Earth's rotation - Results from a simultaneous model of global circulation and tides*. PhD thesis, University of Hamburg, 2002. URL http://ediss.sub.uni-hamburg.de/volltexte/2002/608/pdf/dissertation.pdf.

W. Torge and J. Müller. *Geodesy*. De Gruyter, 4th edition, 2012.

J. Wahr. The effects of the atmosphere and oceans on the Earth's wobble and on the seasonal variations in the length of day - II. Results. *Geophysical Journal of the Royal Astronomical Society*, 74(2):451–487, 1983. URL http://dx.doi.org/10.1111/j.1365-246X.1983.tb01885.x.

J. Wahr. The earth's rotation. *Annual Review of Earth and Planetary Sciences*, 16:231–249, 1988.

J. Wahr. Polar Motion Models: Angular Momentum Approach. In *Forcing of Polar Motion in the Chandler Frequency Band: A Contribution to understand interannual Climate Change*, volume 24 of *Cahiers du Centre Européen de Géodynamique et Séismologie*. Plag, H.P. and Chao, B.F. and Gross, R.S. and Van Dam, T., 2005.

J. Wahr and Z. Bergen. The effects of mantle anelasticity on nutations, earth tides, and tidal variations in rotation rate. *Geophysical Journal of the Royal Astronomical Society*, 87 (2):633–668, 1986. URL http://dx.doi.org/10.1111/j.1365-246X.1986.tb06642.x.

J. Wahr, S. Swenson, and I. Velicogna. Accuracy of GRACE mass estimates. *Geophys. Res. Lett.*, 33(6):L06401–, Mar. 2006. URL http://dx.doi.org/10.1029/2005GL025305.

M. Watkin and Y. Dah Ning. JPL Level-2 Processing Standards Document for Product Release 04. Technical report, 2007. URL http://isdc.gfz-potsdam.de/index.php?name=UpDownload&req=viewsdownload&sid=9.

C. Wilson and R. Vicente. An analysis of the homogeneous ILS polar motion series. *Geophysical Journal of the Royal Astronomical Society*, 62(3):605–616, 1980. URL http://dx.doi.org/10.1111/j.1365-246X.1980.tb02594.x.

C. Wilson and R. Vicente. Maximum likelihood estimates of polar motion parameters. In D. D. McCarthy and W. Carter, editors, *Variations in Earth Rotation*, volume 59 of *American Geophysical Union Geophysical Monograph Series*, pages 151–155. American Geophysical Union, 1990.

C. R. Wilson and R. A. Haubrich. Meteorological Excitation of the Earth's Wobble. *Geophysical Journal of the Royal Astronomical Society*, 46(3):707–743, 1976. URL http://dx.doi.org/10.1111/j.1365-246X.1976.tb01254.x.

J. Wolff, E. Maier-Reimer, and L. S. The Hamburg Ocean Primitive Equation Model H O P E. Technical report, Deutsches Klimarechenzentrum, 1997. URL http://mms.dkrz.de/pdf/reports/ReportNo.13.pdf.

B. Wouters and E. J. O. Schrama. Improved accuracy of GRACE gravity solutions through empirical orthogonal function filtering of spherical harmonics. *Geophys. Res. Lett.*, 34(23):L23711–, Dec. 2007. URL http://dx.doi.org/10.1029/2007GL032098.

P. Xu, Y. Liu, Y. Shen, and Y. Fukuda. Estimability analysis of variance and covariance components. *Journal of Geodesy*, 81:593–602, 2007. URL http://dx.doi.org/10.1007/s00190-006-0122-0.

C. F. Yoder, J. G. Williams, and M. E. Parke. Tidal Variations of Earth Rotation. *J. Geophys. Res.*, 86 (B2):881–891, 1981. URL http://dx.doi.org/10.1029/JB086iB02p00881.

Z. Yu. A generalization theory of estimation of variance-covariance components. *manuscripta geodaetica*, 17:295–301, 1992.

Y. H. Zhou, D. A. Salstein, and J. L. Chen. Revised atmospheric excitation function series related to Earth's variable rotation under consideration of surface topography. *J. Geophys. Res.*, 111(D12):D12108–, June 2006. URL http://dx.doi.org/10.1029/2005JD006608.

L. Zotov and C. Bizouard. On modulations of the Chandler wobble excitation. *Journal of Geodynamics*, 2012. URL http://www.sciencedirect.com/science/article/pii/S0264370712000518?v=s5.

Lebenslauf / Curriculum Vitae

Persönliche Daten

Name:	Andrea Heiker
Geburtsdatum:	4. August 1976
Geburtsort:	Damme (Niedersachsen)
Familienstand:	ledig

Schulbildung

1983 – 1987	Grundschule Neuenkirchen
1987 – 1989	Orientierungsstufe Neuenkirchen-Vörden
1989 – 1996	Gymnasium Damme

Berufliche Laufbahn

10/1996 – 12/2001	Studium im Studiengang Vermessungswesen an der Leibniz Universität Hannover, Abschluss als Dipl.-Ing
01/2002 – 12/2005	Studiengangskoordinatorin für den Studiengang Geodäsie und Geoinformatik an der Leibniz Universität Hannover
04/2006 – 06/2012	Wissenschaftliche Mitarbeiterin am Geodätischen Institut der Leibniz Universität Hannover
11/2012 –	Referendarin im Landesamt für Geoinformation und Landentwicklung Niedersachsen

Forschungsaufenthalte

11/2009 – 12/2009	Deutsches Geodätisches Forschungsinstitut (DGFI) in München
10/2010 – 12/2010	Jet Propulsion Laboratory (JPL) in Pasadena/Kalifornien

Danksagung / Acknowledgement

Diese Dissertation entstand im Rahmen meiner Arbeit im Projekt P9 der DFG-Forschungsgruppe *Earth Rotation and Global Dynamic Processes* (FOR 584). Der Deutschen Forschungsgemeinschaft möchte ich danken, dass sie die Forschungsgruppe im Allgemeinen und das Projekt 9 im Besonderen großzügig finanziert hat.

Meine zwei Forschungsreisen zum DGFI in München und zum JPL in Pasadena/Kalifornien habe ich aus Mitteln der ÖbVI-Ernst-F.-Simon-Stiftung finanziert. Diese Reisen waren für mich sehr wichtig, da ich dort mein Wissen über die zum Teil schwierig zu verstehenden geophysikalischen Modelle erweitern konnte. Für die großzügige finanzielle Unterstützung möchte ich mich bei der Familie Simon bedanken.

Mein herausragender Dank gilt meinem Doktorvater Prof. Hansjörg Kutterer. Er hat meine Forschungsreisen sehr unterstützt, war bei Problemen stets zur Stelle und hat mir gleichzeitig die benötigten Freiräume gelassen. Herzlichen Dank dafür.

Ich bin meinen Korreferenten Prof. Jürgen Müller und Prof. Michael Schmidt ebenfalls zu großem Dank verpflichtet. Sie standen beide schon früh als Korreferenten fest und haben sich beide sehr engagiert eingebracht und mich auf Aspekte aufmerksam gemacht, die ich bis dahin noch nicht bedacht hatte. Ich danke allen drei Gutachtern für die sehr zügige Begutachtung, so dass die Prüfung noch im Jahr 2012 stattfinden konnte.

Zu besonderen Dank bin ich auch Dr.-Ing. Hamza Alkhatib verpflichtet. Er hat mich auf die Monte-Carlo Verfahren aufmerksam gemacht, mich während der letzten, harten Phase sehr unterstützt und mir stets Mut gemacht. Seine konstruktive Kritik hat meine Arbeit signifikant verbessert.

Danken möchte ich auch meinen Eltern. Sie haben mir nicht nur das Studium finanziert, sondern mir immer wieder den Rücken gestärkt.

I would like to express my deep gratitude to Richard Gross from the Jet Propulsion Laboratory in Pasadena/California. He invited me to the JPL and taught me about geophysical models. Furthermore, the JPL funded furthermore a substantial part of the costs for my research stay. This is gratefully acknowledged.